

The mechanics of shear failures in RC slabs based on refined measurements

Présentée le 3 septembre 2021

Faculté de l'environnement naturel, architectural et construit
Laboratoire de construction en béton
Programme doctoral en génie civil et environnement

pour l'obtention du grade de Docteur ès Sciences

par

Raffaele CANTONE

Acceptée sur proposition du jury

Prof. M. E. S. Violay, présidente du jury
Prof. A. Muttoni, Dr M. Fernández Ruiz, directeurs de thèse
Prof. B. Belletti, rapporteuse
Prof. T. Hrynyk, rapporteur
Dr P. Lestuzzi, rapporteur

To my dear parents Antonio and Teresa,
to my sister Angela,
to my wife Valentina . . .

Foreword

The response of reinforced concrete slabs is a topic of research since their early applications in construction. When subjected to one-way action (typically, when slabs are linearly supported and loaded), their behaviour has been approximated to that of beams or narrow slabs strips. However, when subjected to concentrated loads (predominantly two-way action), the treatment of shear has been traditionally addressed on the basis of punching models. Many doubts arise nevertheless on the mechanical adequacy of such simplifications. Particularly, many cases present concentrated loads near linear supports (as columns near walls in buildings or the deck slabs of bridges), where the predominant action (one- or two-way) is unclear. Also, the pertinence of designing wide slabs (subjected to one-way action but whose failure surface may be significantly variable) in the same manner as beams, has been a topic of scientific debate, with diverging conclusions.

To make a step forward, sometimes it is required to make a step back, revisiting previous experiences. Within this frame, it can be noted that previous experimental programmes have been excessively oriented towards the determination of failure loads, but not towards the understanding of the failure mechanics. To a large extent, this was a consequence of the difficulties of performing detailed measurements within concrete slabs, allowing to track the progression of failure surfaces and the redistribution of internal forces. In this thesis, a new vision on this classical topic is presented. Based on the possibilities offered by state-of-the-art measurement techniques, such as Digital Image Correlation or Fibre-Optic Measurements, a series of fundamental tests were performed in order to understand the basic mechanics of bond and dowelling of reinforcement. On the basis of this knowledge, full-scale tests were performed on slabs under different conditions: narrow strips, one-way action, two-way action and hybrid cases. These tests and the interpretation of their results have allowed, for the first time, to observe in a precise manner a number of phenomena explaining the transfer of forces in slabs and their force redistributions. Grounded on this evidence, the thesis presents a series of mechanical models allowing for a detailed description of the kinematical and mechanical response of slabs. This new knowledge is compared to the performed tests as well as others from the literature showing fine agreement. Other than this, the new knowledge presented opens the door to a more general and consistent modelling of the response of reinforced concrete slabs, allowing to track progression of failure surfaces and the redistribution of internal forces.

This thesis has been funded by the Swiss Federal Road Authority, whose support is greatly appreciated.

Lausanne, February 2021

Prof. Aurelio Muttoni

Dr Miguel Fernández Ruiz

Acknowledgements

For the last six years, the Structural Concrete Laboratory (IBETON) of Ecole Polytechnique Fédérale de Lausanne was my home away from home.

All this was possible thanks to the opportunity given to me by Prof. Muttoni, to whom I am very grateful for having conveyed me his passion and dedication, showing always the fascinating side of our profession. My sincere gratitude goes also to Dr Miguel Fernández Ruiz, an admirable human being and gifted beyond compare who was a source of great inspiration.

I would like also to acknowledge the members of the jury. First of all, a huge thanks goes to Prof. Beatrice Belletti who gave me the possibility with Prof. Muttoni to come to EPFL for my master thesis. In addition, I would like to thank Prof. Trevor Hrynyk, Dr Pierino Lestuzzi and Prof. Marie Violay for the revision of the manuscript and for the inspirational questions during the defence.

This work would not have been possible without the Swiss Federal Road Authority (OFROU) whose financial support was greatly appreciated. In addition, I would like to acknowledge Peikko and Ancotech for the interesting collaboration in the first years of the PhD.

During this journey, I had the possibility to meet extraordinary people who constantly inspired me and helped me improve as both an engineer as well as a human being. First of all, I would like to thank my great officemates, Francesco Moccia and Francesco Cavagnis for the daily discussions and for the reciprocal support in the difficult moments, creating a strong bond that will definitely continue.

A special thanks goes also to our dear secretary Yvonne Buehl-Branch, always by our side both for administrative issues and to support us in hard times. I would like also to acknowledge Dr Olivier Burdet for the support in IT issues and for the nice discussions regarding the experimental works.

I would like to thank all my colleagues from IBETON starting from the senior generation who warmly welcomed me in my first years in Switzerland. A special thanks goes to João, Francesco (Cavagnis), Ioannis, Francisco, Jürgen, Fabio, Filip, Darko and Marie-Rose. I am also very grateful to my dear colleagues who spent their whole PhD with me. In particular, I would like to thank Patrick Valeri, Max Tirassa and Francesco (Moccia) for their support and for the activities carried together outside the school. I would like to express my deepest gratitude to the younger generation of colleagues who brought a lovely vitality in the team. In particular, I would like to thank Enrique who shared with me the last months of laboratory testing during the pandemic as well as Diego, Xhemi, Frédéric, Qianhui and Marko. A special thanks goes also to the post-doc Andri Setiawan

for the inspiring collaboration during the last months of the PhD.

EPFL allowed me to meet amazing people from other laboratories. In particular, huge thanks go to Michele, Danilo, Angelica, Francesco (Vanin), Philippe, Dario, Matteo, Cristiano and Martina.

The experimental works performed in these years would not have been possible without the great support and expertise of the technicians at the Structural Laboratory of EPFL (GIS). In particular, I would like to thank Gilles, Serge, Gerald, Armin, Frédérique, Francois and Sylvain for their patience and for the nice ideas, which definitely allowed me to improve the quality of my experimental works.

I would like to express my sincere gratitude to my dear friends met in Lausanne for the unforgettable moments and for the positive spirit that gave me more energy to face the challenges of PhD: Fabio, Alessandro, Marco T., Manuel, Aldo, Luca T., Giovanni, Marina, Federico, Chiara and Sara.

Huge thanks go also to all my friends from Italy who always showed their support and motivated me along this journey: Luca A., Marco B., Francesco F., Gianluca F., Annalisa, Cesare, Gianluca P., Francesco (Cavazzoni), Gianluca B. and Alberto.

Finally, I am deeply grateful to my family. I would like to thank my dear parents, Antonio and Teresa, for their hard work and efforts that enabled me to achieve this goal. I always felt blessed to have you as an example. Huge thanks to my sister, Angela, who always motivated and encouraged me during these years and for our special bond that goes beyond time and distance.

Immense gratitude goes to my wife Valentina for her unconditioned support, for her love and for always taking care of me. The PhD and my arrival in Switzerland allowed me to meet you and I feel very lucky to be at your side in the years to come.

Lausanne, April 28, 2021

R. C.

Abstract

Reinforced concrete planar members, as slabs and shells, are structural elements commonly used in the construction technique, which are typically designed without the arrangement of shear reinforcement. Despite the fact that this solution allows for fast and economic construction, the absence of shear reinforcement can give rise to the potential localization of strains within a critical shear crack and eventually to the shear failure of the member before reaching its flexural capacity. In the case of redundant systems, most research on the mechanics of shear failures has been devoted to the strength of the member, neglecting in many cases the development of shear deformations due to inclined cracking as well as the redistributions of internal forces, which are instrumental for the analysis of the response of these members. This situation is to a large extent a consequence of the lack of consistent experimental observations of the strain field of reinforced concrete members. The present thesis addresses the analysis of the mechanics of shear failures in reinforced concrete slabs. The contribution to the state-of-the-art includes a series of theoretical works explaining the observed responses for a series of experimental programmes. These experimental campaigns comprise tests in tension, shear tests in one- and two-way slabs as well as punching tests. For their instrumentation, in addition to classical measurement devices, Fibre-Optic Measurements and Digital Image Correlation were intensively used.

This thesis starts by revisiting the basis of the interaction between reinforcement and concrete. A series of bond tests show the stress concentrations occurring near the ribs and its complex transfer of forces with the surrounding concrete. In addition, tests on beams failing in shear show a complex interaction between bond stresses and kinking on the reinforcement due to the development of dowel action. These phenomena are normally neglected for concrete design due to the ductile nature of reinforcement, but may be relevant for fatigue and negative tension-stiffening effects.

An important step in the knowledge is performed on the understanding of the shear response with respect to the characterization of the deformations in concrete members. Based on a series of test results, a complete description of the deformation field (including shear strains) is presented. On that basis, a rational model is proposed, consistent with the mechanical model of the Critical Shear Crack Theory. This model allows for a precise description of the response and also to describe the through-thickness distribution of the shear deformation.

A general frame for modelling of reinforced concrete slabs is thus presented accounting for the redistribution of internal forces during propagation of the shear crack. This approach is used to investigate a testing programme performed on three wide slabs, analysing in a scientific manner the influence of the width of the member on the shear resistance. The detailed experimental data allow to capture the crack propagation and internal forces redistributions. Clear conclusions and answers are obtained, showing the influence of the shape of the failure surface and of its propagation on the load-carrying capacity.

The research ends with a final investigation on the dowelling action of compression reinforcement, with an application to slabs failing in punching. Based on a large testing programme including eleven axisymmetric punching tests, an analytical approach is developed to estimate the contri-

bution of the dowel action on the load-carrying capacity. This approach is formulated within the frame of the Critical Shear Crack Theory, and is incorporated in a consistent and efficient manner for design purposes.

Keywords: reinforced concrete slabs, shear strength, shear deformations, crack kinematics, shear redistributions, dowel action, Critical Shear Crack Theory, Digital Image Correlation, Fibre Optic Measurements.

Résumé

Les éléments plaque en béton armé, comme les dalles et les coques, sont des éléments structurels couramment utilisés dans la domaine de la construction, qui sont généralement conçus sans armatures d'effort tranchant. Bien que cette solution permette une construction rapide et économique, l'absence d'armature d'effort tranchant peut entraîner la localisation potentielle de déformation dans la fissure critique et finalement la rupture à l'effort tranchant de l'élément avant qu'il n'atteigne sa capacité flexionnelle. Dans le cas des systèmes avec une capacité de redistribution, la plupart des recherches sur les mécanismes de rupture à l'effort tranchant ont porté sur la résistance de l'élément, négligeant dans de nombreux cas le développement des déformations à l'effort tranchant dues à la fissuration inclinée ainsi que les redistributions des efforts internes, qui sont essentielles lors de l'analyse de ces éléments. Cette situation est dans une large mesure la conséquence du manque d'observations expérimentales solide du champ de déformation des éléments en béton armé.

À cet égard, ce travail est consacré à l'analyse des mécanismes de ruptures à l'effort tranchant dans les dalles en béton armé. Les nouvelles avancées dans l'état de l'art comprennent une série de travaux théoriques expliquant les réponses observées pour une série de programmes expérimentaux. Les programmes expérimentaux ont compris des essais de traction, de dalles comprenant un champ de cisaillement parallèle et non parallèle ainsi que des essais de poinçonnement. Concernant les instruments de mesures, en plus des dispositifs de mesure classiques, les mesures par fibres optiques et la corrélation d'images ont été utilisées intensivement.

La thèse débute par un réexamen des bases de l'interaction entre l'armature et le béton. Une série d'essai d'adhérence montre les concentrations de contraintes se produisant près des nervures et la complexité du transfert d'efforts avec le béton environnant. De plus, des essais sur des poutres avec rupture à l'effort tranchant montrent une interaction complexe entre les contraintes d'adhérence et la flexion locale des armatures dû au développement de l'effet goujon. De tels phénomènes sont normalement négligés lors du dimensionnement en raison de la ductilité des armatures, mais peuvent être pertinents pour la fatigue et les effets du « negative tension-stiffening ».

Une étape importante dans la connaissance est également réalisée sur la compréhension de la réponse à l'effort tranchant en termes de déformations pour les éléments en béton. Sur la base d'une série de résultats d'essais, une description complète du champ de déformation (y compris les déformations d'effort tranchant) est présentée. Sur cette base, un modèle est proposé, en accord avec le modèle mécanique de la Théorie de la Fissure Critique. Il permet une description précise de la réponse et également décrit la distribution sur toute l'épaisseur des déformations.

Sur la base des résultats précédents, une approche générale pour la modélisation des dalles en béton armé est présentée, comprenant notamment les redistributions des efforts internes lors de la propagation de la fissure d'effort tranchant. Cette approche est également utilisée pour étudier un programme d'essai spécifique réalisé sur des dalles larges, en analysant l'influence de la largeur d'un élément sur la résistance à l'effort tranchant. Les données expérimentales détaillées permettent de saisir la propagation de la fissure et les redistributions des efforts internes. Des conclusions et des

réponses claires sont obtenues, montrant l'influence de la forme de la surface de rupture et de sa propagation sur la charge de rupture.

La recherche se termine par une étude finale sur l'effet goujon de l'armature en compression, avec application aux ruptures de dalles au poinçonnement. Sur la base d'un vaste programme expérimentale comprenant onze essais sur dalles testées au poinçonnement, une approche analytique est développée pour estimer la contribution de l'effet goujon. Cette approche a été développée dans le cadre de la Théorie de la Fissure Critique, et a été incorporée de manière efficace pour le dimensionnement.

Keywords: dalles en béton armé, résistance à l'effort tranchant, déformation à l'effort tranchant, cinématique de la fissure, redistribution de l'effort tranchant, effet goujon, Théorie de la Fissure Critique, corrélation d'images, mesures par fibres optiques.

Zusammenfassung

Flachförmige Stahlbetonbauteile, wie Platten und Schalen, sind in der Bautechnik weit verbreitete Konstruktionselemente, die typischerweise ohne Schubbewehrung gebaut werden. Diese Lösung ermöglicht eine schnelle und wirtschaftliche Konstruktion, aber das Fehlen der Schubbewehrung kann zu einer potenziellen Lokalisierung von Spannungen innerhalb eines kritischen Schubrisses und schliesslich zum einem Schubversagen des Bauteils bei Lasten unter die Biegetragfähigkeit führen. Bei redundanten Systemen fokussierte vorwiegend die Forschung im Bereich der Schubversagensmechanik auf die Festigkeit des Bauteils. In vielen Fällen wurde die Entwicklung von Scherverformungen aufgrund von schrägen Rissen sowie die Umverteilung von internen Kräften, die für die Analyse der Reaktion von redundanten Bauteilen entscheidend sind, vernachlässigt. Dies folgt zu einem grossen Teil von einem Mangel an konsistenten experimentellen Beobachtungen des Dehnungsfeldes von Stahlbetonbauteilen. Die vorliegende Arbeit befasst sich mit der Analyse der Mechanik des Schubversagens in Stahlbetonplatten. Als neuer Stand der Technik, sie umfasst theoretische Arbeiten zur Erklärung der beobachteten Reaktionen und eine Serie von experimentellen Versuchen, die mit innovativen Messtechniken durchgeführt wurden. Die Versuche untersuchten das Verhalten auf Zug, auf Schub in ein- und zweiachsigen Platten sowie auf Durchstanzen. Für die Instrumentierung wurden neben klassischen Messgeräten auch faseroptische Messungen und digitale Bildkorrelation intensiv eingesetzt.

In der Arbeit werden zunächst die Grundlagen der Interaktion zwischen Bewehrung und Beton aufgearbeitet. Eine Serie von Verbundversuchen zeigt die im Bereich der Rippen auftretenden Spannungskonzentrationen und deren komplexe Kraftübertragung im umgebenden Beton. Darüber hinaus zeigen Versuche an schubversagenden Trägern eine komplexe Interaktion zwischen Verbundspannungen und Knicken der Bewehrung infolge der Dübelwirkung. Solche Phänomene werden normalerweise bei der Betonbemessung aufgrund der duktilen Natur der Bewehrung vernachlässigt, können aber für Ermüdung und negative Zugversteifungseffekte relevant sein. Eine wichtige Erkenntnis ist gewonnen mit dem Verständnis des Schubverhaltens aufgrund der Verformungen von Betonbauteilen. Basierend auf einer Serie von Versuchsergebnissen wird eine vollständige Beschreibung des Verformungsfeldes (einschliesslich Scherdehnungen) vorgestellt. Auf dieser Grundlage wird ein rationales Modell vorgeschlagen, das mit dem mechanischen Modell der Kritischen Riss Theorie übereinstimmt. Es ermöglicht eine genaue Beschreibung der Antwort und auch die Beschreibung ihrer Verteilung über die Dicke.

Basierend auf den bisherigen Erkenntnissen wird ein allgemeiner Rahmen für die Modellierung von Stahlbetonplatten vorgestellt, der insbesondere Umverteilungen von Schnittgrössen während der Ausbreitung des Schubrisses umfasst. Dieser Ansatz wurde in einem speziellen Versuchsprogramm an breiten Platten verwendet, um auf wissenschaftliche Weise den Einfluss der Breite eines Bauteils auf die Schubfestigkeit zu analysieren.

Das Programm umfasste eine grosse Anzahl von detaillierten Messungen, die es ermöglichten, die Rissausbreitung und die Umverteilung der inneren Kräfte zu erfassen. Es wurden klare Schlussfolgerungen und Antworten erhalten, die den Einfluss der Form der Bruchfläche und ihrer Ausbreitung

auf die Bruchlast zeigen.

Die Forschung endet mit einer abschliessenden Untersuchung der Dübelwirkung der Druckbewehrung in Platten, die im Durchstanzen versagen. Basierend auf einem umfangreichen Versuchsprogramm wird ein analytischer Ansatz entwickelt, um diesen Beitrag abzuschätzen. Dieser Ansatz wurde im Rahmen der Kritischen Riss Theorie formuliert und in einer konsistenten und effizienten Weise für Bemessungszwecke eingesetzt.

Schlüsselwörter: Stahlbetonplatten, Schubfestigkeit, Scherverformungen, Risskinematik, Schubumverteilung, Dübelwirkung, Kritischen Riss Theorie, digitale Bildkorrelation, faseroptische Messungen.

Riassunto

Strutture piane in cemento armato, come lastre e gusci, sono elementi strutturali comunemente usati nel campo della costruzione, tipicamente progettati senza la disposizione di armature a taglio. Malgrado questa soluzione permetta una costruzione veloce ed economica, l'assenza di armatura a taglio può dare luogo alla potenziale localizzazione di deformazioni lungo una fessura critica di taglio e alla rottura a taglio dell'elemento strutturale prima di raggiungere la sua capacità flessionale.

Nel caso di sistemi con capacità di redistribuzione, la maggior parte della ricerca scientifica sulla meccanica delle rotture a taglio è stata dedicata alla resistenza dell'elemento, trascurando, in molti casi, lo sviluppo delle deformazioni a taglio dovute alla presenza di fessure inclinate così come la redistribuzione degli sforzi interni, i quali rappresentano un parametro significativo per l'analisi della risposta globale di tali elementi. Questa situazione è in gran parte una conseguenza della mancanza di osservazioni sperimentali dettagliate del campo di deformazione di elementi in calcestruzzo armato.

La presente tesi affronta l'analisi della meccanica delle rotture a taglio di piastre in cemento armato. I nuovi progressi nello stato dell'arte comprendono una serie di lavori teorici che spiegano il comportamento osservato attraverso una serie di campagne sperimentali. Tali campagne sperimentali comprendono prove a trazione, prove su travi, prove su piastre soggette a campi di taglio parallelo e non parallelo, come anche prove a punzonamento. Per quanto riguarda le tecniche di misura adottate, oltre ai dispositivi di misurazione classici, sono stati utilizzati intensamente fibre ottiche (implementate nelle barre d'armatura) e la correlazione digitale di immagini.

La tesi esordisce rivisitando le basi dell'interazione tra armatura e calcestruzzo. Una serie di prove di aderenza mostrano le concentrazioni di sforzo locali che si verificano in vicinanza delle nervature delle barre d'armatura e il complesso trasferimento di forze con il calcestruzzo circostante. Inoltre, prove su travi con rottura a taglio mostrano la complessa interazione tra le sollecitazioni dovute all'aderenza e la flessione locale dell'armatura a causa dell'attivazione dell'effetto piolo. Questi fenomeni sono normalmente trascurati per la progettazione del calcestruzzo armato a causa della natura duttile dell'armatura, ma possono essere rilevanti per il comportamento a fatica e per gli effetti sul tension-stiffening negativo (per elementi soggetti a carichi ciclici).

Un passo importante nella comprensione della risposta strutturale a taglio è svolto, in particolare, per quanto riguarda la caratterizzazione delle deformazioni di elementi in calcestruzzo. Sulla base di una serie di risultati sperimentali, è presentata una descrizione completa del campo di deformazione (comprese le deformazioni di taglio). Su questa base, un approccio di calcolo è proposto, in accordo con il modello meccanico della Teoria della Fessura Critica. Esso permette una descrizione precisa sia della risposta strutturale globale sia della distribuzione delle deformazioni a taglio lungo lo spessore dell'elemento.

Sulla base dei risultati precedenti, è in seguito presentato un approccio per la modellazione di piastre in cemento armato, tenendo conto, in particolare, delle redistribuzioni degli sforzi interni dovuti alla propagazione della fessura di taglio. Tale metodologia è utilizzata per analizzare i

risultati di una campagna sperimentale eseguita su piastre larghe, analizzando l'influenza della larghezza dell'elemento sulla resistenza al taglio.

Le dettagliate osservazioni sperimentali permettono di seguire la propagazione della fessura a taglio e le ridistribuzioni degli sforzi interni. Tali misure consentono di ottenere conclusioni e risposte chiare, mostrando l'influenza della forma della superficie di rottura e della sua propagazione sul carico di rottura.

La ricerca si conclude con un'indagine sul contributo dell'effetto piolo dell'armatura compressa, in particolar modo per quanto riguarda l'applicazione a piastre con rotture a punzonamento. Sulla base di un'ampia campagna di prove, un approccio analitico è sviluppato al fine di stimare il contributo dell'effetto piolo sulla resistenza a punzonamento. Tale approccio è stato formulato nell'ambito della Teoria della Fessura Critica, ed è stato incorporato in modo efficiente ai fini della progettazione.

Parole chiave: piastre in cemento armato, resistenza a taglio, deformazioni a taglio, cinematica della fessura, ridistribuzioni a taglio, effetto piolo, Teoria della Fessura Critica, correlazione digitale di immagini, fibre ottiche.

Resumen

Los elementos planos de hormigón armado, como losas y láminas, son elementos estructurales usados comúnmente en la construcción, normalmente diseñados sin armadura de cortante. A pesar de que este tipo de solución permite una construcción rápida y económica, la ausencia de armadura de cortante puede provocar la localización de deformaciones en una fisura crítica y causar la rotura a cortante del elemento antes de alcanzar su capacidad a flexión. En el caso de sistemas estructurales redundantes, gran parte de la investigación sobre los mecanismos de rotura a cortante se ha centrado en la resistencia de los elementos, obviando en muchos casos el desarrollo de deformaciones de cortante debidas tanto a la inclinación de las fisuras como a las redistribuciones internas de esfuerzos, que son fundamentales para el análisis del comportamiento de este tipo de elementos. Esta situación es consecuencia en gran medida de la falta de observaciones experimentales consistentes de los campos de deformaciones en elementos de hormigón armado.

Esta tesis aborda el análisis de los mecanismos de rotura a cortante en losas de hormigón armado. La contribución al estado del arte incluye una serie de trabajos teóricos que explican los comportamientos observados en un conjunto de campañas experimentales. Dichas campañas constan de ensayos a tracción, ensayos de cortante en losas unidireccionales y bidireccionales, así como ensayos de punzonamiento. Para su instrumentación, además de métodos de medida convencionales, se han empleado exhaustivamente mediciones mediante Fibra Óptica y Correlación Digital de Imagen (DIC).

Esta tesis comienza por revisar la base de la interacción entre la armadura y el hormigón. Una serie de ensayos de adherencia muestran las concentraciones de tensiones que se producen alrededor de las corrugas y los complejos mecanismos de transferencia de fuerzas con el hormigón circundante. Asimismo, varios ensayos en vigas con roturas por cortante esclarecen la compleja interacción que se produce entre las tensiones de adherencia y las desviaciones localizadas en la armadura debido a la acción del efecto pasador (dowel action). Estos fenómenos suelen ignorarse en el diseño de estructuras de hormigón debido a la ductilidad de la armadura, pero pueden ser relevantes en problemas de fatiga o por un efecto negativo de la contribución del hormigón entre fisuras (tension stiffening). Un paso importante en el avance del conocimiento se ha dado en la comprensión de la relación entre la respuesta a cortante y la caracterización de las deformaciones en elementos de hormigón. En base a una serie de ensayos, se presenta una descripción completa de los campos de deformaciones (incluyendo deformaciones de cortante). Sobre esta base, se ha propuesto un modelo congruente con el modelo mecánico de la Teoría de la Fisura Crítica (CSCT). Dicho modelo proporciona una descripción precisa del comportamiento, así como una definición de la distribución de las deformaciones de cortante a lo largo del espesor del elemento.

Por consiguiente, se introduce un marco general para la modelización de losas de hormigón armado que tiene en consideración las redistribuciones internas de esfuerzos durante la propagación de la fisura crítica de cortante. Este enfoque se ha empleado para analizar una campaña experimental consistente en tres losas de gran anchura, estudiando desde una perspectiva científica la influencia de la anchura de un elemento en su resistencia a cortante. La información detallada extraída

de los ensayos ha permitido capturar la propagación de las fisuras y las redistribuciones internas de esfuerzos. Así, se han encontrado respuestas y alcanzado conclusiones claras en relación a la influencia de la forma de la superficie de rotura y su propagación en la capacidad portante del elemento.

El trabajo concluye con una investigación final de la contribución de la armadura de compresión mediante efecto pasador, aplicado a roturas por punzonamiento en losas. En base a una extensa campaña experimental que incluye once ensayos de punzonamiento axisimétricos, se ha desarrollado un enfoque analítico para estimar la contribución del efecto pasador en la resistencia global. Esta formulación se incluye en el marco teórico de la Teoría de la Fisura Crítica (CSCT), y está enunciada de una forma congruente y eficiente, permitiendo su aplicación en el diseño estructural.

Palabras clave: losas de hormigón armado, resistencia cortante, deformaciones de cortante, cinemática de la fisura, redistribuciones de cortante, efecto pasador (dowel action), Teoría de la Fisura Crítica (Critical Shear Crack Theory, CSCT), Correlación Digital de Imagen (DIC), Mediciones mediante Fibra Óptica.

Contents

Foreword	iv
Acknowledgements	v
Abstract	vii
Résumé	ix
Zusammenfassung	xi
Riassunto	xiii
Resumen	xv
1 Introduction	1
1.1 Context and motivation	1
1.2 Objectives	3
1.3 Scientific contributions of the thesis	3
1.4 Structure of the thesis	4
1.5 List of publications	5
2 A detailed view on the rebar-to-concrete interaction based on refined measurement techniques	9
2.1 Introduction	10
2.2 Experimental programme	12
2.3 Pull-out tests	13
2.4 Tension tests	17
2.5 Beam tests	26
2.6 Conclusions	34
2.7 Appendix. Response of tension ties including its unloading response	35
3 Characterization of shear deformations in reinforced concrete members without shear reinforcement	43
3.1 Introduction	44
3.2 Analysis of the displacement and strain field in concrete beams and slabs	46
3.2.1 Testing programme by Cavagnis et al. [23, 24]	46
3.2.2 Definition of kinematical parameters	47
3.2.3 Detailed analysis of the displacement field of RC members	48
3.3 Assumed development of cracking and kinematical parameters	53
3.3.1 Cracking pattern and kinematics	53
3.3.2 Flexural and shear deformations	56
3.3.3 Through-thickness distribution of shear deformations in a smeared approach	57

3.3.4	Shear deformations in the post-peak stage	58
3.4	Implications for modelling	59
3.4.1	Validation of the numerical approach	61
3.4.2	Discussion of the numerical results	62
3.5	Conclusions	65
3.6	Appendix A. Development of the sub-horizontal branch BF of the shear crack	66
3.7	Appendix B. Derivation of cross-sectional response of RC members	67
4	Shear force redistributions and resistance of slabs and wide beams	75
4.1	Introduction	76
4.2	Test programme	81
4.2.1	Main parameters of the specimens and test setup	81
4.2.2	Measurement techniques	84
4.3	Test results	85
4.4	Detailed measurements of displacement and strain fields	89
4.4.1	Slab SC71	89
4.4.2	Slabs SC72 and SC73	91
4.5	Considerations on the response of wide members failing in shear	94
4.6	Modelling of reinforced concrete slabs subjected to concentrated loads and implications for design	97
4.7	Conclusions	99
4.8	Appendix. Elastic-plastic stress fields approach	101
5	Enhancing punching strength and deformation capacity of flat slabs	107
5.1	Introduction	108
5.2	Experimental program	110
5.2.1	Main parameters and test setup	110
5.2.2	Horizontal studs	111
5.2.3	Test results	113
5.2.4	Activation of horizontal dowels	116
5.3	Design for punching of slab-column connections accounting for dowelling action	117
5.3.1	Basic assumptions of CSCT	118
5.3.2	Consideration of dowelling action on punching shear response	118
5.4	Conclusions	125
6	Conclusions and Outlook	131
6.1	Introduction	131
6.2	Conclusions	133
6.3	Outlook and future works	135

Chapter 1

Introduction

1.1 Context and motivation

The mechanics of shear failures in reinforced concrete members has been a topic of debate in the last century. Based on extensive experimental programmes, the shear capacity was observed to be governed by several parameters which are correlated to the material properties, such as the concrete strength and roughness of the crack, and to the localization of strains within a critical shear crack leading to failure [1–5]. On the basis of observations performed mostly on beam specimens or slab strips with prismatic section (whose width is significantly lower than the shear span), analytical and mechanical models have been proposed accounting consistently for different shear–transfer actions [3, 6–8].

However, the direct application of such approaches remains still debatable in the case of redundant systems, as slabs and shells, where the propagation of inclined shear cracks can be associated to the redistribution of internal forces. Notably, it can be noted that significant efforts were mainly devoted to the resistance of the member [9–15] neglecting, in most cases, the uneven distribution of shear forces and the development of shear strains associated to cracked concrete.

With respect to one–way planar members, such as wide beams and slabs subjected to strip loads, there is still disagreement in the scientific community on the influence of the width of the member on the actual shear capacity. Despite strong similarities with beams tested in laboratory, differences can exist due to the distribution of shear strengths along the member which can lead potentially to redistributions of forces between weaker and stronger regions [15–19].

In addition, this can be also the case of slabs subjected to concentrated loads near linear supports (see Figure 1.1a) where high concentrations of shear forces lead some sections to reach their maximum capacity while others have still the potential to increase locally the level of shear force [9, 12, 20, 21]. Even if the resistance of such members is generally calibrated with tests on narrow beams (Figure 1.1b), it can be noted that the response at failure of such members differs significantly from shear failures observed in prismatic members, Figure 1.1b. The acting bending moments and shear forces at the shear critical region are not constant along the width of the member (see Figure 1.1b) and the distribution of internal actions can vary with the level of load due to redistribution of shear and moment fields after cracking [9]. In this framework, the role of shear deformations becomes significant since it was observed to govern, together with the flexural response, the behaviour of reinforced concrete slabs failing in shear.

Despite the significance of shear strains, most research on the modelling of reinforced concrete slabs was addressed to the analysis of flexural deformations focusing on the development of advanced models based on refined moment–curvature laws [22] or layered nonlinear finite elements [23–25].

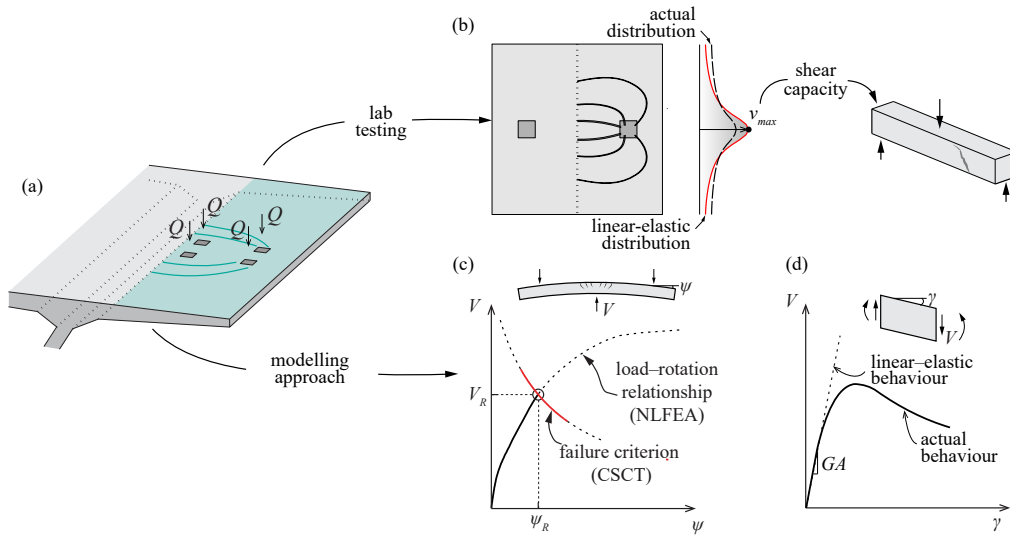


Figure 1.1: (a) slab subjected to concentrated loads; (b) modelling of the actual condition in laboratory and distribution of shear forces in slabs subjected to concentrated loads; and modelling of the load–displacement response: (c) flexural behaviour and (d) through–thickness shear response.

Typically, such modelling approaches were coupled with a suitable failure criterion in shear [3, 26] in order to reproduce out-of-plane shear failures, Figure 1.1c, showing results in sound agreement with the experimental observations. On the other hand, the through–thickness behaviour was generally assumed linear-elastic neglecting the presence of inclined cracking and the influence of the shear deformation, Figure 1.1d.

Efforts to evaluate in a sound manner shear deformations were recently proposed by some researchers [23, 27] with the aim to characterize the through–thickness shear strain distribution. Though, a consistent approach describing the development of shear strains is still required for a better understanding of the redistribution of internal forces in reinforced concrete slabs.

The absence of reliable mechanical models characterizing the development of shear strains was mostly related to a lack of refined experimental measurements on the shear deformations of reinforced members both before and after reaching the maximum shear capacity. Recently, a notable step forward has been performed on measurement techniques allowing for an accurate tracking of the concrete surface displacements as well as of the reinforcement strains [28–34].

In this thesis, taking advantage of such techniques, a detailed investigation of the mechanics of shear failures in reinforced concrete slabs is performed based on refined measurements on the concrete surfaces of beams and slabs using Digital Image Correlation [35], as well as by tracking reinforcement strains with Fibre Optic strain sensors [36]. With this respect, different testing programmes on reinforced concrete members (beams and slabs) were carried out providing new observations on the actual propagation of the failure surface and the development of the shear deformations before and after attaining their maximum capacity. A detailed description of the propagation of shear cracks in reinforced concrete slabs without shear reinforcement is presented with the aim to analyse the mechanical and geometrical parameters affecting the response at failure, such as the clear shear span, the width of the member and the distribution of shear forces. In addition, several phenomena associated to compatibility of deformations (due to shearing or bending of the bars, such as dowel action) were investigated showing the complexity of the interactions between reinforcement and the surrounding concrete as well as its implications on a series of aspects related to brittle failure modes.

1.2 Objectives

As presented in the previous section, a series of questions remain still open. This thesis is thus oriented towards an in-depth investigation of the mechanics of shear failures in reinforced concrete slabs without shear reinforcement enlarging the knowledge on their response. The main objectives of this work are thus the following:

- Contribute with innovative measurements techniques to better understand the rebar-to-concrete interaction and its implications on phenomena involved in shear failures, such as stress concentrations at rebars due to cracks, dowel action and the development of inclined shear cracking in case of cyclic and monotonic loading.
- Provide an approach to assess consistently shear deformations of reinforced concrete slabs based on experimental observations of the concrete surface obtained with Digital Image Correlation.
- Develop a mechanical model for the characterization of the shear deformation (and its through-thickness distribution) in accordance with the main principles of the Critical Shear Crack Theory [8, 37].
- Characterize the distribution of the cross sectional shear deformations in view of a potential implementation within a multi-layered model of a slab element.
- Evaluate the influence of the shape and of the propagation of the failure surface on the response of wide beams and slabs failing in shear.
- Investigate the significance of redistributions of internal forces developing in shear-critical regions and their influence on the load-carrying capacity of reinforced concrete slabs.
- Analyse the influence of the width of the member on the shear capacity of wide beams and slabs.
- Validate the proposed mechanical model on test data of wide beams and slabs subjected to strip loads and concentrated loads providing recommendations for the design and the assessment of these members.
- Investigate the phenomenon of dowel action of compression reinforcement in reinforced concrete slabs failing in punching and derive a practical design approach accounting for its contribution on the load-carrying capacity.

1.3 Scientific contributions of the thesis

The main original scientific contributions of this work can be resumed as follows:

- To provide novel experimental data on the behaviour of reinforced concrete beams and slabs failing in shear using state-of-the-art measurement techniques.
- To evaluate the actual interactions between the reinforcement and the surrounding concrete showing the influence of compatibility of deformations on a series of phenomena engaged in brittle failures, such as strain localization at cracks and shearing/bending of reinforcement.
- To investigate the development of shear deformations in beams and slabs as well as the redistribution of internal forces before and after attaining the maximum shear capacity by means of targeted experimental programmes.
- To derive a mechanical model which allows reproducing accurately the development of shear strains and to predict the load-carrying capacity of redundant systems in accordance with the main principles of the Critical Shear Crack Theory.

- To provide new insights on the role of shear redistributions in wide beams and slabs based on the refined modelling of the through-thickness behaviour.
- To provide experimental data on the influence of the clear shear span and of the width of the member on the shear capacity of beams and slabs subjected to strip loads and to concentrated loads near linear supports.
- To show the influence of the mechanical and geometrical parameters on the load-carrying capacity of redundant systems on the basis of experimental observations and tests collected from literature.
- To provide practical recommendations for the design and assessment of wide beams and slabs failing in shear.
- To investigate the contribution of dowel action in flat slabs supported on columns and to propose a design approach allowing to evaluate the activation of the shear dowels on the basis of the flexural deformation of the member.

1.4 Structure of the thesis

This work is a compilation of four scientific journal articles. Including the introduction, this thesis is structured in six chapters as follows:

- **Chapter 1** presents the main topics challenged in this thesis as well as the objectives and main contributions of this work. A list of publications is also provided.
- **Chapter 2** presents the results of an experimental programme on bond, tension and beam tests with the insight provided by detailed observations on the rebars based on Fibre-Optic Measurements (FOM). This investigation shows the complexity of the interactions engaged between the rebars and the surrounding concrete as well as the influence of compatibility of deformations.
- **Chapter 3** presents a refined investigation of the kinematics observed in shear tests on beams without shear reinforcement [4, 5]. On this basis, a mechanical model to describe the development of shear strains and its through-thickness distribution is derived consistently with the Critical Shear Crack Theory [3]. This allows determining redistributions of internal forces in reinforced concrete slabs as well as its load-carrying capacity.
- **Chapter 4** presents the results of an experimental programme on three cantilever slabs subjected to strip loads and concentrated loads, showing the significance of the shear deformation and of the redistribution of internal forces on the response of the member. The comprehensive approach presented in *Paper 3* is thus adopted to determine the response of slabs with different loading and support conditions providing practical recommendations for the design practice.
- **Chapter 5** presents the outcomes of an experimental programme carried out on eleven punching tests on interior slab-column connections. A novel shear-reinforcing systems is introduced showing its potential to enhance the punching strength of slab-column connections by making use of large-diameter horizontal double-headed studs acting as shear dowels. On the basis of the theoretical frame of the Critical Shear Crack Theory (CSCT) [38], a design approach is proposed with the aim to evaluate the contribution of the shear dowels on the maximum punching capacity.
- **Chapter 6** summarizes the main conclusions of this work and provides an outlook on potential future research.

1.5 List of publications

This research was conducted at the Structural Concrete Laboratory (IBETON) of the Swiss Federal Institute of Technology of Lausanne (EPFL) resulting in the following publications:

- Cantone R., Fernández Ruiz M., Bujnak J., Muttoni A. (2019). Enhancing Punching Strength and Deformation Capacity of Flat Slabs. *ACI Structural Journal*, V. 116(5), pp. 261-274.
- Cantone R., Fernández Ruiz M., Muttoni A. (2020). A detailed view on the rebar-to-concrete interaction based on refined measurement techniques. *Engineering Structures*, V. 226. 111332.
- Cantone R., Setiawan A., Fernández Ruiz M., Muttoni A. Characterization of shear deformations in reinforced concrete members without shear reinforcement. *Engineering Structures*. [submitted for review, February 2021].
- Cantone R., Fernández Ruiz M., Muttoni A. Shear force redistributions and resistance of slabs and wide beams. *Structural Concrete*. [accepted for publication, April 2021].

A more detailed list of publications, including conference papers and other works can be found in the last page of this manuscript (see curriculum vitae).

Bibliography

- [1] G. N. J. Kani. The riddle of shear failure and its solution. *ACI Journal*, 61(4):441–468, 1964.
- [2] G. N. J. Kani. How safe are our large reinforced concrete beams? *ACI Journal*, 64(3):128–141, 1967.
- [3] Aurelio Muttoni and Miguel Fernández Ruiz. Shear Strength of Members without Transverse Reinforcement as Function of Critical Shear Crack Width. *ACI Structural Journal*, 105(2): 163–172, 2008.
- [4] Francesco Cavagnis, Miguel Fernández Ruiz, and Aurelio Muttoni. Shear failures in reinforced concrete members without transverse reinforcement: An analysis of the critical shear crack development on the basis of test results. *Engineering Structures*, 103:157–173, 2015.
- [5] Francesco Cavagnis, Miguel Fernández Ruiz, and Aurelio Muttoni. An analysis of the shear-transfer actions in reinforced concrete members without transverse reinforcement based on refined experimental measurements. *Structural Concrete*, 19(1):49–64, 2017.
- [6] Frank J Vecchio and Michael P Collins. The modified compression field theory for reinforced concrete elements subjected to shear. *ACI Journal*, 83(2):219–231, 1986.
- [7] Yuguang Yang. *Shear Behaviour of Reinforced Concrete Members without Shear Reinforcement A New Look at an Old Problem*. PhD thesis, Delft (Netherlands), 2014.
- [8] Francesco Cavagnis, Miguel Fernández Ruiz, and Aurelio Muttoni. A mechanical model for failures in shear of members without transverse reinforcement based on development of a critical shear crack. *Engineering Structures*, 157:300–315, 2018.
- [9] Francisco Natário, Miguel Fernández Ruiz, and Aurelio Muttoni. Shear strength of RC slabs under concentrated loads near clamped linear supports. *Engineering Structures*, 76:10–23, 2014.
- [10] Karin Reissen and Josef Hegger. Experimentelle Untersuchungen zur mitwirkenden Breite für Querkraft von einfeldrigen Fahrbahnplatten. *Beton- und Stahlbetonbau*, 108(2):96–103, 2013.
- [11] Eva Olívia Lantsoght, Cor Van Der Veen, Ane De Boer, and Joost C. Walraven. One-way slabs subjected to combination of loads failing in shear. *ACI Structural Journal*, 112(4):417–426, 2015.
- [12] Juan Sagaseta, Aurelio Muttoni, Miguel Fernández Ruiz, and Luca Tassinari. Non-axis-symmetrical punching shear around internal columns of RC slabs without transverse reinforcement. *Magazine of Concrete Research*, 63(6):441–457, 2011.
- [13] Karin Reissen and Josef Hegger. Experimentelle Untersuchungen zum Querkrafttragverhalten von auskragenden Fahrbahnplatten unter Radlasten. *Beton- und Stahlbetonbau*, 108(5):315–324, 2013.
- [14] Eva Olívia Lantsoght, Cor Van Der Veen, and Joost C Walraven. Shear in One-Way Slabs under Concentrated Load Close to Support. *ACI Structural Journal*, 110(2):275–284, 2014.
- [15] Edward G Sherwood, Adam Scott Lubell, Evan C. Bentz, and Michael P Collins. One-Way Shear Strength of Thick Slabs and Wide Beams. *ACI Structural Journal*, 103(6):794–802, 2006.
- [16] Antonio Conforti, Fausto Minelli, and Giovanni A. Plizzari. Wide-shallow beams with and without steel fibres: A peculiar behaviour in shear and flexure. *Composites Part B: Engineering*, 51:282–290, 2013.

-
- [17] Antonio Conforti, Fausto Minelli, Andrea Tinini, and Giovanni A. Plizzari. Influence of polypropylene fibre reinforcement and width-to-effective depth ratio in wide-shallow beams. *Engineering Structures*, 88:12–21, 2015.
- [18] Antonio Conforti, Fausto Minelli, and Giovanni A. Plizzari. Influence of width-to-effective depth ratio on shear strength of reinforced concrete elements without web reinforcement. *ACI Structural Journal*, 114(4):995–1006, 2017.
- [19] Adam Scott Lubell. *Shear in wide reinforced concrete members*. PhD thesis, University of Toronto, Canada, 2006.
- [20] Francisco Natário, Miguel Fernández Ruiz, and Aurelio Muttoni. Experimental investigation on fatigue of concrete cantilever bridge deck slabs subjected to concentrated loads. *Engineering Structures*, 89:191–203, 2015.
- [21] Juan Sagasetta, Luca Tassinari, Miguel Fernández Ruiz, and Aurelio Muttoni. Punching of flat slabs supported on rectangular columns. *Engineering Structures*, 77:17–33, 2014.
- [22] Jürgen Einpaul, Miguel Fernández Ruiz, and Aurelio Muttoni. Influence of moment redistribution and compressive membrane action on punching strength of flat slabs. *Engineering Structures*, 86:43–57, 2015.
- [23] Trevor D Hrynyk and Frank J Vecchio. Capturing Out-of-Plane Shear Failures in the Analysis of Reinforced Concrete Shells. *Journal of Structural Engineering (United States)*, 141(12):11, 2015.
- [24] Beatrice Belletti, Rita Esposito, and Joost Walraven. Shear Capacity of Normal , Lightweight and High-Strength Concrete Beams according to Model Code 2010 . II : Experimental Results versus Nonlinear Finite Element Program Results. *Journal of Structural Engineering, ASCE*, 139(9):1600–1607, 2013.
- [25] Beatrice Belletti, Aurelio Muttoni, Simone Ravasini, and Francesca Vecchi. Parametric analysis on punching shear resistance of reinforced-concrete continuous slabs. *Magazine of Concrete Research*, 71(20):1083–1096, 2018.
- [26] Aurelio Muttoni, Miguel Fernández Ruiz, Evan C. Bentz, Stephen J Foster, and V. Sigrist. Background to the Model Code 2010 Shear Provisions - Part II Punching Shear. *Structural Concrete*, 14(3):204–214, 2013.
- [27] Chong Yik M. Goh and Trevor D Hrynyk. Nonlinear finite element analysis of reinforced concrete flat plate punching using a thick-shell modelling approach. *Engineering Structures*, 224:111250, 2020.
- [28] Neil A. Hoult, Omurden Ekim, and Ryan Regier. Damage/Deterioration Detection for Steel Structures Using Distributed Fiber Optic Strain Sensors. *Journal of Engineering Mechanics*, 140(12):9, 2014.
- [29] Matthew B. Davis, Neil A. Hoult, Sanchit Bajaj, and Evan C. Bentz. Distributed Sensing for Shrinkage and Tension-Stiffening Measurement. *ACI Structural Journal*, 114(3):753–764, 2017.
- [30] Severin Haefliger, Jaime Mata-Falcón, and Walter Kaufmann. Application of distributed optical measurements to structural concrete experiments. In *SMAR 2017 Proceedings*, volume 159, 2017.
- [31] A. Brault and Neil A. Hoult. Distributed Reinforcement Strains: Measurement and Application. *ACI Structural Journal*, 116(4), 2019.

-
- [32] Jack J Poldon, Neil A. Hoult, and Evan C. Bentz. Distributed Sensing in Large Reinforced Concrete Shear Test. *ACI Structural Journal*, 116(5):235 – 245, 2019.
- [33] Jaime Mata-Falcón, Severin Haefliger, Minu Lee, Tena Galkovski, and Nicola Gehri. Combined application of distributed fibre optical and digital image correlation measurements to structural concrete experiments. *Engineering Structures*, 225, 2020.
- [34] Zachary Broth and Neil A. Hoult. Dynamic distributed strain sensing to assess reinforced concrete behaviour. *Engineering Structures*, 204:110036, 2020.
- [35] Correlated Solutions. *Vic-3D 2010, Reference Manual*. 2010.
- [36] Luna Technologies Inc. *Optical Backscatter Reflectometer 4600 User Guide*. Luna Technologies, Blacksburg, VA, 2013.
- [37] Miguel Fernández Ruiz, Aurelio Muttoni, and Juan Sagaseta. Shear strength of concrete members without transverse reinforcement: A mechanical approach to consistently account for size and strain effects. *Engineering Structures*, 99:360–372, 2015.
- [38] Aurelio Muttoni. Punching shear strength of reinforced concrete slabs without transverse reinforcement. *ACI Structural Journal*, 105(4):440–450, 2008.

Chapter 2

A detailed view on the rebar-to-concrete interaction based on refined measurement techniques

This chapter is the post-print version of the following article:

Cantone R., Fernández Ruiz M., Muttoni A. A detailed view on the rebar-to-concrete interaction based on refined measurement techniques. *Engineering Structures*. Vol. 226. 2021. <https://doi.org/10.1016/j.engstruct.2020.111332>.

The authors of this publication are Raffaele Cantone (PhD Candidate), Miguel Fernández Ruiz (Senior lecturer and thesis co-director) and Prof. Aurelio Muttoni (thesis director). This work was performed by the first author (Raffaele Cantone) under the supervision of Dr. Miguel Fernández Ruiz and Prof. Aurelio Muttoni who provided valuable feedbacks and carried out detailed revisions of the manuscript.

The main contributions of Raffaele Cantone with respect to the production of this chapter are the following:

- Implementation of Fibre-Optical measurements on steel rebars for a detailed evaluation of reinforcement strains.
- Preparation and testing of two pull-out tests, eight tension tests for bare and embedded reinforcement subjected to cyclic loading and three four-point bending tests on beams failing in shear subjected to cyclic loading.
- Analysis of the experimental measurements obtained with Digital Image Correlation and Fibre Optic strains sensors.
- New insights on the mechanical engagement between the reinforcement and the concrete matrix by means of the analysis of bond stresses, residual crack openings and negative tension-stiffening effects.
- Analysis of the development of delamination cracks, of the local kinking of rebars at cracks (due to compatibility of deformations) and the evaluation of dowelling forces at shear (inclined) cracks.
- Production of the figures and tables included in the article.
- Preparation of the manuscript of the article.

Abstract

Simplified assumptions have traditionally been made on the rebar–to–concrete interaction in structural concrete to calculate the stress state in rebars. Such assumptions typically consider a uniform stress state in the reinforcement at a given cross section, neglecting compatibility of deformations due to bending of the bar. Such simplifications are fully justified due to the relatively ductile behaviour of the reinforcement. When the ductility is however not sufficient, as for instance in case of fatigue effects in metallic reinforcement or in case of brittle non–metallic reinforcement, corrections have in many cases been proposed on an empirical base. A step forward in the understanding of these latter cases requires a detailed insight of the mechanisms of transfer of forces and the actual strain state of embedded reinforcement, which has not been possible in the past due to limitations in measurement systems.

Within this frame, this paper revisits the results of classical tests on bond, tension and bending with the insight provided by detailed measurements on the rebars. On the basis of Fibre–Optic Measurements (FOM) performed along the length of a bar and at different locations, the results show the complexity of the actual interactions between the reinforcement and the surrounding concrete as well as the influence of compatibility of deformations on their response. The results provide a new perspective on the rebar–to–concrete interaction and show its implications on a series of phenomena related to brittle failure modes.

Keywords: rebar–to–concrete interaction; bond; stress concentration; fibre optic strain sensors; shear failure; dowel action; cyclic response of concrete

2.1 Introduction

Structural concrete is a highly complex composite material in which the interaction between the concrete matrix and the embedded reinforcement bars has traditionally been approached for design purposes with simplified methods. In most cases, assuming that the reinforcement presents a large deformation capacity and toughness, several phenomena associated with compatibility of deformations (due to shearing or bending of the bars) can be neglected, as well as those related to stress concentrations resulting from the mechanical engagement of the ribs of the bars.

Some instances of phenomena traditionally neglected, such as the consideration of a non-uniform profile of stresses in the longitudinal reinforcement due to the curvature of plane sections in bending (a phenomenon already acknowledged by Ritter in 1899, [1], see Figure 2.1a) or dowelling of reinforcement in the shear verification of beams and slabs, Figure 2.1b. With respect to the steel–to–concrete interaction [2, 3] the bond stress is usually considered as distributed over the nominal interface surface, but shows in fact high concentrations at the ribs (Figure 2.1c), where the influence of transverse strains in the bar and the presence of local punching cracks plays a major role [4, 5].

These simplifications consider in fact a uniform stress state at each section of a rebar. Such consideration is reasonable for most design purposes but a fundamental understanding of the actual response of concrete is required to clarify its limits of applicability and to yield to more comprehensive design approaches. This is particularly relevant for instance with respect to brittle reinforcement response, as for non – metallic reinforcement [6]. Also, such considerations might play a governing role for some phenomena where failure is associated to stress concentrations even at serviceability limit state, as for fatigue issues [7, 8]. For the latter, the actual strains might notably differ from the calculated values if compatibility of deformations [7] and stress concentrations are neglected.

The lack of detailed experimental data on the rebar–to–concrete interaction has been associated to the limitations of conventional measurement devices. Typically, measurements have been performed so far by recording displacements (by means for instance of Linear Variable Displacement

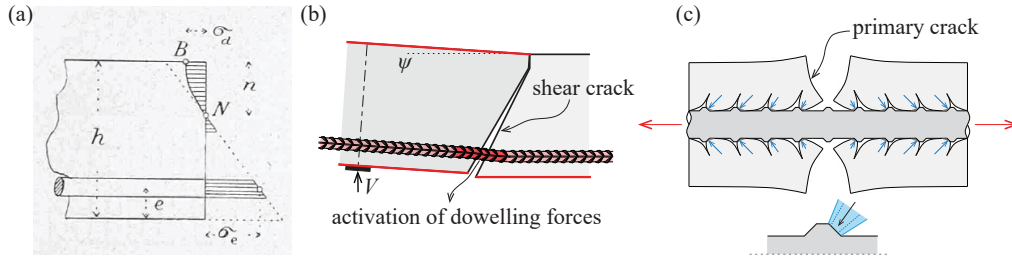


Figure 2.1: rebar-to-concrete interactions: (a) bending of the reinforcement according to Ritter [1]; (b) dowel action; and (c) mechanical rib engagement with cracks according to Goto et al. [4].

Transformers, LVDTs) or by gluing strain gages on the concrete or rebar (the latter severely influencing bond properties if glued on the bar surface or providing a measurement near the bar axis if glued on longitudinally-cut bars). These techniques have however been significantly improved in recent times. With respect to data acquisition on concrete surface (strains and displacement fields), a notable step forward has been performed with Digital Image Correlation (DIC) measurement systems [9]. DIC enables detailed and continuous readings of the displacement field on the concrete surface [10] allowing to calculate on that basis strain fields and relative displacements of crack lips. This has allowed for detailed understanding of the kinematics developed by shear and flexural cracks [11] and their associated understanding of load-carrying actions [12, 13]. Although concrete surface data gathered by DIC can be used for evaluation of the reinforcement response (as dowel action, [13]), this technique provides no direct measurements on the local strain state of the reinforcement bars. With this respect, the implementation of Fibre-Optical Measurement systems (FOM, [14]) in steel rebars is allowing for high quality readings on the surface of reinforcement. FOM allows for continuous readings along a bar at different locations and at high frequencies. This allows observing high strain gradients in a bar, along its axis and for different locations of the cross section.

Recent works [15–21] have shown that the acquisition of strain measurements on reinforcement surface could provide detailed information about the interactions engaged between reinforcement and the surrounding concrete with respect to the cracking stage and the cyclic degradation of concrete. Amongst the first experiences, it is relevant to cite the works by Davis et al. [17] focusing on bare bars and reinforced concrete ties investigated by means of fibre optic strain measurements. Also, detailed developments on distributed sensing techniques for the loading response of large reinforced concrete members have been performed by Poldon et al. [19] and Brault et al. [20] in conjunction with surface measurements. More recently, FOM sensors used for detection of degradation mechanisms related to cyclic loading have also been implemented by Broth et al. [21].

By making use of these techniques, this paper revisits the results of classical tests on reinforced concrete elements by means of detailed measurements performed with FOM glued on the surface of steel rebars combined with DIC readings for concrete surface. The investigation focuses on three different types of structural elements addressing a number of responses:

- Two pull-out tests — Evaluation of stress concentration at the ribs of rebars, Figure 2.2a.
- Eight tension tests for bare and embedded reinforcement subjected to cyclic loading: detailed analysis of residual crack openings and negative tension-stiffening, Figure 2.2b.
- Three four-point bending tests on beams failing in shear subjected to cyclic loading: development of curvatures at the reinforcement, dowel action and development of cover delamination due to kinematic compatibility, Figure 2.2c.

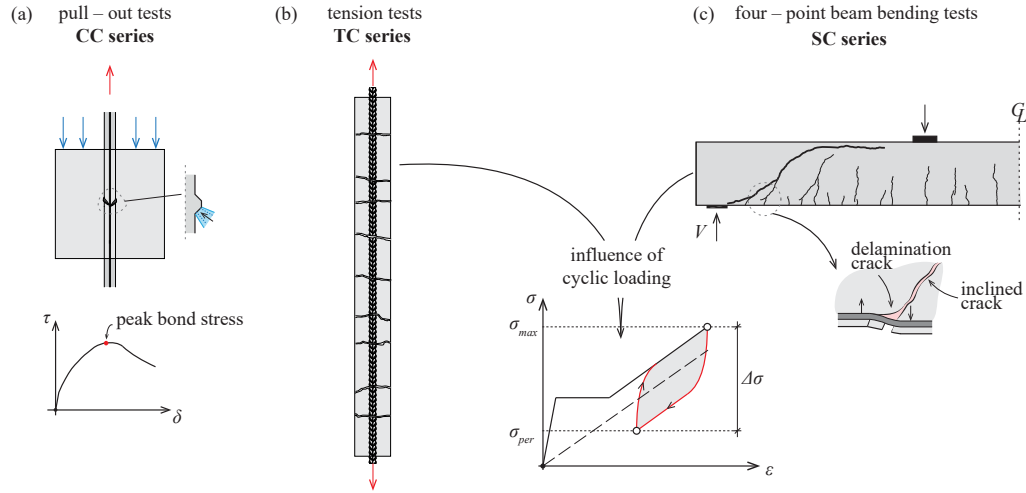


Figure 2.2: Experimental investigation on: (a) monotonic pull-out tests; (b) tensile tests subjected to cyclic loading; (c) four-point bending tests on beams subjected to cyclic loading.

The results show the complexity of the interactions between reinforcement and the surrounding concrete as well as the influence of compatibility of deformations on their response. On this basis, a number of implications for practical design are presented and discussed.

2.2 Experimental programme

All experiments have been carried out in the Structural Concrete Laboratory of École Polytechnique Fédérale de Lausanne (Switzerland).

Measurement techniques

For DIC measurements, pictures were generally acquired with a frequency ranging between 0.5 and 2 Hz, using two SVCam-hr29050 sensor cameras (29 Mpx), in combination with controlled lighting conditions. Random speckle pattern was applied on the concrete surface by means of spray painting (with a size of 1 ± 0.5 mm). The displacement analysis was then performed with Vic3D software [9], using a subset size of 29×29 pixels yielding to a displacement error below 1/50 times the size of the pixel (pixel size: $500 \mu\text{m}$).

Moreover, strain measurements on the rebar surface based on Rayleigh scattering [22] were used (Odisi-B version by *Luna Innovations* [14]). Odisi-B version performs measurements by means of an Optical Frequency Domain Reflectometry (OFDR) which allows obtaining strain profiles at relatively high sampling rates and refined spatial resolution (with an error in the strain measurement of about $25 \mu\epsilon$). Regarding fibre optics, its structure may be split in three main components (see Figure 2.3): core, cladding and coating. The core is the medium in which light is propagating, the cladding allows transmitting the light exclusively along the fibre optical sensor. The coating is an external protection which prevents the core to be damaged. In this research, polyimide coating was used ensuring negligible slip between the core and the medium in which the fibre optical cables were embedded. Fibre optics were embedded along steel rebars according to the procedure as follows :

- I. 1mm–depth grooves were performed along two or four sides of the rebar by means of a thin cutting disc on an angle grinder which was fixed to a cart in order to maintain the alignment of the notch with respect to the rebar (the area of each groove was about 3 mm^2 corresponding

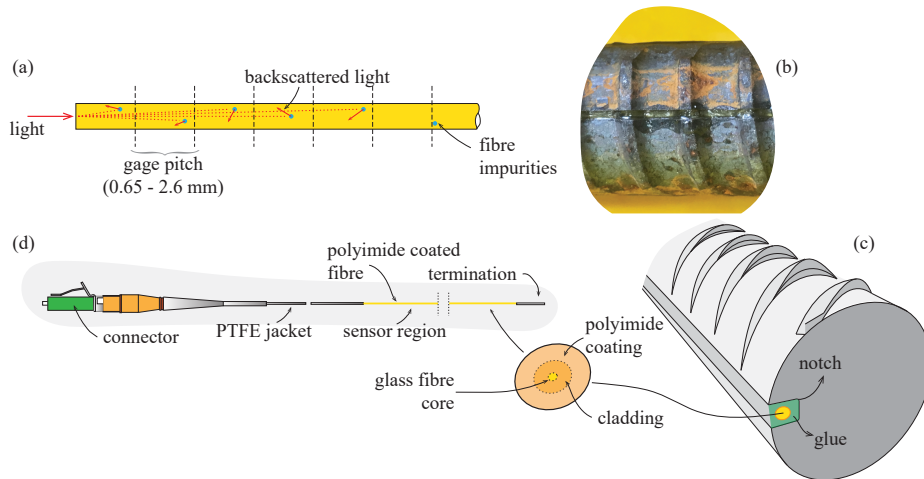


Figure 2.3: FOM measurements: (a) back-scattering mechanism due to fibre core impurities ; (b) view of the fibre-optic sensor glued to a steel rebar; (c) sketch of the fibre optical cable placed in the groove and adhering to the steel due to two-component glue and (d) description of the fibre optical cable structure with angle polished connector on one side and termination which avoids light reflection.

to a bar area reduction per groove of about 3.80% in $\phi 10$ bars, 0.95% in $\phi 20$ bars and 0.79% in $\phi 22$ bars).

- II. 125 μm polyimide fibre optics were placed at the bottom of the groove and fixed with scotch tape to ensure the position of the fibre. Two-component glue was then placed in the groove avoiding relative slip between the fibre and the steel rebar.
- III. An Angle-Polished Connector was then spliced at one end of the fibre glued in the groove. The connector was necessary to send a light wave into the core through Odisi-B interferometer. On the other end of the fibre, a termination was then provided avoiding reflection of the light.

During the measurements, 0.65 mm spatial resolution was used (*i.e.* gauge pitch). Depending on the test, two or four fibres were installed on the bars (the gauge pitch provides the maximum possible spatial resolution of the system).

2.3 Pull-out tests

Main parameters and test setup

Two pull-out tests were performed with the aim of investigating the interaction between concrete and ribs on the rebar surface, see Figure 2.4a. Two types of tests were carried out to investigate two different failure modes (local crushing or shearing-off) occurring at the rebar-to-concrete interface. For test CC01, all ribs but one were mechanically removed from the bar: the contact between the rebar and the concrete was in addition disabled by placing a thin layer of Teflon (see Figure 2.4b). This test aims at investigating the contact forces between one rib and the surrounding concrete in case of local crushing, Figure 2.4b. In test CC02, all ribs but two were removed and bond was disabled except between the investigated ribs by arranging a rubber layer sufficiently thick (2 mm) to avoid engaging of the first rib. To avoid friction between concrete and rubber, a thin Teflon layer was placed on top of it. This test was addressed at the resistance of concrete between ribs to be sheared - off (see Figure 2.4c).

Table 2.1: Main parameters of pull-out tests

Specimen	f_c , MPa	ϕ , mm	rib spacing, mm	f_y , MPa	Type
CC01	41.0	22	8.2	701	one rib (teflon)
CC02	42.6		8.2		two ribs (teflon + rubber)

The rebars were equipped with four optical fibres glued in 1-mm depth grooves and embedded in 200×200 mm concrete cubes (Figure 2.4). All specimens were cast with normal-strength concrete whose compressive strength at the day of testing ranged between 41.0 and 42.6 MPa (average of three compressive tests on 160×320 mm concrete cylinders). The maximum aggregate size was 16 mm for all test specimens. The cement was CEM II/B-M (T-LL) 42.5N, in accordance with [23], with a water-to-cement ratio equal to 0.53. The embedded rebars $\phi 22$ consisted of high-strength (S670) steel with a yield strength $f_y = 701$ MPa determined according to EN ISO 6892-1 (0.2% of residual plastic strain, refer to the details in Table 2.1). Ribs were approximately 1 mm-height and 8.2 mm-spaced leading to a measured bond index f_R of 0.12 (evaluated by surface scan). During casting, the bar was placed horizontally.

The test setup is presented in Figure 2.4d. All tests were performed according to a displacement-control protocol with a displacement rate ranging between 0.01 mm/s (ascending branch) up to 0.05 mm/s (softening branch). The typical duration of one test was about 2–8 minutes up to reaching the maximum load.

Test results

The measured bond-slip curves are presented in Figures 2.5a–b. The relative slip between the rebar and concrete surface was measured by setting a Linear Variable Differential Transformer (LVDT) on the loaded bar end while the bond stress is averaged on the area defined by the nominal perimeter ($\pi \cdot 22$ mm) times the rib spacing (8.2 mm). The measured strains on the sides of the rib (blue and red lines for compression and tension values, respectively) is additionally shown as a function of the bond stresses τ in Figures 2.5c–d. As it can be seen in Figure 2.5, the overall behaviour for different failure modes investigated differs considerably in terms of maximum peak stresses as well as the potential displacement capacity in the softening branch. For test CC01, the peak is reached for an average bond stress τ of 59.2 MPa, corresponding to a relative slip at peak load of 6.45 mm. After reaching the maximum load, the response was relatively tough (only small decrease of the bond stress with increasing slips up to 10 mm) during the softening phase, see Figure 2.5a. With respect to the shear-off failure corresponding to test CC02 (Figure 2.5b), failure occurred at lower average bond stresses τ , of about 20 MPa. The associated slip was also lower, around 1.1 mm and the test followed later a relatively brittle response in the softening phase (60% strength reduction develops for relatively slips ranging between 2.5 and 5.5 mm which can be explained by the reduction of the contact area with increasing slip as shown with the dotted line in Figure 2.5b).

The longitudinal strain profiles measured from the analyser are shown in Figures 2.5e–f for tests CC01 and CC02 respectively (with positive strains referring to member elongation). Several loading steps are selected between 5% and 100% of the maximum measured bond stress τ . Figures 2.5e–f show a strong gradient of strains at the vicinity of the rib due to engagement of contact forces between concrete and ribs. Several phenomena can be observed with respect to the response of the specimens. For test CC01, the surface strains can reach in the vicinity of the rib very high values (even higher than the yield strain of about $3.5 \text{ m}\epsilon$) despite the low average bar strain values ($\simeq 0.5 \text{ m}\epsilon$, calculated by dividing the maximum force by the nominal cross section of the bar and the elastic modulus). Such concentrations of strains localize in a region with a length similar to one diameter before and after the rib (total disturbed zone of approximately two bar diameters). The length of the disturbed zone is however not constant. It increases for low values of τ up to

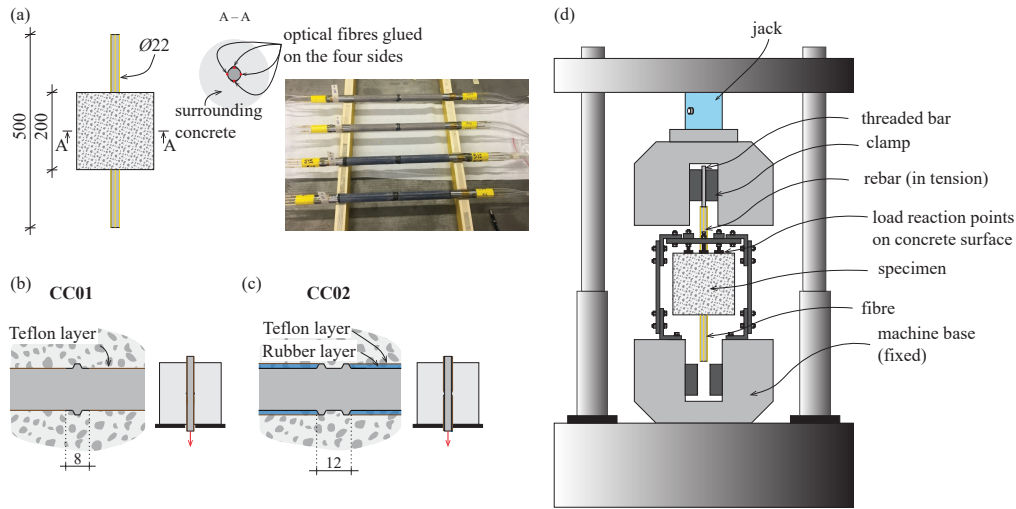


Figure 2.4: Pull-out tests — (a) sketch of the specimens with focus on the optical fibres glued at the rebar surface; (b) pull-out test type CC01 for the investigation of concrete crushing (one rib); (c) pull-out test type CC02 for the investigation of shearing-off between ribs; and (d) view of the test setup (units in mm)

approximately 25 MPa. Thereafter (refer to values above 40 MPa in Figure 2.5e), the length of the disturbed zone remains roughly constant.

During the first phase, the strains in both sides of the ribs increase roughly linearly (Figure 2.5c). Thereafter, once the disturbed zone does not increase in length, the strain increases more than proportionally (refer to sudden change of slope in Figure 2.5c). This can also be observed in the bond-slip curve (Figure 2.5a) associated to a softer response. Moreover, as can be seen in Figures 2.5c–d, even if these cases should represent "good bond conditions" according to Eurocode 2 [24], rather different level of strains are recorded at the top and bottom side of the bar with respect to the casting direction. This difference can potentially be explained by the voids under the bar resulting from bleeding and plastic settlement of fresh concrete just after casting [25].

A similar response is also observed for test CC02 (two ribs) with the same development of two regimes (Figure 2.5f). The length of the disturbed zone is in this case smaller and comparable to the rib distance (0.4 times the bar diameter). The failure at a lower load and more brittle response can in this case be associated to the shear – off of concrete between ribs (Figure 2.5b) limiting the contact area with increasing slip.

Interpretation of test results

The experimental results have shown a number of phenomena governing the rebar-to-concrete response:

- Strong strain (and stress) gradients occur near the ribs.
- Such disturbances are located at the surface in regions not larger than one bar diameter. When more than one rib is engaged, the disturbed zone with strain concentrations and gradients at the surface may develop in the whole distance between ribs.
- The surface strains can locally attain very high values. In the performed tests, although the average bar strain was well beyond the yield threshold of the bar (about 25% of the yield strain), the surface strains indicated locally values above the yield strain.

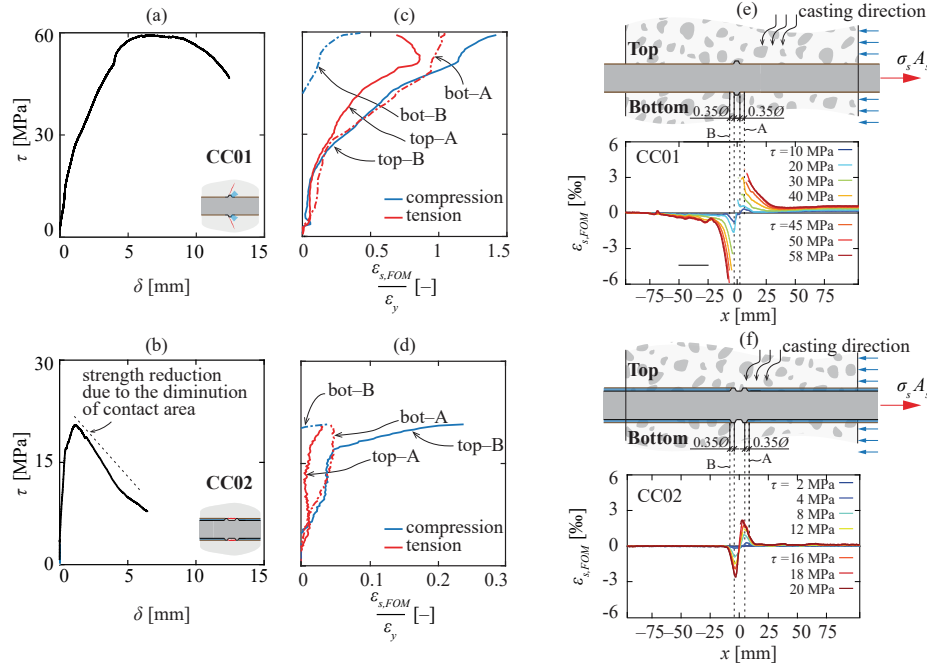


Figure 2.5: Pull-out tests results: bond stress τ – slip δ in the rebar for specimens (a) CC01 and (b) CC02; bond stress τ – normalized strain $\epsilon_{s,FOM}/\epsilon_y$ for top (continuous lines) and bottom (dashed lines) fibres in sections A and B for specimens (c) CC01 and (d) CC02 (sections A and B are located at 0.35ϕ from rib edges); profiles of measured strains $\epsilon_{s,FOM}$ in top fibre (with respect to casting direction) for specimens (e) CC01; and (f) CC02

A potential explanation of the observed response may be found in the spreading of the local contact forces in the rebar, developed at the rib as shown in Figure 2.6a. The measured strain profile over the line A–A (Figure 2.6b) is consistent with the development of compressive and tensile stresses in the bar which carry the contact force between the concrete and the rib. Such stress concentrations can thus be detrimental to the fatigue strength of the reinforcement bar. This is in agreement with the observation that the fatigue strength of bars embedded in concrete is typically lower than the fatigue strength of bare bars [26]. It shall however be noted that when the strength in a concrete member is governed by the reinforcement, the rebar sections at the cracks reach yielding. This implies that, at the crack location, no rib-to-concrete interaction happens, and in the vicinity, the plastic lateral contraction of a bar reduces (together with the resistance of local punching cracks [4]) the bond stresses.

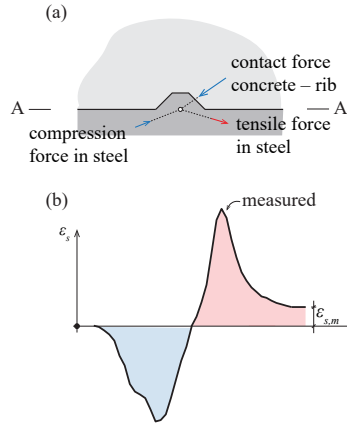


Figure 2.6: Mechanical engagement of bond: (a) forces at concrete–rib interface; and (b) measured strain profile at section $A - A$.

2.4 Tension tests

Main parameters and test setup

Five tension tests subjected to cyclic loading were performed on prismatic reinforced concrete ties with 100×100 mm square cross section and 1150 mm side length (consistently with the experimental programme of Farra and Jaccoud [27]). They were completed with three additional tests on bare rebars. The specimens were reinforced with one single rebar placed either centred with respect to the cross section of the tie (TC04, TC05, TC06) or eccentric (TC07, TC08). All members were tested under cyclic loading with a nominal target ratio R between the minimum (σ_{min}) and the maximum (σ_{max}) stress in the rebar equal to 0.10 ($\sigma_{max}=275$ MPa and $\sigma_{min}=27.5$ MPa). The maximum applied stress (σ_{max}) was set at 275 MPa and was kept constant for all tests. The tests were displacement–controlled with a displacement rate ranging between $0.5 \mu\text{m/s}$ (embedded rebars) and 0.05 mm/s (bare rebars). In the reinforced ties, this led to approximately two minutes to perform one cycle, except for the first cycle in which a reduced strain rate ($0.1 \mu\text{m/s}$) was imposed in order to properly follow the cracking process. For every test, the loading protocol consisted of 100 cycles according to the displacement rate mentioned above.

All specimens were cast with normal–strength concrete whose compressive strength at the day of testing ranged between 35.3 and 35.7 MPa. Direct tension tests on concrete cylinders were also performed showing a tensile strength at 28 days of 2.1 MPa. The maximum aggregate size was 16 mm for all test specimens. The cement used was CEM II/B-M (T-LL) 42.5N, in accordance with [23], with a water-to-cement ratio of about 0.5.

The longitudinal reinforcement consisted of $\phi 10$ cold – worked rebars (yield strength calculated according to EN ISO 6892-1 [28]), $\phi 20$ hot-rolled reinforcing bars with a well-defined yield plateau and high–strength S670 $\phi 22$ reinforcing bars (yield strength calculated according to EN ISO 6892-1 [28]). Three nominal reinforcement ratios were investigated ranging between 0.78 % and 3.80 %. Refer to details in Table 2.2 and Figure 2.7a. The specimens were cast horizontally in the position shown in Figure 2.7b. Figure 2.7c shows the test setup adopted in the current programme. Tests were performed by clamping the bottom side of the rebar and pulling upwards on the top side of the specimen (using a Schenck hydraulic jack with a total capacity of 1 MN). Rebars were equipped with four optical fibres glued on the four sides while concrete surface behaviour was tracked by performing DIC and LVDTs measurements on two opposite sides of the specimens (see Figure 2.7). Out–of–plane displacements of the eccentrically loaded specimens needed to be controlled in order to avoid splitting of the concrete cover close to the edges of the member (due to clamping effect of

Table 2.2: Main parameters of tensile tests*

specimen	ϕ , [mm]	ρ , [%]	type	position	f_c , [MPa]	f_y , [MPa]	COV, [%]
TC01	10	—	bare	—	—	539	0.42
TC02	20	—				518	0.11
TC03	22	—				701	0.43
TC04	10	0.78	embedded	centred	35.3	539	0.42
TC05	20	3.14		centred	35.5	518	0.11
TC06	22	3.80		centred	35.5	701	0.43
TC07	20	3.14		ribs against sides	35.6	518	0.11
TC08	20	3.14		ribs against cover	35.7	518	0.11

* COV refers to the yield strength of reinforcement.

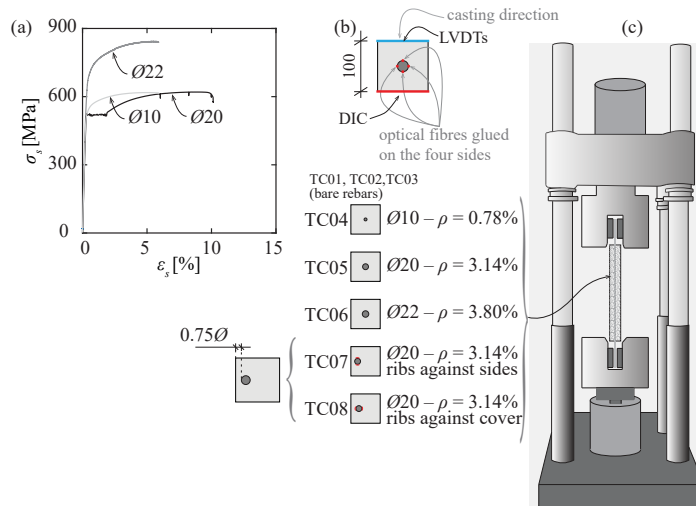


Figure 2.7: Tensile tests: (a) measured stress–strain relationships of reinforcement bars; (b) specimen cross section and main mechanical properties; (c) front view of test setup.

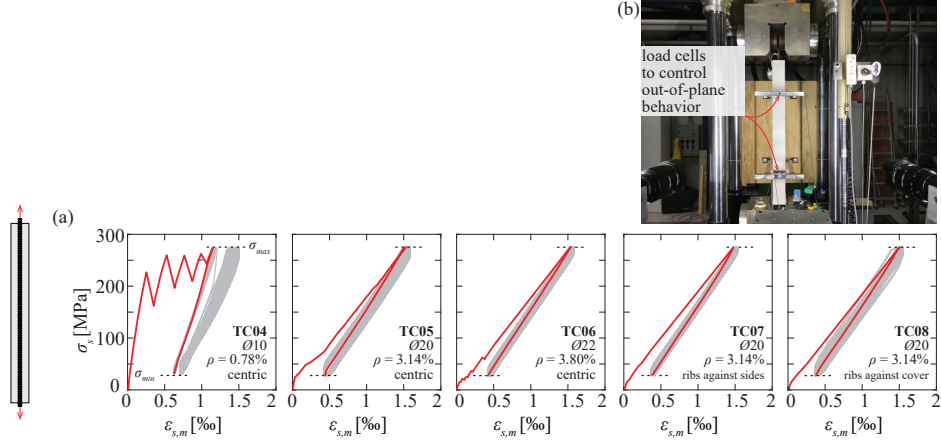


Figure 2.8: Tensile tests: (a) steel average stress – local average strains for embedded rebars under cyclic loading; and (b) front view of test setup for eccentric rebars (refer to red curves for first loading cycle and grey curves for envelope of all cycles).

the loading machine). Thus, two symmetric load cells were placed along the member in order to control out-of-plane behaviour.

Test results

The measured average steel stress (total force divided by cross section area of steel bar) – average steel strain curves are presented in Figure 2.8 both for reinforced concrete tension members with centred rebars (TC04, TC05, TC06) and for members with eccentric rebars (TC07, TC08). The average steel stress is calculated as the applied tensile force divided by the nominal rebar area (calculated as $\pi\phi^2/4$). As for the previous tests, four fibres were glued in the rebars. In Figure 2.8, the average local steel strain is calculated by averaging the local longitudinal steel strains resulting from FOM measurements over the whole length of the concrete tie. The observed cracking patterns of the tested specimens loaded until failure are illustrated in Figure 2.9. Cracks developed mostly perpendicular to the longitudinal direction of the member and its spacing was largely governed by the reinforcement ratio. During first loading, primary cracks formed and cracking was stable during the cycles except for specimen TC04 in which the last primary crack developed during the second load cycle (refer to stress–strain curve in Figure 2.8a and to Figure 2.9). After the load cycles and during final loading to failure, additional secondary cracks developed as well as splitting cracks parallel to the reinforcement (refer to cracks in light grey in Figure 2.9).

Figure 2.10 presents the strain results developed during the loading process including 100 cycles of loading and unloading, ranging between the maximum rebar stress $\sigma_{max} = 275$ MPa and the minimum stress $\sigma_{min} = 27.5$ MPa. The steel stresses were calculated from the measured longitudinal strains (with a spatial resolution of 0.65 mm) by smoothing over a length equal to two times the bar diameter (in agreement to the disturbed length observed in the pull-out tests) and by assuming $E_s = 200000$ MPa. Details of the response for an unloading cycle (after six loading cycles) are also presented in Figures 2.10b-d.

Several outcomes may be highlighted from these results. A first fact refers to the profiles of stresses (Figure 2.10c derived from the FOM measurements). Before unloading (load level $LL1$ in Figure 2.10c), it can be noted that the maximum stress develops at the location of the cracks with a rather linear decrease of stresses at the sides. This observation is relatively in fair agreement with the consideration of a constant bond law between the bar and the concrete (as adopted for instance by the tension chord model [29], [30]).

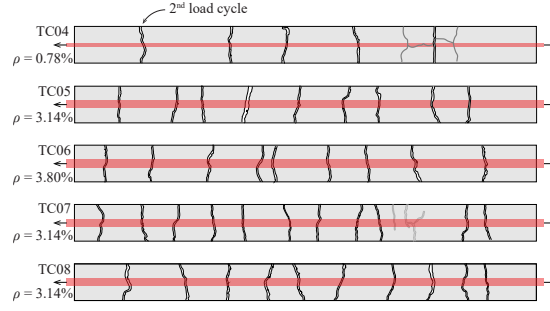


Figure 2.9: Tensile tests: cracking patterns of tested specimens (cracks in light grey developed after all load cycles, during monotonic loading up to failure; for specimens with eccentric bars, the surface on the bar’s side is shown)

This result is confirmed by the calculated bond stresses τ_b derived from equilibrium considerations:

$$\Delta\sigma_s \frac{\pi}{4} \phi^2 = \tau_b \pi \phi \Delta x \rightarrow \tau_b = \frac{\phi}{4} \cdot \frac{\Delta\sigma_s}{\Delta x} \quad (2.1)$$

As presented in Figure 2.10d, the calculated values show a plateau ranging between 5 and 7 MPa, in good agreement to the expression for this purpose proposed by Marti et al. [29]:

$$\tau_b = 0.6 f_c^{2/3} \quad (2.2)$$

During unloading (refer for instance to load level *LL7* of cycle #6 in Figures 2.10c–d), the bond stresses reduce and reach even negative values (as consistently adopted in approaches reproducing negative tension-stiffening [31–34]). This yields eventually to a relatively constant value of the stresses along the bar. It is interesting to note that, except at the location of cracks, the steel bar is subjected to a stress range which is fairly lower than the one corresponding to a bare bar (this yields to implications on the fatigue response of ties as it will be later discussed).

Another interesting fact that can be directly derived from FOM is the degradation of bond with increasing number of cycles, Figure 2.10e. This phenomenon has been already observed by a number of researchers [5, 7, 8, 35–38]. A clear degradation can be observed particularly at the first loading cycles but without stabilization after 100 cycles. This trend seems to confirm the reductions proposed by Tassios [35] and Balazs [8], with a reduction of 30% of the uniform bond strength after cyclic loading. Also, the same phenomenon is observed for the bond values in the unloading phase (Giuriani [39]), as can be seen in Figure 2.10f, in which bond degradation could be outlined as a function of the level of steel stress.

A more detailed insight of the bond degradation with cycles is presented in Figure 2.10g as a bond–slip relationship for the section with maximum bond stresses (section *M* in Figure 2.10d). The slip is calculated by integration of average rebar strains (assuming negligible concrete strains) from the point with no relative slip (section *O* in Figure 2.10d). During the first monotonic loading (blue part), the results show both the bond activation and the small unloading steps happening when new cracks develop under controlled deformation (sudden drops in the force and in the bond stress). During the first total unloading, the bond stresses were not negative, but close to zero. As the number of cycles increased, the maximum bond stress reduced following the degradation of bond, and negative values of the bond stress were also reported (in close agreement to the observations of Giuriani [39]). One can also observe that the bond degradation during the small unloading steps due to the development of new cracks is of the same order of magnitude of the degradation during the 100 loading and unloading cycles. Consistent measurements were also obtained for other sections of the rebar.

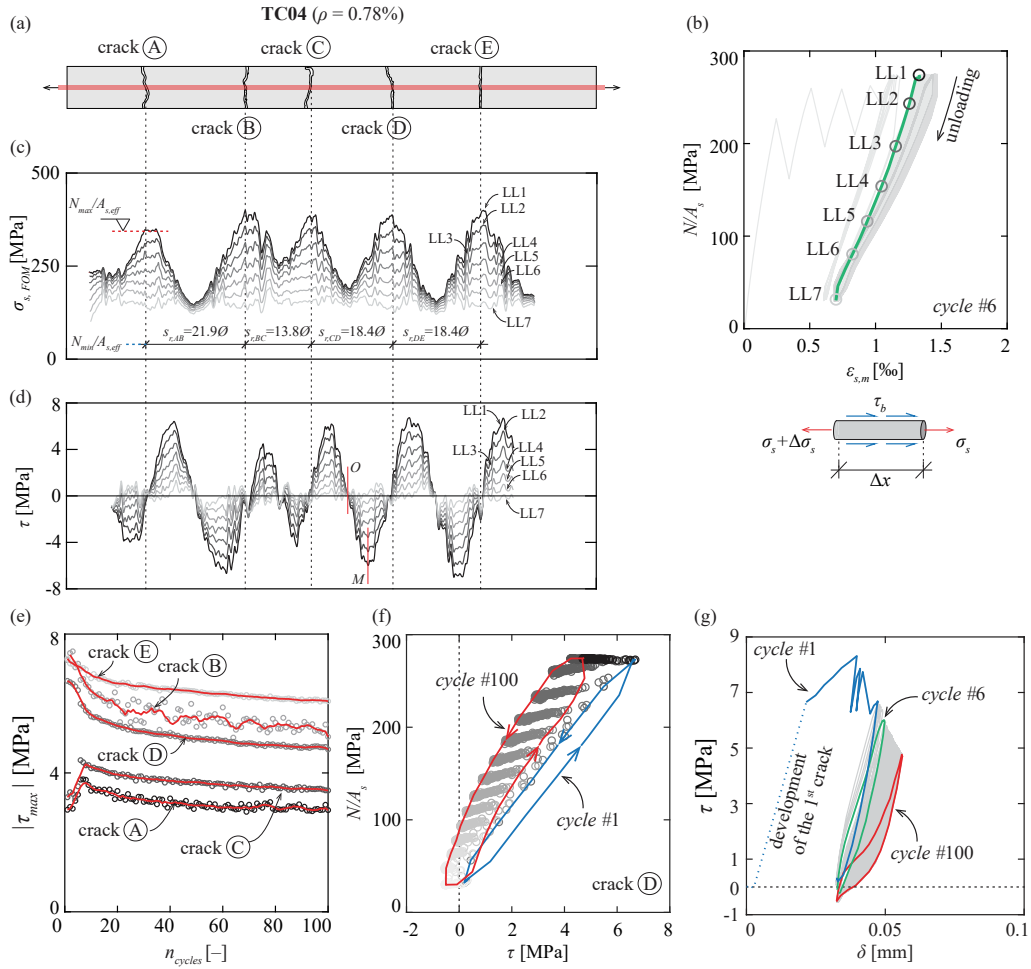


Figure 2.10: Tensile tests — specimen TC04: (a) cracking pattern in the cyclic loading phase; (b) stress-strain relationship for all cycles (in grey) and cycle #6 (in green) indicating load levels; (c) profiles of stresses $\sigma_{s,FOM}$ calculated on the basis of measured strains (FOM) and (d) profiles of bond stresses τ along the steel rebar; (e) bond stresses degradation for the selected cracks due to cyclic loading as a function of number of cycles (peak bond stress τ_{max}); (f) bond stresses in the loading and unloading phases as a function of the stress N/A_s in the rebar during cyclic loading; and (g) bond-slip relationship for a section located at maximum bond stress (3ϕ from the crack).

Interpretation of test results

As already outlined in Section 2.1, structural concrete is a composite material in which the understanding of the mechanical engagement between the concrete matrix and steel interface (bond) is instrumental for the evaluation of crack widths and the overall stiffness of cracked concrete members (both under service conditions or at failure [32–34]). So far, several mechanical models accounting for tension–stiffening by means of simplified or realistic bond–slip laws have been proposed mostly addressed to the case of monotonic loading [29, 30, 40]. Fewer approaches exist on the response of concrete members subjected to cyclic or fatigue loading, in particular with respect to the evaluation of residual crack openings and the negative tension–stiffening effects [32, 34]. The physical approach proposed by [32] will be adopted in the following for the interpretation of the test results of the experimental programme performed on tension members and beams. The main assumptions of this approach [32] are highlighted below (details of the equations of [32] used for the comparisons presented in this paper are given in Appendix 2.7):

- Bond between concrete and reinforcement is assumed to follow a rigid–plastic law (Figure 2.11a.1). As already shown in Figure 2.10c, this approach leads to reasonable results (relatively constant values of bond stresses between cracks).
- The concrete response at the cracks (including softening, unloading and residual opening due to imperfect closure of cracks) is accounted for by means of the approach proposed by Hordijk [37], considering also residual crack openings due to imperfect crack closure, (Figure 2.11a.2). In–between cracks, concrete is assumed to have an elastic response (whose strains are generally neglected), Figure 2.11a.3.
- Reinforcement is assumed to remain elastic, Figure 2.11a.4.

On this basis [32], the loading and unloading response can be characterized by three regimes of behaviour, see Figure 2.11b:

- **Stage a:** unloading during the crack development phase.
- **Stage b:** unloading during the stabilized cracking phase where bond stresses may correspond to loading or unloading conditions.
- **Stage c:** unloading during stabilized cracking phase where bond stresses correspond only to unloading conditions.

The results of this approach are compared in Figures 2.11c–e to the experimental measurements for the representative specimen TC04. As presented in Figure 2.11c, despite the strong simplification of the behaviour, the analytical model reproduces in a suitable manner the relationship between the average crack opening and the steel stress, in particular, if bond degradation after a number of cycles is accounted for (refer to the dashed line in Figure 2.11c). The analytical results in terms of steel stresses and bond stresses, Figures 2.11d–e, were obtained by setting the location of the cracks at the actual ones and calculating the slopes of the stress profile on the basis of the governing bond strength:

- $\tau_{a0} = 0.6f_c^{2/3}$ for loading under short–term conditions [29, 32].
- $\tau_{a\infty} = 0.7\tau_{a0}$ for cyclic loading conditions [8, 35].
- $\tau_{i0} = 0.15f_c^{2/3}$ for unloading under short–term conditions [29, 32].
- $\tau_{i\infty} = 0.5\tau_{i0}$ for cyclic unloading conditions [39].

In addition, it shall be observed that, in specimen TC04, all cracks did not fully develop along the whole cross section during cyclic loading (refer to cracking pattern in Figure 2.11). In these cases, the bars experienced local bending, which justifies why the measured steel stresses are in certain

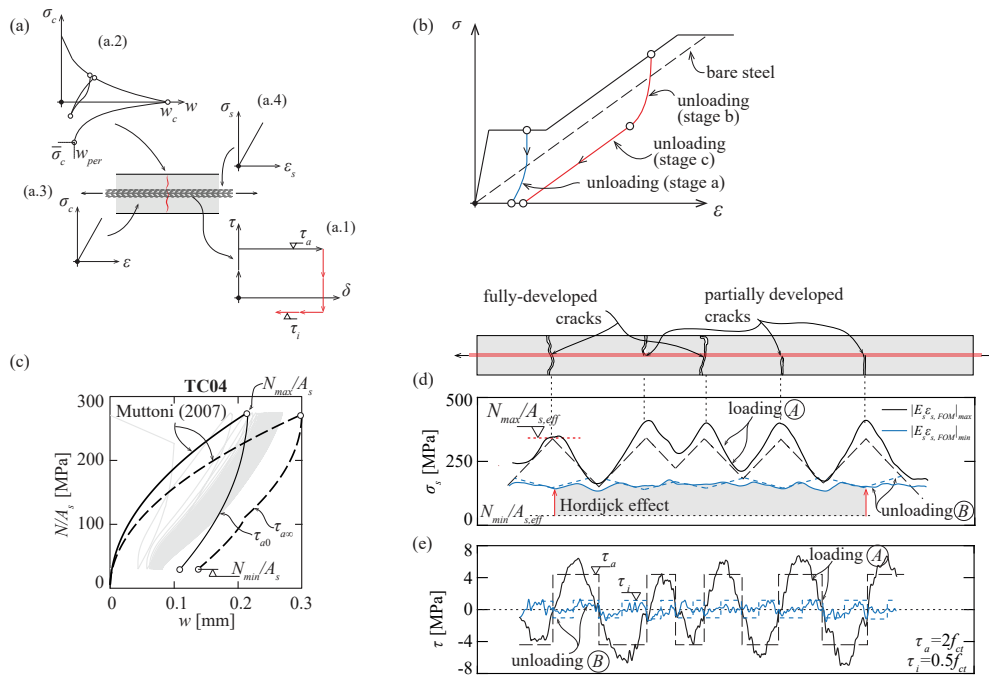


Figure 2.11: Negative tension-stiffening: (a) assumptions of approach by Muttoni and Fernández Ruiz [32]: (a.1) bond between concrete and reinforcement under cyclic loading (rigid-plastic law); (a.2) concrete response (Hordijck [37]); (a.3) elastic behaviour of concrete; (a.4) elastic behaviour of steel; (b) stress-strain response of reinforced concrete tie and different unloading stages; comparison of analytical model by [32] ($k=0.95$, $\tau_a=2f_{ct,eff}$, $\tau_i=0.5f_{ct,eff}$) with test results obtained for tie TC04 ($\rho=0.78\%$) with respect to (c) loading average stress (N/A_s) - average crack opening (w); (d) steel stress distribution and (e) bond stresses distribution for steel stress corresponding to $N_{max}/A_{s,eff}$ (black lines) and $N_{min}/A_{s,eff}$ (blue lines).

cases above the threshold of $N_{max}/A_{s,eff}$ (where $A_{s,eff}$ is the effective area of the bar accounting for the reduction due to the presence of four grooves).

On the whole, the comparison shows a satisfactory agreement (particularly in fully–developed cracks) and a realistic reproduction of the different phenomena (bond slopes, short–term and cyclic loading conditions) are suitably reproduced. This analysis shows that, at the location of the cracks, the stresses vary according to the external applied force and the residual stresses generated by the imperfect closure of cracks (refer to Hordijk’s effect in Figures 2.11a,2,d). In–between cracks, however, the difference of stresses is significantly lower due to the bond stresses. This might be a potentially favourable effect with respect to fatigue issues (refer to the grey–shaded region in Figure 2.11d in which the imperfect crack closure of crack lips leads to larger stresses in the bar). The global response of the tie seems to be mostly influenced by the total amount of available reinforcement. This leads to different development of the maximum–minimum steel stresses with the number of cycles as well as in terms of maximum and minimum average strains of the tie. Figure 2.12 presents for instance, a comparison of the behaviour at the location of a selected crack (refer to crack D in Figures 2.12a–b) for specimens TC04 and TC06 (with reinforcement ratios equal to 0.78% and 3.80% respectively). The steel stress behaviour is presented in two critical sections, Figure 2.10d:

- Section 1 corresponding to the location of the peak of bond stress τ_{max} at the vicinity of crack D (refer to Figures 2.12a–b).
- Section 2 located in-between two cracks, as shown in Figure 2.12.

As can be seen from the hysteretic behaviour in Figures 2.12a–b in terms of resultant steel stress N/A_s and measured steel stress $\sigma_{s,FOM}$, the effects of residual concrete tensile strength at maximum load and compressive stresses in concrete at minimum load can be clearly outlined from the evolution of steel stresses between the first and the last cycle. In particular, the evolution of the residual concrete tensile strength may be identified in the loading branch of the first loading cycle in which after the unstabilized cracking process, the steel stress at the crack approaches that of a bare bar. Then, negative tension-stiffening effects and the compressive stresses in concrete at the crack section develop with the number of cycles. This gives rise to steel stresses at the crack which are larger than the stresses of a bare bar, especially at the minimum level of stress σ_{min} . This fact can represent a favourable effect with respect to fatigue verification, since reduced stress variations develop on the reinforcement at the crack section. This aspect seems to be more pronounced in specimen TC04 with a low reinforcement ratio (and thus higher influence of bond stresses in the response) leading to minimum stresses in the reinforcement larger than the ones for specimen TC06 (with higher reinforcement ratio). With respect to concentrations of stresses, the section in-between cracks (section 2 in Figures 2.12a–b) is the least critical, associated to the lowest variation of stresses. The largest variation of average stress occurs at the location of the crack (with only differences with respect to a bare response due to the effect of imperfect closure of cracks as described by Hordijk, Figure 2.11a.2). However, in terms of local stress variations near the surface of the bar, probably the most critical section is at the location with the most unfavourable combination of variation of average stresses and stress gradients related to bond and stress concentrations near the ribs.

Regarding steel strains at minimum load (dashed lines in Figure 2.12g) and maximum load (continuous lines in Figure 2.12g), the following issues may be outlined:

- The reinforcement ratio plays a significant role with respect to the residual strain of the tie: larger residual strains can be observed after several cycles for lower reinforcement ratios, attaining maximum values which range between 1 and 3.5 times the values of bare bars.

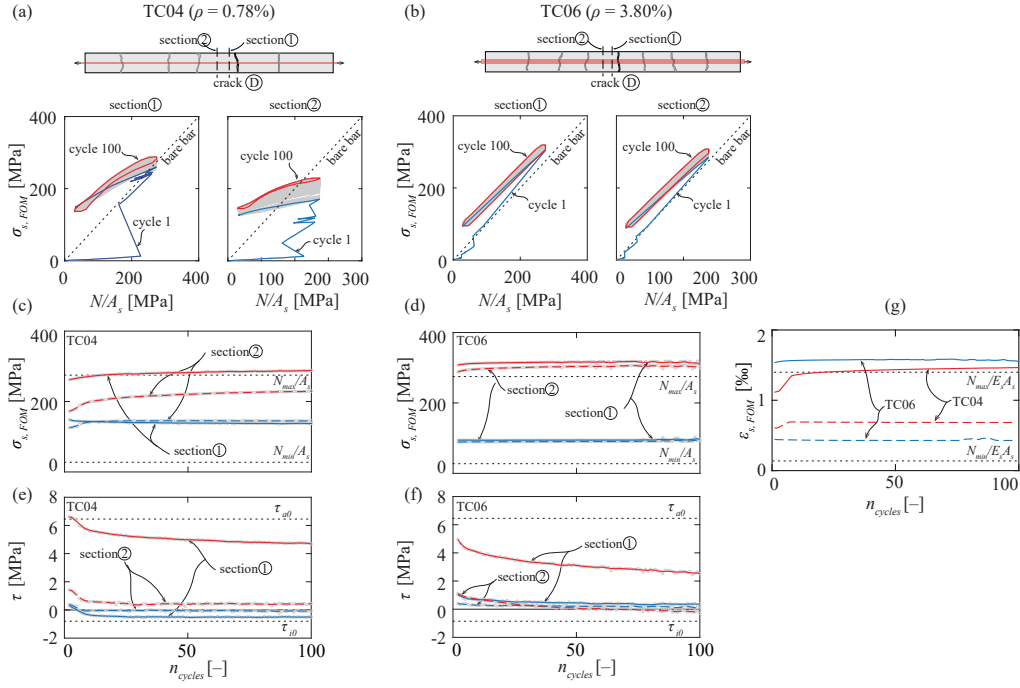


Figure 2.12: Average stress in the loading/unloading phase N/A_s with respect to calculated stresses $\sigma_{s,FOM}$ on the basis of measured FOM strains for specimens (a) TC04 and (b) TC06 (refer to blue curves for first load cycle and red curves for last cycle); calculated stresses $\sigma_{s,FOM}$ on the basis of measured FOM strains at the maximum loading stress N_{max}/A_s and minimum loading stress N_{min}/A_s with the number of cycles for specimens (c) TC04 and (d) TC06; bond stresses τ at the maximum loading stress N_{max}/A_s and minimum loading stress N_{min}/A_s for specimens (e) TC04 and (f) TC06 (values plotted in section 1 at the location of peak bond stress and section 2 located in-between cracks); and (g) average strains in the tie at the maximum loading stress N_{max}/A_s and minimum loading stress N_{min}/A_s with the number of cycles.

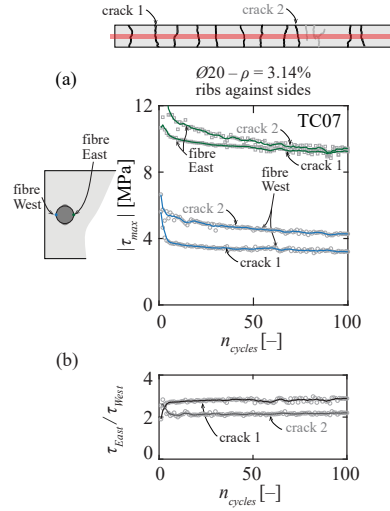


Figure 2.13: Specimen TC07 with eccentric bar: (a) bond stress degradation; and (b) ratio between maximum bond stresses of fibre at the inner side (fibre East) and fibre close to free surface (fibre West) for two selected cracks.

- The average strain at N_{max}/A_s increases with the number of cycles leading to larger crack openings.
- These aspects could be detrimental for service limit state verifications (higher crack widths with increasing number of cycles), but potentially beneficial for fatigue in case of redistribution of internal forces.

With respect to the behaviour of eccentric bars, its response is shown in Figure 2.13 for specimen TC07 (with ribs against the sides). Differently from tests with centred bars in which bond stresses are relatively uniform around the perimeter of the bar, when the bar is eccentric, the distribution of bond stresses is no longer uniformly distributed along the control perimeter of the bar. Figure 2.13a presents the measured peak bond stress τ_{max} with the number of cycles (in a similar manner as in Figure 2.10d) for two fibres located respectively at the side of the free surface (refer to fibre West) and in the inner side (fibre East). Degradation of bond stresses is consistently observed, in similar proportions as those of centric tests [8, 35]. Moreover, for ties with eccentric bars, reduced bond stresses developed at the side of the free surface with respect to the inner sides of the bar. This can be explained by the potential spalling of concrete cover [41] for the faces close to the free surfaces leading to lower peak bond stresses as well as to more pronounced degradations with the number of cycles of the latter, see Figure 2.13b.

2.5 Beam tests

Main parameters and test setup

Three four – point bending tests were performed on 3.0 m reinforced concrete beams with 0.30 x 0.32 m cross section, Figure 2.14. The nominal effective depth was constant for all tests and equal to 274 mm. Two concentrated forces were introduced symmetrically by means of two hydraulic jacks with a total capacity of 1 MN. The jacks were fixed to an external steel frame and placed at a constant distance to the support equal to 875 mm, representing a shear span of $3.2d$. The beams were supported on two 50×300 mm steel plates which were arranged on two bearings allowing

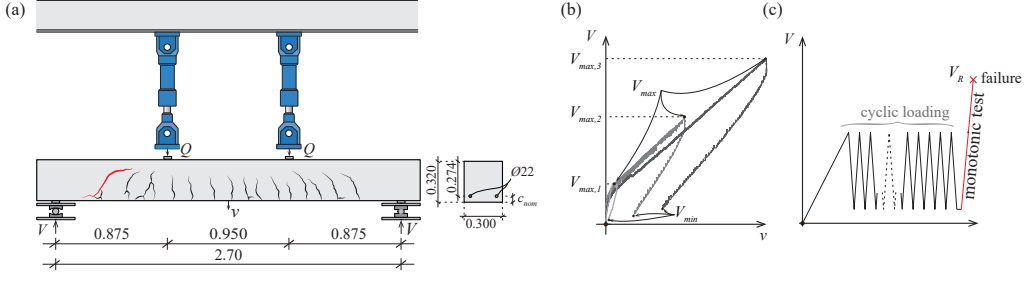


Figure 2.14: Beam tests: (a) front view of test setup; (b) load levels selected for the cyclic loading; and (c) loading pattern (quasi-static cyclic loading + monotonic test until failure); (shear force V at supports including self-weight).

Table 2.3: Main parameters and measured shear strengths of beam tests

	$V_{cycl,max}$ [kN]	$V_{cycl,min}$ [kN]	$R = V_{min}/V_{max}$	f_c [MPa]	V_R [kN]
SC75	27.8	5.27	0.19	33.3	95.4
SC76	54.0	7.25	0.13	36.0	97.1
SC77	86.4	10.2	0.12	36.6	80.7

for free rotation and longitudinal displacements of the supports. All beams were cast with normal strength concrete whose compressive strength at the testing day ranged between 33.2 and 36.6 MPa (average of three compressive tests on 160 x 320 mm concrete cylinders). The maximum aggregate size was 16 mm for all test specimens. The cement type was CEM II/B-M (T-LL) 42.5N, in accordance with [23], with a water-to-cement ratio equal to 0.45. The flexural reinforcement of all beams consisted of two high strength $\phi 22$ reinforcing bars (yield strength $f_y=701$ MPa, $\rho=0.92\%$) and no compression reinforcement was provided. The nominal concrete cover c_{nom} was 35 mm. Additional details are given in Table 2.3. The concrete surface behaviour was tracked by means of digital image correlation. In addition, FOM sensors were glued (both on the top and bottom side) in one of the two bars forming the flexural reinforcement. All members were tested in displacement-control mode with a loading rate ranging between 0.01 and 0.05 mm/s (typical test duration of 15 minutes). Every member was first subjected to 50 quasi-static load cycles, then unloaded and reloaded until shear failure occurred on one side. Regarding the maximum force $V_{cycl,max}$ during cyclic action, three load levels were investigated with the three beams (see also Table 2.3):

- Beam SC75, load level I – $V_{cycl,max}$ corresponding to the flexural cracking development.
- Beam SC76, load level II – $V_{cycl,max}$ corresponding to $0.5 - 0.55V_R$ (where V_R refers to the ultimate failure load)
- Beam SC77, load level III – $V_{cycl,max}$ corresponding to the onset of the quasi – horizontal branch of the shear critical crack (refer to [42] for additional details).

The maximum shear force $V_{cycl,max}$ during cyclic loading corresponds to the shear force at supports.

Test results

The measured load – displacement curves (shear force V at support including the self-weight) are shown in Figure 2.15 for the three members with three different load levels $V_{cycl,max}$. The vertical displacement is evaluated by means of a LVDT placed at the centre of the beam. In all specimens, an increase of vertical displacement was observed due to the effect of cyclic loading. For specimens SC75, SC76, this can be attributed to the cyclic response of concrete and to bond degradation. Larger residual crack openings also developed for increasing number of cycles as well as higher strains in rebars at maximum shear force $V_{cycl,max}$. No shear failure occurred in these two tests

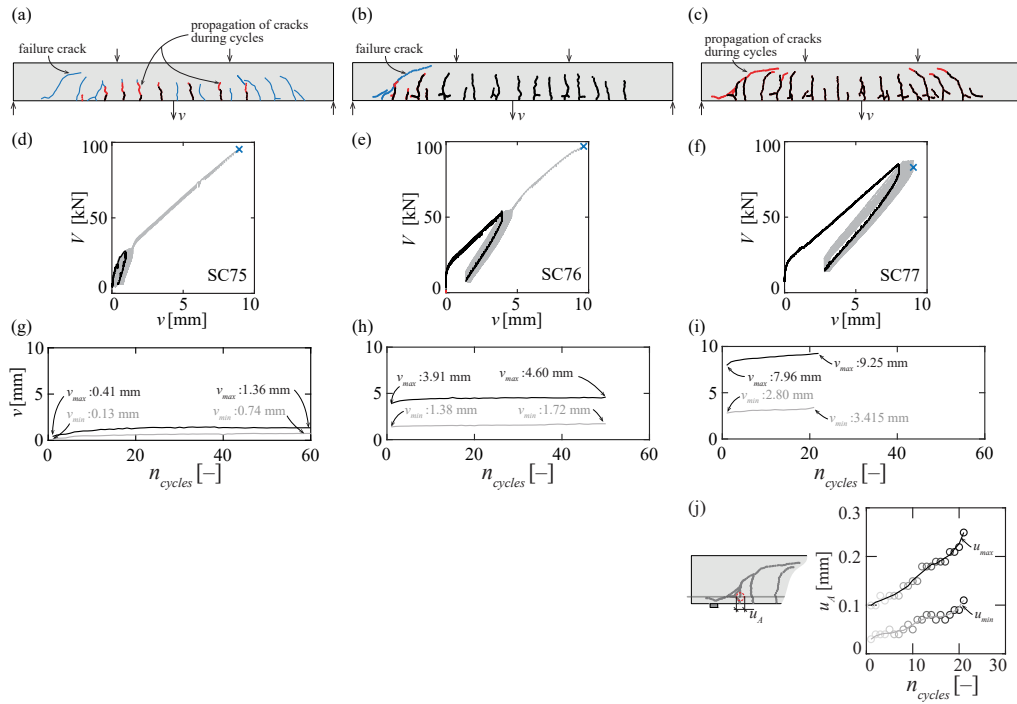


Figure 2.15: Cracking pattern after first cycle (in black), propagation during cyclic loading (in red), at failure (in blue) for beams: (a) SC75 (b) SC76 (c) SC77; load–displacement curves $V - v$ for beams (d) SC75; (e) SC76 and (f) SC77; maximum deflection developed during cyclic loading for beams (g) SC75; (h) SC76 and (i) SC77; and (j) development of horizontal component of crack opening u_A at the level of the flexural reinforcement with the number of cycles for the shear critical crack leading to the failure of member SC77.

during the cycles.

For specimen SC77, the development of the quasi–horizontal shear crack during the loading cycles gave rise to a failure in shear at a maximum shear force $V_{cycl,max}$ equal to 84% of the reference shear failure load V_R (average of shear failure loads measured in specimens SC75 and SC76). Failure occurred by propagation of the critical shear crack.

Details on the evolution of the midspan displacement with the cycles are additionally shown in Figures 2.15d–f obtained from LVDT and DIC readings. It can be noted a significant increase in the maximum deflection during the cycles (black curves in Figures 2.15g–i, particularly during the first ones) as well as a residual deflection (light grey curves). To a large extent, these phenomena can be related to the imperfect closure of cracks lips, to the degradation of bond properties and to the development of negative tension–stiffening effects.

As previously mentioned, beam SC77 was subjected to load cycles in which the maximum applied shear force corresponded to the formation of the quasi – horizontal branch of the critical shear crack. During the cyclic process, the member failed in shear due to propagation of the crack tip towards the load introduction plate, Figure 2.15c. This development was accompanied by the evolution of the horizontal crack opening u_A at the level of the flexural reinforcement towards the loading plate, see Figure 2.15j (black curves for maximum horizontal crack opening and light grey curves for residual crack opening).

In addition to DIC, FOM sensors were installed in the top and bottom surfaces of steel rebars. The strains were evaluated with a spatial resolution of 0.65 mm and the raw results were smoothed over an average length equal to two times the bar diameter (as for tests on ties, according to the disturbed region observed in pull–out tests). Figures 2.16b–c show the FOM results for all cycles

with respect to the top and bottom rebar surface (values at maximum and minimum applied shear forces $V_{cycl,max}$ and $V_{cycl,min}$). In the beam region with constant bending moment, it can be noted a difference between top and bottom rebar strain at each section. In particular, the bottom strain results consistently higher than top rebar strain. This can be explained by the curvature of the rebar as already stated by Ritter [1] (refer to Figure 2.1b), an aspect usually neglected for design. Such response is however not observed in other regions, namely in regions subjected to a combination of bending and shear. For these regions, the effect of inclined shear cracks allows for activation of dowelling forces, thus leading to relatively high and concentrated curvatures at the opposite sides of an inclined crack (double-hinge mechanism) dominating the difference between top and bottom bar strains.

On this basis, by assuming plane sections of the bar to remain plane and an elastic-plastic behaviour of the steel, the normal forces and bending moments in the bar can be determined by integration of the cross-sectional stresses, see Figure 2.16d. The profiles of average rebar stresses $\sigma_{s,FOM}$ are shown in Figure 2.16e. The measured values are also compared with the theoretical stresses resulting from beam analysis considering cracked conditions (lever arm $z = d - c/3$ where c is the height of the compression zone calculated assuming elastic behaviour of the compression zone and neglecting tension-stiffening). It can be noted that the calculated values locally underestimate the measured stresses at the maximum load $V_{cycl,max}$, in particular in regions with inclined shear cracking. This phenomenon has been consistently observed in such members [13] and can be explained by the development of inclined shear cracks [43] (according to the shift of bending moments). On the other hand, at minimum shear forces $V_{cycl,min}$, the analytical values largely underestimate the average measured rebar stresses. In particular, the measured stress variations in the rebar during cycles attain values (≈ 180 MPa) which are 30% lower than the calculated stress variations for a fully-cracked response (≈ 250 MPa). It can be noted that this lower variation of stresses have favourable implications on the potential fatigue response of reinforcement.

Moreover, the marked localization of bar bending clearly stems out in Figure 2.16f (resulting from the shift on the position of the waves of the strain profile along the longitudinal direction, Figures 2.16b-c), owing to the local kinking in the bar, Figures 2.16g-h.

Interpretation of test results

As already noted by Ritter [1], the consideration of an average stress in the cross section of a bar is a simplification of its actual response, as a non-uniform profile of stresses in the longitudinal reinforcement develops due to the curvature of plane sections [1]. The reality is in fact even more complex, as once cracking occurs at a section, the steel bar is actually kinked with concentrated curvatures at the location of the cracks, see Figure 2.16g. Kinking of the bar is thus associated to the activation of transverse forces at the location of cracks, whose local force distribution is outlined in Figure 2.16h. As a consequence, transversal compressive and tensile forces develop in the vicinity of the crack, being a potential source for longitudinal delamination cracks together with other phenomena (as bond splitting [44] stresses or spalling due to deviation forces [45]).

The effects of local kinking of the bar can be observed also in Figure 2.17 for the region in pure bending (between loads, refer for instance to crack 3 in blue). The FOM readings show in this region low or no curvatures between cracks (due to the fact that the bar is embedded in uncracked concrete with limited deformation), but relatively high and concentrated curvatures at the location of the cracks. These effects can also be clearly appreciated in the region subjected to bending and shear (red and green cracks for instance in Figure 2.17). In this region, flexural cracks develop in an inclined manner (Cavagnis et al. [10]) and their opening leads kinematically to the development of a delamination crack and dowelling of the reinforcement (refer to Figure 2.2c). In this case, other than the peaks of positive strains at the location of the cracks, negative curvatures develop along and at the end of the delamination crack indicating the presence of bending associated to

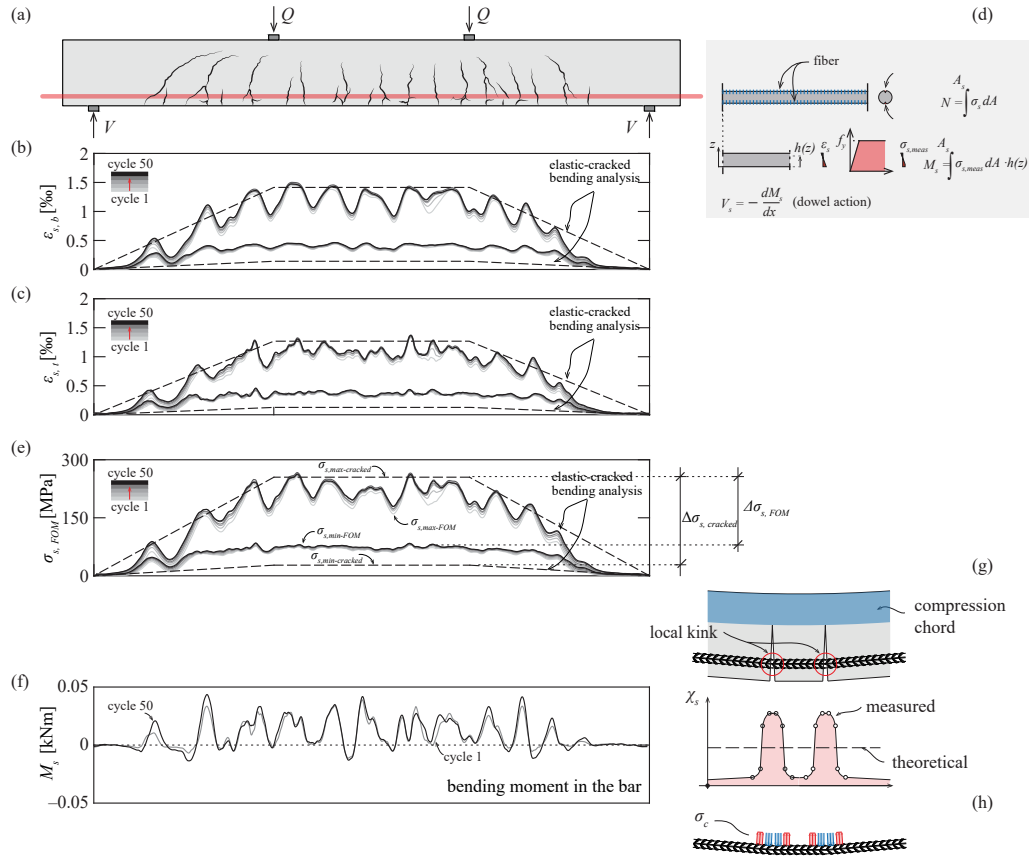


Figure 2.16: Beam SC76 — (a) cracking pattern observed at failure; profiles at maximum and minimum load for selected cycles (refer to colour scale at top left side); (b) measured rebar strains $\epsilon_{s,b}$ at bottom side; (c) measured rebar strains $\epsilon_{s,t}$ at top side; (d) description of fibre position and approach for calculating rebar internal forces; (e) comparison between calculated average stresses $\sigma_{s,FOM}$ from FOM strains and steel stresses according to an elastic–cracked calculation $\sigma_{s,cracked}$; (f) bending moments in the reinforcing bar M_s ; (g) localized kinking of the bar in a cracked section with schematic representation of local increase of curvature χ_s ; and (h) local contact forces due to kinking of the bar.

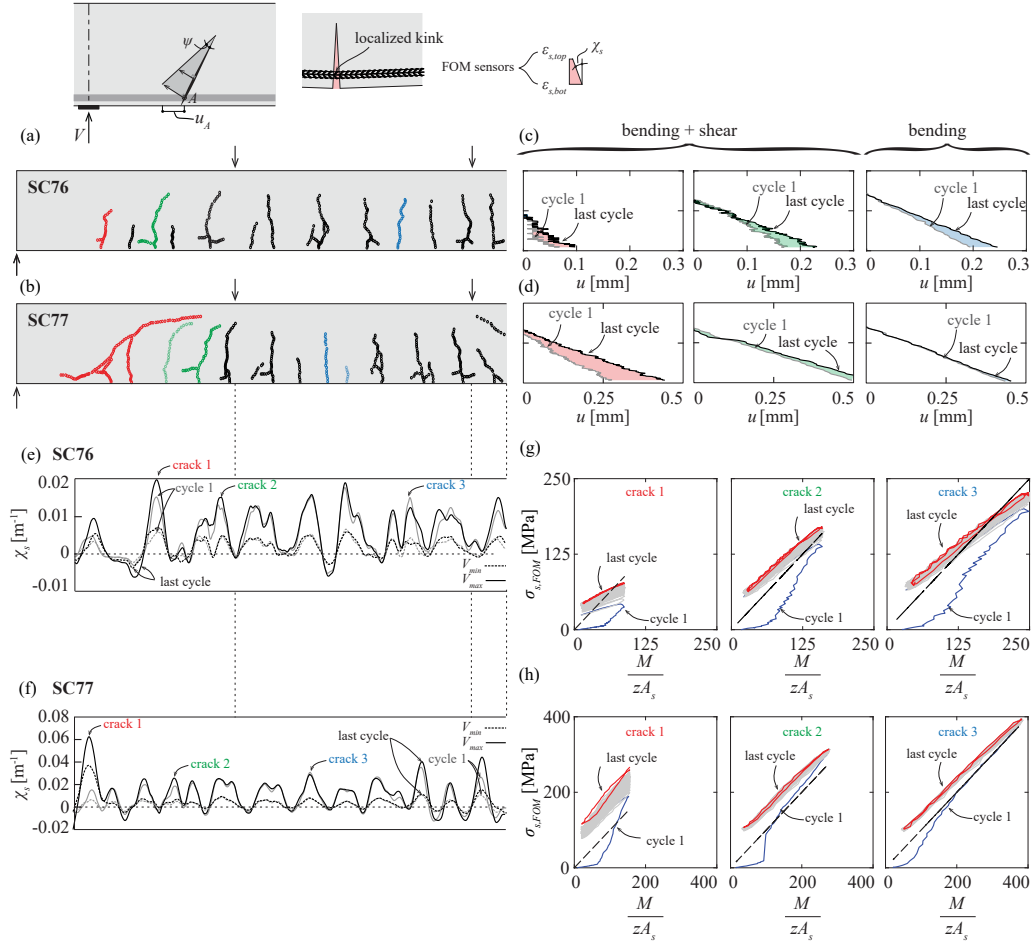


Figure 2.17: Cracking pattern observed with DIC during cyclic loading for beams (a) SC76 and (b) SC77; evolution of horizontal crack opening u between first (grey lines) and last (black lines) load cycle for three selected cracks (refer to red, green and blue cracks) for beams (c) SC76 and (d) SC77; profiles of measured rebar curvatures between first (grey lines) and last (black lines) load cycles at the maximum rebar stress N_{max}/A_s (continuous lines) and minimum rebar stress N_{min}/A_s (dashed lines) for specimens (e) SC76 and (f) SC77; and $\sigma_{s,FOM} - M/zA_s$ behaviour during cyclic loading for three selected cracks in the region with combined bending and shear actions (red and green cracks) or with just bending actions (blue cracks) for specimens (g) SC76 and (h) SC77.

dowelling of the reinforcement (Figure 2.2c). The horizontal component of the crack opening u over the height (Figures 2.17c–d), obtained by means of DIC, reveals that in the region subjected to pure bending, the profile is almost linear. In addition, there is some moderate increment of the crack opening under cyclic loading, which can be attributed primarily to bond degradation (refer to Section 2.4). This phenomenon is however significantly more pronounced in the region subjected to bending and shear where inclined cracks develop (refer particularly to red crack in specimen SC77, Figure 2.17d). This is justified, other than bond degradation, by the progression of the delamination crack and its associated increase of strains in the reinforcement, [10, 42] (refer to the behaviour in Figures 2.17g–h in terms of measured steel stress $\sigma_{s,meas}$ – steel stress in the bar M/zA_s according to an elastic–cracked calculation) and by the progression of the upper tip of the crack towards the loading plate (upper quasi–horizontal branch of the crack).

The progression of the delamination crack and the upper branch of the shear crack are further explained in Figure 2.18. According to the kinematics of an inclined crack (Figure 2.2c), a delamination crack develops due to dowel action of the reinforcement [42, 43]. Such progression is shown in Figure 2.18b with respect to the DIC readings, with the most inclined cracks leading to larger progressions. In the delaminating region, bond stresses are disabled or reduced. As a consequence, the average reinforcement strain increases significantly. This fact is clearly perceptible in specimen SC77 (corresponding to the most inclined and developed shear crack), with large increments of strains at the delamination region as the critical shear crack progresses with the number of cycles (Figure 2.18d). Such increase of measured strains in the delamination region is in agreement to the theoretical considerations performed by Fernández Ruiz et al. [43] and require to be accounted for a suitable evaluation of the shear strength (refer to Figure 2.18f).

In addition, other than the delamination crack, the shift of bending moments needs to be considered in order to properly evaluate the stress state close to failure at the level of the flexural reinforcement, [13] (see Figures 2.18f–h). This was already acknowledged by Cavagnis et al. [13], which considered that all cracks tributary to the critical shear crack give rise to a rather linear profile of the horizontal component of the crack width u (which is in fact proportional to the bending moment at the crack tip). This fact is clearly visible from the shift of the steel stress behaviour presented in Figures 2.17g–h in terms of local steel stresses $\sigma_{s,FOM}$ with respect to M/zA_s (where M is the acting bending moment, $z = d - c/3$ is the lever arm according to an elastic–cracked analysis and A_s is the area of flexural reinforcement). The propagation of the shear crack with the number of cycles was particularly observed in specimen SC77 failing during the loading cycles. For this specimen, the critical shear crack progressed both with respect to its upper quasi–horizontal branch and to the development of the delamination crack (Figures 2.18b,2,f,1) [46]. This progression was associated to an increase of the dowel action of the reinforcement calculated on the basis of its strains (Figures 2.18g–h). It can be noted that a consistent prediction of the failure load can be performed on the basis of the theoretical approach presented by Fernández Ruiz et al. [46], with an estimated failure load of 81.5 kN, closing matching the actual one of 80.7 kN (where the estimated failure load is calculated by considering a monotonic shear resistance $V_{R1} = 96.2$ kN – average of failure loads of specimens SC75 and SC76 – and failure after 22 cycles).

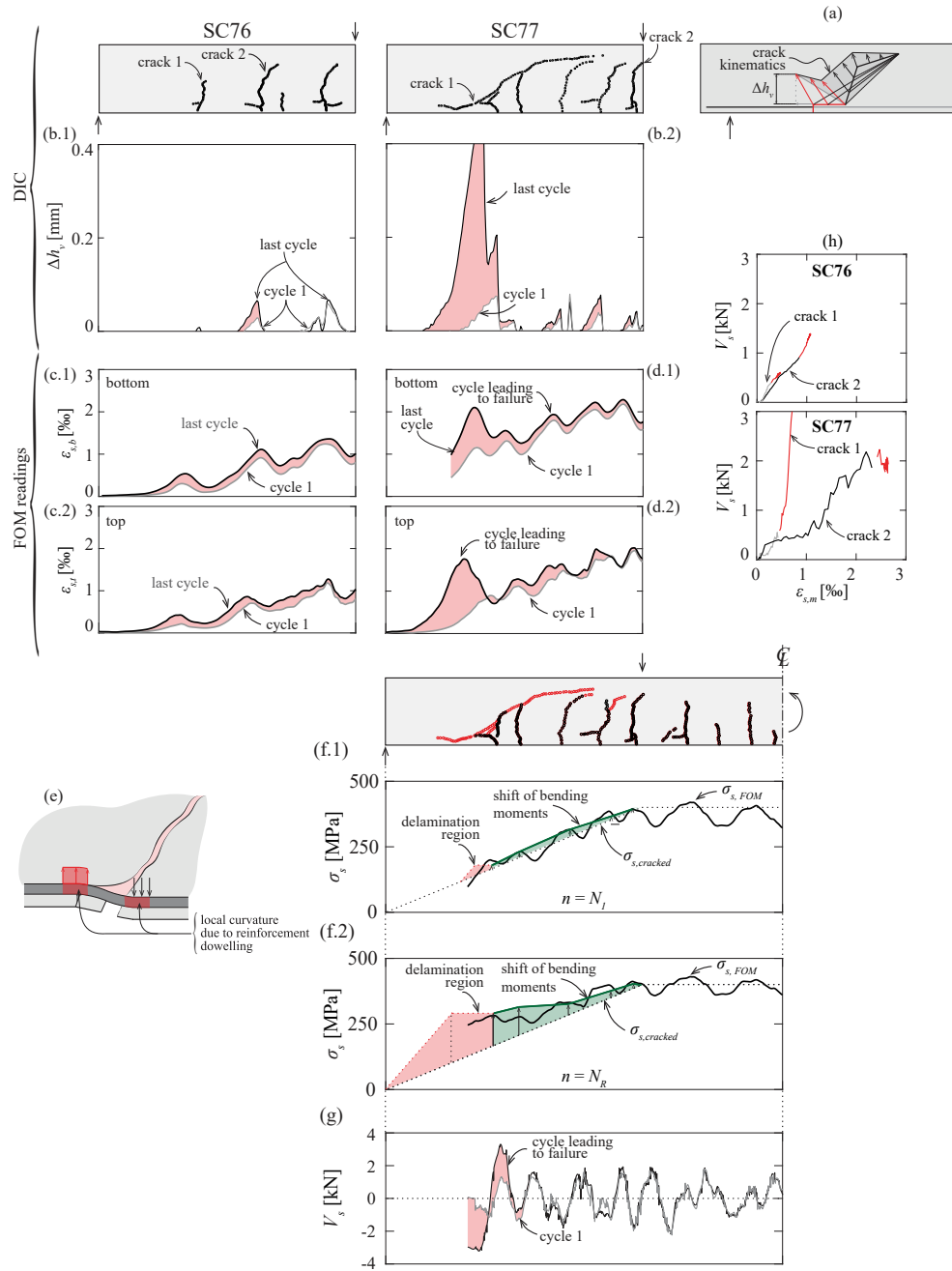


Figure 2.18: (a) geometry of critical shear crack and delamination cracks [43]; vertical crack opening Δh_v for beams (b.1) SC76 and (b.2) SC77; profiles of bottom and top strains at the maximum and minimum level of shear force for beams (c.1)-(c.2) SC76 and (d.1)-(d.2) SC77, respectively; (e) local curvature due to dowelling of reinforcement; stress at the flexural reinforcement: comparison between measured stresses $\sigma_{s,FOM}$ and calculated stresses $\sigma_{s,cracked}$ in a bare bar according to an elastic-cracked analysis, for specimen SC77 after (f.1) the first cycle and (f.2) the cycle leading to failure $N = N_R$; (g) profile of dowelling forces during the first and last load cycle for specimen SC77; and (h) dowelling forces developing at the level of flexural reinforcement for two selected cracks (grey and black lines refer to V_s developed in the first cycle, red curves are the peak dowelling forces at each cycle).

2.6 Conclusions

Recent advancements on measurement techniques allow for a notable step forward in the understanding of the actual response of embedded reinforcement and its interaction with concrete. In particular, the implementation of Fibre-Optical-Measurement systems (FOM) is allowing for high quality readings of the longitudinal strains in a rebar with low disturbance of the behaviour.

This paper revisits the interaction between reinforcement and concrete by performing tests on three different types of structural elements: pull-out tests, tension tests on ties subjected to cyclic loading and four-point bending tests under cyclic loading. A special attention is set on the response of potentially brittle phenomena (sensitive to stress concentrations and crack propagations), such as fatigue under cyclic loading or shear failures in beams without transverse reinforcement.

The main conclusions of this research are listed below:

Pull-out tests

- Strong strain (and stress) gradients are measured near to the ribs of bars, originated by local contact forces due to mechanical engagement.
- The observed strain gradients and high strain values observed in the rebars confirm that tension tests on bare rebars for the evaluation of the material strength under fatigue loading can be unsuitable to characterize the response of embedded reinforcement.

Tension tests

- The profile of measured strains in reinforced concrete ties confirmed the suitability of considering rigid-plastic bond laws as a rough but sound simplification.
- FOM measurements show the development of negative tension-stiffening effects during the unloading process. Bond degradation was tracked with the number of cycles providing results in sound agreement with reductions proposed in the literature (both for peak bond values τ_a and for negative values of the bond stress τ_i).
- Measured stress variations during unloading can significantly differ from values calculated on bare bars (which could be favourable for fatigue verification) due to a large extent by the imperfect closure of cracks.

Beam tests

- Local kinking of rebars was observed at bending (vertical) cracks due to compatibility of deformations. Such kinking originates local transverse tensile stresses in the concrete leading to the potential development of longitudinal delamination cracks and cover spalling.
- Lower stress variations due to bending were detected in the longitudinal reinforcement with respect to theoretical values calculated with elastic-cracked analyses due to imperfect closure of cracks and negative tension-stiffening effects. As for the reinforced concrete ties, this has favourable implications on the fatigue response of reinforced concrete members.
- Based on the recorded strain profiles and by derivation of the calculated bending moments in the longitudinal bars, FOM allows quantifying the dowel action at shear (inclined) cracks.
- The level of maximum shear force plays a significant role in the propagation of shear cracks leading to failure. Shear displacements were observed in regions subjected to shear forces, thus leading to the formation of delamination cracks. Such cracks lead to a loss of the bond strength and to an increase of the opening of the critical shear crack. The development of the delamination crack is also associated to dowelling forces in the reinforcement (potentially detrimental for fatigue issues), but this effect is mostly noticeable when the specimen is near to its shear failure.

2.7 Appendix. Response of tension ties including its unloading response

This Appendix presents the model developed by Muttoni and Fernández Ruiz (2007) [32] to evaluate the response of tension ties including their unloading response. The formulas presented herein have been used for the evaluation of the analyses presented in this paper.

Regarding monotonic loading of a reinforced concrete member, once cracking occurs, the cross – sectional equilibrium of forces may be described in the following manner:

$$\sigma A = \sigma_s A_s + \sigma_c A_c \quad (2.3)$$

in which σ is the average stress in the tie, A the gross area, σ_s the steel stress and σ_c the concrete stress. If the tensile softening of concrete is neglected at the crack location, the average stress σ corresponds to $\sigma_{sa}\rho$, being ρ the reinforcement ratio and σ_{sa} the steel stress at the crack. Considering a rigid–plastic law for bond over the transfer length l_{ba} [29], from the equilibrium of forces it may be established the equation describing the longitudinal steel stress in the loading regime (refer to the dashed lines Figure 2.19a), as follows:

$$\sigma_{sa} \frac{\pi}{4} \phi^2 = \pi \phi l_{ba} \tau_a \quad (2.4)$$

The maximum value of the transfer length $l_{ba,max}$ is derived by considering that at the end of the crack development phase the steel stress $\sigma_{sa} = \frac{f_{ct,eff}}{\rho}$:

$$l_{ba,max} = \frac{\phi f_{ct,eff}}{4\rho\tau_a} \quad (2.5)$$

where $f_{ct,eff}$ is the effective concrete tensile strength.

Since the crack opening is the integration of the difference between steel and concrete strains along the concrete member, the crack width w after the loading process may be derived as:

$$w = \frac{\sigma_{sa}^2 \phi}{4E_s \tau_a} = \frac{\sigma^2 \phi}{4\rho^2 E_s \tau_a} \quad (2.6)$$

So, considering the maximum transfer length $l_{ba,max}$, the crack opening in the stabilized cracking phase results:

$$w = \left(\frac{2\sigma_{sa}}{E_s} - \frac{f_{ct,eff}}{\rho E_s} \right) \frac{\phi f_{ct,eff}}{4\rho\tau_a} \quad (2.7)$$

During the unloading process, Figure 2.11b, the complex geometry of crack lips yields to residual crack openings. An estimate of these residual crack openings was performed by Hordijk [37, 38] who derived empirically the stress necessary to reclose the crack as a function of the crack width. Thus, due to crack closure, concrete develops compressive stress which cannot be neglected in the cross – sectional equilibrium, Figure 2.11a.2. The average stress during unloading is then:

$$\sigma_{per} = \sigma_{si}\rho + \bar{\sigma}_c \quad (2.8)$$

considering that the stress is $\Delta\sigma = \Delta\sigma_s\rho - \bar{\sigma}_c$, with $\bar{\sigma}_c$ according to [37], Figure 2.11d.

$$\bar{\sigma}_c = f_{ct,eff} \left(0.004 \left(\log \left[\frac{w}{w_c} \right] \right)^5 - 0.16 \sqrt{1 - \frac{w}{w_c}} \right) \quad (2.9)$$

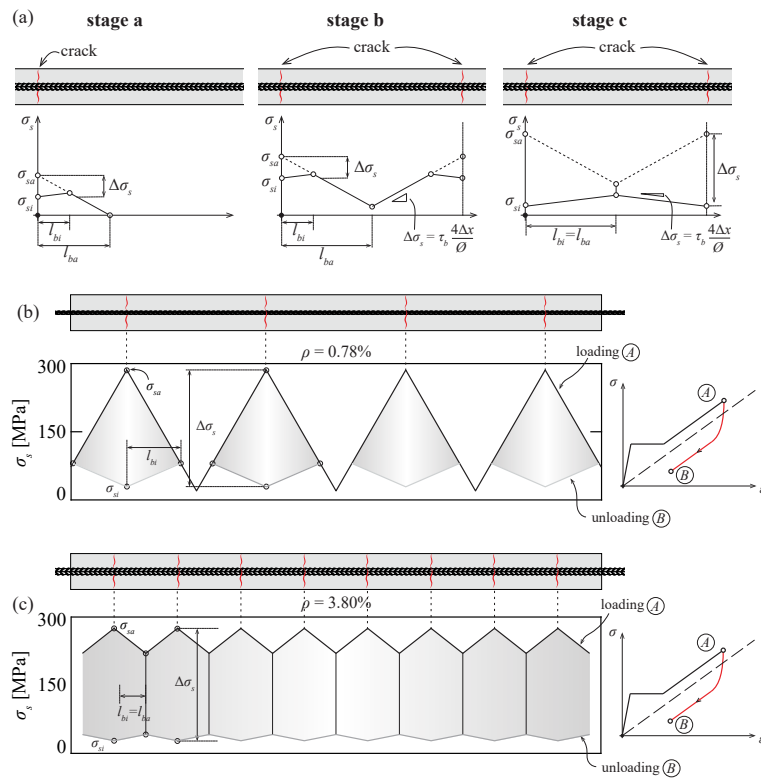


Figure 2.19: Negative tension–stiffening: (a) different unloading stages; comparison of steel stress distribution for two reinforced concrete ties with reinforcement ratios equal to (b) 0.78% and (c) 3.80% respectively – black lines refer to maximum steel stress (loading phase) while grey lines refer to minimum steel stress (unloading phase).

As shown in [32], the crack width during the unloading process w_{per} needs to be calculated in a different manner as a function of the regime (cracking process / stabilized cracking) in which unloading is performed, Figure 2.11b:

- **Stage a** – unloading in the crack development stage

$$w_{per} = \left[(\sigma_{per} + \Delta\sigma)^2 - (\Delta\sigma + \bar{\sigma}_c)^2 \frac{\tau_a}{\tau_a + \tau_i} \right] \frac{\phi}{4\rho^2 E_s \tau_a} \quad (2.10)$$

- **Stage b** – Unloading in the stabilized cracking: $l_{bi} < l_{ba,max}$

$$w_{per} = \left[2(\sigma_{per} + \Delta\sigma) - f_{ct,eff} - \frac{\Delta\sigma + \bar{\sigma}_c}{f_{ct,eff}} \frac{\tau_a}{\tau_a + \tau_i} \right] \frac{\phi f_{ct,eff}}{4\rho^2 E_s \tau_a} \quad (2.11)$$

- **Stage c** – Unloading in the stabilized cracking: $l_{bi} = l_{ba,max}$

$$w_{per} = \left[2(\sigma_{per} - \bar{\sigma}_c) + \frac{\tau_i f_{ct,eff}}{\tau_a} \right] \frac{\phi f_{ct,eff}}{4\rho^2 E_s \tau_a} \quad (2.12)$$

Figure 2.19 presents, for instance, the results of this approach [32] for two concrete ties (same geometry of the tests in Section 2.4) with reinforcement ratios equal to 0.78% and 3.80% respectively (as for specimens TC04 and TC06). The results are provided both for loading and unloading stages (a target ratio R equal to 0.1 and a maximum rebar stress equal to 275 MPa is imposed in accordance with loading rates of the tests). The results show that crack spacing is largely governed by reinforcement ratio and the specimen with ρ equal to 0.78% remains in stage *b* after unloading while the specimen with ρ equal to 3.80% reaches stage *c* of the behaviour, Figure 2.19a.

Notation

A	gross cross-sectional area
A_s	reinforcement cross-sectional area
$A_{s,eff}$	effective reinforcement cross-sectional area
c_{nom}	nominal concrete cover
χ_s	local curvature of the rebar
d_{nom}	nominal effective depth of the beam
δ	relative bar-concrete slip
$\Delta\sigma$	stress variation
$\Delta\sigma_s$	stress variation in the reinforcement
Δh_v	transversal shear displacement of reinforcement
ϵ_s	bar strain
$\epsilon_{s,m}$	bar average strain
$\epsilon_{s,FOM}$	FOM strains
$\epsilon_{s,t}$	top bar strain obtained with FOM measurements
$\epsilon_{s,b}$	bottom bar strain obtained with FOM measurements
E_s	elastic steel modulus
f_c	concrete cylinder compressive strength
f_y	yield strength of reinforcement
$f_{ct,eff}$	concrete effective tensile strength
ϕ	bar diameter
l_{ba}	transfer length
$l_{ba,max}$	maximum transfer length
l_{bi}	unloaded transfer length
M	bending moment
n_{cycles}	number of cycles
N	normal force
ψ	rotation of the shear crack
ρ	reinforcement ratio A_s/A
R	target ratio between maximum and minimum applied forces
σ	average stress of the tie
σ_s	average stress in the reinforcement
$\sigma_{s,FOM}$	stress in the reinforcement calculated with FOM strains
$\sigma_{s,cracked}$	stress in the reinforcement calculated according to an elastic-cracked analysis
σ_{sa}	steel stress at crack location after loading
σ_{si}	steel stress at crack location after unloading
σ_{per}	residual stress
σ_{max}	maximum steel stress
σ_{min}	minimum steel stress

$\bar{\sigma}_c$	concrete stress after unloading
σ_c	concrete stress
τ	bond stress
τ_b	rigid-plastic bond stress
τ_a	rigid-plastic bond stress for monotonic loading
τ_{a0}	loading bond stress in the first loading cycle
$\tau_{a\infty}$	loading bond stress after large number of unloading-reloading cycles
τ_i	loading bond stress after unloading
τ_{i0}	loading bond stress after first unloading
$\tau_{i\infty}$	unloading bond stress after large number of unloading-reloading cycles
τ_{max}	peak bond stress calculated from FOM strains
τ_{west}	bond stress of the fibre close to the free surface
τ_{east}	bond stress of the fibre at the inner side
u	horizontal crack opening
u_A	horizontal crack opening in section A
v	beam deflection
v_{max}	maximum beam deflection
V	applied shear force
$V_{cycl,max}$	maximum level of shear force applied on beams
$V_{cycl,min}$	minimum level of shear force applied on beams
V_R	ultimate shear resistance
V_s	dowelling force of reinforcement
w_c	maximum crack width at which concrete tensile softening stresses are transmitted
w_{per}	crack width after unloading
x	position along the specimen
z	lever arm

Bibliography

- [1] W. Ritter. Die Bauweise Hennebique. *Schweizerische Bauzeitung*, 6(33.7):49–52, 1899.
- [2] FIB Bulletin 10. *Bond of reinforcement in concrete*. Lausanne (Switzerland), 2000.
- [3] Pietro Giovanni Gambarova, Giovanni Plizzari, and G. Rosati. Bond mechanics including pull-out and splitting failures. *FIB Bulletin 10: Bond of Reinforcement in Concrete*, pages 1–98, 2000.
- [4] Yukimasa Goto and Koji Otsuka. Internal Cracks Formed in Concrete Around Deformed Tension Bars. *ACI Journal Proceedings*, 68(4):244–251, 1971.
- [5] Miguel Fernández Ruiz, Aurelio Muttoni, and Pietro Giovanni Gambarova. Analytical modeling of the pre – and post – yield behavior of bond in reinforced concrete. *Journal of Structural Engineering*, 133(10):1364–1372, 2007.
- [6] Patrick Valeri, Miguel Fernández Ruiz, and Aurelio Muttoni. Experimental research on textile reinforced concrete for the development of design tools. In *Proceedings of the 12th fib International PhD Symposium in Civil Engineering*, pages 169–176, Prague, Czech Republic, 2018.
- [7] Miguel Gómez Navarro and Jean Paul Lebet. Concrete cracking in composite bridges: Tests, models and design proposals. *Structural Engineering International: Journal of the International Association for Bridge and Structural Engineering (IABSE)*, 11(3):184–190, 2001.
- [8] G. Balázs. Fatigue of Bond. *ACI Materials Journal*, 88(6):620–630, 1991.
- [9] Correlated Solutions. *Vic-3D 2010, Reference Manual*. 2010.
- [10] Francesco Cavagnis, Miguel Fernández Ruiz, and Aurelio Muttoni. Shear failures in reinforced concrete members without transverse reinforcement: An analysis of the critical shear crack development on the basis of test results. *Engineering Structures*, 103:157–173, 2015.
- [11] Francesco Cavagnis, Miguel Fernández Ruiz, and Aurelio Muttoni. An analysis of the shear-transfer actions in reinforced concrete members without transverse reinforcement based on refined experimental measurements. *Structural Concrete*, 19(1):49–64, 2017.
- [12] Miguel Fernández Ruiz and Aurelio Muttoni. Size effect in shear and punching shear failures of concrete members without transverse reinforcement: Differences between statically determinate members and redundant structures. *Structural Concrete*, 19(1):65–75, 2018.
- [13] Francesco Cavagnis, Miguel Fernández Ruiz, and Aurelio Muttoni. A mechanical model for failures in shear of members without transverse reinforcement based on development of a critical shear crack. *Engineering Structures*, 157:300–315, 2018.
- [14] Luna Technologies Inc. *Optical Backscatter Reflectometer 4600 User Guide*. Luna Technologies, Blacksburg, VA, 2013.
- [15] Neil A. Houtt, Omurden Ekim, and Ryan Regier. Damage/Deterioration Detection for Steel Structures Using Distributed Fiber Optic Strain Sensors. *Journal of Engineering Mechanics*, 140(12):9, 2014.
- [16] Ryan Regier and Neil A. Houtt. Concrete deterioration detection using distributed sensors. *Proceedings of the Institution of Civil Engineers - Structures and Buildings*, 168(2):118–126, 2015.

- [17] Matthew B. Davis, Neil A. Hoult, Sanchit Bajaj, and Evan C. Bentz. Distributed Sensing for Shrinkage and Tension-Stiffening Measurement. *ACI Structural Journal*, 114(3):753–764, 2017.
- [18] António Barrias, Joan R Casas, and Sergi Villalba. Embedded Distributed Optical Fiber Sensors in Reinforced Concrete Structures—A Case Study. *Sensors*, 18(4), 2018.
- [19] Jack J Poldon, Neil A. Hoult, and Evan C. Bentz. Distributed Sensing in Large Reinforced Concrete Shear Test. *ACI Structural Journal*, 116(5):235 – 245, 2019.
- [20] A. Brault and Neil A. Hoult. Distributed Reinforcement Strains: Measurement and Application. *ACI Structural Journal*, 116(4), 2019.
- [21] Zachary Broth and Neil A. Hoult. Dynamic distributed strain sensing to assess reinforced concrete behaviour. *Engineering Structures*, 204:110036, 2020.
- [22] Xin Lu. *Coherent Rayleigh time domain reflectometry : novel applications for optical fibre sensing*. PhD thesis, École Polytechnique Fédérale de Lausanne, 2016.
- [23] EN 197-1:2011. *Cement - Part 1: Composition, specifications and conformity criteria for common cements*. Brussels, Belgium, 2011.
- [24] EN1992-1-1:2004. Design of Concrete Structures - Part 1: General Rules and Rules for Buildings. Technical report, Brussels, Belgium, 2004.
- [25] Francesco Moccia, Xavier Kubski, Miguel Fernández Ruiz, and Aurelio Muttoni. The influence of casting position and disturbance induced by reinforcement on the structural concrete strength. *Structural Concrete*, 2020.
- [26] G. P. Tilly. Fatigue of Steel Reinforcement Bars in Concrete: a Review. *Fatigue & Fracture of Engineering Materials & Structures*, 2(3):251–268, 1979.
- [27] Bicher Farra and J.-P. Jaccoud. Influence of concrete and reinforcement on cracking of concrete structures. Technical report, Test Rep. of Short-Term Imposed Strains on Ties, IBAP, Pub. 140, École Polytechnique Fédérale de Lausanne, Lausanne (Switzerland), 1993.
- [28] ISO 6892-1:2019. Metallic materials — Tensile testing — Part 1: Method of test at room temperature. 1(112):70, 2019.
- [29] Peter Marti, Manuel Alvarez, Walter Kaufmann, and Viktor Sigrist. Tension Chord Model for Structural Concrete. *Structural Engineering International*, 8(4):287–298, 1998.
- [30] Manuel Alvarez. *Influence of bond behaviour in the deformation capacity of reinforced concrete*. PhD thesis, ETH Zurich (Switzerland), 1998.
- [31] A. Kenel. *Biegetragverhalten und Mindestbewehrung von Stahlbetonbauteilen*. Ph.d thesis, ETH Zurich (Switzerland), 2002.
- [32] Aurelio Muttoni and Miguel Fernández Ruiz. Concrete Cracking in Tension Members and Application to Deck Slabs of Bridges. *Journal of bridge engineering*, 12(5):646–653, 2007.
- [33] Carlos Zanuy, Pablo de la Fuente, and Luis Albajar. Estimation of parameters defining negative tension stiffening. *Engineering Structures*, 32(10):3355–3362, 2010.
- [34] Carlos Zanuy. Investigating the negative tension stiffening effect of reinforced concrete. *Structural Engineering and Mechanics: An international journal*, 34(2):189–211, 2010.

- [35] T. P. Tassios and P. J. Yannopoulos. Analytical Studies on Reinforced Concrete Members Under Cyclic Loading Based on Bond Stress-Slip Relationships. *Journal of the American Concrete Institute*, 78(3):206–216, 1981.
- [36] H. A.W. Cornelissen and H. W. Reinhardt. Uniaxial tensile fatigue failure of concrete under constant-amplitude and programme loading. *Magazine of Concrete Research*, 36(129):216–226, 1984.
- [37] D.A. Hordijk. *Local approach to fatigue of concrete*. PhD thesis, Technische Universiteit Delft, 1991.
- [38] D.A. Hordijk. Tensile and tensile fatigue behaviour of concrete; experiments, modelling and analyses. *Heron*, 37(1):1–79, 1992.
- [39] Ezio Giuriani. Experimental Investigation on Bond-Slip Law of Deformed bars in Concrete. In *IABSE Colloquium*, pages 121–142, Delft, Netherlands, 1981.
- [40] G. Balázs. Cracking analysis based on slip and bond stresses. *ACI Materials Journal*, 90(4): 340–348, 1993.
- [41] Fabio Brantschen, Duarte Faria, Miguel Fernández Ruiz, and Aurelio Muttoni. Bond behaviour of straight, hooked, U-shaped and headed bars in cracked concrete. *Structural Concrete*, 17(5):799–810, 2016.
- [42] Francesco Cavagnis. *Shear in reinforced concrete without transverse reinforcement: from refined experimental measurements to mechanical models*. PhD thesis, EPFL – École polytechnique fédérale de Lausanne, 2017.
- [43] Miguel Fernández Ruiz, Aurelio Muttoni, and Juan Sagaseta. Shear strength of concrete members without transverse reinforcement: A mechanical approach to consistently account for size and strain effects. *Engineering Structures*, 99:360–372, 2015.
- [44] Ralejs Tepfers. A Theory of Bond Applied to Overlapped Tensile Reinforcement Splices for Deformed Bars. *Chalmers University, P-73:2, Division of Concrete structures*, page 328, 1973.
- [45] Miguel Fernández Ruiz, Sylvain Plumey, and Aurelio Muttoni. Interaction between Bond and Deviation Forces in Spalling Failures of Arch-Shaped Members without Transverse Reinforcement. *ACI Structural Journal*, 107(3):346–354, 2011.
- [46] Miguel Fernández Ruiz, Carlos Zanuy, Francisco Natário, J.M. Gallego, L. Albajar, and Aurelio Muttoni. Influence of fatigue loading in shear failures of reinforced concrete members without transverse reinforcement. *Journal of Advanced Concrete Technology*, 13(5):263–274, 2015.

Chapter 3

Characterization of shear deformations in reinforced concrete members without shear reinforcement

This chapter is the pre-print version of the article *Characterization of shear deformations in reinforced concrete members without shear reinforcement*, submitted to the journal *Engineering Structures* in February 2021. The authors of the publication are Raffaele Cantone (PhD Candidate), Andri Setiawan (postdoctoral researcher), Dr. Miguel Fernández Ruiz (Senior lecturer and thesis co-director) and Prof. Aurelio Muttoni (thesis director). The provisional reference is: **Cantone R., Setiawan A., Fernández Ruiz M., Muttoni A.** Characterization of shear deformations in reinforced concrete members without shear reinforcement. *Engineering Structures*.

This work was developed by the first author (Raffaele Cantone) under the supervision of Dr. Miguel Fernández Ruiz and Prof. Aurelio Muttoni (thesis director) who provided valuable feedback and proof-read in detail the manuscript. The numerical calculations were performed in collaboration with the second author (Andri Setiawan) whose contribution is deeply acknowledged. The main contributions of Raffaele Cantone with respect to the production of this chapter were the following:

- Analysis of the refined measurements performed on shear tests of beams without shear reinforcement.
- Development of a mechanical model to describe the development of shear deformations.
- Characterization of the through-thickness distribution of shear deformations to predict the load-carrying capacity of redundant systems.
- Perform numerical analyses with a condensed approach accounting for the development of shear strains and redistributions of shear forces.
- Validation of the mechanical model against test data providing new insights on internal forces redistribution.
- Production of the figures and tables included in the article.
- Preparation of the manuscript of the article.

Abstract

The load-carrying capacity of many reinforced concrete structures is governed by shear failures, occurring before reaching the flexural capacity of the member. For redundant systems, such as slabs subjected to concentrated loads, local shear failures (typically initiated at locations with highest shear forces) can however occur after redistributions of internal forces due to the propagation of the shear cracks. Such process can depend upon the development of shear strains and the softening response of the member and can be stable or unstable. A suitable understanding and modelling of the complete shear response of reinforced concrete, including its deformations both for its pre- and post-peak branches, is thus instrumental for a consistent and comprehensive analysis of the shear response and strength of redundant elements.

Such topic has received little attention in the past and analyses of redistributions of internal forces in concrete structures are often performed on the basis of refined flexural models, but coarse considerations for shear strains (typically elastic laws). This situation is a consequence of the lack of consistent experimental measurements on the shear deformations of reinforced members both before and after reaching the maximum shear capacity. Currently, however, the advent of refined measurements techniques such as Digital Image Correlation allows for an accurate tracking of the shear strains and for a fundamental understanding of its development. In this paper, taking advantage of such techniques, a comprehensive approach for determining the shear strains and their distribution across the depth of a section is presented. This approach allows reproducing accurately the development of shear strains and to predict the load-carrying capacity of redundant systems. The model is validated with selected test data and is considered as an effort to contribute to future numerical implementations of reinforced concrete shell models with realistic out-of-plane responses.

3.1 Introduction

Reinforced concrete can be considered as one of the most versatile and widespread construction techniques. Many elements, particularly slabs and shells, are normally built without arranging shear reinforcement, see Figure 3.1. This allows for fast and economic construction, but requires to ensure the transfer of shear forces also in presence of cracks. With this respect, the absence of shear reinforcement can lead to a localization of strains within a critical shear crack, governing the strength and deformation capacity. This can be the case of failures in shear (as one-way slabs or beams, where the principal directions of the shear field are parallel [1, 2]), Figure 3.1a, and punching shear (as two-way slabs, where the principal directions of the shear field are radial [3, 4]), Figure 3.1b. Situations in-between shear in one-way slabs and pure punching cases can also be found in practice (where the principal directions of the shear field are neither parallel nor perfectly radial), as regions close to elongated columns or when a concentrated load acts near a linear support, Figure 3.1c.

Most research on the topic of shear failures in redundant systems accounting for the progression of a shear crack has been traditionally oriented towards the resistance of the member [5–10]. Scanty research has however been devoted to the development of shear strains associated to cracked concrete and particularly to the through-thickness distribution of shear strains of a section [11, 12]. Such strains have nevertheless been observed to govern, together with the flexural response, the potential redistribution of internal forces occurring in redundant systems as flat slabs or continuous beams [6, 8, 13]. This phenomenon is of great significance for a number of cases. One relates to the punching strength of elongated columns [14]. In this case, some regions near the corners (subjected to higher shear demand) can be in the softening response while others have not yet attained their maximum potential strength. As a consequence, redistributions in the shear field can occur. If the less stressed regions of the column (middle of elongated column) have the capacity to compensate

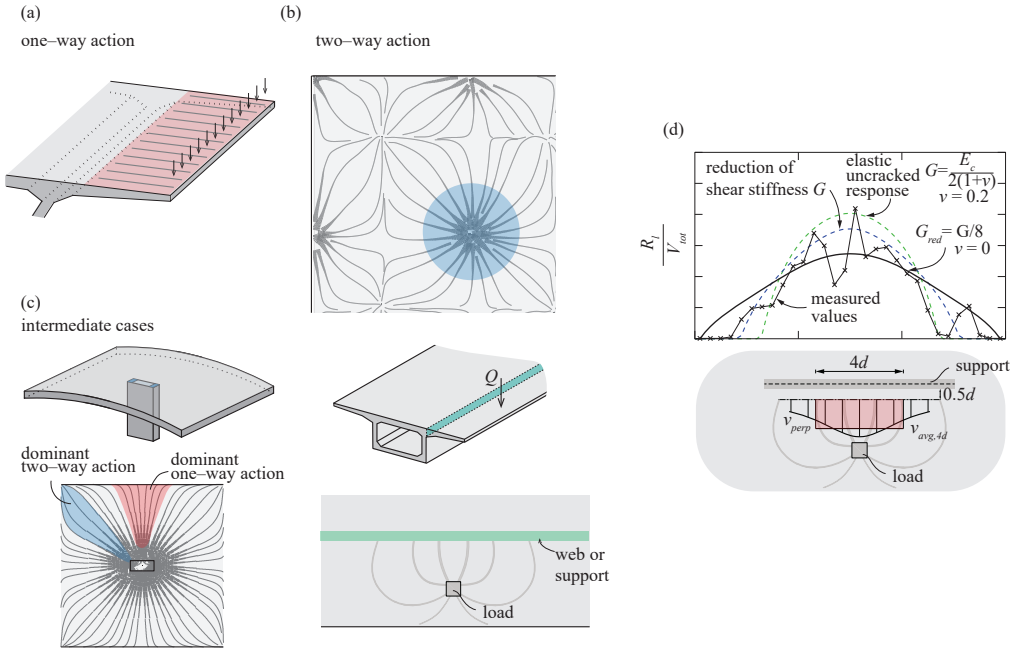


Figure 3.1: Shear failures in slabs: (a) shear field distribution in slabs subjected to strip loading; (b) two-way shear distribution in flat slabs supported on square or circular columns; (c) intermediate cases with uneven distribution of the shear field: flat slabs supported on rectangular columns [14] and slabs subjected to concentrated loading close to linear supports [6, 13]; (d) comparison of measured reactions and distributions calculated for different assumptions on stiffness [6]

for the decrease of strength of the others (near corners) [10, 14], then a stable increase of the capacity of the connection can be observed during the formation of the failure surface. Such results have also been confirmed for other design situations [9]. Another relevant case relates to shear failures when a concentrated load is applied near a linear support (Figure 3.1c). In this situation, as shown by Natario et al. [6, 13], the region of the support closer to the load attains first its capacity and can enter into a softening phase. The rest of the slab can however be capable of compensating for the localised softening and the total applied force can still be increased. Such response was confirmed experimentally by means of the redistribution of the measured reactions (see Figure 3.1d, [6, 13]). Based on these results, Natario et al. suggested a simplified approach based on reduced values for the Poisson's coefficient ($\nu=0$) and torsional stiffness ($G_{red}=G/8$) as well as a full redistribution of shear forces in a length equivalent to four times the effective depth of the slab (see Figure 3.1d).

With respect to the flexural response of a slab, significant efforts have been devoted to this topic and advanced models are currently available, based on refined moment–curvature laws or multi-layered nonlinear finite elements [11, 15, 16]. Also, particular solutions have been proposed for axisymmetric cases (slabs around columns or concentrated loads) [17], showing sound accuracy in the evaluation of the flexural deformations after cracking and accounting for membrane action. Most of the previous models couple the bending response with a failure criterion in shear in order to reproduce out-of-plane shear failures. This allows determining crack widths from the flexural response and, on that basis, to estimate the shear resistance (as an alternative to a full volumetric finite-element analysis [18]). Within this frame, the use of the Critical Shear Crack Theory (CSCT) has shown to be an efficient tool, as its failure criterion for shear is formulated in terms of flexural deformations (see Figure 3.2a) [3, 4]. This is a promising approach and one of the most advanced manners to investigate punching shear failures (provisioned as the most refined Level-of-

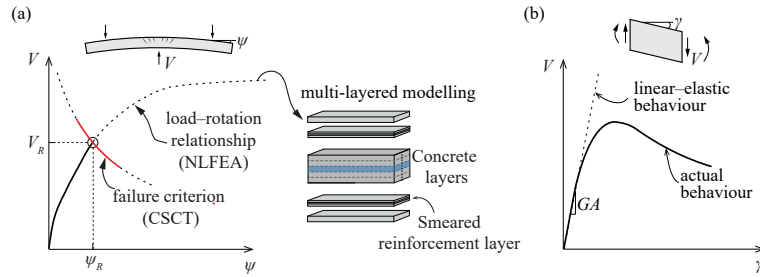


Figure 3.2: Refined modelling: (a) flexural behaviour and (b) through-thickness shear response

Approximation in *fib*'s Model Code 2010 [19]). It remains however open a number of aspects for a comprehensive implementation of such approach, notably a consistent method for determining the shear strains [11, 20]. This information, see Figure 3.2b, will allow for a proper modelling of the redistributions in the shear field and internal forces, as well as for the propagation of the critical shear crack for non axisymmetric cases.

Efforts to develop a more comprehensive formulation of the shear strains developing within a concrete member have been recently proposed by means of a characterization of the through-thickness shear strain distribution. For instance, Hrynyk and Vecchio [11] extended standard shell element formulations using the Disturbed Stress Field Model (DSFM) and assuming a given shape of the transverse shear strain profile (constant or parabolic). Further applications have also been performed to flat slabs failing in punching showing sound agreement compared to test results [12]. Alternative approaches coupling the shear and bending response have also been developed considering the adoption of joint elements located along a given control perimeter. These approaches have been mostly used for the evaluation of punching failures and the progressive collapse of flat slabs, resulting in sound agreement with the test results and giving new insights in terms of redistribution of internal forces close to supports [9, 21, 22].

All these potential modelling alternatives require nevertheless a reliable law describing the development of shear strains (and their through-thickness distribution for some of them [11]). Despite previous efforts [6, 9, 20], a consistent approach is not yet available for this purpose. Within this frame, the aim of this paper is to present a detailed analysis on the basis of advanced measurement techniques of the actual strain field of reinforced concrete members. A mechanical model is proposed on this basis, considering flexural and shear strains as well as their through-thickness distribution. The implications of this work are eventually discussed with respect to modelling of reinforced concrete slabs and its results are used to predict the redistributions of internal forces and load-carrying capacity related to shear for a number of selected tests on slabs.

3.2 Analysis of the displacement and strain field in concrete beams and slabs

3.2.1 Testing programme by Cavagnis et al. [23, 24]

The analysis of the displacement and strain field is performed using the detailed experimental results presented by Cavagnis et al. [23, 24] on reinforced concrete beams without shear reinforcement. The original test series consisted of 20 beams (25 tests) tested under several loading conditions. In this work, only cantilever beams are investigated, Table 3.1. The selected specimens have a rectangular cross section (0.25m-width and 0.6m-height) with constant flexural reinforcement ($\rho=0.886\%$, $2\phi 28$ in the tension and compression side; effective flexural depth $d=0.556$ m).

Table 3.1: Main parameters of specimens selected from testing programme by Cavagnis et al. (2017) [24]

Test	L [m]	a [m]	M/Vd [-]	f_c [MPa]	q [kN/m]	V_R [kN]
SC70	–	3.85	6.92	33.3	–	114
SC61	–	2.45	4.41	35.3	–	103
SC64	–	1.75	3.15	35.6	–	108
SC68	–	1.40	2.52	32.6	–	124
SC67	–	1.05	1.89	32.0	–	393
SC58	4.20	–	3.78	36.1	50.6	213
SC59	3.50	–	3.15	35.5	52.3	183
SC62	2.80	–	2.52	35.8	62.1	174
SC66	2.10	–	1.89	31.2	91.4	192

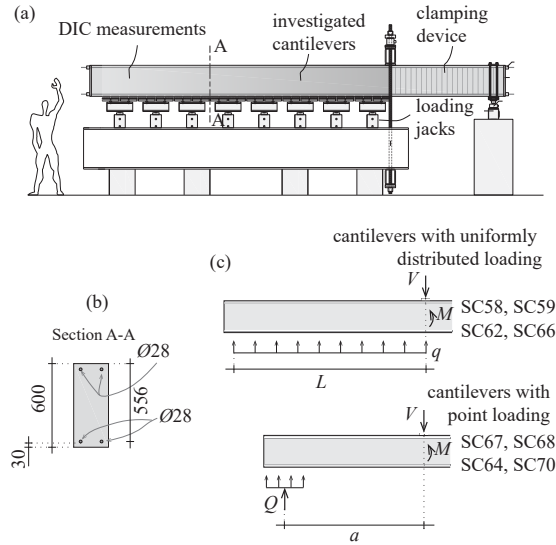


Figure 3.3: Experimental programme by Cavagnis et al. [23, 24]: (a) test setup; (b) cross section; and (c) loading conditions of specimens selected (adapted from [23])

All specimens were cast with normal-strength concrete with a maximum aggregate size of 16 mm and a compressive strength at the day of testing between 31.2 and 36.1 MPa. The flexural reinforcement consisted of high-strength reinforcement steel with a yield strength of 713 MPa. The tests were performed with the setup presented in Figure 3.3a, allowing for varying shear slenderness as well as for different loading conditions (concentrated or uniformly distributed loads). Conventional measurements (LVDTs, inclinometers) were combined with measurements on the concrete surface by means of Digital Image Correlation (DIC). Such measurements allowed tracking the displacement field of the members prior to failure at a frequency ranging between 0.5 and 2 Hz. Table 3.1 and Figure 3.3 summarize all properties of the investigated members (for additional details regarding the experimental programme, please refer to [23, 24]).

In this work, new insights on the displacement field measured by Cavagnis et al. [23, 24] will be presented with the aim to characterize the global response and the through-thickness strain field of a concrete member.

3.2.2 Definition of kinematical parameters

Surface displacements are tracked using DIC readings by adopting a grid of points equally spaced. For each point, horizontal (u) and vertical (w) displacements are determined. On this basis, for a given portion of the continuum (refer for instance to the four nodal points in Figure 3.4a), the average flexural and shear strains of the cross section can be described by rotations and shear

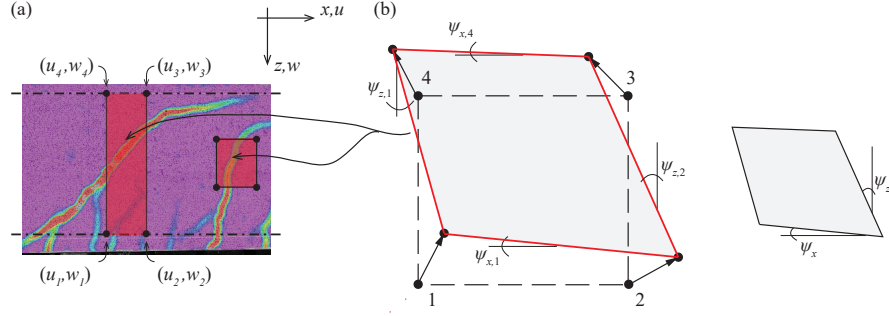


Figure 3.4: Kinematical parameters: (a) locations of top and bottom fibre selected for the evaluation of cross-sectional behaviour and (b) definition of kinematic parameters for rotations on the basis of DIC measurements (sign convention: ψ_z positive if counter-clockwise, ψ_x positive if clockwise).

strains, as follows:

$$\psi = \begin{cases} \psi_{zi} = \frac{u_j - u_i}{z_j - z_i} & \text{if } i = 1, 2 \text{ and } j = 4, 3 \\ \psi_{xi} = \frac{w_j - w_i}{x_j - x_i} & \text{if } i = 1, 4 \text{ and } j = 2, 3 \end{cases} \quad (3.1)$$

Where the different rotations refer to:

- $\psi_{z,1}$ and $\psi_{z,2}$ are defined as rotations of the vertical segments (segments $\bar{14}$ and $\bar{23}$ in Figure 3.4b).
- $\psi_{x,1}$ and $\psi_{x,4}$ are defined as rotations of the horizontal segments (segments $\bar{12}$ and $\bar{43}$ in Figure 3.4b).

Thus, the average rotation of vertical segments is $\psi_z = \frac{\psi_{z,1} + \psi_{z,2}}{2}$ while the average rotation of horizontal segments is $\psi_x = \frac{\psi_{x,1} + \psi_{x,4}}{2}$. The average shear strain of the element is then defined as:

$$\gamma_{sec} = \psi_x + \psi_z \quad (3.2)$$

The average horizontal elongation is $\Delta u = \frac{u_3 + u_2 - (u_1 + u_4)}{2}$ while the vertical expansion results $\Delta w = \frac{w_2 + w_1 - (w_3 + w_4)}{2}$.

3.2.3 Detailed analysis of the displacement field of RC members

In this section, a detailed analysis of the cantilever beam subjected to point loading SC61 [23, 24] is presented. Figure 3.5 shows the different kinematical parameters previously defined at two load levels. These parameters are evaluated for the whole section with two series of points (spaced 10 mm in the longitudinal direction) along the extreme fibres of the member (refer to Figure 3.5a). Figure 3.5b shows the distribution of rotations along the beam (where the rotation is set to null at the clamping section for comparison purposes). With respect to the shear strains, which result from the sum ($\psi_x + \psi_z$) between the rotation of horizontal and vertical segments (see Figure 3.5c), despite the fact that the shear force is constant for this test, they are significantly higher in the cracked region than in the uncracked region. In addition, for moderate load levels ($0.7V_R$), the shear deformation seems to be proportional to the bending moment, whereas close to failure (V_R), a local increase in the region of the critical shear crack can be observed. The longitudinal deformation and the vertical expansion ($\Delta u/\Delta x, \Delta h$) of the member are presented in Figures 3.5d-e. For the

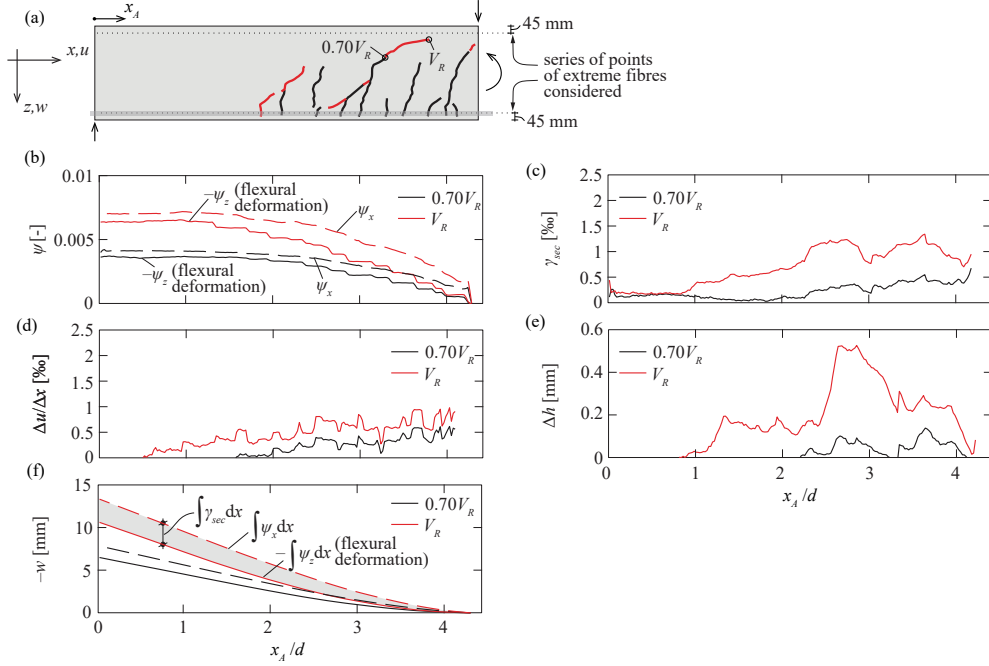


Figure 3.5: Specimen SC61: (a) cracking pattern (level of load referring to the instantaneous tip of the cracks); (b) rotations of vertical segments ψ_z compared to rotations of horizontal segments ψ_x ; (c) shear strain γ_{sec} ; (d) longitudinal deformation $\Delta u/\Delta x$ (evaluated over a contributive length equal to $d - c$); (e) vertical expansion Δh ; and (f) vertical displacements w calculated from the integration of rotations ψ_z and ψ_x (plots correspond to load levels equal to $0.70V_R$ (black curves) and V_R (red curves), where V_R refers to the maximum shear capacity)

latter, it should be noted that it develops in the region with inclined cracking and increases notably when the inclined cracks develop in the compression zone (associated to larger crack widths and to the propagation of the crack, see Figure 3.5e).

Figure 3.5f presents the integration of rotations of vertical and horizontal segments ($\int \psi_z$ and $\int \psi_x$). The contribution of shear strains on the total vertical displacements results from the sum ($\int \psi_z + \int \psi_x$). As it can be seen, the integration of the rotation of vertical segments (rotation ψ_z , which corresponds to the flexural contribution) leads to somewhat lower vertical displacements than those calculated from the rotations of horizontal segments ψ_x (which accounts for flexural and shear contributions and corresponds to the total measured displacements). With respect to the shear strains, up to 70% of the maximum load, vertical displacements due to shear are rather small compared to flexural deformations. However, as the load level approaches its maximum value, displacements associated to shear become significant attaining values of about 20–25% of the total vertical displacements, which can be relevant for the evaluation of the deformation capacity of reinforced concrete members subjected to bending and shear.

For a complete evaluation of the strain field in a concrete member, the longitudinal behaviour of the cross section shown in Figure 3.5 needs to be combined with the response considering the through-thickness distribution of strains. Figure 3.6 shows the response in the region where the critical shear crack develops assuming a distance equal to $d - c$ to estimate the contributive length influencing the opening of the critical shear crack according to [24] (where d refers to the effective depth and c to the depth of the compression zone [1]). In the following, the theoretical value of c is considered, which can be calculated assuming that plane sections remain plane and that all

materials behave elastically (tensile strength of concrete neglected):

$$c = n_E \cdot \rho \cdot d \left(\sqrt{1 + \frac{2}{n_E \rho}} - 1 \right) \quad (3.3)$$

with $n_E = \frac{E_s}{E_c}$, E_s and E_c refer to the moduli of elasticity of the reinforcement and concrete respectively and ρ is the reinforcement ratio.

The analysis is performed by discretization of the surface with a mesh at a constant distance (Δx) equal to three times the aggregate size ($d_g=16$ mm). Adopting the approach explained in Figure 3.4, the local behaviour of every element of the mesh (refer to Figure 3.6a) can be obtained by evaluation of the rotation of vertical (ψ_z) and horizontal (ψ_x) segments, local shear strains γ , horizontal elongation Δu and vertical expansion Δh . The results are presented at different heights of the member, by averaging measured values along the corresponding horizontal slices (shown in red in Figures 3.6b–d).

As presented in Figure 3.6b, the horizontal elongation Δu is rather linear over the depth, in agreement with the assumption that plane sections remain plane after deformation. For load levels up to $0.7V_R$, the point of zero elongation is near to the theoretical neutral axis, whereas it moves upwards as soon as the shear cracks propagates inside the theoretical compression zone. The measured shear strains γ averaged over the contributive horizontal length $d - c$ (Figure 3.6c) exhibit a fairly linear increase towards the tensile zone in agreement with the increase of horizontal and vertical crack opening at the level of the flexural reinforcement. In this case, the compression zone is affected by shear deformations also before the propagation of the critical shear crack, but their magnitude is rather small and become notable only for higher shear forces. It should be noted that between 60% of V_R and V_R , the critical shear crack developed in a stable manner, gradually increasing its length and opening for higher levels of load. According to the measurements, the sub–horizontal branch in the upper part of the shear critical crack developed roughly at 60% of the failure load V_R . At load levels higher than 80% of V_R , primary and secondary cracks started to merge and delamination cracks developed along the reinforcement, leading to an increase of the strain at the level of the flexural reinforcement.

The stages of crack development can be clearly identified with respect to the increment of shear strain γ_{sec} (calculated by adopting the approach presented in Section 3.2.2; refer to sketch and formula in Figure 3.6e). As it can be observed, at about 50–60% of the failure load, the shear strain γ significantly increased, with a change of slope associated to the development of the sub–horizontal crack in the compression zone.

Vertical expansion

Figure 3.7 presents the vertical expansion Δh observed in the investigated beams (refer to Table 3.1 and [24] for additional details; refer to Figure 3.6d for typical through–thickness distribution). The vertical expansion Δh was estimated in the section where the observed critical shear crack intersected the flexural reinforcement (refer to green lines in Figure 3.7). As it can be observed, the vertical expansion occurs notably after the development of diagonal cracking. After reaching the maximum load, in many cases, a stable softening phase is observed followed by an unstable failure process, Figure 3.7i. With respect to the response in the softening phase of test SC66, Figure 3.7h shows the relative crack lips displacements of the critical shear crack. It can be observed that after reaching the maximum load, the increments of displacements are almost vertical.

Figure 3.7i presents a normalized relationship between shear force and shear strain after maximum load (γ_R is the shear deformation calculated according to Figure 3.6e at maximum load). Different curves are observed depending mostly on the shape of the critical shear crack. For instance, it can be noted that the shear critical cracks for beams SC59 and SC68 are flatter (with longer branches of the sub–horizontal crack leading to the activation in the softening phase of larger shear strains)

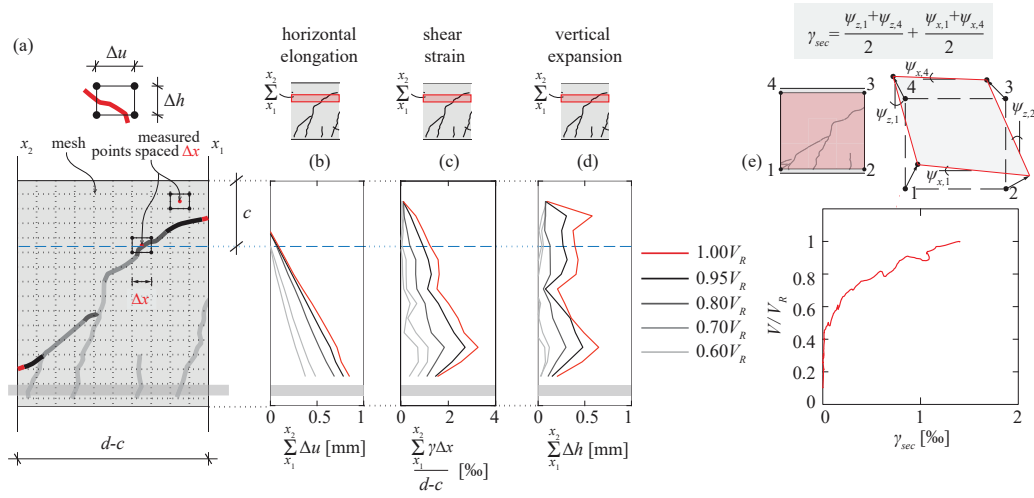


Figure 3.6: Strain field analysis of test SC61: (a) mesh for through-thickness analysis; through-thickness distribution of (b) horizontal elongation Δu , (c) shear strain γ , (d) vertical expansion Δh and (e) average shear strain of the critical shear crack calculated with the approach presented in Section 3.2.2 (refer to sketch at the top)

than the ones in SC66 and SC67 which show a brittle softening behaviour. An estimate of the level of deformation in the post-peak stage will be discussed later in Section 3.3.4.

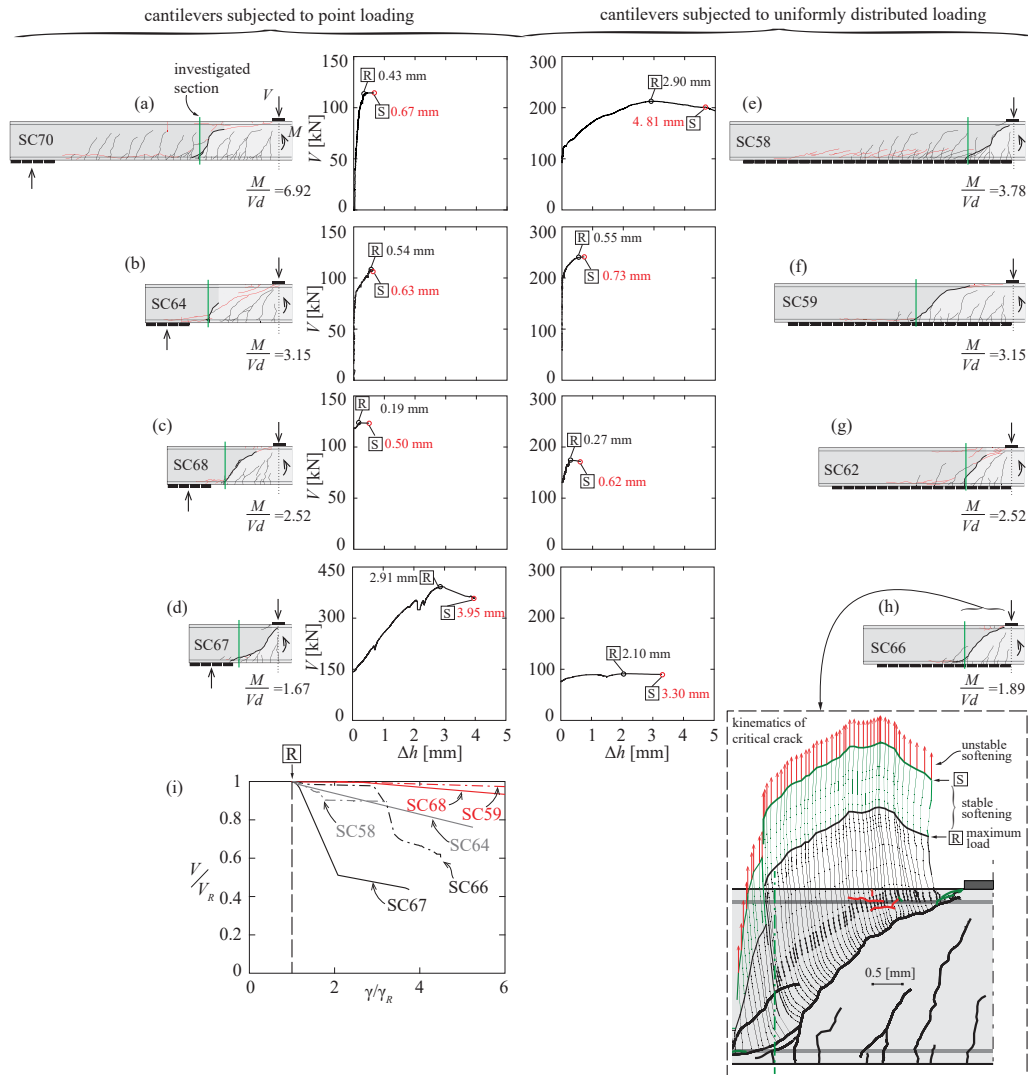


Figure 3.7: Vertical expansion Δh – shear load V for cantilever beams subjected to point loading (a) SC70; (b) SC64; (c) SC68; (d) SC67 and uniformly distributed loading (e) SC58; (f) SC59; (g) SC62; (h) SC66 (with a detail of the critical shear crack kinematics close to failure); and (i) post-peak behaviour (the vertical expansion is measured in the section where the critical shear cracks intercept the flexural reinforcement indicated by green lines on the cracking pattern). 'R' refers to the situation under the maximum shear capacity and 'S' to the stage just before the unstable increase of displacements

3.3 Assumed development of cracking and kinematical parameters

3.3.1 Cracking pattern and kinematics

In this section, the model developed by Cavagnis et al. [2, 25] for the shear resistance of members without shear reinforcement is described and adapted to predict the flexural and shear deformations in regions with inclined shear cracks. According to this approach, the response of a member can be described as a function of the propagation of the critical shear crack which depends on the level of applied shear force. This consideration leads to the following stages: (i) uncracked phase; (ii) development of a quasi-vertical branch AB of the shear crack (Figure 3.8a); (iii) development of a sub-horizontal branch BF of the shear crack (Figure 3.8b); and (iv) development of a delamination crack at the level of the flexural reinforcement (Figure 3.8c).

With respect to the quasi-vertical branch AB of the shear crack, its inclination depends both on the level of flexural moment and shear force. As acknowledged by Cavagnis et al. [2, 25], the inclination β_{AB} (Figure 3.8a) can be estimated as $\beta_{AB} = 45^\circ + 15^\circ \alpha_A^{1/3} \leq 90^\circ$ where $\alpha_A = \frac{M_A}{V_A d}$ is the shear slenderness ratio, with M_A and V_A representing the bending moment and the shear force respectively at the section A where the investigated crack intercepts the flexural reinforcement. Once flexural cracking occurs, it is assumed to develop instantaneously up to the neutral axis (the concrete tensile strength near the crack tip is neglected). The spacing of flexural cracks at the level of the reinforcement is governed by the bond strength between the flexural reinforcement and the tensile strength of the surrounding concrete (influenced thus by the bar diameter and the reinforcement ratio). However, for slabs and members without web reinforcement, the cracks at the level of the flexural reinforcement usually merge at some distance from the reinforcement and only some of them reach the neutral axis (see primary cracks in Figure 3.8c). According to the experimental observations of Cavagnis et al. [2, 25], the average distance between primary flexural cracks can be estimated at mid-height of a beam to be equal to $0.56d$ ($\approx 0.8(d-c)$). Before formation of the critical shear crack, this distance approximates also the length where the strains of the flexural reinforcement contribute to the opening of the crack. However, when the critical shear crack develops together with a delamination crack along the reinforcement, its opening depends on a contributive distance which is higher [26]. Such contributive length can be estimated, for the critical shear crack, as approximately $d - c$ [2].

When only the quasi-vertical branch of the shear crack is present, the portion of concrete between two flexural cracks acts as a cantilever clamped in the compression zone (the so-called Kani's tooth [27], Figures 3.8d–f). When the load increases, the vertical tensile stresses at the clamped zone of the cantilever reach eventually the tensile strength of concrete (Figure 3.8e) giving rise to the progression of the crack in a sub-horizontal manner (branch BF in Figure 3.8b). It can be also noted that the resistance of the tooth is affected by the inclination of the shear crack (refer to the quasi-vertical branch inclination in Figure 3.8e) due to the fact that the level arm between the resultants of the concrete tensile stresses on both sides of the tooth is $0.8(d-c) \cdot \cos \beta_{AB}$ (Figure 3.8e).

As acknowledged by Cavagnis et al. [2, 25], by accounting for the cantilever action and the residual tensile strength of concrete, the level of load at which the sub-horizontal cracking starts developing (called V_{AF} , moment in which the tensile strength is reached at the clamping region of the tooth), can be calculated as follows (for a detailed derivation refer to Appendix 3.6):

$$V_{AF} = \frac{f_{ct} b z}{7.5} \left[\frac{1}{2} + \sqrt{\frac{1}{4} + 7.5^2 \frac{w_F \rho E_s}{d f_{ct}} \frac{\cos \beta_{AB}}{[\alpha_A + (1 - \frac{c}{d}) \cot \beta_{AB}] (1 - \frac{c}{d})}} \right] \quad (3.4)$$

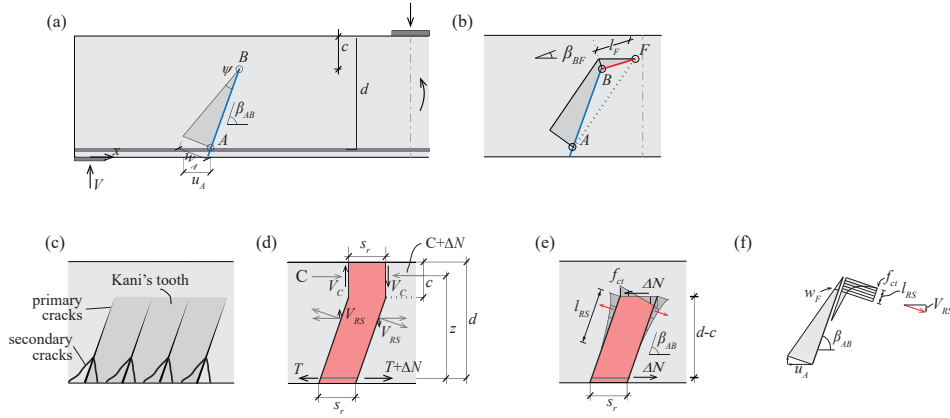


Figure 3.8: Crack development stages: (a) formation of quasi-vertical branch AB; (b) development of the sub-horizontal branch and tooth model; (c) tooth between primary cracks; (d) internal forces; (e) forces on the concrete tooth and (f) residual concrete tensile strength on the quasi-vertical branch AB as a function of crack opening.

where f_{ct} is the tensile strength of concrete, $w_F = G_F/f_{ct}$ (where G_F is the fracture energy of concrete), β_{AB} is the inclination of the primary flexural crack, z is the lever arm, b is the width of the member, α_A is the shear slenderness ratio $\frac{M_A}{V_A \cdot d}$ and c is the depth of the compression zone. With the development of the sub-horizontal branch of the crack, aggregate interlocking can be activated in the branch AB and residual tensile stresses develop also between point B and the tip of the crack F [26]. These shear-transfer actions allow in general increasing the shear force, and the resistance is eventually reached for a critical length $l_{F,max}$ of the sub-horizontal branch of the critical shear crack (Figure 3.8b). According to Cavagnis et al. [2, 25], $l_{F,max}$ can be approximated as $d/6$ for calculation of the shear resistance. Nevertheless, for a more detailed investigation of the crack development and crack opening, this assumption should be improved, accounting for the influence of the shear slenderness ratio on the length $l_{F,max}$. Based on the observations by Cavagnis [28], the length $l_{F,max}$ can actually be assumed to increase linearly with the shear slenderness α_A within the limits $d/6$ and $d/2$ ($l_{F,max}=d/6 \leq \alpha_A d/6 \leq d/2$). In addition, its development can be assumed to increase linearly with the shear force between V_{AF} and the shear resistance V_R ($l_F = l_{F,max} \frac{V-V_{AF}}{V_R-V_{AF}}$). With respect to the inclination of the sub-horizontal branch, the same value β_{BF} assumed by Cavagnis et al. [2, 25] can be adopted (i.e. $\beta_{BF}=22.5^\circ$).

It can be noted that, due to the inclination of the critical shear crack, the crack opening at the level of the reinforcement has not only a horizontal component u_A , but also a vertical component v_A . The ratio between these components depends on the position of the centre of rotation, which can generally be assumed to be located at the tip of the crack (point F, Figure 3.9a, [2, 26]). According to experimental observations, small values of the vertical component v_A result in the opening of the secondary crack CD (Figure 3.9b) and bending of the flexural reinforcement between C and A (activating dowel action as described by Cavagnis et al. [2, 25]). For larger vertical displacements (which typically occur for small inclinations β_{AB} or when the centre of rotation F moves away from B), a delamination crack develops along the reinforcement (branch EC in Figure 3.9b).

With respect to the horizontal component of the crack opening u_A , which accounts for the opening of the primary and secondary cracks, it can be calculated by integrating the reinforcement strain along the distance l_b and by neglecting the concrete strain. The peak strain occurs at point A, where the main flexural crack intercepts the reinforcement (or other secondary cracks merged with the primary crack, Figure 3.9b). It can be calculated on the basis of the acting moment at section

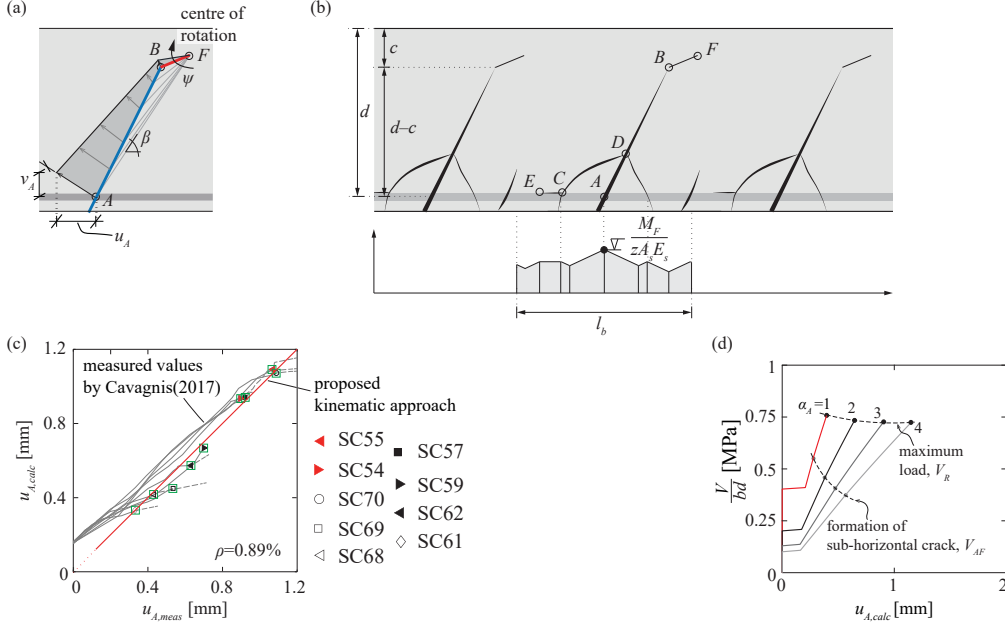


Figure 3.9: (a) assumed shape and kinematics of critical shear crack; (b) cracks and assumed steel strains; (c) comparison between the measured crack opening $u_{A,meas}$ and the value $u_{A,calc}$ calculated according to Eq. 3.6 and (d) calculated crack opening as a function of the shear force for different crack positions (defined with parameter $\alpha_A = \frac{M_A}{V_A \cdot d}$ and for members with the same cross section as the experimentally investigated specimens). Parameters: $f_c=35.3$ MPa, $b=0.25$ m, $d=0.556$ m and $\rho = 0.89\%$.

F by neglecting the effect of the stresses acting on the branches AB and BF as follows:

$$\epsilon_s = \frac{M_F}{z \cdot A_s \cdot E_s} \quad (3.5)$$

where A_s is the longitudinal reinforcement, E_s is the modulus of elasticity of the reinforcement steel and z is the lever arm of the internal forces, which can be estimated by assuming a linear distribution of stresses in the compression zone ($z = d - c/3$). By neglecting the effect of tension stiffening and assuming that the effective length contributing to the crack opening is equal to $d - c$ [2], the crack opening u_A can be finally calculated as:

$$u_A = \frac{M_F}{A_s \cdot E_s} \frac{d - c}{d - c/3} \quad (3.6)$$

Figure 3.9c shows the comparison between the measured opening $u_{A,meas}$ and the value $u_{A,calc}$ calculated according to Eq. 3.6 (where the location F corresponds to the measured position of the crack tip). For low levels of load, one can observe that the crack opening is overestimated as tension stiffening is neglected and the assumed integration length l_b of the strains is overestimated (l_b can be larger than the crack distance only due to the delamination crack). However, when the level of force is closer to the shear resistance (symbols in the diagram refer to maximum loading), Eq. 3.6 provides a fairly consistent estimate of the crack opening.

Figure 3.9d shows in addition the calculated crack opening as a function of the shear force for different crack positions (defined with parameter $\alpha_A = M_A/V_A d$ and considering members with the same cross section as the experimentally investigated specimens). For levels of load below V_{AF} (before the development of the sub-horizontal branch of the cracks), the behaviour is linear whereas, for higher shear forces, the crack opening increases more than proportionally.

3.3.2 Flexural and shear deformations

The shear deformation of the cross section can be calculated along the distance $d - c$ considering the kinematics and associated deformations of an inclined shear crack, see Figures 3.10a–b, where the average rotation of the vertical segments is (refer to Eq. 3.1):

$$\psi_z = -\frac{\psi}{2} \quad (3.7)$$

while the average rotation of the horizontal segments is (Eq. 3.1):

$$\psi_x = \frac{\psi}{l_b} \left(\frac{l_b}{2} + d_{cr} \cot \beta \right) = \frac{\psi}{2} + \psi \cot \beta \frac{d_{cr}}{l_b} \quad (3.8)$$

where β refers to the angle between the crack tip and the point at which the critical shear crack intercepts the flexural reinforcement and d_{cr} to the height between the crack tip and the flexural reinforcement. For cases when $V_A \leq V_{AF}$ (before propagation of the sub–horizontal branch, Figure 3.10a) $\beta = \beta_{AB}$ and $d_{cr} = d - c$. On the contrary, when $V_A > V_{AF}$ (after propagation of the sub–horizontal branch, Figure 3.10b), $\beta = \beta_{AF}$ and $d_{cr} = d - c + l_F \sin \beta_{BF}$.

By considering that $\gamma_{sec} = \psi_x + \psi_z$ (Eq. 3.2), the shear deformation of the cross section results:

$$\gamma_{sec} = \psi_x + \psi_z = \psi \cot \beta \frac{d_{cr}}{l_b} \quad (3.9)$$

Since $\psi d_{cr} = u_A = \epsilon_{s,m} l_b$:

$$\gamma_{sec} = \epsilon_{s,m} \cot \beta \quad (3.10)$$

where the average deformation can be calculated on the basis of Eq. 3.5 with $M_F = M_A + V_A d_{cr} \cot \beta$:

$$\epsilon_{s,m} = \frac{M_A + V_A d_{cr} \cot \beta}{z E_s A_s} \quad (3.11)$$

Since the curvature can be expressed as:

$$\chi = \frac{\epsilon_{s,m}}{d_{cr}} \quad (3.12)$$

and considering that $EI = z d_{cr} E_s A_s$, the following flexibility matrix can be derived:

$$\begin{bmatrix} \chi \\ \gamma_{sec} \end{bmatrix} = \begin{bmatrix} k_{11} & k_{12} \\ k_{21} & k_{22} \end{bmatrix} \begin{bmatrix} M_A \\ V_A \end{bmatrix} = \begin{bmatrix} \frac{1}{EI} & \frac{d_{cr} \cot \beta}{EI} \\ \frac{d_{cr} \cot \beta}{EI} & \frac{d_{cr}^2 \cot^2 \beta}{EI} \end{bmatrix} \begin{bmatrix} M_A \\ V_A \end{bmatrix} = \frac{1}{EI} \begin{bmatrix} 1 & d_{cr} \cot \beta \\ d_{cr} \cot \beta & d_{cr}^2 \cot^2 \beta \end{bmatrix} \begin{bmatrix} M_A \\ V_A \end{bmatrix} \quad (3.13)$$

It can be noted that the flexibility matrix is symmetric and the off–diagonal terms (refer to terms k_{12} and k_{21} in Eq. 3.13) represent a significant contribution to the total deformations of the cross section. In particular, regarding the matrix terms referring to the shear strain γ_{sec} , the off–diagonal term (k_{21}) is in general larger than the direct contribution of the shear force on the shear deformation (k_{22}). This fact suggests that the effect of the acting bending moment M on the total shear deformation is not negligible and becomes increasingly significant for higher shear slenderness α_A (associated to more inclined shear cracks). This confirms previous observations (Figure 3.5c) that for low shear forces, the shear deformation is proportional to the moment, whereas for higher shear forces, in the region of the critical shear crack (increasing value of $\cot \beta$), the contribution of the shear force also becomes notable.

Figure 3.10c shows the comparison between measured and calculated average shear strain of the cross section (γ_{sec}) over the contributive length $l_b = d - c$ as a function of the applied level of load (V/V_R). It can be observed that, prior to failure, the calculated shear strain is generally larger than the measured values due to the potential contribution of tension–stiffening which is

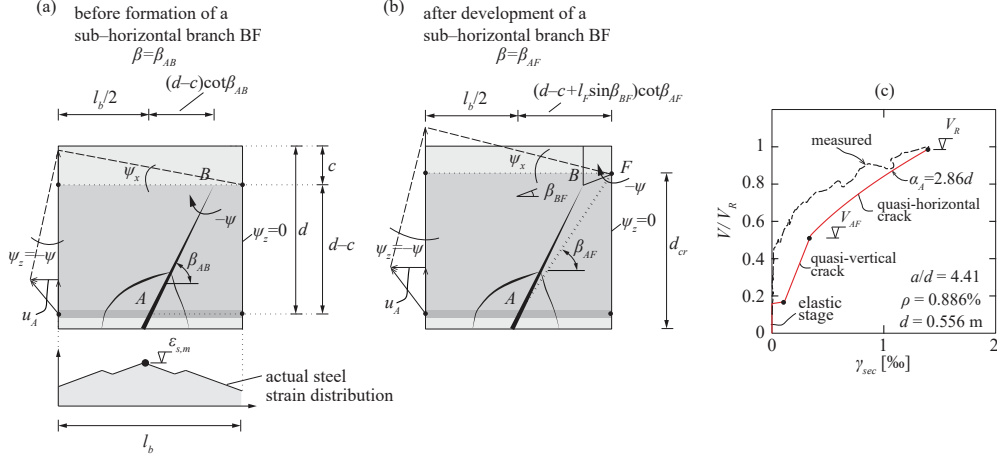


Figure 3.10: Shape and kinematics of an inclined shear crack (a) before the breakout of the concrete tooth ($V \leq V_{AF}$) and (b) after the development of the sub-horizontal branch BF of the shear crack and (c) comparison of measured and calculated load–shear strain relationship ($V/V_R - \gamma_{sec}$) for the shear critical crack presented in Figure 3.6 (test SC61)

neglected in this approach. However, the kinematical approach predicts in a sound manner the measured shear strain close to failure (refer to γ_{sec} in Figure 3.6e), when tension–stiffening effects have a lower influence. For a more detailed prediction of shear deformations for lower shear forces, a variable secant flexural stiffness EI (to be used in Eq. 3.13) could be considered accounting for tension–stiffening.

3.3.3 Through–thickness distribution of shear deformations in a smeared approach

In previous Section 3.3.2, the kinematical parameters and geometry of inclined shear cracks have been detailed for the evaluation of flexural and shear deformations of the cross section. The derived approach (flexibility matrix in Eq. 3.13) refers to the average response of a segment of length $d - c$ where an inclined shear crack develops. Such integrated response allows already for calculation of the structural response of the member as it will be presented in Section 3.4. In this section, a detailed analysis of the through–thickness distribution of deformations is introduced on the basis of the assumed cracking pattern and kinematics. The aim of this approach is to characterize the shear deformation at every location of a cross section according to a smeared approach, in view of a potential implementation of the previous approach within a multi-layered model of a slab element.

The calculation of the through–thickness shear strains can be performed after flexural cracking accounting for the fact that the curvature χ_i can be calculated on the basis of the acting bending moment and shear force at the crack tip (see Eq. 3.12). At a given fibre (characterized by the depth z_i with respect to the flexural reinforcement), the maximum principal strain results thus $\epsilon_{1,i} = \chi_i \times \frac{d_{cr} - z_i}{\sin\beta_i}$ developing at an angle β_i , Figure 3.11a. On this basis, and neglecting the principal compressive strain, the state of strains can be calculated with Mohr’s circle of strains, Figure 3.11b, as follows:

$$\gamma_i = \epsilon_{1,i} \sin 2\beta_i \quad \epsilon_{x,i} = \epsilon_{1,i} \sin^2 \beta_i \quad \epsilon_{z,i} = \epsilon_{1,i} \cos^2 \beta_i \quad (3.14)$$

Once the strain of each fibre is defined, profiles of flexural and shear deformation can be established. For instance, Figures 3.11c–e present the calculated deformations compared to the experimental

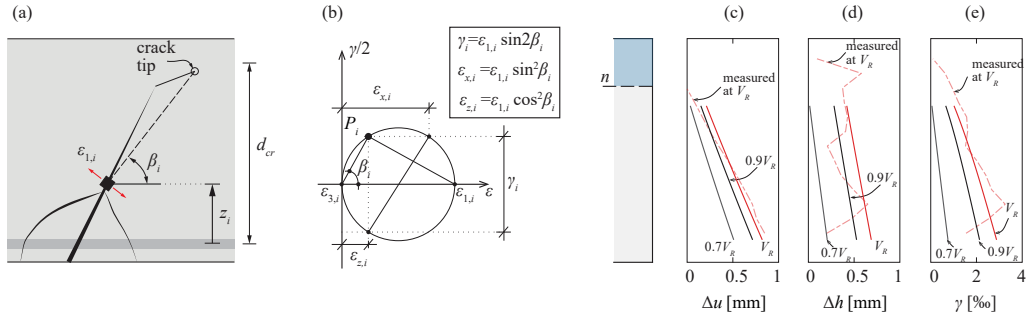


Figure 3.11: Through–thickness distribution according to a smeared approach: (a) inclined crack and local kinematics at a given depth z_i ; (b) Mohr’s circle and calculated profiles and comparison with measurements (test SC61) of (c) longitudinal expansion; (d) vertical expansion and (e) shear deformation.

measurements in Figure 3.6. The comparison shows sound agreement in terms of horizontal and vertical expansion as well as shear deformation at maximum load (both in terms of calculated strains and the corresponding profile).

With respect to the shear deformations, their profile (Figure 3.11e) is observed to be linear before propagation of the sub–horizontal branch, turning into bilinear thereafter. It can be noted that the level of average shear deformation γ_{sec} previously calculated in Section 3.3.2 should correspond to the average of the profile of shear strains calculated in this Section (strains developing between the centroid of the flexural reinforcement and the position of the crack tip). This is exact prior to the development of the sub–horizontal branch (Figure 3.8a) when the resulting profile is linear (see Figure 3.11e for lower load levels). Slight differences occur when the sub–horizontal branch develops (Figure 3.8b) as the profile is bilinear due to the variable angle β_i (see Figure 3.11e for higher load levels). The differences between the two formulations (considering smeared strains at any section or concentrated crack openings averaged over a length l_b) remain however low (generally lower than 5%).

For more details, 3.7 presents the complete derivation of all equations in order to obtain the results presented in Figures 3.11c–e.

3.3.4 Shear deformations in the post–peak stage

With respect to the softening response, the development of shear deformation is related to the vertical displacement experienced between the crack lips (refer to crack kinematics in Figure 3.7h), which triggers the activation of dowelling forces and tensile stresses in the concrete along the sub–horizontal branch of the critical shear crack. In the following, a proposal to estimate such vertical displacement is presented on the basis of the available experimental observations. It should be noted that this proposal is intended as a first approach to the phenomenon, since it is based on a limited number of experimental data, and future work will be required to consolidate or to define it on the basis of a mechanical model.

The post–peak response can be characterized on the basis of the Δh measurements presented in Figure 3.7. Despite some level of scatter, a stable increase Δh of approximately 50% with respect to the one attained at maximum load (point "R") can in general be assumed for an approximately constant level of load corresponding to a deformation plateau at maximum load up to point "S" (before unstable increase of displacements, Figure 3.12a).

After the plateau at maximum load, an unstable drop of the load occurs in general. In this phase, dowel action can be identified as the main shear–carrying action governing the post–peak

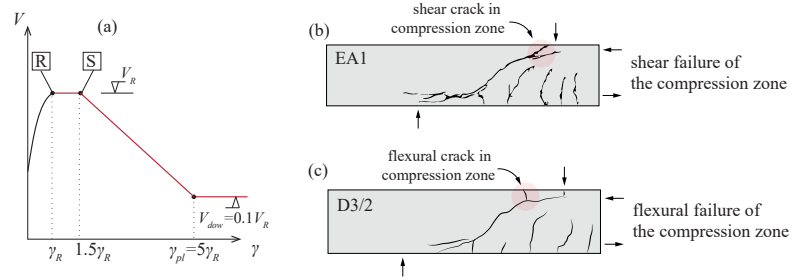


Figure 3.12: (a) shear force V – shear strain γ relationship at maximum load and in the post-peak stage; response after peak load – failure modes experience by compression zone in shear tests by Leonhardt and Walther [33]: (b) shear failure and (c) flexural failure of compression zone.

resistance [29–31]. It can be noted that the contribution of dowelling action is related to several parameters. In particular, with respect to the dowel action of the reinforcement in the tension zone, its contribution depends mainly on the distance between the critical shear crack and the support, as well as on the bar diameter and associated strains of the reinforcement [31, 32]. Concerning the flexural reinforcement in the compression zone, the contribution of dowel action is related to the distance of the tip of the critical shear crack to the load. On this basis, two different failure modes can be observed [29] leading potentially to (i) a shear failure of the compression zone for steeper shear cracks (developing near to the load introduction plate, see Figure 3.12b) or to (ii) a flexural failure of the compression zone governed by tensile strength of concrete and the activation in tension of the reinforcement in the compression zone (when the sub-horizontal branch of the shear crack is rather flat and long, see Figure 3.12c). A detailed calculation of these contributions is relatively complex. As a simplified approach, based on the experimental observations presented in Figure 3.7i, it will be considered that after the plateau at maximum load, the shear force drops to a value corresponding to approximately 10% of the maximum capacity (V_R). This drop of the load is associated to an increase on the shear deformation, which is estimated equal to four times the shear deformation at maximum load γ_R ($\gamma_{pl} \approx 5\gamma_R$), see Figure 3.12a. These considerations allow for a safe estimate of the observed response after maximum capacity according to the presented experimental results (Figure 3.7i, envelope of observed responses for different critical shear crack shapes and locations). In addition, in absence of refined data, the transition between the peak load and the resistance related to dowelling action can be considered to follow a linear trend, see Figure 3.12a. As previously stated, this is only intended as a first approach to the phenomenon (allowing for calculation of redistributions) and will require future work to be refined and consolidated.

3.4 Implications for modelling

Based on the previous model, the flexural and shear deformations can be calculated on a rational basis both in terms of average values (Section 3.3.2) as well as at the cross-sectional level (Section 3.3.3). This allows determining the shear strain–shear force relationship for a section of a member as well as its through-thickness distribution. This information is relevant for modelling of reinforced concrete slabs subjected to shear forces as it allows considering the progressive development of a shear failure surface and its associated redistributions of internal forces. The implementation of the previous shear response within a general finite-element model of a slab can be performed following different approaches, notably:

- **Layered–shell analysis.** As already shown in Figure 3.11, the mechanical model can describe the through–thickness strain field of a cross section as discussed in Section 3.3.3. This technique is particularly suitable for an implementation in finite element layered–shell ap-

proaches, with the significant advantage that it does not presume a simplified shear strain profile (constant or parabolic through-thickness shear strain distribution [11, 12]), but that it is calculated for each case. In addition, unlike standard layered approaches which consider a constant transverse shear stiffness [17, 20], this model is able to follow the actual stiffness degradation due to the presence of shear forces as well as its associated redistributions.

- **Lumped approach.** Despite the advantages of the layered-shell approach, the numerical implementation and solution procedure may be cumbersome [11]. Thus, a condensed response can alternatively be adopted, by considering the cross section shear force-shear strain response presented in Section 3.3.2, see Figure 3.10. This consideration allows incorporating the most fundamental aspects of the model (shear stiffness degradation) but in a simple manner in terms of numerical implementation.

In the following, the second approach will be used to investigate on the potential of this technique to simulate failures in shear for cases where the development of the critical shear crack occurs gradually leading to redistributions of internal forces. This simplified method grounds on the following assumptions:

- Reinforced concrete slabs are modelled with four-nodes multilayered shell elements (the commercial software SAP2000 [34] is used in this work). The flexural behaviour accounts for concrete cracking, tension-stiffening, yielding and hardening of reinforcing bars. Concrete is considered as a non-linear material (Modified Darwin-Pecknold Concrete Model, [34]) with Poisson's coefficient ν equal to zero. Concrete tensile strength and tension-stiffening effects are implemented in the constitutive laws of reinforcement which is considered as an equivalent tie with a quadrilinear law (considering tensile strength of concrete, development of cracking stage, stabilized cracking stage and yielding). The stiffness of this equivalent tie is reduced by a factor k_β (equal to 0.8) which accounts for the orthogonal layout of the reinforcement [3] and considers as contributive surface for tension-stiffening effects a region equal to 20% of the total height of the slab .
- An average stress-strain law is considered for the cross-sectional behaviour (see Figure 3.10c and refer to Section 3.3.2).
- In order to model properly the out-of-plane shear response (see Figure 3.13a), the load-shear deformation $V-\gamma$ should be implemented in principle all over the reinforced concrete member. This approach would allow crack localization to develop as a function of the acting internal forces without imposing a prescribed control section in which all deformations localize. For matter of simplicity, the out-of-plane shear response is accounted for by interface of joint elements (spring element) located at a control section ($0.5d$ from the point of maximum shear force, typically at support or near to concentrated loads), Figure 3.13a, consistently with the control section of the Critical Shear Crack Theory [9]. The spring element is a single degree of freedom spring representing the out-of-plane shear deformation and forces. In order to ensure compatibility of other degrees of freedom, equal constraints are used to ensure translation in the other 2 directions and 3 rotations. The $V-\gamma$ behaviour is simplified with a quadrilinear law, as presented in Figure 3.13b, with the maximum shear capacity governed by the local level of deformation [1]. Regarding the force-displacement response of the joint element, the vertical displacement is calculated as the displacement over the contributive length l_b ($\gamma \times l_b$, where l_b is assumed equal to $d-c$), Figure 3.13a.
- Close to shear failure, after reaching the maximum capacity $v_{R,c}$ associated to a shear strain γ_R , a plateau is assumed (refer to Figure 3.12). Finally, the load is considered to drop at 10% of the maximum shear capacity (rough estimate of the dowelling contribution). The drop of the shear load is associated to a large increase of the shear strain γ_{pl} estimated as four times

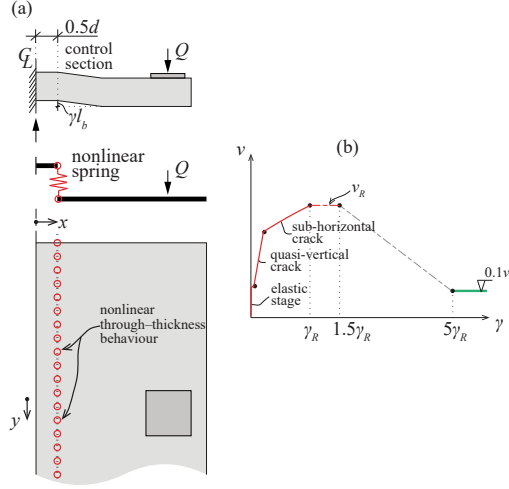


Figure 3.13: (a) modelling approach of slabs subjected to concentrated load (example of cantilever slab on linear support); and (b) quadrilinear law for the through–thickness behaviour with maximum capacity governed by local level of deformation.

the shear strain at maximum load γ_R ($\gamma_{pl} = 5\gamma_R$) according to test results (see Figure 3.7i), Figures 3.13b.

The maximum shear capacity is calculated according to the Critical Shear Crack Theory (CSCT) [1], which is consistent with the refined mechanical model proposed by Cavagnis et al. [2]. The shear strength for a given level of deformation is thus calculated according to the failure criterion of the CSCT as follows [1]:

$$v_{R,c} = \frac{d\sqrt{f_c}}{3} \frac{1}{1 + 120 \frac{ed}{16+d_g}} \quad (3.15)$$

where d_g refers to the maximum aggregate size and the reference strain ϵ is calculated at the control section (located $0.5d$ from a support or a concentrated load) at a given depth ($0.6d$ from the outermost compressed fibre) as a function of the unitary bending moment m :

$$\epsilon = \frac{m}{d\rho E_s (d - c/3)} \frac{0.6d - c}{d - c} \quad (3.16)$$

where the depth of the compression zone c is calculated by Eq. 3.3.

For the control section, the state of flexural strains (and crack widths) can be derived upon the acting moment field and, on that basis, the shear resistance according to Eq. 3.15 (pre-peak response) and Figure 3.12a (post-peak response). When a section enters thus in the post-peak stage, it will reduce the amount of shear force that it can carry, which has to be compensated by other sections located nearby. Such process may be stable or unstable depending to a large extent on the gradients of the shear and moment fields (with higher gradients of shear forces associated to a higher capacity to redistribute internal forces).

3.4.1 Validation of the numerical approach

Shear tests on reinforced concrete slabs (both cantilever and simply supported members) subjected to concentrated loads found in literature (refer to slab tests by Reissen et al. [7], Rombach et al. [5] and Lantsoght et al. [8]) were investigated for the validation of the mechanical model. Since the proposed model has been developed for members failing in one–way shear, only slab tests with clear shear failures (based on cracking pattern observations) were selected for the current

Table 3.2: Main parameters of specimens selected from testing programme by Rombach et al. [5], Reissen et al. [7] and Lantsoght et al. [8]

Source	Test	d [m]	b/d [-]	a_v/d [-]	f_c [MPa]	f_y [MPa]	ρ [%]	Q_R [kN]	Remarks
[5]	VK2V1	0.217	11.1	2.35	46.5	550	1.16	678	CL (CS) + LL*
[5]	VK4V1	0.167	14.4	3.05	42.5	550	1.16	487	CL (CS)
[7]	S25B-2	0.240	10.4	3.13	29.5	900	0.98	780	CL (SS)*
[7]	S35B-2	0.240	14.6	3.13	38.2	900	0.98	1024	CL (SS)
[8]	S25T4	0.265	9.43	2.15	58.6	542	1.00	854	CL' (SS)
[8]	S25T5	0.265	9.43	3.13	58.6	542	1.00	968	CL'*(SS)

*CL: concentrated load; LL: linear load; CL': eccentric concentrated load.

*CS: cantilever slab; SS: simply supported slab.

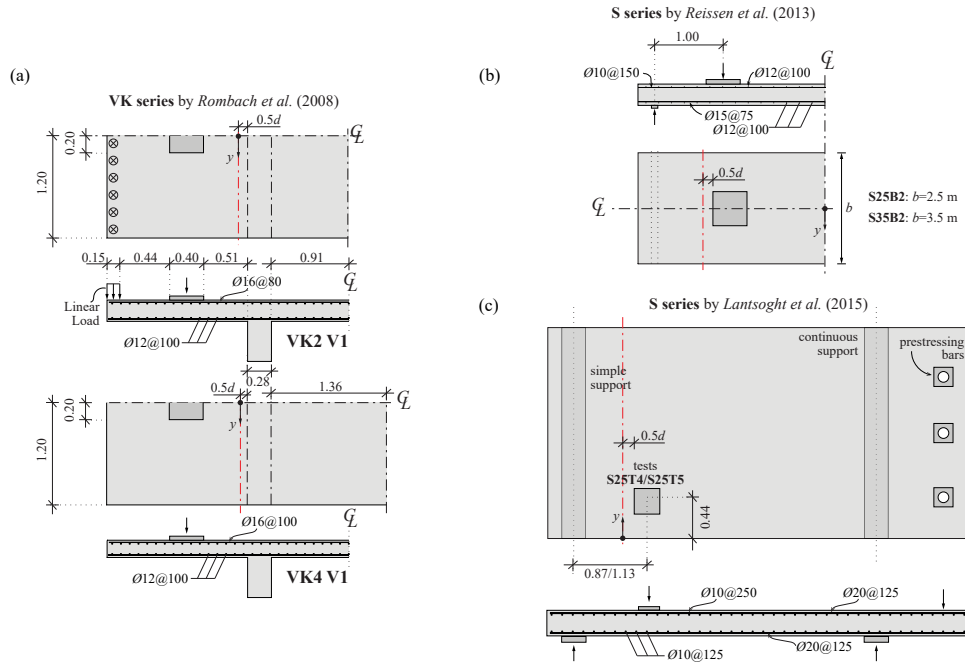


Figure 3.14: Summary of experimental investigations by (a) Rombach et al. (2008) [5], (b) Reissen et al. [7] and (c) Lantsoght et al. [8]

investigation (slab tests failing in punching or in punching–shear close to the loading plate are thus not considered in this study [13]).

Figure 3.14 and Table 3.2 summarize the main geometrical and mechanical properties of the investigated tests. In the testing programme by Rombach et al. [5], cantilever slabs without shear reinforcement were subjected to a centred concentrated load with a clear shear span a_v ranging between $2.35d$ and $3.05d$. For Reissen et al. [7] and Lantsoght et al. [8], the tests were performed on simply supported slabs subjected to a concentrated load with varying slab widths or eccentric loading arrangement close to the slab edge.

3.4.2 Discussion of the numerical results

Figures 3.15a–c present the calculated load–displacement responses for the investigated specimens showing results in consistent agreement with the experimental values, both in terms of calculated shear strengths and deformation capacities at failure, see Table 3.3. When compared to an analysis based on the CSCT without redistributions of internal forces (shear and moment fields proportional to the elastic ones) or with simplified redistributions (averaged shear force in a distance equal to

Table 3.3: Summary of measured-to-predicted results in terms of maximum shear capacity and deformation at failure for tests by Rombach et al. [5], Reissen et al. [7] and Lantsoght et al. [8]

Source	Test	b/d [-]	a_v/d [-]	Q_{test} [kN]	CSCT v_{max}	CSCT $v_{avg,4d}$	Refined CSCT	
					Q_{test}/Q_{calc}	Q_{test}/Q_{calc}	Q_{test}/Q_{calc}	$\delta_{test}/\delta_{calc}$
[5]	VK2V1	11.1	2.35	678	1.30	1.21	1.13	1.55
[5]	VK4V1	14.4	3.05	487	1.26	1.18	0.95	1.09
[7]	S25B-2	10.4	3.13	780	1.58	1.20	1.05	1.02
[7]	S35B-2	14.6	3.13	1024	1.76	1.25	0.95	1.02
[8]	S25T4	9.43	2.15	854	1.60	1.46	0.97	1.16
[8]	S25T5	9.43	3.13	968	1.78	1.59	1.09	1.07
Mean					1.55	1.31	1.02	1.15
COV					0.14	0.13	0.07	0.18

$4d$ as suggested by Natario et al. [6]), it can be noted that the results improve significantly. The mean value of the ratio between the measured and calculated shear capacity is closer to 1.0 with a clear decrease of the scatter of the results (COV=0.07), see Table 3.3.

As presented in Figures 3.15d–i, significant shear redistributions occur once the shear stress reaches its local shear resistance. Some regions enter in a softening phase while others increase their contribution more than proportionally. The loading arrangement, the geometrical parameters of the member and the shear slenderness affect significantly the potential redistributions of shear before failure. As it is pointed out in in Figures 3.15d–e for slab members S25B2 and S35B2, larger redistributions are predicted with increasing slab width or with decreasing shear slenderness. This fact is related to a large extent on larger concentrations of shear forces and thus to higher potential for redistributions for lower shear slenderness and increasing slab width. As a consequence, the beginning of plastic shear deformations (after reaching the local resistance) occur much earlier for slab S35B-2 ($0.66Q_{calc}$) than for slab S25B-2 ($0.78Q_{calc}$), refer to point "R" in Figures 3.15a,d,e. Regarding the loading arrangement, it can be stated that the proposed method is capable to provide reasonable results also for non-symmetric conditions. This is the case for slab tests performed by Lantsoght et al. [8] in which the concentrated load was located close to the slab edge. In this case, regions closer to the load reached the post peak stage ($0.1v_R$) with most of the load carried by side regions. This prediction seems in sound agreement with the experimental observations by Lantsoght et al. [35] who stated that “at 780kN the width of the shear crack was 0,6mm and the crack was slowly growing”. The level of load (90% of the failure load) and the associated crack opening of the shear crack on the side face (large values) can justify the calculated shear capacity and the associated predicted shear distributions presented in Figures 3.15h–i.

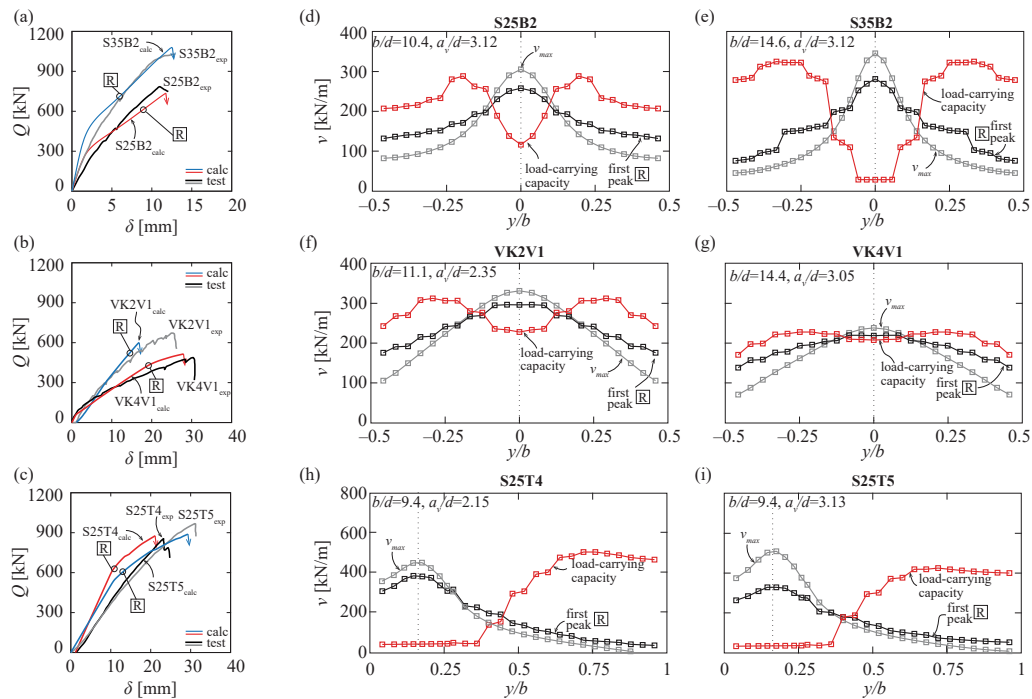


Figure 3.15: Load–displacement curves for tests by (a) Reissen et al. [7]; (b) Rombach et al. [5]; (c) Lantsoght et al. [8]; shear distribution at the control section ($0.5d$ from the point of maximum moment) for tests (d) S25B2, (e) S35B2 by Reissen et al. [7], for tests (f) VK2V1, (g) VK4V1 by Rombach et al. [5] and for tests (f) S25T4, (g) S25T5 by Lantsoght et al. [8]; v_{max} refers to the distribution of shear forces according to linear-elastic calculation (without accounting for nonlinear shear deformations) at maximum load where the shear resistance is calculated according to CSCT, see column (CSCT- v_{max}) in Table 3.3.

3.5 Conclusions

This manuscript presents the results of an investigation on the characterization of the shear force–shear strain response of a reinforced concrete member without shear reinforcement, comprising its through-thickness distribution. The main conclusions are summarized below:

1. The development of shear strains, before and after reaching the local shear resistance, is instrumental for a correct analysis of reinforced concrete slabs. This is particularly the case when concentrations of shear forces occur, as for slabs subjected to concentrated loading. In these cases, significant redistributions of internal forces can follow a local shear failure, and can allow for a further increasing the total load-carrying capacity.
2. Detailed analyses of the strain field show that the through-thickness distribution of the shear deformation depend on the development of the critical shear crack (quasi-vertical branch followed by a flatter branch). In the first stage, the shear deformation can be assumed to be linearly distributed over the cracked portion of the member, whereas in the second stage, the distribution can be assumed to be bilinear.
3. Other than by shear forces, the shear deformations observed in concrete members are to a large extent related to bending since they are originated by the flexural deformations occurring under inclined shear cracking. This fact is particularly relevant once the sub-horizontal branch of the shear cracks develops.
4. After reaching the maximum shear force, significant increases in the shear strains are observed, associated to a quasi-vertical displacement of the sides separated by the critical shear crack. Such behaviour can be considered as a softening law in shear.
5. The kinematical considerations of the Critical Shear Crack Theory can be used to efficiently reproduce the observed strain field, both accounting for its through-thickness distribution and for its global response. Such approach can be formulated by means of simple analytical expressions.
6. The shear response can be efficiently implemented into general finite-element models. This can be performed by means of multi-layered shell elements (allowing to consider the through-thickness distribution) or structural shell elements (where the flexural response and shear stiffness are dealt separately). It is shown by comparison to tests, that significant redistributions of internal forces can be captured with this latter technique.

3.6 Appendix A. Development of the sub–horizontal branch BF of the shear crack

The approach adopted for the development of the sub–horizontal crack is based on an analytical formulation proposed by Cavagnis [28]. In the following, the main equations and derivation of the final formula are presented on the basis of the geometry and kinematics of the shear crack.

According to Cavagnis [28], the quasi–vertical branch of the shear crack is assumed to develop up to the neutral axis (distance between flexural reinforcement and neutral axis equal to $d - c$), Figure 3.8. The portion of concrete between two flexural cracks acts in fact as a cantilever clamped in the compression zone (the so–called Kani’s tooth [27], Figure 3.8e). The original work by Kani [27] accounted only for the cantilever action neglecting the residual tensile strength of concrete which is however taken into account in this approach. The maximum bending moment at the fixed end of the tooth (governed by the tensile strength of concrete, Figure 3.8e) results:

$$\frac{f_{ct} \cdot b \cdot s_r^2}{6} = \Delta N(d - c) - V_{RS} \cdot s_r \quad (3.17)$$

where s_r is the distance between cracks (which can be assumed equal to $0.8(d - c)$), V_{RS} is the contribution due to residual tensile strength of concrete in the quasi–vertical branch of the flexural crack, ΔN is the increase of tensile force and compression force over the length s_r and b is the width of the member. The moment equilibrium of the free body presented in Figure 3.8e is given by:

$$\Delta N \cdot z = V_c \cdot s_r + V_{RS} \cdot s_r \quad (3.18)$$

and the equilibrium of vertical forces gives:

$$V = V_c + V_{RS} \quad (3.19)$$

where V_c is the contribution of the cantilever action which is, at the same time, also the shear force carried by the compression zone (for the development of forces in the compression zone, see [1]). Thus, the shear force component V_c can be calculated as:

$$V_c = \frac{z}{d - c} \left(V_{RS} + \frac{f_{ct} \cdot b \cdot s_r}{6} \right) - V_{RS} \quad (3.20)$$

The total shear force necessary for the development of the sub–horizontal branch of the shear crack results thus:

$$V = V_c + V_{RS} = \frac{z}{d - c} \left(V_{RS} + \frac{f_{ct} \cdot b \cdot s_r}{6} \right) \quad (3.21)$$

The residual tensile strength on the quasi–vertical branch of the shear crack AB can be calculated on the basis of the crack opening (Figure 3.8f) which is characterized by the horizontal opening at the level of the flexural reinforcement u_A . Neglecting the residual tensile strength contribution, the term u_A can be estimated as:

$$u_A = \frac{M_B}{b \cdot d \cdot \rho \cdot E_s} \cdot \frac{l_b}{z} = \frac{V_A [a_A + (d - c) \cot \beta_{AB}]}{b \cdot d \cdot \rho \cdot E_s} \cdot \frac{l_b}{z} \quad (3.22)$$

where a_A is the distance between the support and the location in which the shear crack intercepts the flexural reinforcement, l_b refers to the length of the bonded bar contributing to the crack opening (equal to $d - c$) and z is the lever arm. Assuming that G_F is the fracture energy of concrete and that $w_F = G_F / f_{ct}$ (Figure 3.8f), the contribution of the residual tensile strength of concrete can be concentrated on the stress block shown in Figure 3.8f with the length $l_{RS} = (d - c) \frac{w_F}{u_A}$, so

that V_{RS} becomes:

$$V_{RS} = b \cdot f_{ct} \cdot (d - c) \frac{w_F}{u_A} \cdot \cos(\beta_{AB}) \quad (3.23)$$

Thus, the level of load at which the sub-horizontal cracking develops (denoted V_{AF}), can be calculated for the investigated geometry as follows (see details in Figure 3.8):

$$V_{AF} = \frac{f_{ct} b s_r z}{6(d - c)} \left[\frac{1}{2} + \sqrt{\frac{1}{4} + 36 \frac{w_F}{d} \frac{\rho E_s (1 - \frac{c}{d})^2}{f_{ct} [\alpha_A + (1 - \frac{c}{d}) \cot \beta_{AB}] \frac{l_b}{d} (\frac{s_r}{d})^2} \cos \beta_{AB}} \right] \quad (3.24)$$

By considering, as previously discussed, that $s_r = 0.8(d - c)$ and $l_b = d - c$, the shear force V_{AF} becomes:

$$V_{AF} = \frac{f_{ct} b z}{7.5} \left[\frac{1}{2} + \sqrt{\frac{1}{4} + 7.5^2 \frac{w_F \rho E_s}{d f_{ct}} \frac{\cos \beta_{AB}}{[\alpha_A + (1 - \frac{c}{d}) \cot \beta_{AB}] (1 - \frac{c}{d})}} \right] \quad (3.25)$$

3.7 Appendix B. Derivation of cross-sectional response of RC members

The derivation of the cross-sectional response is presented at an arbitrary depth z_i of a generic cross section x_j . The local kinematics and deformations of an inclined crack will be described by the following parameters: $x_{A,i}$, location in which the shear crack intercepts the flexural reinforcement, z_i investigated depth of the cross section (with respect to the flexural reinforcement, Figure 3.11a), $x_{cr,i}$, location of the crack tip.

Before the onset of flexural cracking, the deformations are calculated as follows:

$$\Delta u = 0; \quad \Delta h = 0; \quad \chi = \frac{M_j}{EI_0}; \quad \gamma = \frac{V_j}{b \cdot h \cdot G}; \quad \epsilon_{x,i} = \chi \times (z_i + c_{cov} - h/2); \quad \epsilon_{z,i} = 0; \quad (3.26)$$

where M_j and V_j are the bending moment and the shear force in section x_j , $EI_0 = E_c \frac{bh^3}{12}$ is the modulus of inertia for uncracked conditions, b and h are the width and the height of the member, c_{cov} is the size of the concrete cover, E_c is the elastic modulus of concrete and $G = \frac{E_c}{2(1+\nu)}$ is the transverse shear modulus (with $\nu = 0.2$).

After onset of cracking, the shear crack is assumed to propagate instantaneously up to the neutral axis (load levels before the formation of the sub-horizontal branch BF). When the level of load V_A is larger then V_{AF} , the sub-horizontal branch of the shear crack also develops (refer to branch BF in Figure 3.8b).

As already presented in Eq. 3.6, the longitudinal crack opening depends on the rotation ψ_i and on the distance between the crack tip and the investigated fibre (defined by the depth $d_{cr,i} - z_i$, see Figure 3.11a). It results thus that the horizontal (Δu_i) and vertical expansion (Δh_i) are:

$$\Delta u_i = \psi_i \cdot (d_{cr,i} - z_i) \quad \Delta h_i = \Delta u_i \cot \beta_i \quad (3.27)$$

where ψ_i is the rotation of the crack (see Eq. 3.6):

$$\psi_i = \frac{u_A}{d_{cr}} = \frac{M_{A,i} + V_{A,i} d_{cr,i} \cot \beta_i}{z A_s E_s} \quad (3.28)$$

The curvature is given by:

$$\chi_i = \frac{M_{A,i} + V_{A,i} d_{cr,i} \cot \beta_i}{EI} \quad (3.29)$$

where EI is the modulus of inertia after cracking ($EI = E_s A_s d_{cr,i} z$) and $d_{cr,i}$ is the height between the flexural reinforcement and the crack tip (see Figure 3.11a).

The principal tensile strain is thus $\epsilon_{1,i} = \chi_i \times \frac{d_{cr,i} - z_i}{\sin \beta_i}$, resulting into:

$$\epsilon_{1,i} = \frac{M_{A,i} + V_{A,i} d_{cr,i} \cot \beta_i}{EI} \frac{d_{cr,i} - z_i}{\sin \beta_i} \quad (3.30)$$

By neglecting the value of the principal compressive strain in the cracked region, the shear strain results:

$$\gamma_i = \epsilon_{1,i} \sin 2\beta_i = 2 \frac{M_{A,i} + V_{A,i} d_{cr,i} \cot \beta_i}{EI} (d_{cr,i} - z_i) \cos \beta_i \quad (3.31)$$

while the longitudinal strain is:

$$\epsilon_{x,i} = \epsilon_{1,i} \sin^2 \beta_i = \frac{M_{A,i} + V_{A,i} d_{cr,i} \cot \beta_i}{EI} (d_{cr,i} - z_i) \sin \beta_i \quad (3.32)$$

and the vertical deformation is:

$$\epsilon_{z,i} = \epsilon_{1,i} \cos^2 \beta_i = \frac{M_{A,i} + V_{A,i} d_{cr,i} \cot \beta_i}{EI} (d_{cr,i} - z_i) \cos \beta_i \cot \beta_i \quad (3.33)$$

Notation

a	shear span
a_A	distance between support and section A
A	gross cross-sectional area
A_s	reinforcement cross-sectional area
α_A	$\frac{M_A}{V_A d}$ in section A
b	width of the member
β_{AB}	angle of quasi-vertical segment of the critical shear crack (segment AB)
β_{BF}	angle of quasi-horizontal segment of the critical shear crack (segment BF)
β_{AF}	angle of the segment AF
β	angle of segment between crack tip and a point at an arbitrary depth z
c_{cov}	size of the concrete cover
C	force of the compression zone
CL	member loaded with concentrated load
CL'	member loaded with eccentric concentrated load
CS	cantilever slab
c	depth of compression zone
χ	curvature
d	effective depth of the member
d_{cr}	height between crack tip and flexural reinforcement
d_g	aggregate size
ΔN	increase of normal force in the bar due to bond
Δu	horizontal elongation
Δh	vertical expansion
Δx	spacing of grid points
δ_{test}	measured vertical displacement
δ_{calc}	calculated vertical displacement
E_c	elastic concrete modulus
E_s	elastic steel modulus
ϵ	reference deformation at a fibre located $0.6d$ from the outermost compressive fibre
ϵ_1	maximum principal strain
ϵ_3	minimum principal strain
$\epsilon_{s,m}$	average deformation
ϵ_x	longitudinal strain
ϵ_z	vertical strain
f_{ct}	concrete tensile strength
f_y	yield strength of reinforcement
f_c	concrete cylinder compressive strength
ϕ	bar diameter
ψ_x	rotation of horizontal segments
ψ_z	rotation of vertical segments
G	shear modulus
G_F	fracture energy of concrete
G_{red}	reduced transverse shear stiffness
γ	local shear strain
γ_{sec}	average shear strain of the cross section
γ_R	shear strain at maximum shear capacity
γ_{pl}	shear strain in the post-peak stage

I	inertia of the cross section
l_F	length of segment B-F of the critical shear crack
$l_{F,max}$	maximum length of segment B-F of the critical shear crack
l_{RS}	width of the stress block developing residual tensile stresses
l_b	length contributive to the crack opening of the critical shear crack
L	length of the member
LL	member loaded with strip load
k_{ij}	terms of flexibility matrix
k_β	stiffness reduction factor accounting for orthogonal layout of reinforcement
m	bending moment per unit width
M	bending moment
M_A	acting bending moment in section A
M_F	acting bending moment at the section corresponding to the tip of the critical shear crack
n_E	ratio between steel and concrete Young modulus
N	normal force
ν	Poisson's coefficient
q	uniformly distributed load
Q	concentrated load
Q_R	concentrated load corresponding to the maximum capacity
Q_{test}	measured maximum capacity
Q_{calc}	calculated maximum capacity
ρ	reinforcement ratio A_s/A
R_l	measured reaction at the linear support
SS	simply supported slab
s_r	spacing between primary flexural cracks
T	tensile force in the bar
u	horizontal displacement
u_A	horizontal crack opening in section A
v	shear force per unit width
v_A	vertical crack opening in section A
$v_{R,c}$	one-way shear capacity for unit width
v_{perp}	unitary shear force perpendicular to control section
$v_{avg,4d}$	average shear force averaged over a distance equal to $4d$
V	shear force
V	shear force in section A
V_{AF}	level of load at which the sub-horizontal cracking develops
V_c	contribution of the cantilever action
V_{dow}	total contribution of dowel action
V_R	maximum shear capacity
V_{RS}	contribution of the residual tensile strength of concrete
V_{tot}	total shear force at the linear support
w	vertical displacement
w_A	crack opening perpendicular to the shear crack in section A
w_c	maximum crack opening due to residual tensile strength of concrete
w_F	crack opening perpendicular to the shear crack associated to the length l_{RS}
x	x-axis
x_A	horizontal distance between the point of zero bending moment and investigated cross section

ψ	rotation of the shear crack
ψ_R	rotation of the shear crack at maximum load
z	lever arm
z_i	vertical position of i -th crack with respect to flexural reinforcement

Bibliography

- [1] Aurelio Muttoni and Miguel Fernández Ruiz. Shear Strength of Members without Transverse Reinforcement as Function of Critical Shear Crack Width. *ACI Structural Journal*, 105(2): 163–172, 2008.
- [2] Francesco Cavagnis, Miguel Fernández Ruiz, and Aurelio Muttoni. A mechanical model for failures in shear of members without transverse reinforcement based on development of a critical shear crack. *Engineering Structures*, 157:300–315, 2018.
- [3] Aurelio Muttoni. Punching shear strength of reinforced concrete slabs without transverse reinforcement. *ACI Structural Journal*, 105(4):440–450, 2008.
- [4] João T. Simões, Miguel Fernández Ruiz, and Aurelio Muttoni. Validation of the Critical Shear Crack Theory for punching of slabs without transverse reinforcement by means of a refined mechanical model. *Structural Concrete*, 19(1):191–216, 2018.
- [5] G A Rombach and S Latte. Shear resistance of bridge decks without shear reinforcement. In *Tailor Made Concrete Structures – Walraven & Stoelhorst (eds)*, pages 519–526, 2008.
- [6] Francisco Natário, Miguel Fernández Ruiz, and Aurelio Muttoni. Shear strength of RC slabs under concentrated loads near clamped linear supports. *Engineering Structures*, 76:10–23, 2014.
- [7] Karin Reissen and Josef Hegger. Experimentelle Untersuchungen zur mitwirkenden Breite für Querkraft von einfeldrigen Fahrbahnplatten. *Beton- und Stahlbetonbau*, 108(2):96–103, 2013.
- [8] Eva Olívia Lantsoght, Cor Van Der Veen, Ane De Boer, and Joost C. Walraven. One-way slabs subjected to combination of loads failing in shear. *ACI Structural Journal*, 112(4):417–426, 2015.
- [9] Andri Setiawan, Robert Lars Vollum, Lorenzo Macorini, and Bassam Izzuddin. Efficient 3-D modelling of punching shear failure at slab-column connections by means of nonlinear joint elements. *Engineering Structures*, 197:109372, 2019.
- [10] Juan Sagaseta, Aurelio Muttoni, Miguel Fernández Ruiz, and Luca Tassinari. Non-axis-symmetrical punching shear around internal columns of RC slabs without transverse reinforcement. *Magazine of Concrete Research*, 63(6):441–457, 2011.
- [11] Trevor D Hrynyk and Frank J Vecchio. Capturing Out-of-Plane Shear Failures in the Analysis of Reinforced Concrete Shells. *Journal of Structural Engineering (United States)*, 141(12):11, 2015.
- [12] Chong Yik M. Goh and Trevor D Hrynyk. Nonlinear finite element analysis of reinforced concrete flat plate punching using a thick-shell modelling approach. *Engineering Structures*, 224:111250, 2020.
- [13] Francisco Natário, Miguel Fernández Ruiz, and Aurelio Muttoni. Experimental investigation on fatigue of concrete cantilever bridge deck slabs subjected to concentrated loads. *Engineering Structures*, 89:191–203, 2015.
- [14] Juan Sagaseta, Luca Tassinari, Miguel Fernández Ruiz, and Aurelio Muttoni. Punching of flat slabs supported on rectangular columns. *Engineering Structures*, 77:17–33, 2014.
- [15] Beatrice Belletti, Rita Esposito, and Joost Walraven. Shear Capacity of Normal , Lightweight and High-Strength Concrete Beams according to Model Code 2010 . II : Experimental Results versus Nonlinear Finite Element Program Results. *Journal of Structural Engineering, ASCE*, 139(9):1600–1607, 2013.

- [16] Beatrice Belletti, Aurelio Muttoni, Simone Ravasini, and Francesca Vecchi. Parametric analysis on punching shear resistance of reinforced-concrete continuous slabs. *Magazine of Concrete Research*, 71(20):1083–1096, 2018.
- [17] Jürgen Einpaul, Miguel Fernández Ruiz, and Aurelio Muttoni. Influence of moment redistribution and compressive membrane action on punching strength of flat slabs. *Engineering Structures*, 86:43–57, 2015.
- [18] Graeme J. Milligan, Maria Anna Polak, and Cory Zurell. Finite element analysis of punching shear behaviour of concrete slabs supported on rectangular columns. *Engineering Structures*, 224:111189, 2020.
- [19] fib (International Federation for Structural Concrete). *fib Model Code for Concrete Structures 2010*. Ernst & Sohn, 402 p, Germany, 2013.
- [20] Jürgen Einpaul, Robert Lars Vollum, and Antonio Pinho Ramos. Punching shear behaviour of edge column connections in continuous flat slabs. *IABSE Symposium Report*, 109(40): 1750–1757, 2017.
- [21] Leila Keyvani, Mehrdad Sasani, and Yaser Mirzaei. Compressive membrane action in progressive collapse resistance of RC flat plates. *Engineering Structures*, 59:554–564, 2014.
- [22] Jinrong Liu, Ying Tian, Sarah L. Orton, and Aly M. Said. Resistance of Flat-Plate Buildings against Progressive Collapse. I: Modeling of Slab-Column Connections. *Journal of Structural Engineering (United States)*, 141(12):1–13, 2015.
- [23] Francesco Cavagnis, Miguel Fernández Ruiz, and Aurelio Muttoni. Shear failures in reinforced concrete members without transverse reinforcement: An analysis of the critical shear crack development on the basis of test results. *Engineering Structures*, 103:157–173, 2015.
- [24] Francesco Cavagnis, Miguel Fernández Ruiz, and Aurelio Muttoni. An analysis of the shear-transfer actions in reinforced concrete members without transverse reinforcement based on refined experimental measurements. *Structural Concrete*, 19(1):49–64, 2017.
- [25] Francesco Cavagnis, João T. Simões, Miguel Fernández Ruiz, and Aurelio Muttoni. Shear strength of members without transverse reinforcement based on development of critical shear crack. *ACI Structural Journal*, 117(1):103–118, 2020.
- [26] Miguel Fernández Ruiz, Aurelio Muttoni, and Juan Sagaseta. Shear strength of concrete members without transverse reinforcement: A mechanical approach to consistently account for size and strain effects. *Engineering Structures*, 99:360–372, 2015.
- [27] G. N. J. Kani. The riddle of shear failure and its solution. *ACI Journal*, 61(4):441–468, 1964.
- [28] Francesco Cavagnis. *Shear in reinforced concrete without transverse reinforcement: from refined experimental measurements to mechanical models*. PhD thesis, EPFL – École polytechnique fédérale de Lausanne, 2017.
- [29] Aurelio Muttoni. *Die Anwendbarkeit der Plastizitätstheorie in der Bemessung von Stahlbeton*. PhD thesis, Institut für Baustatik und Konstruktion ETH Zürich, 1990.
- [30] Raffaele Cantone, Miguel Fernández Ruiz, Jan Bujnak, and Aurelio Muttoni. Enhancing Punching Strength and Deformation Capacity of Flat Slabs. *ACI Structural Journal*, 116(5): 261 – 274, 2019.
- [31] Frederik Autrup and Linh C Hoang. Experimental investigation of dowel action in RC beams without shear reinforcement. In *fib Symposium*, Shanghai, 2020.

- [32] T Baumann and Hubert Rusch. Versuche zum studium der Verdübelungswirkung der Biegezugbewehrung eines Stahlbetonbalkens. *Deutscher Ausschuss für Stahlbeton*, 210:83, 1970.
- [33] Fritz Leonhardt and René Walther. *Schubversuche an einfeldrigen Stahlbetonbalken mit und ohne Schubbewehrung*, volume 151. Wilhelm Ernst & Sohn, Berlin, Germany, 1962.
- [34] SAP2000. CSI Analysis Reference Manual. 2017.
- [35] Eva Olívia Lantsoght. Tests of reinforced concrete slabs subjected to a line load and a concentrated load - Experimental data. (Report nr. 25.5-12-12):271, 2012.

Chapter 4

Shear force redistributions and resistance of slabs and wide beams

This chapter is the pre-print version of the article *Shear force redistributions and resistance of slabs and wide beams*, accepted for publication in *Structural Concrete* in April 2021.

The authors of the publication are Raffaele Cantone (PhD Candidate), Dr. Miguel Fernández Ruiz (Senior lecturer and thesis co-director) and Prof. Aurelio Muttoni (thesis director).

The provisional reference is:

Cantone R., Fernández Ruiz M., Muttoni A. Shear force redistributions and resistance of slabs and wide beams. *Structural Concrete*.

The present work was developed by the first author (Raffaele Cantone) under the supervision of Dr. Miguel Fernández Ruiz and Prof. Aurelio Muttoni (thesis director) who provided relevant feedbacks and proofread the manuscript intensively. In addition to the original manuscript, this chapter includes an appendix which details the equations to describe the elastic-plastic stress field approach used in the numerical calculations.

The main contributions of Raffaele Cantone with respect to the production of this chapter were the following:

- Collect the experimental findings available in the literature on reinforced concrete wide beams and slabs subjected to strip and concentrated loads.
- Perform an experimental programme including three cantilever slabs subjected to strip loads and concentrated loads.
- Measurements of the kinematics of reinforced concrete slabs with Digital Image Correlation and of the strains of the flexural reinforcement with Fibre Optic strain sensors.
- Analysis and discussion of the test results, focusing particularly on the propagation of the failure surface and on the significance of shear redistributions in wide members.
- Validate the comprehensive approach presented in Chapter 3 with tests performed in the current experimental programme and with tests from the literature showing the influence of geometrical and mechanical parameters on the load-carrying capacity.
- Production of the figures and tables included in the article.
- Preparation of the manuscript of the article.

Abstract

Redistribution of shear forces in reinforced concrete members without shear reinforcement is a key aspect for the assessment of the shear capacity of slabs and wide beams, particularly when they are subjected to concentrated forces. Such redistributions are due to the nonlinear response of reinforced concrete in bending (related to concrete cracking, tension-stiffening and possible reinforcement yielding) and shear (notably after development of inclined cracks). They have the potential to significantly modify the shear and moment fields during loading and to further allow for a load increase even when some sections have already attained their local shear resistance. This aspect, with significant practical implications, has traditionally been neglected for design. The latter is usually performed based on linear-elastic analyses for calculation of internal forces (including sometimes simplified rules to account for redistributions) and verifying the strength on the basis of resistance models developed for beams or narrow slab strips. Such simplified approaches are to a large extent justified by the lack of reliable models to assess the redistribution capacity of wide beams and planar members as slabs and shells.

This work presents a research addressed at this topic. It introduces the results of an experimental programme performed on three cantilever slabs linearly supported and subjected either to strip loads or to concentrated loads. Shear redistributions close to failure are investigated on the basis of refined measurements performed on the concrete surface (by means of Digital Image Correlation) or on the reinforcement bars (by means of Fibre Optic Measurements). The results show the significance of several mechanical parameters, as well as how shear redistributions occur whenever some regions are in softening (post-peak behaviour) while others have still not attained their local shear resistance.

On this basis, a comprehensive approach is presented for determining the redistributions of internal forces developing in the shear-critical regions and to predict the shear capacity of reinforced concrete slabs subjected to concentrated loads near linear supports. The performance of such approach is eventually validated against test data and practical recommendations are proposed for design and assessment of wide beams and slabs failing in shear.

4.1 Introduction

The shear capacity of reinforced concrete members without shear reinforcement has been a classical topic of research and discussion during the last century. Following extensive experimental programmes typically performed on simply supported beams under concentrated loads, several parameters were observed to influence the shear strength. Some are related to material properties, such as the concrete strength or crack roughness and fracture properties. Others are related to the opening of the critical shear crack governing the strength [1–3], influenced by both the strains in the cracked region and by its size (typically characterized by the effective depth d). Based on these observations on beam specimens, different analytical and mechanical models have been proposed in the past, accounting for different shear-transfer actions [3–6]. These models have typically been validated and calibrated on the basis of experiments performed in beams or slab strips with prismatic section (whose width b is significantly lower than the shear span a) and subjected to uniform loading conditions through the width.

The direct application of such models to the shear design of wide planar members (slabs and shells, see for instance Figure 4.1a) is however debatable. Two cases can be distinguished:

- Planar one-way members. This case is typically found in linearly supported one-way slabs subjected to distributed loading, see Figure 4.1b. This case has strong similarities with beams as those tested in laboratories. However, differences also exist as the shear strength along

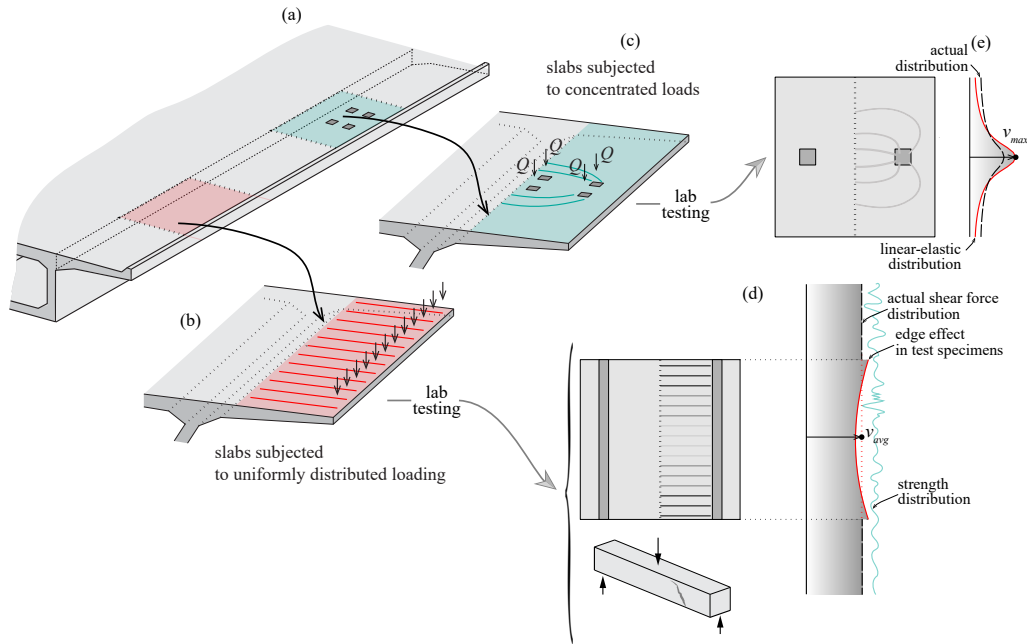


Figure 4.1: (a) instance of a bridge deck subjected to different load combinations; shear transfer modes in (b) one-way slab subjected to uniform loading and (c) slab subjected to concentrated loads; modelling of the actual condition in laboratory: distribution of shear forces for one-way slabs loaded (d) uniformly along the full width (onset of boundary effects in lab testing with respect to actual conditions) and (e) subjected to concentrated loads.

the member might not be constant (due to statistical scatter) and redistributions between weaker and stronger sections are possible.

- Planar members developing two-way action. This case can be found in linearly supported slabs subjected to concentrated loads (see Figure 4.1c) or in slabs supported by short walls and columns. In this case, high concentrations of shear forces occur and some sections can attain their resistance (or be in a softening phase) while others still have the potential to carry higher levels of shear force. This case has thus a strong potential for redistribution of shear forces [7–10].

With respect to the first case, there is still disagreement within the scientific community on the influence of the width of a member on the actual shear resistance which is normally not considered in design provisions. In this regard, one of the first studies on the influence of the width-to-depth ratio b/d on beams was performed by De Cossio in 1962, [11]. The author performed an extensive experimental programme on 57 beams with the aim to study the effect on the shear strength of dimensions (measured in that work as the area $b \times d$, with values of d ranging between 60 mm and 340 mm) and of the ratio b/d . From the experimental evidences, De Cossio stated that a larger width-to-depth ratio could lead to an increase of the shear capacity of the member. Nevertheless, it needs to be pointed out that such conclusion can be misleading since the influence of size effect was not accounted for in his study. Thus, in some cases, while maintaining the same shear resisting area ($b \times d$), De Cossio inverted the depth d and the width b observing an enhancement of the shear capacity which, in fact, can probably be attributed to a reduction of the effective depth d (so called size effect) [12].

Later, in 1967 Kani [2] performed a similar investigation on the width-to-depth ratio consisting of shear tests on beams with different shear span ratios (a/d) and different width-to-depth ratio ($b/d=0.56$ and $b/d=2.2$ but maintaining a constant effective depth $d=272$ mm). The wide beam

tests gave rise to results above and below the corresponding shear strengths of the four times narrower beams, with a difference lower than 10%. Thus, no significant increase of shear capacity due to the width of the member was clearly observed in these tests [2]. Regan and Rezai-Jorabi [13] also investigated the influence of the member width in one-way slabs showing a slight decrease of the shear resistance with increasing slab width.

Kani's observation (no influence of the width of the member) was confirmed by Lubell et al. [14, 15] and Sherwood et al. [16] who carried out experimental programmes on wide beams showing no significant enhancement or detrimental effect of the shear resistance with increasing member width. Recently, similar conclusions on the shear capacity of one-way slabs were found also by Gurutzeaga et al. [17]. On the other hand, different outcomes were observed by Conforti et al. [18–20] who recently carried out a comprehensive testing programme including three series of shear tests on beams without shear reinforcement (24 tests) with the aim to investigate the influence of the ratio b/d on the shear capacity. Based on the experimental evidences, they asserted that for ratios b/d higher than one, an increase of the shear capacity could be observed (maintaining constant all other parameters) giving rise to an enhancement of 25% of the shear capacity for b/d increasing from 1 to 3, whereas beyond $b/d=3$, no further increase was observed. Figure 4.2a reports the measured shear capacity observed amongst the testing programmes mentioned above.

Moreover, it shall be noted that several questions remain open on the representativeness of tests performed in the laboratory. For instance, Poisson's effects in the compression zone of slabs induce transverse curvatures which can modify the distribution of internal forces and reactions, also for the case of strip loads (see Figure 4.1b). Also, comparing results of narrow and wide beams is arguable accounting for the variability of the resistance along a control section (see Figure 4.1b) and how it develops spatially as a shear failure surface.

With respect to concrete slabs subjected to concentrated loads near linear supports, failures in shear differ significantly from test failures observed in prismatic members. The acting bending moments and shear forces at the shear critical region are not constant along the width of the member and the distribution of internal actions can vary with the level of load due to redistribution of shear and moment fields after cracking and/or yielding of the flexural reinforcement [7]. Several authors have performed experimental programmes with the aim to study the shear resistance and the main parameters governing the capacity of these members at failure. A summary of such tests is presented in Figure 4.2b. The ultimate shear resistance is normalized adopting the effective width b_w according to *fib*'s Model Code 2010 [21] in order to account for the size of the loading plate in a simplified manner, the effective depth, for the load position and for the boundary conditions (see details for the perimeter in Figure 4.2b).

Concerning cantilever slabs subjected to concentrated loads, Nataro et al. [7] carried out an experimental programme on slabs without shear reinforcement with different shear span (a_v/d). According to this research, for larger shear spans (between 3 and 4), a reduction of the acting unitary shear force (due to the spreading of the load) was accompanied by an increase of the unitary bending moment in the critical zone, resulting in an increase of the crack opening, a reduction of the shear resistance and a rather constant load-carrying capacity. Similar conclusions were also found by Rombach et al. [22].

With respect to the influence of the width of the member, Regan and Jorabi [13] performed an extensive testing programme on 29 simply supported wide beams subjected to concentrated loads. Their results showed a mild decrease of the shear capacity with increasing slab width, Figure 4.2b. Similarly, Rombach et al. [22] and Reissen and Hegger [23] observed results in accordance with test results by Regan and Jorabi [13]. On the other hand, Lantsoght et al. [24–26] showed an increase of the load-carrying capacity with increasing slab width.

Regarding slabs subjected to point loading, it should be noted that a sound assessment of the

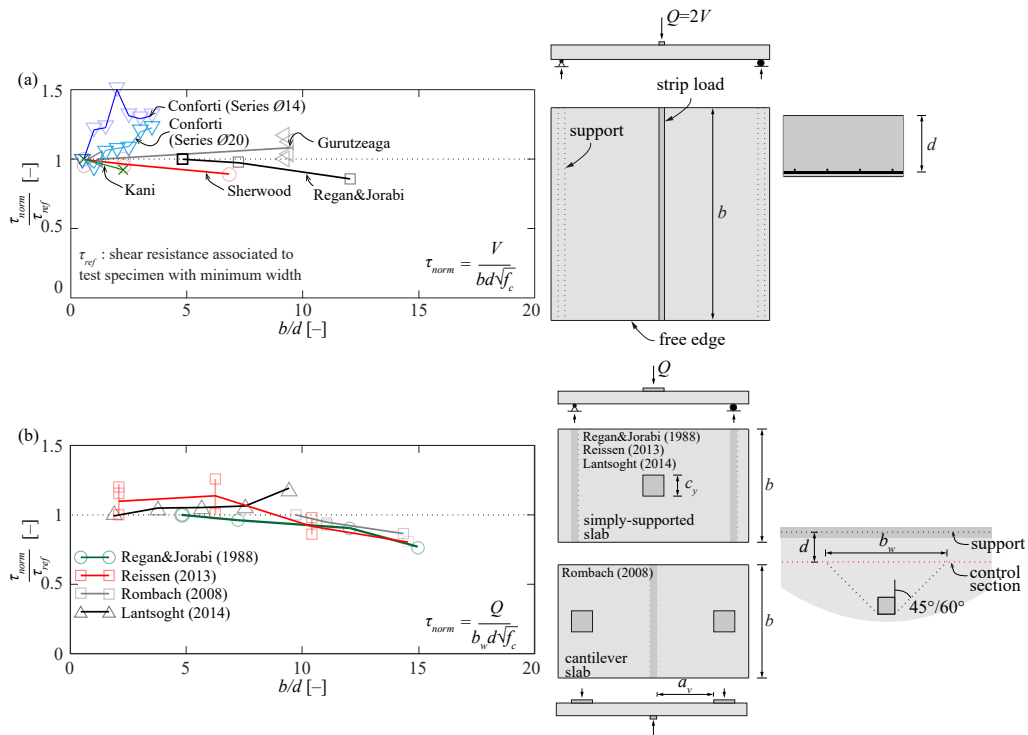


Figure 4.2: Normalized measured shear resistance with respect to reference normalized shear resistance τ_{ref} as a function of the slab width-to-depth ratio b/d for (a) members with strip loading along the full width of the member and (b) members subjected to concentrated loads (τ_{ref} is the normalized measured shear resistance of the test specimen with the minimum width for every investigated experimental programme).

ultimate capacity requires a suitable evaluation of the distribution of the internal forces accounting for nonlinear flexural and shear deformations and their associated redistributions. A practical method to verify this type of slabs consists in calculating a nominal shear force by dividing the total shear force due to concentrated loads by the length at a control section b_w (assuming a constant shear force in the perimeter). This effective width is typically estimated on the basis of geometric rules (as for instance proposed in some design codes [21, 27]) and is compared to the unitary shear resistance of an equivalent beam. The rules for estimating the effective width b_w can however significantly vary. For instance, in EN1992:1-1:2004 [27], the Dutch annex ($b_{w,EC2-NL}$) proposes a 45-degree load spreading method from the centre of the loading plate while the French annex ($b_{w,EC2-FR}$) suggests the spreading of the load from the farthest side of the load, Figure 4.3a. According to *fib*'s Model Code 2010, in addition to the geometric rules described above, the effective width $b_{w,MC10}$ is related also to the boundary conditions (clamped or simply supported conditions), Figure 4.3a. In practice, this approach can be used only for the case of a single load, since for multiple loads, their interaction cannot be considered in a rational manner (leading to overly conservative or non-conservative results depending on the distances between loads and the control section).

A more refined approach (also to avoid the shortcoming in case of multiple loads) requires the evaluation of internal forces with finite element models assuming linear-elastic behaviour of concrete with a reduced value of the shear modulus and assuming a reduced Poisson's coefficient to account for cracking (for instance, according to Natario et al. [7], suitable estimates can be calculated reducing the elastic shear modulus by a factor 8 and a Poisson's coefficient equal to zero). Also, averaging the distribution of internal forces over given widths have been proposed in the past to consider in a simplified manner the redistributions of internal forces near failure (as for instance a distance equal to $4d$ as suggested by Natario et al. [7], see Figure 4.3b).

In the framework of the response of reinforced concrete members without shear reinforcement, Chapter 3 presented a mechanical model allowing to determine flexural and shear strains developing in concrete slabs subjected to bending and shear forces. Based on the shape and kinematics of the critical shear crack (Figure 4.3c), the shear-force-shear strain relationship ($v - \gamma$) can be established as a function of the level of load. Thus, this relationship can be implemented in a condensed manner by means of joint elements located at a prescribed control section (similarly to the approach by Setiawan et al. [28]) accounting for the development of inclined shear cracks. These considerations are relevant for the modelling of reinforced concrete slabs subjected to significant shear forces as it allows accounting for the progressive development of the shear failure surface and the associated redistributions of internal forces (see Figure 4.3d). The results of this latter approach have been validated for a number of selected test data showing sound agreement both in terms of predicted strength and deformation capacity (see Chapter 3).

This paper presents a contribution on the topic of the redistributions of shear forces in slabs, focusing on its implications for wide members and slabs subjected to concentrated forces near linear supports. The research is supported by an experimental programme consisting of three specimens focusing on the differences between wide and narrow members and the influence of concentrated load spreading.

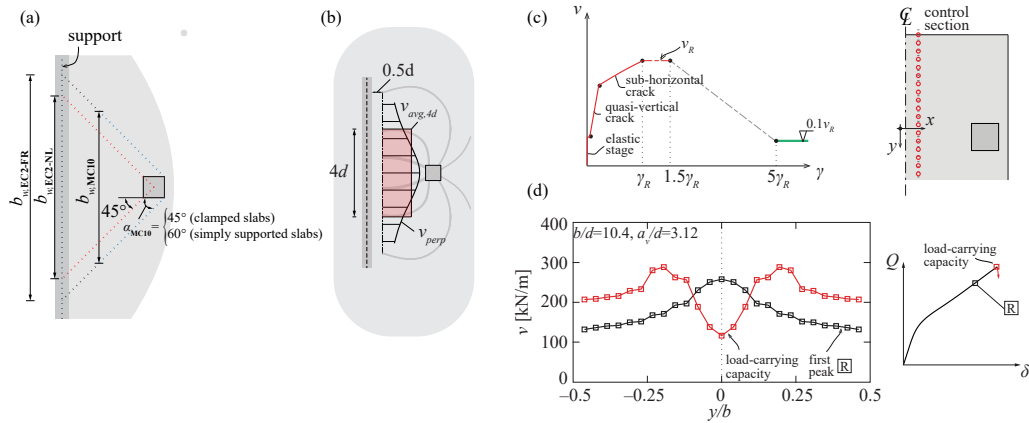


Figure 4.3: (a) definition of effective width according to *fib*'s Model Code 2010; (b) average of shear forces over a distance equal to $4d$ as suggested by Natario et al. [7]; (c) mechanical model presented in Chapter 3 to determine shear deformations and (d) calculated shear redistributions.

4.2 Test programme

An experimental programme on three full-scale reinforced concrete slabs with a central linear support was performed at the Structural Concrete Laboratory of École Polytechnique Fédérale de Lausanne (Switzerland). The testing programme included the following tests:

- **SC71** – concrete slab specimen subjected to a concentrated load Figure 4.4a (see test setup in Figure 4.5a).
- **SC72** – concrete slab subjected to strip loads, Figure 4.4b (see test setup in Figures 4.5b,c).
- **SC73** – reinforced concrete slab (identical to test SC72) in which one half of the member was divided in 15 slab strips subjected to a strip load along the full width of the member, Figure 4.4c (see test setup in Figures 4.5b,c). Every slab strip was detached from the others thus providing a total of 15 results for specimen SC73 (refer to slab strips definition in Figure 4.4c). The slab strips were separated during casting by thin steel plates which were then removed after curing.

4.2.1 Main parameters of the specimens and test setup

All slabs were square in plan with a side dimension of 3.0 m and a nominal thickness of 0.25 m. The specimens were supported on a central linear support (80-mm wide I-shaped aluminum profile [7]) and subjected either to two symmetric concentrated loads (SC71) or to two symmetric strip loads along the full width of the member (SC72, SC73). The geometry of the specimens and loading conditions were also selected to allow direct comparisons to other experimental tests already performed by the authors [7, 8]. In order to ensure failure to occur at the desired region, the other half was strengthened with shear reinforcement. The flexural reinforcement is shown in Figure 4.6 and detailed in Table 4.1. At free edges parallel to the support, the top and bottom reinforcements in x -direction (perpendicular to the support) were protruding to allow fixing the fibre optics and were connected with C-links. For slab SC71, the same C-links were also provided at free edges perpendicular to the support whereas for slabs SC72 and SC73, no edge reinforcement was provided to avoid any shear reinforcement in the investigated region.

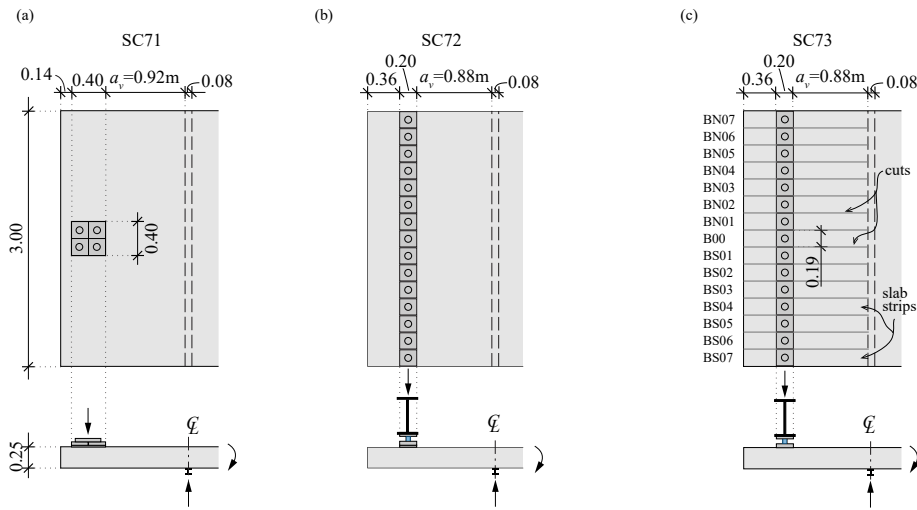


Figure 4.4: Geometry of tested specimens: (a) SC71; (b) SC72; (c) SC73.

Slab SC71

Loads were introduced with two hydraulic jacks supported on a steel frame fixed to the strong floor of the laboratory with a total capacity of 2×1.2 MN (refer to Figure 4.5a). The clear shear span a_v (Figure 4.4a) was equal to 0.92 m (4.38d). The size of the load introduction plates was 0.4×0.4 m and the load was applied through a 10 mm thick neoprene pad. Each load was introduced in this area by means of four 0.2×0.2 m steel plates with a larger steel plate as a spreader in order to distribute the load as uniformly as possible over the square contact area (for details of the load introduction device, see [7]).

Slabs SC72 and SC73

The clear shear span a_v was equal to 0.88 m (4.17d) for slabs SC72 and SC73 (refer to Figures 4.4b–c). Four hydraulic jacks with a total capacity of 4×1 MN transferred their load by means of four 75-mm steel rods connected to two steel beams (2×2 C-profiles $H=0.56$ m, $B=0.18$ m, $L=4.20$ m, $I=0.012$ m⁴, see Figures 4.5b–c). Four load cells were placed at the end of the steel rods in order to check the total applied vertical force. In addition, in order to control the distribution of the applied load over the width of the member (only for the tested side), 15 load cells spaced 200 mm were fixed to the bottom surface of the double-C profiles and put in contact with the surface of the slab. Between the load cells and the surface of the slab, 15 steel plates ($0.19\text{m} \times 0.20\text{m}$) and a thin layer of plaster were arranged in order to obtain levelled surfaces. Other than these load cells, the total load was also controlled with two load cells fixed to the steel rods. On the uninvestigated side (equipped with shear reinforcement), the C-beams pushing downward were directly in contact with the surface of the slab (without load cells) through a 3m-long rounded profile (hinge allowing for rotation) fixed to the bottom surface of the beams (refer to hinge in Figure 4.5b). At this side, the total load was controlled exclusively with two load cells fixed to the steel rods.

Material properties

All slabs were cast with normal-strength concrete whose compressive strength at the day of testing ranged between 32.5 and 44.2 MPa (average of three compressive tests on 160×320 mm concrete

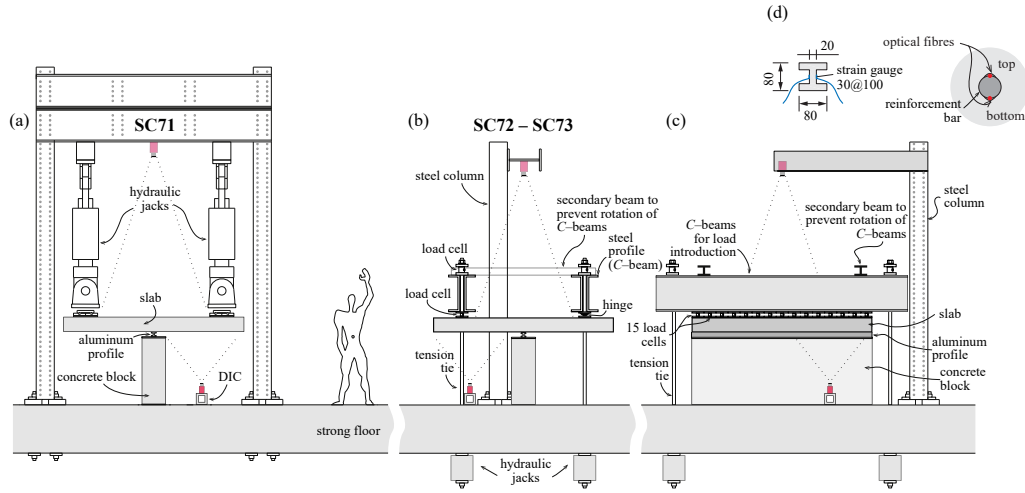


Figure 4.5: Test setup: front view for slab (a) SC71 and (b) SC72–SC73; side view of slabs SC72, SC73; (d) strain gauges glued on the aluminium profiles and location of fibres glued on the surface of the reinforcement with respect to casting direction.

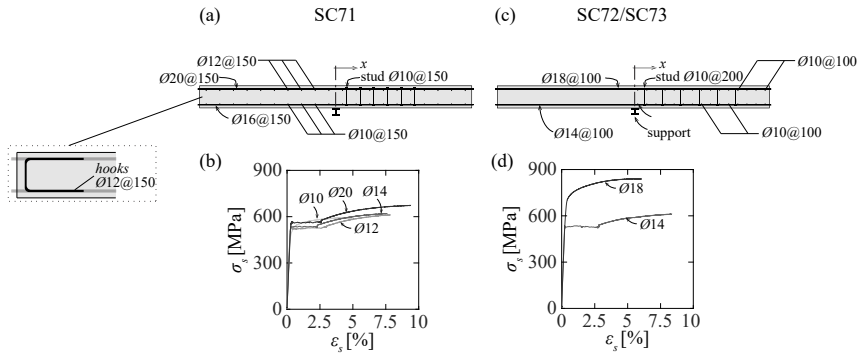


Figure 4.6: (a) reinforcement layout of specimens and (b) measured stress—strain relationships of reinforcement bars for slab SC71; (c) reinforcement layout of specimens and (d) measured stress—strain relationships of reinforcement bars for slabs SC72, SC73.

Table 4.1: Reinforcement of the three specimens*

Specimen	top reinforcement		bottom reinforcement	
	<i>x</i> -axis	<i>y</i> -axis	<i>x</i> -axis	<i>y</i> -axis
SC71	$\phi 20@150$ $d_{xt}=210\text{mm}$ $\rho=1.00\%$	$\phi 12@150$ $d_{yt}=194\text{mm}$ $\rho=0.39\%$	$\phi 16@150$ $d_{xb}=212\text{mm}$ $\rho=0.63\%$	$\phi 10@150$ $d_{yb}=199\text{mm}$ $\rho=0.26\%$
SC72,SC73	$\phi 18@100$ $d_{xt}=211\text{mm}$ $\rho=1.21\%$	–	$\phi 14@100$ $d_{xb}=213\text{mm}$ $\rho=0.72\%$	–

*See also Figure 4.6; *x*-axis is perpendicular to the linear support (nominal values of the effective depths, for actual values, see Table 4.3).

Table 4.2: Mechanical properties of the reinforcement

ϕ [mm]	f_y [MPa] ^a	f_t [MPa]	Type
10	523	601	cold-worked
12	523	623	hot-rolled
14	532	622	hot-rolled
16	533	625	hot-rolled
18	727	842	high-strength
20	562	678	hot-rolled

^a Offset yield-point at 0.2% strain for cold-worked and high-strength bars

Table 4.3: Main properties of tested specimens

Test	type	b [m]	a_v/d [-]	ρ [%]	d_{xt} [m]	f_y [MPa]	f_c [MPa]
SC71	CL	3.0	4.38	1.00	0.204	562	44.2
SC72	SL	3.0	4.17	1.21	0.209	727	40.7
SC73*	SS	0.188	4.17	1.27	0.208	727	32.5

*Average values of the 15 slab strips (refer to Table 4.4 for details); effective depth and yield strength refer to the main reinforcement in x -direction; *CL*: slab subjected to concentrated loads; *SL*: slab subjected to strip loads; *SS*: slab strips subjected to concentrated loads.

Table 4.4: Main properties of slab strips in test SC73

type	b [mm]	d_{xt} [mm]	$\tau = \frac{Q_R}{bd}$ [MPa]	$\frac{Q_R}{bd\sqrt{f_c}}$ [$\sqrt{\text{MPa}}$]
B00	188	212	1.273	0.223
BN1	186	212	1.355	0.232
BS1	185	210	1.123	0.197
BN2	189	210	1.313	0.230
BS2	188	208	1.435	0.252
BN3	188	208	1.235	0.217
BS3	189	205	1.331	0.233
BN4	189	208	1.223	0.215
BS4	186	205	1.289	0.226
BN5	189	210	1.296	0.227
BS5	188	207	1.137	0.199
BN6	189	210	1.157	0.203
BS6	184	210	1.470	0.258
BN7	190	207	1.167	0.205
BS7	188	205	1.14	0.200
Mean	188	208	1.26	0.221
COV	0.01	0.01	0.087	0.087

cylinders), see details for each specimen in Table 4.3. The maximum aggregate size was 16 mm for all test specimens and the concrete cover was maintained constant in the testing programme and equal to 30 mm. The average reinforcement mechanical properties of the flexural reinforcement (three tests per bar diameter) for all slabs are presented in Figure 4.6 and Table 4.2.

4.2.2 Measurement techniques

Recently, a notable step forward has been performed with respect to tracking of the displacement field in the concrete surface [29–32], as well as measurements of rebar strains [31–35]. These tools allowed for new insights on the response of concrete members, showing the complexity of the interactions between reinforcement and the surrounding concrete as well as the influence of compatibility of deformations on their response [32].

In this testing programme, refined measurements were performed in all slabs by combining conventional techniques (LVDTs, inclinometers, strain gauges) with detailed surface measurements of concrete and embedded reinforcement. In particular, the tracking of concrete surface (Digital Image Correlation, DIC) was performed by recording the displacement fields of top and bottom surfaces of the slab allowing for calculation of kinematics of failure surfaces, Figure 4.5. In addition, several bars per slab were equipped with Fibre-Optical Measurement systems (FOM) allowing for high quality readings of the reinforcement deformations.

For DIC measurements, pictures were acquired during the tests (frequency ranging between 0.5 and 2 Hz) with two SVCam-hr29050 sensor cameras (29 Mpx) for the top surfaces and MANTA G-504B (5 Mpx) for tracking displacements of the bottom and side surfaces. Before the tests, care was devoted to obtain a good calibration with controlled lighting and temperature conditions, since they have been shown to be significant parameters for the reduction of the noise in the measurement error [31]. Images at zero displacements and strains were taken before the tests and a noise ranging between 1/40 and 1/50 times the size of the pixel was observed (pixel size $\approx 500 \mu\text{m}$).

Random speckle pattern was applied on the concrete surface by means of spray painting (with size ranging between 0.5 and 1 mm). The displacement analysis was then performed with Vic3D software [36], using a subset size of 29 x 29 pixels.

Regarding FOM measurements, 2 mm–depth and 2 mm–wide grooves were performed on top and bottom sides of rebar surfaces (with respect to casting direction) and 125 μ m polyimide fibre optics (similar to [31]) were glued in the grooves, see Figure 4.5d. Strain measurements on the rebar surface were performed through Odisi–B version by Luna Innovations [37]). During the tests, 0.65 mm spatial resolution was used. The available Odisi–B version allowed for a maximum of four channels with continuous readings. For this reason, loading steps were established in order to allow for measurements of all rebars whose strain profiles could not be measured continuously. Details of the technique followed can be found elsewhere [32].

Displacements and rotations were tracked during the tests with LVDTs (fixed on the bottom concrete surface) and inclinometers located on the top surface. The support system (aluminium profile) was equipped with 30 strain gauges spaced 100 mm to record the distribution of the reactions (see [7] for details). Load was applied monotonically up to failure with a loading rate of 25 kN per minute except for slab SC71, where ten loading cycles (between F_{max} =200 kN, F_{min} =20 kN and target ratio R =0.1) were performed for measurement of the residual rebar stresses on the flexural reinforcement.

4.3 Test results

Figures 4.7a–c present the load–displacements curves for all tests. The deflection δ was measured at the centre of the loading plate for slab SC71, while for specimens SC72 and SC73, the measurements were performed at the axis of the load introduction along the full width of the member (refer to Figure 4.7; measurements taken at the soffit of the slab). It can be observed that, after attaining the maximum load, slab SC71 (subjected to a concentrated load) presented a softening phase with a relatively smooth decrease of the total load associated to a significant increase of the vertical displacement. After 7% decrease of the total load, the onset of a local failure around the load introduction plate was observed.

With respect to specimen SC72, the distribution of vertical displacements was almost uniform along the width of the member due to the stiffness of the steel profiles, Figure 4.7b. Once the maximum load was attained, failure was not sudden but after a redistribution phase giving rise to a gradual failure of the member.

Differently to members SC71 and SC72, the individual strips of slab SC73 failed in a brittle manner, as presented in Figure 4.7c. As soon as the maximum shear capacity of each slab strip was reached, a sudden drop of the force was observed. As discussed in the following, a reduced redistribution between strips was possible and after some strip failures, the propagation of failure caused a sudden drop of the load.

The observed cracking patterns for all slabs are also presented in Figures 4.7d–f with respect to top, bottom and side surfaces as well as saw-cuts after failure. For specimen SC71, cracks in the top surface were almost parallel in the region close to the support while they developed in a tangential manner close to the load introduction plate (one–way action governing near the linear support and two–way action governing near the concentrated load). Cracks in the bottom surface developed radially with respect to the load introduction plate. In the softening phase, new cracks formed at the top and side face triggered by the onset of a local failure at the vicinity of the load introduction plate (refer to "post–peak cracks" in Figure 4.7d). The observed failure crack in the central section (after saw-cut of the member) is also shown in Figure 4.7d. The shear crack started as a flexural crack developing then in an almost horizontal manner in the compression zone towards the support and towards the edge of the load introduction plate along the top reinforcement.

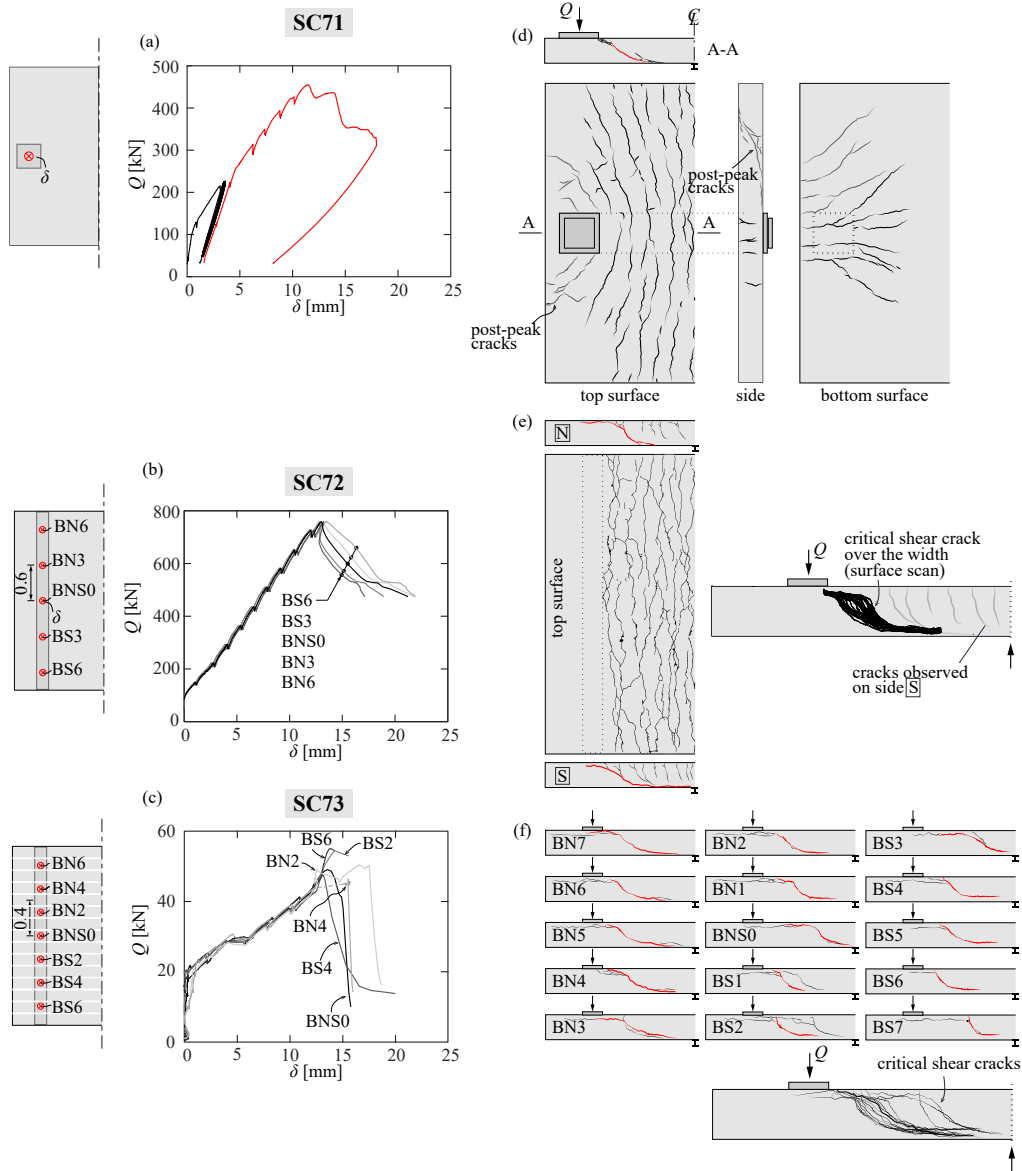


Figure 4.7: load–displacement curves for specimen (a) SC71; (b) SC72; (c) SC73 (displacement δ is measured at the bottom surface according to red markers shown on the left side); observed cracking pattern (d) for slab SC71 at top/bottom surfaces, sawcut of the section A-A; observed shear cracks: (e) at the top surface, at the sides and the whole failure surface (obtained from surface scan over the width of the slab) for slab SC72; and (f) observed shear cracks for all slab strips of test SC73 and region covered by failure cracks.

Table 4.5: Measured shear resistance of tested specimens

Test	type	b [m]	a_v [-]	Q_R [kN]	$\frac{Q_R}{b_w d \sqrt{f_c}}$ [$\sqrt{\text{MPa}}$]
SC71*	CL	3.0	4.38	455	0.127
SC72	LL	3.0	4.17	759	0.190
SC73*	SS	0.188	4.17	49.2	0.221 (0.087)

*average values of the 15 slab strips (value in bracket refers to coefficient of variation); b_w is calculated according to *fib*'s MC2010 [21] (see details in Table 4.4)

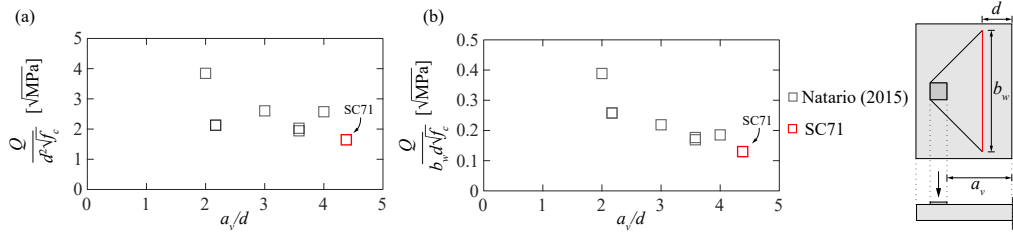


Figure 4.8: Comparison of resistance of slab SC71 and cantilever slabs subjected to concentrated loads by Natario et al. [7, 8]: (a) normalized load-carrying capacity and (b) normalized shear resistance ($\rho=1\%$).

Since one-way action was dominant in slabs SC72 and SC73, flexural cracks developed parallel to the support in the top tension zone without cracks in the compression zone. Regarding slab SC72, the failure cracks on the side faces were rather flat, propagating close to failure horizontally towards the loading plates and in the compression zone. The internal development of the failure surface is also presented in Figure 4.7e (measured by surface scan of slab portions after testing) showing variations in the slope of the failure surface in the longitudinal direction (parallel to the support). Figure 4.7f presents the failure shear cracks developed in all 15 slab strips of test SC73. It can be noted that shear cracks did not always develop in the same location and presented relatively high variability. Table 4.5 presents a summary of the maximum shear capacity observed during the tests and normalized values with respect to the effective width b_w according to *fib*'s MC2010 [21] (normalized shear resistance). For slab SC73, the average result and coefficient of variation of the 15 strips is presented (details of the shear failure loads of each strip can be found in Table 4.4).

Specimen SC71 can be directly compared to the tests performed by Natario et al. [8] on identical specimens and loading dimensions but with different clear shear spans. This comparison (see Figure 4.8) shows that the load-carrying capacity (normalized by the effective depth and the square root of the concrete compressive strength) decreases for increasing slenderness, confirming the result of the previous experimental programmes [7, 8]. An even clearer trend can be observed by normalizing the load carrying capacity by the width b_w according to *fib*'s Model Code 2010 [21]. Even though a higher shear span leads to a more uniform distribution of shear stresses, the strain effect can play a significant role on the maximum shear resistance since larger bending moments (and their associated crack openings) give rise to a decrease of the shear resistance [7]. In addition, for increasing shear span, the redistribution capacity becomes more limited.

Regarding slabs with strip loads along the full width of the member (SC72, SC73), a lower normalized shear strength was observed for slab SC72, which was 16 times wider than the slab strips of specimen SC73. As shown in Table 4.5, the nominal shear strength of SC72 was 14% lower than the average strength of SC73. Figure 4.9 presents a closer look to the distributions of load on slab SC72 measured with the load cells (Figure 4.9a) and of the reaction forces (measured with the strain gauges glued on the aluminium support, see Figure 4.9b). Sound agreement was found between the total measured load Q and the integration of reactions along the width of the member (with relative errors at maximum load of about 0.4%). As can be seen from Figure 4.9a, larger loading

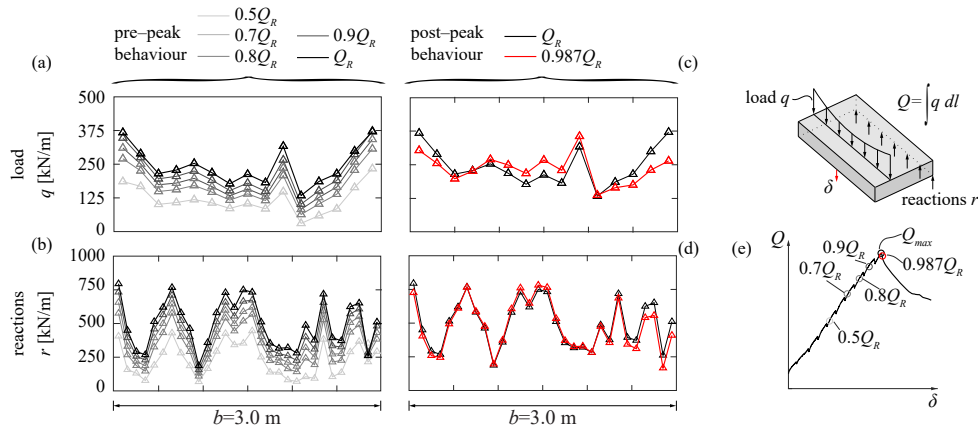


Figure 4.9: Test specimen SC72: distribution of loads ((a) and (c)) and reactions ((b) and (d)) before ((a) and (b)) and after maximum load ((c) and (d)); (e) load–displacement relationship with load levels represented in Figures (a)–(d).

forces have been measured on the edges of the slab. This can be explained by the flexibility of the load-introduction steel profiles (increase of contact forces at the edges). Other sources explaining the deviation from a constant distribution of load and reaction can be found in the uneven support conditions (the aluminium profile was supported on three 1m-width concrete blocks, Figure 4.5) and potentially by the Poisson's coefficient of the compression zone (providing longitudinal curvature). After reaching maximum load (during the post-peak phase), the differences from a constant load profile reduced, with a decrease of the forces at the sides and an increase in the inner part (see Figure 4.9c), which can be attributed to the progression of the failure surface and to internal force redistributions. With respect to the measured reactions (Figures 4.9d), such response was also observed, but milder differences were recorded, which could be potentially related to smaller influence of the flexibility of the loading profiles.

The distribution of the normalized shear strengths measured for the slab strips of specimen SC73 (strips with $b/d \approx 0.9$) are presented in Figure 4.10a. An average shear stress of 1.25 MPa ($0.22 \sqrt{\text{MPa}}$ if normalized with respect to $f_c^{1/2}$) was measured with a coefficient of variation equal to 8.7%. As already described, slab SC73 exhibits an average shear resistance 14% higher than the equivalent wider member ($b/d=14.2$). An explanation of this difference can be found in the stress concentrations at the edges observed in slab SC72. Figure 4.10b presents the distribution of loading forces close to the maximum load and in the post-peak phase. It can be noted that more limited redistributions develop after the first local failure (which occurred at 98% of the maximum load) compared to specimen SC72 (see Figure 4.9). This can be related to the fact that the continuity for test SC73 is ensured only at the load application region, whereas for member SC72, the continuity is ensured over the whole surface of the member.

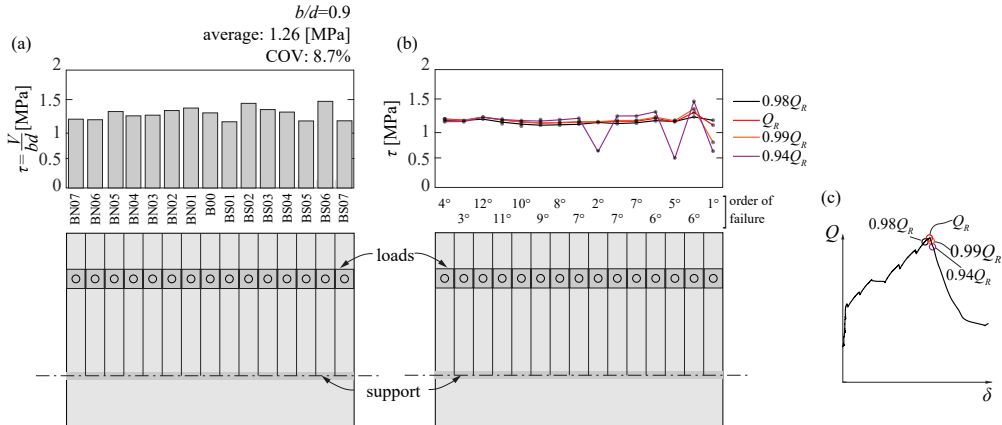


Figure 4.10: Specimen SC73: (a) maximum shear resistance for each strip (normalised with measured effective depth and actual width measured for each strip); (b) failure sequence and associated loads.

4.4 Detailed measurements of displacement and strain fields

As mentioned above, detailed measurements of the displacement and strain field were performed on the concrete surface as well as on the flexural reinforcement. These measurements allowed gathering new insights on the amount of redistributions of forces occurring close to failure.

4.4.1 Slab SC71

The refined tracking of the displacement field of the top and bottom surfaces allows for the calculation of the global displacement field of the slab and the associated crack kinematics with the level of load. Figures 4.11d–f present the evolution with the applied load Q of the vertical expansion Δh of the slab. The order of magnitude of the measured expansion (up to some millimetres) suggests that it is associated to the vertical component of crack openings (shear cracks and delamination crack). At maximum load Q_R , the vertical component of crack opening develops mostly in the region close to the loading plate with values ranging between 0.2 mm and 0.5 mm. Once the maximum load is attained, the shear failure surface progresses in the regions nearby with significant increase of vertical expansion attaining in the post-peak phase values of about 4–5 mm at a level of load corresponding to 94% of the maximum load, Figures 4.11e,f.

The shear deformation γ_{xz} (Figures 4.11g–i) is calculated as the sum between the rotation of horizontal segments ψ_x and the rotation of vertical segments ψ_z (refer to Figure 4.11b for more details). It can be noted that shear strains are associated to the development of a failure surface whose width is about $6d$ for $Q = 0.96Q_R$ (after reaching the maximum load, Figure 4.11f). This confirms that slabs subjected to concentrated loads near linear supports allow for a partial activation of the slab width before failure in agreement with the findings of Natario et al. [7]. With respect to the shear force redistributions, in this case, they do not lead to a notable increase of the resistance, but they enhance the deformation capacity. This could be related to the fact that in the case of slab SC71, the concentrated load was located relatively far from the support (clear shear span $a_v = 4.38d$), thus not allowing the same amount of shear redistributions as observed in Natario’s tests [8]. It can be noted that the response of the slab at maximum load is less brittle than in the case of beams, with larger rate of increase of the vertical opening at a rather constant level of load (increase of 300% of Δh associated to a 4% decrease of the total load Q_R), refer to profiles shown in Figures 4.12b–d. The failure region, where the inclined shear crack develops, locates close to the load introduction plate (see significant increase of thickness in Figure 4.11f).

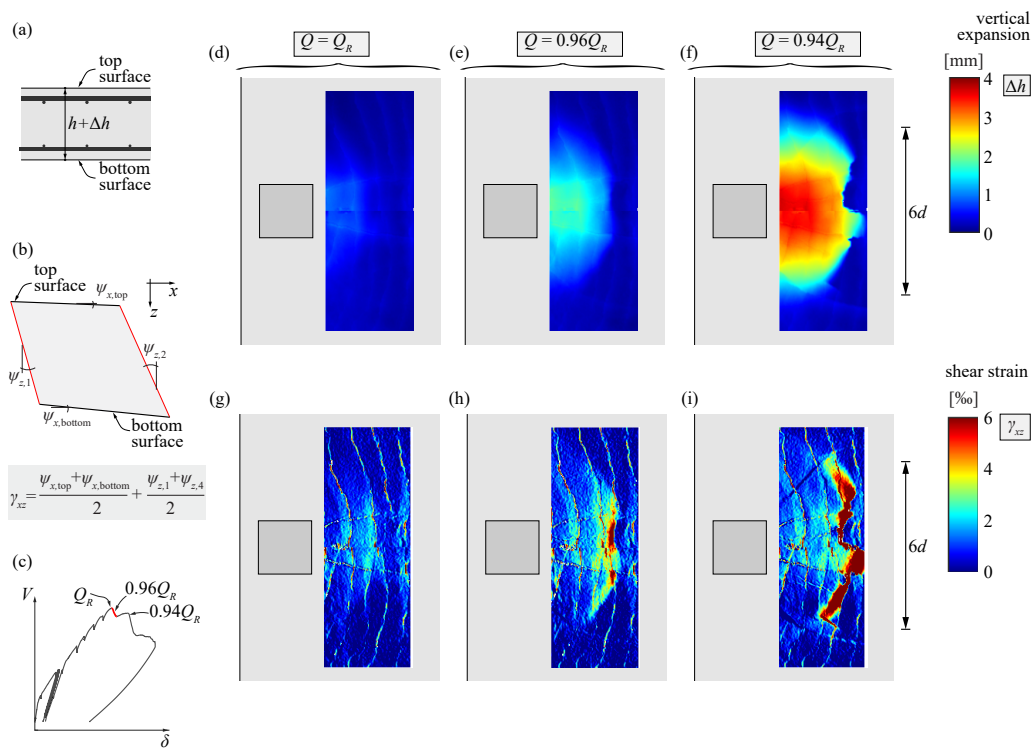


Figure 4.11: Analysis of displacement field for slab SC71: (a) definition of (a) vertical dilation Δh and (b) shear strain γ ; (c) load levels investigated; vertical dilation Δh at (d) peak load Q_R and in the post-peak stage at (e) $0.96Q_R$ and (f) $0.94Q_R$; shear strain γ_{xz} at (g) peak load Q_R and in the post-peak stage at (h) $0.96Q_R$ and (i) $0.94Q_R$.

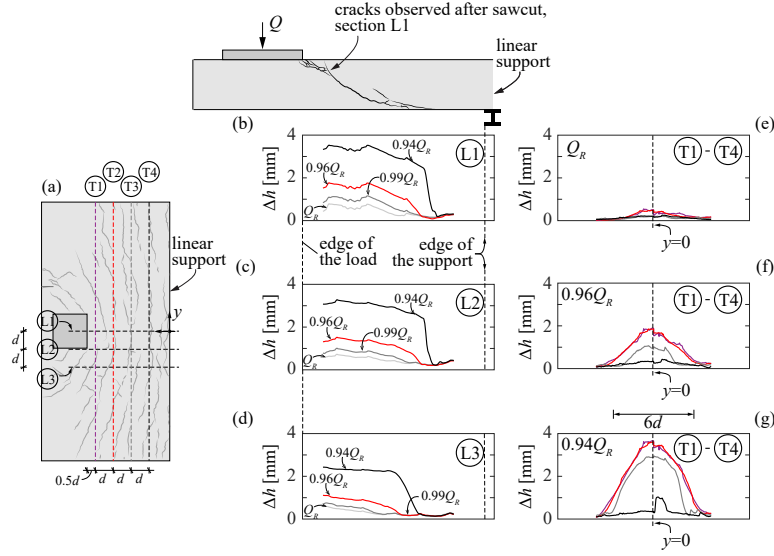


Figure 4.12: Analysis of displacement field for slab SC71: (a) sketch of investigated sections: vertical expansion for (b) section $L1$ at the axis of the load, (c) section $L2$ (spaced d from the axis of the load) and (d) section $L3$ (spaced $2d$ from the axis of the load); profiles of vertical expansion Δh (refer to section T1 through T4) at (e) peak load Q_R and in the post-peak stage at (f) $0.96Q_R$ and (g) $0.94Q_R$.

The concentration of shear deformations near to the support (see Figures 4.11h–i) is associated to a local effect related to the fact that the sub-horizontal branch of the shear crack reaches the slab soffit. The development of larger vertical component of crack openings and shear strains close to the loading plate gave rise to redistributions of internal forces in the flexural reinforcement. With this respect, Figure 4.13 presents the internal forces (normal force N_t and dowelling force $V_{dow,t}$) in selected reinforcing bars equipped with FOM measurements. The internal forces are calculated considering an elastic-plastic behaviour of the steel from the integration of the measured FOM strains in the top and bottom surface of the bar consistently with the methodology presented in Chapter 2 [32]. At 80% of the maximum capacity ($0.8Q_R$), normal forces in the tensile reinforcement are rather proportional to the bending moments (with local decreases of the normal force due to tension-stiffening contribution, see Figures 4.13b–d). Before the maximum capacity, an increase of the normal force in the bars (refer to grey-shaded area in Figures 4.13b–d) is observed, related to the opening of inclined cracks, see Chapter 3 (this is also confirmed by the activation of dowelling forces in the reinforcement, see 4.13e–g). After maximum load, the increase concentrates in the load introduction zone (refer to green-shaded areas) following the development of a delamination crack and the associated reduction of bond stresses along the top reinforcement [38]. With increasing vertical crack opening after peak load Q_R , the development of larger shear strains (due to the increase of Δh) gives rise to local bending of the bar and to the activation of significant dowelling forces (ranging between 5 and 12 kN in each bar), Figures 4.13e–g.

4.4.2 Slabs SC72 and SC73

For a closer look to the development of shear cracking in slab SC72, the failure surface observed along the width of the slab was scanned with a laser scan allowing to measure the geometry and roughness of the shear crack. As can be seen from the scanned failure surface in Figure 4.7e, the shear crack did not develop identically along the full width of the member. This observation is in agreement with the experimental evidences pointed out by Conforti et al. [20] which noted the same development of the shear crack for wide shallow members.

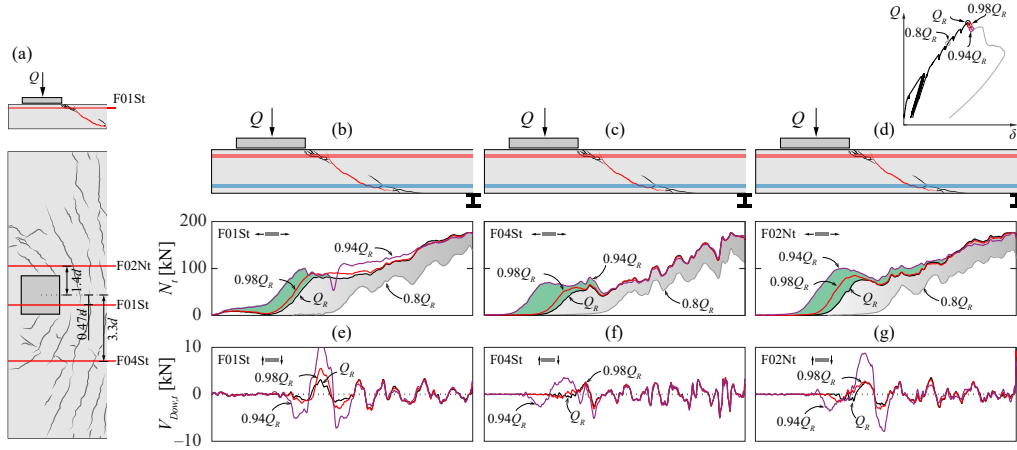


Figure 4.13: FOM measurements for slab SC71 – (a) position of investigated rebars; profiles of normal forces N_t in the top reinforcement for bars (b) F01St (0.1 m from the axis of the load) (c) F04St (0.4 m from the axis of the load) and (d) F02Nt (0.7 m from the axis of the load); profiles of dowelling forces $V_{Dow,t}$ in the top reinforcement of one reinforcement bar: (e) F01St, (f) F04St and (g) F02Nt (load levels selected equal to $0.8Q_R$, Q_R during pre-peak stage, $0.98Q_R$, $0.94Q_R$ during post-peak stage)

The uneven development of the failure shear cracks can justify some level of redistributions close to failure. With this respect, Figure 4.14 outlines the distribution of vertical expansion Δh prior to the maximum load and in the post-peak response. It should be noted that the concentration of shear stresses near the free edges (observed earlier in Figure 4.9) can explain a different extent of the vertical expansion Δh along the width of the member, see Figures 4.14a–b. Concerning the vertical expansion at maximum load, Figure 4.14a, it ranged between 0.4 mm (in a region located $b/4$ from the slab side face) and 0.2 mm (at inner regions and at the side face, Figure 4.14b). After attaining the maximum load Q_R , a significant evolution of the vertical component of the crack opening can be observed at almost constant applied load (refer to vertical component of crack displacements in Figure 4.14d). Figures 4.14c–d present the kinematics at selected load steps of all shear cracks observed on the free surface at the slab edge (refer to surface S in Figure 4.7e). Before the maximum load is attained, rather low vertical crack displacements are measured (about 0.1–0.2 mm). After attaining the maximum capacity, significant vertical crack displacements (about 4–5 mm) are observed (refer in particular to green-shaded region in Figure 4.14d).

Concerning the response of the flexural reinforcement, in the region where it is intercepted by the critical shear crack, a similar response as for specimen SC71 is observed. The increase of vertical displacement is associated to a reduction of the bond stresses due to the development of delamination cracks (refer to grey-shaded areas in Figures 4.15b–c) and to the local kinking of the reinforcement (see Chapter 2 [32]).

With this respect, it should be noted that negligible dowelling forces are calculated at the inner regions of the slab at maximum load (refer to black curve of bar F04St in Figure 4.15d). Once the maximum load is attained, dowelling forces $V_{Dow,t}$ remain roughly constant at the slab edge (bar F10St) and increase significantly at the centre of the slab attaining values between 4 and 8 kN (shear force per bar) before failure of the member, Figures 4.15d–e.

Regarding slab SC73, different critical shear cracks developed at failure for the 15 slab strips tested, Figure 4.7f. This fact influences the ultimate shear capacity since the geometry and roughness of the crack affects significantly the contribution of the main shear-carrying actions [39, 40]. With this respect, concerning the analysis of crack kinematics of slab strip BS07 (see Figure 4.16), a brittle behaviour can be observed. In particular, after attaining the maximum load, the increase

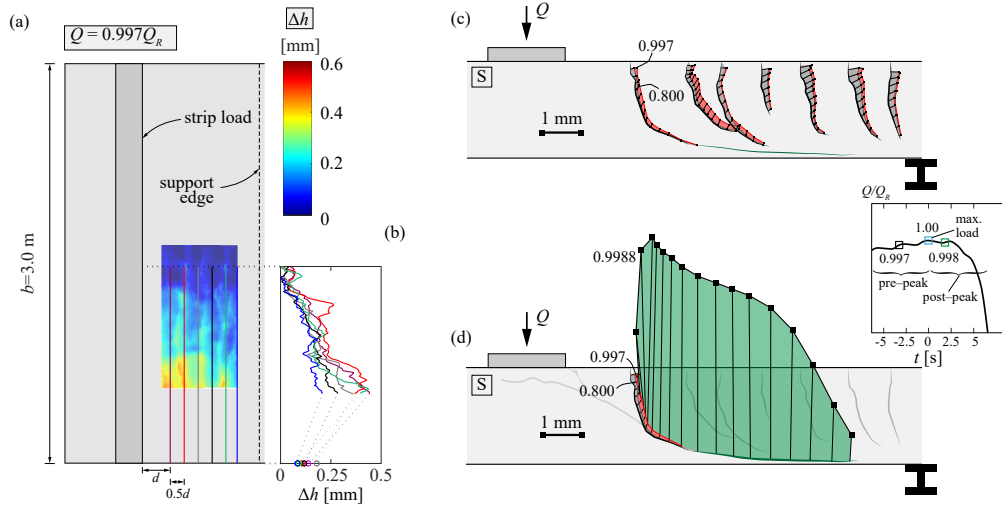


Figure 4.14: Analysis of displacement field for slab SC72: (a) contour and (b) profiles of vertical crack opening Δh in the longitudinal direction for selected control sections; development of cracking and relative crack displacements at selected load steps at slab edge (refer to surface "S" in Figure 4.14d)(c) until the maximum shear capacity; and (d) during the descending branch of the load.

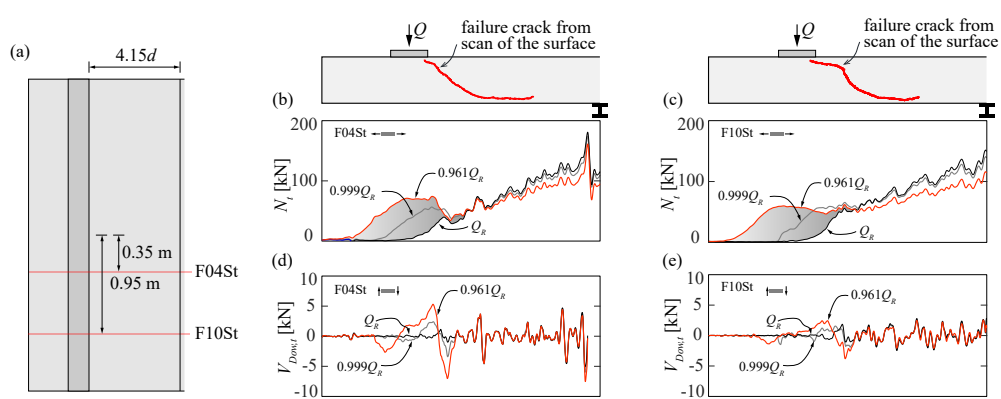


Figure 4.15: FOM measurements for slab SC72: (a) investigated sections; profiles of normal forces N_t at selected steps measured in the top flexural reinforcement: (b) bar F04St and (c) bar F10St; profiles of calculated dowelling forces $V_{Dow,t}$ at selected steps for top bars (d) F04St and (e) F10St (load steps were selected at maximum load Q_R and just thereafter).

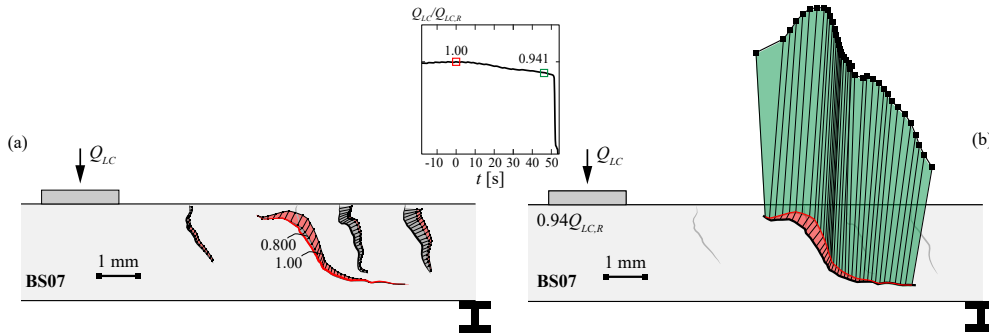


Figure 4.16: slab SC73 – development of cracking and relative crack displacements for slab strip BS07 at selected load steps (a) until the maximum load and (b) in the post-peak stage.

of the vertical component of the crack opening is associated to a significant drop of the load (a smaller decrease of load was observed in slab SC72, Figure 4.14d). The more brittle response of slab strips SC73 can be attributed to the fact that limited redistribution capacity was present (due to the separation of the slab strips compared to the full section of slab SC72, only redistribution capacity at the location of the load introduction).

4.5 Considerations on the response of wide members failing in shear

In the following, the results of the tests performed in this experimental programme as well as tests in the literature will be investigated in the framework of the Critical Shear Crack Theory [3] allowing for new insights on the structural behaviour of beams and slabs subjected to strip loads. With this respect, Figure 4.17 presents a comparison between measured and predicted shear resistances (for the tests described above and others from the literature). In this comparison, the acting shear force and the corresponding resistance are assumed to be constant over the width. It can be noted that for lower values of member width ($b/d \leq 1$), the predicted shear resistance is in sound agreement with the experimental results (average ratio between the measured and calculated resistances close to 1.0 and coefficient of variation of about 10%). This trend is however different for intermediate width-to-depth ratios ($1 \leq b/d \leq 5$) where the calculated values are safe on average. This behaviour can be explained by the shape and development of the critical shear crack which has a range of variation (see Figure 4.7e). Such variability can have a favourable effect allowing for redistributions and potential enhancement of the shear capacity.

The favourable effect due to the variability of the failure surface seems to decrease when the slab width increases beyond a certain threshold ($b/d > 5$). In particular, for larger ratios b/d , the favourable effect of the uneven geometry of the shear crack can be compensated by the difficulty to apply constant loads over the width in experiments and by other effects as the effect of the curvature parallel to the linear support (due to Poisson's coefficient of the compression zone). For these reasons, the potential to have shear force concentrations in wider members increases. This fact is also confirmed by the response of slab member SC72 in which, despite redistributions were measured close to failure, no clear enhancement of the total load was observed (see Figures 4.9, 4.17).

A more detailed explanation on the positive influence of the variation of the shape of the critical shear crack on the shear strength can be justified on the basis of the principles of the CSCT [3, 40]. According to the mechanical model proposed by Cavagnis et al. [40] (in accordance with the CSCT [3]), the inclination of primary flexural cracks β_{AB} (see Figure 4.18a) can be estimated

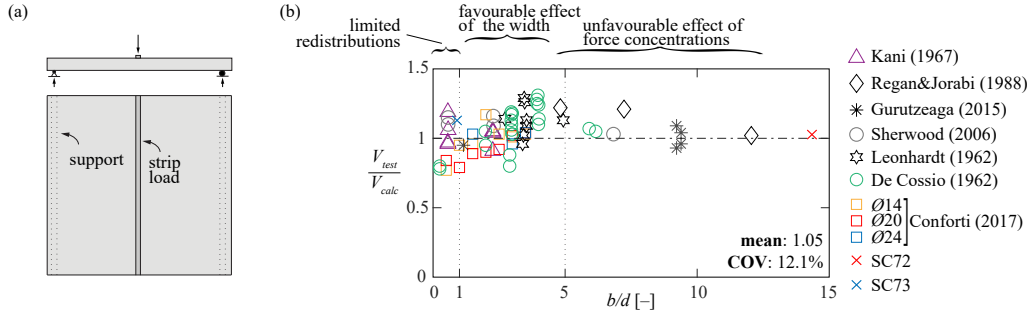


Figure 4.17: (a) wide beams and slabs subjected to strip loads and (b) measured-to-predicted shear capacity as a function of width-to-depth ratio of slabs tested in this experimental programme as well as tests in the literature.

as $\beta_{AB} = 45^\circ + 15^\circ \alpha_A^{1/3} \leq 90^\circ$, where $\alpha_A = \frac{M_A}{V_A \cdot d}$ is the shear slenderness ratio, M_A and V_A are the acting moment and shear force respectively in section A (location in which the shear crack intercepts the flexural reinforcement). According to Cavagnis et al. [40], the critical shear crack is assumed to have a bilinear shape with the centre of rotation located approximately at the tip of the crack. Before the development of the sub-horizontal branch of the shear crack (see branch BF in Figure 4.18a), it was observed that primary flexural cracks develop at a distance s_r , which can be estimated approximately as $0.8(d - c)$ [30] (where d is the effective width of the member and c is the depth of the compression zone). Based on the assumed shape and kinematics of the critical shear crack, the mechanical model by Cavagnis et al. [40] allows to evaluate the shear resistance at the location of every potential shear crack, see Figure 4.18a. It can be noted that accounting for all shear-carrying actions, the shear capacity results approximately constant (the shear resistance has a low sensitivity to the location of the shear crack).

Nevertheless, it needs to be highlighted that the geometry of inclined shear cracks can be pretty scattered over the range of observed shear cracks in the experimental tests by Cavagnis [30]. Particularly, a rather large scatter is observed both with respect to the distance between primary flexural cracks (denoted as s_r) as well as on their inclination β_{AB} (see Figures 4.18b–c). These parameters play a significant role on the response of the member as a function of the level of load. In particular, an increase of the spacing between primary flexural cracks enhances the level of shear force (V_{AF} in Figure 4.18d), which corresponds to the breakout of the concrete tooth and to the development of the sub-horizontal branch of the critical shear crack (branch BF in Figure 4.18a). The level of load V_{AF} is also affected by the inclination β_{AB} of the flexural shear cracks leading to lower levels of load V_{AF} for steeper shear cracks (see Figure 4.18e). Regarding the shear capacity, it can be noted that the development of the sub-horizontal crack does not prevent the shear force to increase [30]. In particular, steeper primary flexural cracks provide larger shear capacities (Figure 4.18e). This is related to the fact that higher aggregate interlock stresses can be activated as soon as primary flexural cracks are more vertical.

With respect to the slab strips of test SC73 (where limited redistributions can occur due to the separation between adjacent strips), the variability of the shape and position of the shear cracks affects thus the shear strengths resulting in the distribution shown in Figure 4.18f. For continuous wide members, as test SC72, the variability on the geometry of the shear crack can have a potential favourable effect on the resistance of the member, as the development of potential shear cracks along the width of the member can be restrained by the presence of uncracked regions.

The resulting geometry, more uneven, can lead to a potential increase of the resistance of the member due to enhanced aggregate interlock stresses. For instance, such deviations and uneven shape of the shear cracks can be observed in Figure 4.18g with respect to the the failure surface of

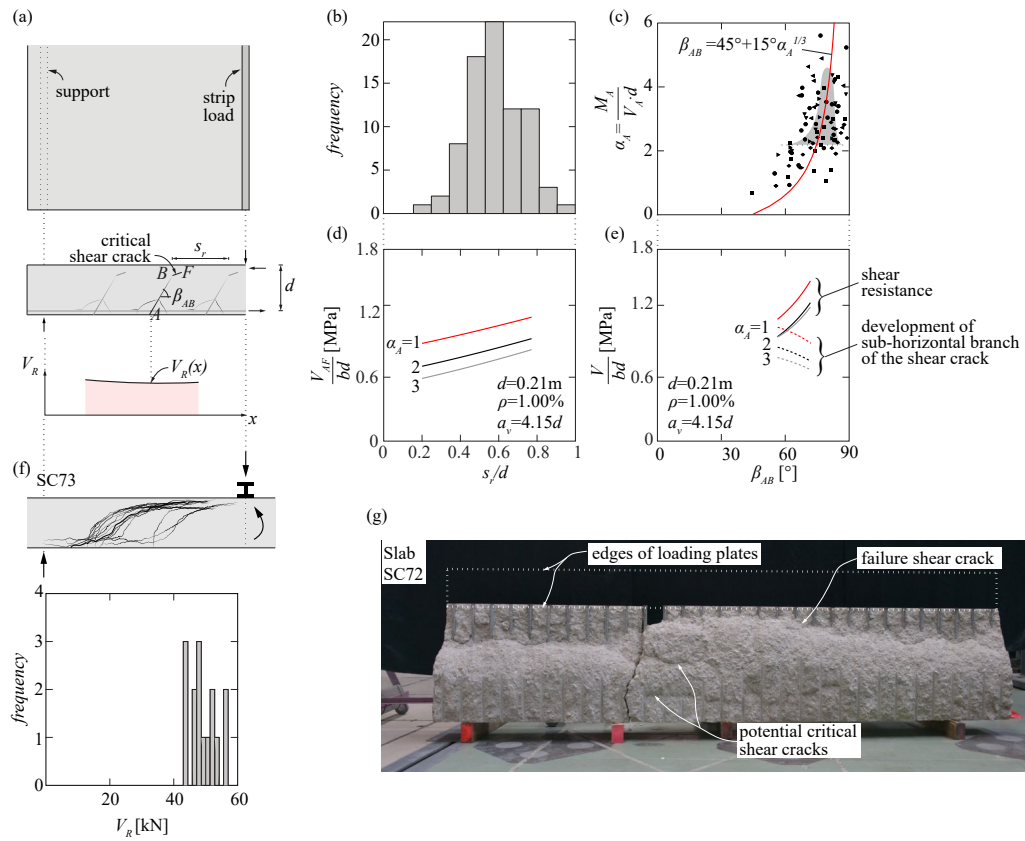


Figure 4.18: (a) shape of the critical shear crack and shear resistance at every location [40]; (b) measured distance between primary flexural cracks; (c) angle of primary flexural cracks β_{AB} with respect to shear slenderness α_A [29]; resistance of the tooth prior to the development of the sub-horizontal branch of the shear crack (d) as a function of the crack spacing (s_r/d) and (e) of the inclination of primary flexural cracks β_{AB} [40]; (f) resistance of slab strips in test SC73; and (g) failure crack observed in test SC72 with indication of the potential critical shear cracks.

slab SC72 (where different potential shear cracks develop over the width of the member without becoming critical).

4.6 Modelling of reinforced concrete slabs subjected to concentrated loads and implications for design

The response of slabs subjected to concentrated loads is different to that of beams and slabs subjected to strip loads. Since shear forces develop neither in a completely parallel nor in a perfectly radial manner, complex curved-shaped failure surfaces can be observed leading to intermediate failure modes between shear and punching. In the following, the evaluation of internal actions is performed by means of a layered shell approach (four-nodes multilayered shell elements using the commercial software SAP2000 [41]) where the flexural response accounts for the nonlinear behaviour of concrete (concrete cracking, tension-stiffening) and steel reinforcement (yielding and hardening of reinforcing bars, refer also to Chapter 3).

With respect to slab SC71, Figure 4.19a presents the principal directions of the shear field at a level of load equalling the maximum capacity Q_R ($Q_R=455\text{kN}$). As it can be observed from the experimental cracking pattern (Figure 4.7d), the critical section was potentially located close to the loading plate (region with the highest shear forces) giving rise to a local failure at the slab edge. Shear deformations are in this numerical approach concentrated in joint elements, following the lumped approach by Setiawan et al. [28].

On this basis, two control sections are investigated for slab SC71: (i) a control section located $0.5d$ from the linear support (assuming parallel distribution of shear forces) and (ii) a control section located close to the load application plate (see Figures 4.19a-b). Regarding the control section close to the loading plate, since the corresponding shear force distribution is both radially distributed (close to the loading plate) and parallel (on the straight segments), two different responses were provided to the joint elements with the aim to characterize differently two-way and one-way action (see Figure 4.19b). The two-way shear joint is modelled according to the approach proposed by Setiawan et al. [28] for characterizing the response of flat slabs supported on columns failing in punching. Regarding the one-way shear joint, the response follows the principles presented in Chapter 3 (grounded on a similar consideration as [28]). It should be noted that a control section with an angle of 45° with respect to the slab edge was assumed (see Figure 4.19b). This fact implies that the deformation ϵ (perpendicular to the control section, see Figure 4.19b) for the calculation of the shear capacity according to the Critical Shear Crack Theory [3] needs to be evaluated in the direction perpendicular to the assumed control section accounting for the actual layout of the flexural reinforcement. For this purpose, based on the acting bending and torsional moments m_x, m_y, m_{xy} , the deformation ϵ was derived by means of an elastic-plastic stress field analysis [42] (see Appendix 4.8).

Figure 4.19c presents a comparison between the measured and calculated load-displacement response. As can be seen, the implementation allows for a sound estimate of the response of slab SC71 both in terms of the ultimate shear capacity as well as the overall stiffness. However, it can be noted that close to failure, the adopted approach can underestimate the total displacement of the slab. This fact is mostly due to the assumption of the concentration of the shear deformations in selected control sections rather than smearing them over the concrete member.

The same approach introduced in Chapter 3 is now used for the analysis of wide reinforced concrete slabs failing in one-way action together with a series of simplified design approaches based on CSCT and *fib*'s Model Code 2010. To that aim, only slab tests with clear shear failures (based on cracking pattern observations) were selected for the current investigation. Figures 4.19d-f present a

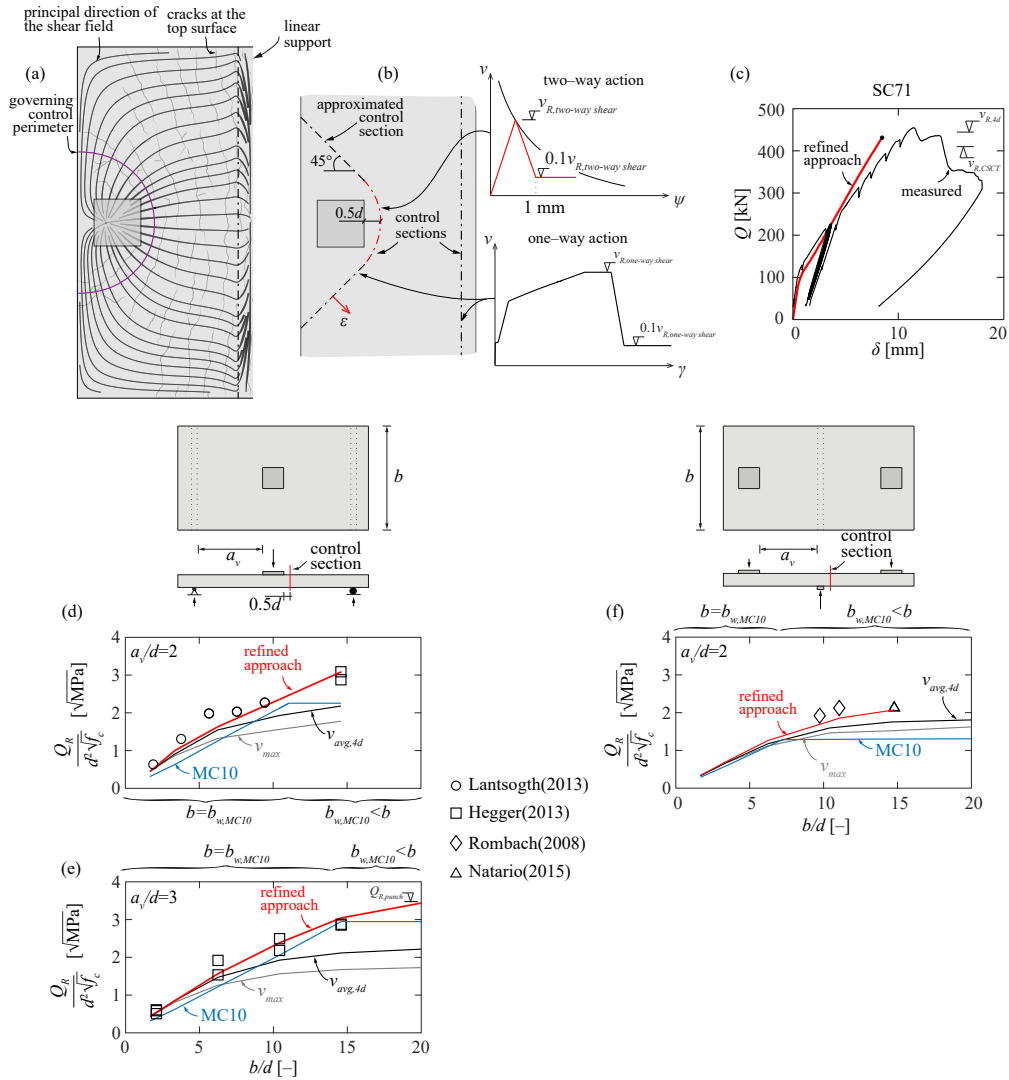


Figure 4.19: (a) shear field for a level of load corresponding to the maximum capacity of the member ($Q_R=455$ kN); (b) assumed control sections for estimation of the maximum capacity; (c) measured load-displacement response and comparison with calculated values; comparison between measured and calculated load-carrying capacities evaluated on the basis of the shear resistance according to CSCT [3] and the shear distribution according to an elastic analysis (v_{max}), averaged over a length of $4d$ ($v_{avg,4d}$), the rules of fib's Model Code 2010 [21] and the refined approach defined in this work for simply supported slabs with (d) $a_v/d=2$; (e) $a_v/d=3$ and cantilever slabs with (f) $a_v/d=2$ (Parameters: $d=0.24$ m, $f_c=38$ MPa, $\rho=1.00\%$).

comparison between measured and calculated load-carrying capacities for different width-to-depth ratio (b/d). The predictions are performed with the following approaches: (i) maximum shear force calculated without accounting for shear deformations (v_{max}); (ii) average of the unitary shear force v over a distance equal to $4d$ [7] ($v_{avg,4d}$); (iii) shear force calculated dividing the applied load Q by a nominal width b_w according to *fib*'s Model Code 2010 and (iv) refined approach accounting for the shear deformations as described above (see Chapter 3). For all cases, the shear resistance is calculated according to CSCT [3].

As can be seen in Figures 4.19d–e for the case of simply supported slabs, the refined approach provides results in sound agreement with all experimental observations. It should be noted that an increase of the ratio b/a_v (width of the member b and clear shear span a_v) is associated to an increase of the load-carrying capacity until a certain threshold ($b/d \approx 15$ for the investigated cases). Beyond this threshold, the shear capacity of the member remains rather constant (see Figure 4.19d) or it is potentially limited by a local failure in punching around the loading plate (see Figure 4.19e).

The enhancement of the load-carrying capacity with increasing member width can be related to the highest potential for redistribution of internal forces. When the response is calculated on the basis of the maximum acting shear force according to a linear-elastic analysis, safe predictions of the failure load are obtained (see Figures 4.19d–e). As proposed by Natario et al. [7], the unitary shear force v can thus be averaged over a length equal to $4d$ to account for nonlinear bending and shear deformations. This consideration improves the predictions but remains still safe for larger ratios b/d . The predictions using MC2010 provide reasonable results in some cases, but overly conservative predictions in others.

For practical design and assessment, it can be stated that a Levels-of-approximation approach seems a suitable strategy [43]. Simple analyses without redistributions can be performed on the basis of an elastic distribution of internal forces, that can be progressively refined by considering some level of redistribution. This can be done for instance according to simplified perimeters as those suggested by Natario. As the most refined Level-of-Approximation, a nonlinear analysis can be performed, considering the actual redistribution capacity along a control section.

4.7 Conclusions

This work presents an experimental and numerical investigation of shear redistributions and the associated resistances of wide beams and slabs without shear reinforcement. The investigation is supported by refined measurements performed on three reinforced concrete slabs subjected to strip and concentrated loads. The nonlinear finite elements analyses are conducted using shell elements where the out-of-plane shear deformations are calculated on the basis of a mechanical model. The main conclusions are listed below:

1. The width of a member failing under predominant one-way action is a parameter that can influence the shear strength under some circumstances.
2. For wide beams subjected to strip loading, a slight increase of the shear resistance can be observed up to ratios b/d (width-to-effective depth) equal to 5. This is explained by the variability of the failure surface that allows for redistributions of internal forces and enhances the shear resistance.
3. For wider members ($b/d > 5$), a smaller increase of the load-carrying capacity is observed, as the effects related to concentration of forces at the boundaries (due for instance to uneven load/support conditions or to Poisson's effect of the compression region) become governing. In general, both effects compensate and the resistance can be safely estimated on the basis of that of narrow members.

4. For linearly supported slabs subjected to concentrated loads, the influence of the slab width is notable. This is due to the enhanced capacity of these members to redistribute internal forces while developing the complete failure surface. For this case, calculations considering redistributions of internal forces are advised for a realistic estimate of the failure load.
5. Practical rules for redistribution of internal forces (based on a constant or variable length) are suitable for design. They provide reasonable estimates but remain generally safe. Best estimates of the strength require a nonlinear analysis of the response of the member, considering the post-peak shear response of the concrete sections.

4.8 Appendix. Elastic-plastic stress fields approach

An approach based on elastic-plastic stress fields is used in order to derive the deformation and associated shear capacity. Knowing the acting bending and torsional moments m_{Ex}, m_{Ey} and m_{Exy} (x, y corresponding to the direction of the flexural reinforcement), the principal strains ϵ_1, ϵ_2 and angle θ could be derived in a iterative manner (by means of Newton-Raphson method) with Mohr's circle of strains. The deformations ϵ_x, ϵ_y can be expressed as:

$$\epsilon_x = \epsilon_1 \cos^2 \theta + \epsilon_2 \sin^2 \theta \quad \epsilon_y = \epsilon_1 \sin^2 \theta + \epsilon_2 \cos^2 \theta \quad (4.1)$$

The reinforcement forces per unit width $t_{Rx,s}, t_{Ry,s}$ are:

$$t_{Rx,s} = a_s E_s \epsilon_x \leq a_s \cdot f_{yx} \quad t_{Ry,s} = a_s E_s \epsilon_y \leq a_s \cdot f_{yy} \quad (4.2)$$

where a_s is the reinforcement area per unit width, f_{yx}, f_{yy} the yielding strength of reinforcement in x, y direction, E_s the steel Young modulus. The stresses of concrete in the principal directions are (neglecting concrete tensile strength):

$$\sigma_{c1} = E_c \epsilon_1 \leq f_{cp} \quad \sigma_{c2} = E_c \epsilon_2 \leq f_{cp} \quad (4.3)$$

where f_{cp} is the effective concrete compressive strength ($f_{cp} = (\frac{30}{f_c})^{1/3} \cdot f_c \leq f_c$). The resistant concrete stresses $t_{Rx,c}, t_{Ry,c}, t_{Rxy,c}$ result:

$$t_{Rx,c} = t (\sigma_{c1} \cos^2 \theta + \sigma_{c2} \sin^2 \theta) \quad (4.4)$$

$$t_{Ry,c} = t (\sigma_{c1} \sin^2 \theta + \sigma_{c2} \cos^2 \theta) \quad (4.5)$$

$$t_{Rxy,c} = t (\sigma_{c1} \sin \theta \cos \theta + \sigma_{c2} \sin \theta \cos \theta) \quad (4.6)$$

where t is the depth of the layer contributive to the compression/tension chord. Knowing that the resisting internal forces are given by the sum of concrete and steel stresses:

$$t_{Rx} = t_{Rx,c} + t_{Rx,s} \quad t_{Ry} = t_{Ry,c} + t_{Ry,s} \quad t_{Rxy} = t_{Rxy,c} \quad (4.7)$$

the equilibrium is satisfied if they are equal to the acting external forces t_{Ex}, t_{Ey}, t_{Exy} :

$$t_{Ex} = \frac{m_x}{z} \quad t_{Ey} = \frac{m_y}{z} \quad t_{Exy} = \frac{m_{xy}}{z} \quad (4.8)$$

where z is the assumed lever arm between tension and compression chord. Once the state of strain (ϵ_1, ϵ_2) in equilibrium with the external forces m_x, m_y, m_{xy} is known, the deformation associated to an arbitrary plane can be derived as follows:

$$\epsilon_n = \epsilon_1 \sin^2 \theta + \epsilon_2 \cos^2 \theta \quad (4.9)$$

Notation

a	shear span
a_v	clear shear span
a_s	unitary reinforcement cross-sectional area
α_A	$\frac{M_A}{V_A d}$ in section A
$\alpha_A MC10$	angle of spreading of the load according to MC10
b	width of the member
B	width of the C-profiles
b_w	effective width of the member
$b_{w,EC2-FR}$	effective width of the member according to French Annex
$b_{w,EC2-NL}$	effective width of the member according to Dutch Annex
$b_{w,MC10}$	effective width of the member according to MC10
β_{AB}	angle of quasi-vertical segment of the critical shear crack (segment AB)
β_{BF}	angle of sub-horizontal segment of the critical shear crack (segment BF)
c	depth of compression zone
c_y	size of the loading plate in the direction parallel to the support
d	effective depth of the member
d_{xt}	effective depth of top reinforcement in x -direction
d_{yt}	effective depth of top reinforcement in y -direction
d_{xb}	effective depth of bottom reinforcement in x -direction
d_{yb}	effective depth of bottom reinforcement in y -direction
Δh	vertical expansion
δ	measured vertical displacement
E_c	elastic concrete modulus
E_s	elastic steel modulus
ϵ_1	maximum principal strain
ϵ_2	minimum principal strain
ϵ_x	strain in x -direction
ϵ_y	strain in y -direction
f_y	yield strength of reinforcement
f_{yx}	yield strength of reinforcement in x -direction
f_{yy}	yield strength of reinforcement in y -direction
f_c	concrete cylinder compressive strength
f_{cp}	effective concrete compressive strength
f_t	maximum strength of reinforcement
ϕ	bar diameter
G	shear modulus
γ	shear strain
γ_R	shear strain at maximum load
H	height of C-profiles
I	cross section inertia
L	length of the member
m_x	bending moment in x -direction
m_y	bending moment in y -direction
m_{xy}	torsional moment
M	bending moment
M_A	bending moment in section A

N_t	normal force in top reinforcement
ν	Poisson's coefficient
q	uniformly distributed load
Q	concentrated load
Q_R	load-carrying capacity
Q_{LC}	concentrated load of slab strip
$Q_{LC,R}$	load-carrying capacity of slab strip
r	reactions over the linear support
ρ	reinforcement ratio
s_r	crack spacing
σ_{c1}	maximum concrete principal stress in 1-direction
σ_{c2}	minimum concrete principal stress in 2-direction
t	depth of the cross section contributive to the tension/compression chord
$t_{Rx,s}$	resistant unitary force of reinforcement in x -direction
$t_{Ry,s}$	resistant unitary force of reinforcement in y -direction
$t_{Rx,c}$	resistant unitary force of concrete in x -direction
$t_{Ry,c}$	resistant unitary force of concrete in y -direction
$t_{Rxy,c}$	torsional resistance of concrete per unit width
t_{Ex}	acting unitary force in x -direction
t_{Ey}	acting unitary force in y -direction
t_{Exy}	acting tangential forces per unit width
t_{Rx}	resistant unitary force in x -direction
t_{Ry}	resistant unitary force in y -direction
t_{Rxy}	resistant tangential forces per unit width
θ	angle of principal directions
v	shear force per unit width
$v_{avg,4d}$	average shear force acting in a distance $4d$
v_{perp}	shear force perpendicular to control section
v_R	maximum shear capacity per unit width
$v_{R,c}$	shear capacity for unit width according to CSCT
$v_{R,one-way shear}$	one-way shear capacity for unit width
$v_{R,two-way shear}$	two-way punching capacity for unit width
V	shear force
V_A	shear force in section A
V_{AF}	level of load at which the sub-horizontal cracking develops
$V_{dow,t}$	dowelling force of the top flexural reinforcement
V_R	shear resistance
x	x -axis (perpendicular to linear support)
y	y -axis (parallel to linear support)
ψ	rotation of the shear crack
ψ_x	rotation of horizontal segments
ψ_z	rotation of vertical segments

Bibliography

- [1] G. N. J. Kani. The riddle of shear failure and its solution. *ACI Journal*, 61(4):441–468, 1964.
- [2] G. N. J. Kani. How safe are our large reinforced concrete beams? *ACI Journal*, 64(3):128–141, 1967.
- [3] Aurelio Muttoni and Miguel Fernández Ruiz. Shear Strength of Members without Transverse Reinforcement as Function of Critical Shear Crack Width. *ACI Structural Journal*, 105(2):163–172, 2008.
- [4] Frank J Vecchio and Michael P Collins. The modified compression field theory for reinforced concrete elements subjected to shear. *ACI Journal*, 83(2):219–231, 1986.
- [5] Aurelio Muttoni. Punching shear strength of reinforced concrete slabs without transverse reinforcement. *ACI Structural Journal*, 105(4):440–450, 2008.
- [6] Yuguang Yang. *Shear Behaviour of Reinforced Concrete Members without Shear Reinforcement A New Look at an Old Problem*. PhD thesis, Delft (Netherlands), 2014.
- [7] Francisco Natário, Miguel Fernández Ruiz, and Aurelio Muttoni. Shear strength of RC slabs under concentrated loads near clamped linear supports. *Engineering Structures*, 76:10–23, 2014.
- [8] Francisco Natário, Miguel Fernández Ruiz, and Aurelio Muttoni. Experimental investigation on fatigue of concrete cantilever bridge deck slabs subjected to concentrated loads. *Engineering Structures*, 89:191–203, 2015.
- [9] Juan Sagaseta, Aurelio Muttoni, Miguel Fernández Ruiz, and Luca Tassinari. Non-axis-symmetrical punching shear around internal columns of RC slabs without transverse reinforcement. *Magazine of Concrete Research*, 63(6):441–457, 2011.
- [10] Juan Sagaseta, Luca Tassinari, Miguel Fernández Ruiz, and Aurelio Muttoni. Punching of flat slabs supported on rectangular columns. *Engineering Structures*, 77:17–33, 2014.
- [11] Roger Diaz De Cossio, J. Moe, P. L. Gould, and J. G. Meason. Shear and Diagonal Tension. *ACI Journal Proceedings*, 59(11):1323–1339, 1962.
- [12] Michael P Collins and Daniel Kuchma. How Safe Are Our Large, Lightly Reinforced Concrete Beams, Slabs, and Footings? *ACI Structural Journal*, 96(4):482–490, 1999.
- [13] P E Regan and H. Rezai-Jorabi. Shear resistance of one-way slabs under concentrated loads. *ACI Structural Journal*, 85(2):150–157, 1988.
- [14] Adam Scott Lubell. *Shear in wide reinforced concrete members*. PhD thesis, University of Toronto, Canada, 2006.
- [15] Adam Scott Lubell, Evan C. Bentz, and Michael P Collins. Influence of longitudinal reinforcement on one-way shear in slabs and wide beams. *Journal of Structural Engineering*, 135(1):78–87, 2009.
- [16] Edward G Sherwood, Adam Scott Lubell, Evan C. Bentz, and Michael P Collins. One-Way Shear Strength of Thick Slabs and Wide Beams. *ACI Structural Journal*, 103(6):794–802, 2006.
- [17] Mikel Gurutzeaga, Eva Oller, Carlos Ribas, Antoni Cladera, and Antonio Marí. Influence of the longitudinal reinforcement on the shear strength of one-way concrete slabs. *Materials and Structures/Materiaux et Constructions*, 48(8):2597–2612, 2015.

- [18] Antonio Conforti, Fausto Minelli, and Giovanni A. Plizzari. Wide-shallow beams with and without steel fibres: A peculiar behaviour in shear and flexure. *Composites Part B: Engineering*, 51:282–290, 2013.
- [19] Antonio Conforti, Fausto Minelli, Andrea Tinini, and Giovanni A. Plizzari. Influence of polypropylene fibre reinforcement and width-to-effective depth ratio in wide-shallow beams. *Engineering Structures*, 88:12–21, 2015.
- [20] Antonio Conforti, Fausto Minelli, and Giovanni A. Plizzari. Influence of width-to-effective depth ratio on shear strength of reinforced concrete elements without web reinforcement. *ACI Structural Journal*, 114(4):995–1006, 2017.
- [21] fib (International Federation for Structural Concrete). *fib Model Code for Concrete Structures 2010*. Ernst & Sohn, 402 p, Germany, 2013.
- [22] G A Rombach and S Latte. Shear resistance of bridge decks without shear reinforcement. In *Tailor Made Concrete Structures – Walraven & Stoelhorst (eds)*, pages 519–526, 2008.
- [23] Karin Reissen and Josef Hegger. Experimentelle Untersuchungen zur mitwirkenden Breite für Querkraft von einfeldrigen Fahrbahnplatten. *Beton- und Stahlbetonbau*, 108(2):96–103, 2013.
- [24] Eva Olívia Lantsoght, Cor Van Der Veen, and Joost C Walraven. Shear in One-Way Slabs under Concentrated Load Close to Support. *ACI Structural Journal*, 110(2):275–284, 2014.
- [25] Eva Olívia Lantsoght, Cor Van Der Veen, Ane De Boer, and Joost C. Walraven. Influence of width on shear capacity of reinforced concrete members. *ACI Structural Journal*, 111(6):1441–1449, 2014.
- [26] Eva Olívia Lantsoght, Cor Van Der Veen, Ane De Boer, and Joost C. Walraven. One-way slabs subjected to combination of loads failing in shear. *ACI Structural Journal*, 112(4):417–426, 2015.
- [27] prEN 1992-1-1:2018. *Eurocode 2: Design of concrete structures—Part 1: General rules and rules for buildings*. European Committee for Standardization (CEN), Brussels, Belgium, 2018.
- [28] Andri Setiawan, Robert Lars Vollum, Lorenzo Macorini, and Bassam Izzuddin. Efficient 3-D modelling of punching shear failure at slab-column connections by means of nonlinear joint elements. *Engineering Structures*, 197:109372, 2019.
- [29] Francesco Cavagnis, Miguel Fernández Ruiz, and Aurelio Muttoni. Shear failures in reinforced concrete members without transverse reinforcement: An analysis of the critical shear crack development on the basis of test results. *Engineering Structures*, 103:157–173, 2015.
- [30] Francesco Cavagnis. *Shear in reinforced concrete without transverse reinforcement: from refined experimental measurements to mechanical models*. PhD thesis, EPFL – École polytechnique fédérale de Lausanne, 2017.
- [31] Jaime Mata-Falcón, Severin Haefliger, Minu Lee, Tena Galkovski, and Nicola Gehri. Combined application of distributed fibre optical and digital image correlation measurements to structural concrete experiments. *Engineering Structures*, 225, 2020.
- [32] Raffaele Cantone, Miguel Fernández Ruiz, and Aurelio Muttoni. A detailed view on the rebar-to-concrete interaction based on refined measurement techniques. *Engineering Structures*, 226, 2021.
- [33] Severin Haefliger, Jaime Mata-Falcón, and Walter Kaufmann. Application of distributed optical measurements to structural concrete experiments. In *SMAR 2017 Proceedings*, volume 159, 2017.

-
- [34] Jack J Poldon, Neil A. Hoult, and Evan C. Bentz. Distributed Sensing in Large Reinforced Concrete Shear Test. *ACI Structural Journal*, 116(5):235 – 245, 2019.
- [35] Zachary Broth and Neil A. Hoult. Dynamic distributed strain sensing to assess reinforced concrete behaviour. *Engineering Structures*, 204:110036, 2020.
- [36] Correlated Solutions. *Vic-3D 2010, Reference Manual*. 2010.
- [37] Luna Technologies Inc. *Optical Backscatter Reflectometer 4600 User Guide*. Luna Technologies, Blacksburg, VA, 2013.
- [38] Miguel Fernández Ruiz, Aurelio Muttoni, and Juan Sagaseta. Shear strength of concrete members without transverse reinforcement: A mechanical approach to consistently account for size and strain effects. *Engineering Structures*, 99:360–372, 2015.
- [39] Francesco Cavagnis, Miguel Fernández Ruiz, and Aurelio Muttoni. An analysis of the shear-transfer actions in reinforced concrete members without transverse reinforcement based on refined experimental measurements. *Structural Concrete*, 19(1):49–64, 2017.
- [40] Francesco Cavagnis, Miguel Fernández Ruiz, and Aurelio Muttoni. A mechanical model for failures in shear of members without transverse reinforcement based on development of a critical shear crack. *Engineering Structures*, 157:300–315, 2018.
- [41] SAP2000. CSI Analysis Reference Manual. 2017.
- [42] Aurelio Muttoni and Miguel Fernández Ruiz. Champs de contraintes pour le béton structural. *Tracés*, 133(5):17–21, 2007.
- [43] Aurelio Muttoni and Miguel Fernández Ruiz. The levels-of-approximation approach in MC 2010: Application to punching shear provisions. *Structural Concrete*, 13(1):32–41, 2012.

Chapter 5

Enhancing punching strength and deformation capacity of flat slabs

This chapter is the postprint version of the article *Enhancing punching strength and deformation capacity of Flat Slabs*, published in the journal *ACI Structural Journal* in September 2019.

The authors of the publication are Raffaele Cantone (PhD Candidate), Dr. Miguel Fernández Ruiz (Senior lecturer and thesis co-director), Jan Bujnak (Research and Development manager in Peikko) and Prof. Aurelio Muttoni (thesis director). The complete reference is the following:

Cantone R., Fernández Ruiz M., Bujnak J., Muttoni A. Enhancing punching strength and deformation capacity of flat slabs. *ACI Structural Journal*. Vol. 116(5). pp. 261-274. 2019.

The experimental tests presented in this chapter were performed in IBETON as part of a private project funded by Peikko. This work was developed by the first author (Raffaele Cantone) under the supervision of Dr. Miguel Fernández Ruiz and Prof. Aurelio Muttoni (thesis director), who contributed thoroughly in the analysis of test results and to the theoretical developments of this manuscript.

The main contributions of Raffaele Cantone with respect to the production of this chapter were the following:

- Perform an experimental programme including eleven axisymmetric slab tests for the analysis of the punching resistance of slab-column connections.
- Investigation of a novel system to efficiently reinforce slabs against punching shear by using large-diameter double-headed studs acting as shear dowels.
- Analysis and discussion of the test results.
- Proposal of a design approach accounting for the contribution of dowelling forces, consistent with the main principles of the Critical Shear Crack Theory.
- Production of the figures and tables included in the article.
- Preparation of the manuscript of the article.

Abstract

Punching reinforcement systems have significantly developed in recent years as they allow enhancing the punching resistance of slab–column connections as well as their deformation capacity. These systems, with varying geometry and layout, normally consist of vertical or inclined shear reinforcement with both ends anchored on the compression and tension side of the slab. For very high levels of load, when even common punching reinforcement systems cannot safely ensure the transfer of loads, steel shear heads are usually embedded in the slab to enhance the resistance of the connection. Yet, shear heads might be expensive and difficult to place in construction sites. Following the principle of the dowel action of the compression reinforcement, this paper introduces a novel system to efficiently reinforce slabs against punching shear by using large-diameter double-headed studs acting as shear dowels. This system enhances the performance of shear-reinforced slabs with respect to conventional solutions and might be an efficient alternative to shear heads for a large number of practical situations. The system is validated by means of a specific experimental program including 11 axisymmetric punching tests on interior slab–column connections. The results demonstrate not only the increase of the punching strength but also of the deformation capacity of the connection. It is also shown that the system can be consistently designed accounting for the dowelling forces by making use of the theoretical frame of the Critical Shear Crack Theory (CSCT), allowing to understand the activation of the shear dowels on the basis of the deformation of the member.

5.1 Introduction

Despite the redundancy and robustness in bending of reinforced concrete flat slabs, these structural elements include sensitive regions in which stress concentrations may occur due to the interaction between high flexural and shear demands at the slab–column connections, leading to potentially brittle failure in punching. In the last 60 years, significant improvements on the understanding of the mechanics involved in punching shear failures of slab–column connections have been achieved, comprising both experimental and analytical works [1, 2]. Failures in punching of slabs without transverse reinforcement occur by development of a conical failure surface originated at the supported area, Figure 5.1a. In actual continuous slabs supported on columns, these shear failures usually occur at load levels below that of the flexural resistance of the slab [3, 4] and develop in a brittle manner. To enhance the performance of slab–column connections, punching shear reinforcement is usually arranged as transverse reinforcement in the form of stirrups or headed studs. Failure can still occur in punching by crushing of the concrete struts, Figure 5.1b, development of a conical failure surface within the shear-reinforced area, Figure 5.1c, or by punching outside the shear-reinforced area, Figure 5.1d. In any of these cases, the strength and deformation capacity of the slabs can be significantly increased by allowing for redistributions of internal forces and further activating membrane action [3, 4].

The increase on the performance of shear-reinforced slabs is nevertheless limited by the crushing of the compression struts (depending significantly on the anchorage and detailing rules of the punching reinforcement [5]), which defines the maximum achievable punching strength for a given system. For higher load levels, and when increasing the dimensions of the slab and column are not possible, it is normally necessary to embed steel shear heads within the slab (one instance of steel shear head is shown in Figure 5.1e). Nevertheless, shear heads also present some drawbacks – for instance, the relative high cost and the increased difficulties during construction.

Within this context, in this paper a new punching shear reinforcing system is introduced, allowing to significantly enhance the strength and deformation capacity of slab–column connections but without the need of arranging embedded shear heads. The system uses headed shear heads in-

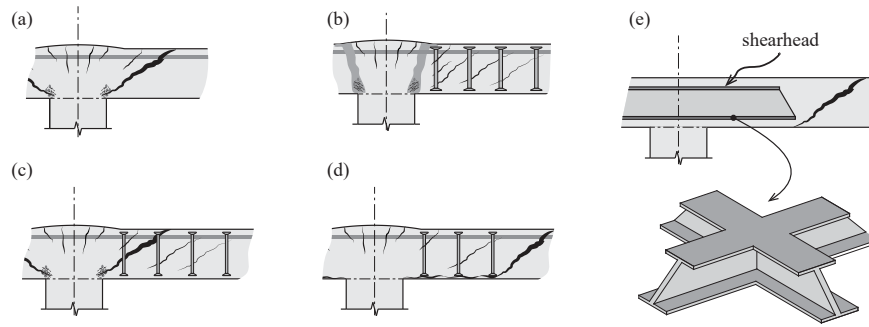


Figure 5.1: Punching failures of flat slabs: (a) members without shear reinforcement; (b) crushing of concrete; (c) cracking development with shear-reinforced zone; (d) punching outside shear-reinforced zone and (e) example of steel shear head embedded in slab.

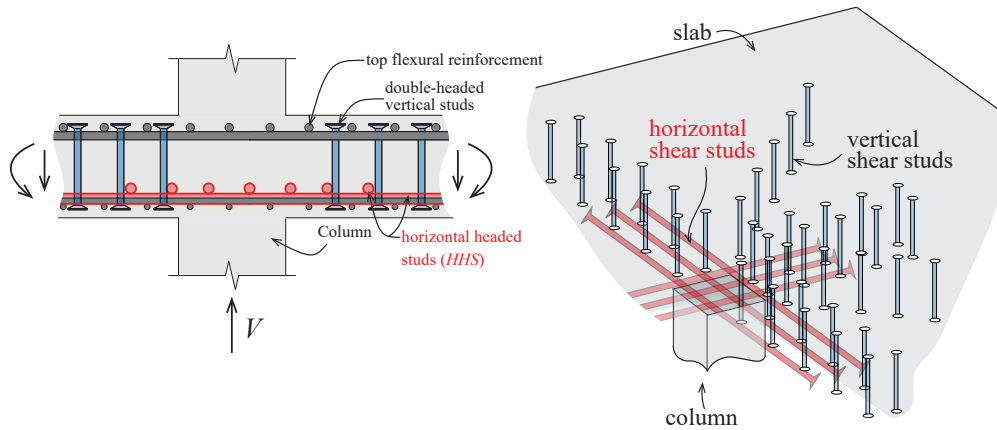


Figure 5.2: Arrangement of innovative shear-reinforcing system with horizontal shear studs.

stalled in a conventional manner (perpendicular to the slab plane) combined with a second family of large-diameter shear studs arranged horizontally in the compression side of the slab (parallel to the slab plane) to activate them as dowel reinforcement (refer to Figure 5.2). The idea grounding this innovative punching reinforcement solution is based on the capacity of the reinforcement in the compression side of the slab to efficiently transfer shear forces as a dowel. This capacity, demonstrated experimentally in many cases for the integrity reinforcement during the post-punching behaviour of flat slabs [6–8], has also been shown to be a potential contribution for beams in shear [9, 10]. In this paper, the results of a test program on 11 slab specimens are presented, comparing the performance of slab-column connections without any shear reinforcement, with conventional double-headed studs and with the innovative punching reinforcing system. The tests are performed on full-scale specimens with different mechanical slenderness (distance between load introduction points and axis of the column divided by the effective depth of the slab) so as to investigate various realistic situations. The enhanced performance is demonstrated, as well as the maximum level of strength that can be attained with this system. On that basis, a consistent model for its design is presented based on the Critical Shear Crack Theory (CSCT). To that aim, the mechanical model for this theory [11, 12] is adapted accounting for the contribution of the horizontal studs activated as dowel reinforcement. This approach is shown to predict the strength of the test results in a consistent manner.

Research significance

Systems to reinforce against punching shear in slab–column connections have remained similar in concept since long, by arrangement of a transverse reinforcement anchored in the compression and tension sides of the slab. When their maximum capacity is attained and the geometry of the slab and of the column cannot be modified, relatively expensive solutions as embedded shear heads have to be used. In addition, in some cases, an enhancement of the deformation capacity is required (in seismic areas, for instance). This paper introduces an innovative solution where the arrangement of a shear head is replaced by a number of large-diameter horizontal shear studs in the compression side of the slab. This solution, significantly more competitive from an economic perspective, allows enhancing the performance of shear-reinforced slab–column connections both in terms of their strength and deformation capacity. The system can thus constitute an interesting and economic alternative to conventional punching shear reinforcing solutions.

5.2 Experimental program

An experimental program on 11 full-size reinforced concrete slabs was carried out in the Structural Concrete Laboratory of École Polytechnique Fédérale de Lausanne (Switzerland). The experimental program included two reference tests without shear reinforcement (PC23 and PC25), two reference tests with standard double-headed vertical (perpendicular to the slab plane) studs (PC24 and PC26), and seven tests with the innovative solution investigated, combination of standard vertical double-headed bars and large-diameter horizontal double-headed bars in the compression face of the slab (PP10 and PP12 to PP17). The geometry of the specimens and loading conditions were also selected to allow direct comparisons to four experimental tests already performed by the authors [13] (PV1, PL1, PL6, and PL7).

5.2.1 Main parameters and test setup

All members were square in plan and with a side dimension of 3000 mm (9.84 ft). The nominal thickness was also constant for all tests and equal to 250 mm (9.84 in.). Loads were introduced at eight points (refer to Figure 5.2) by means of four hydraulic jacks with a total capacity of 4×2.5 MN (4×562 kip). The jacks transferred their load by means of four 75 mm (2.95 in.) steel rods to steel spreader beams, supported each on two loading plates $200 \times 200 \times 40$ mm ($7.87 \times 7.87 \times 1.57$ in.). Three different load introduction radii r_q (Figure 5.4), ranging from 765 to 1505 mm (2.51 to 4.94 ft), were investigated (refer to Table 5.1) representing slab slenderness L/d between 16 and 32 (refer to Figure 5.4a). This variation allowed investigation on the response of the slab–column connections for rather slender to rather squat flat slabs. The slab was finally supported on a central steel column of variable dimensions (refer to Figure 5.4a and Table 5.1). A thin layer of plaster was placed between the steel column and the slab to allow for a distributed load introduction.

All slabs were cast with normal-strength concrete whose compressive strength at the day of testing ranged between 24.9 and 37.0 MPa (3.61 and 5.37 ksi), (average of three compressive tests on 160×320 mm [6.3×12.6 in.] concrete cylinders); refer to the details in Table 5.1. The maximum aggregate size was 16 mm (0.63 in.) for all test specimens. The flexural reinforcement consisted of hot-rolled ($d_b = 20$ mm [0.78 in.]) reinforcing bars with a well-defined yield plateau for the top (tension) side spaced at 100 mm (3.94 in.). The nominal effective depth ($d_{nom} = 210$ mm [8.27 in.]) and the flexural reinforcement ratio ($\rho_l = 1.50\%$) were kept constant for all specimens. This reinforcement amount was selected to have a large flexural capacity and to promote failures in punching shear [11]. After testing, specimens were saw-cut and the actual effective depth was measured; refer to Table 5.1 for details. Cold-worked ($d_b = 14$ mm [0.55 in.]) bars (without a clear yield plateau) were used on the bottom (compression) side with a constant spacing of 100

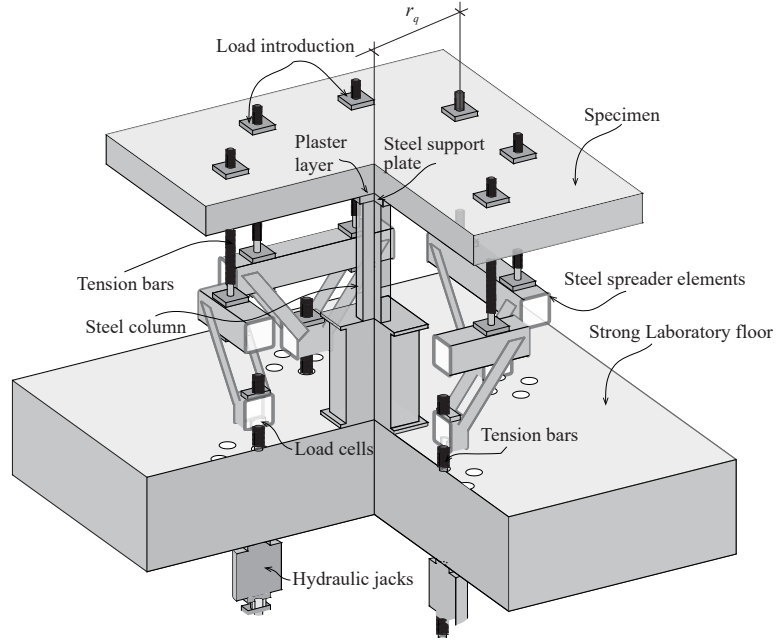


Figure 5.3: View of test setup.

mm (3.94 in.). For all slabs with shear reinforcement (refer to Figure 5.4b), double-headed vertical studs were arranged following a quasi-radial layout (refer to material details in Table 5.2). The nominal radial distance between the column edge and the first stud was $s_0 = 80$ mm (3.15 in.), while the radial distance between consecutive studs s_1 ranged between 105 and 160 mm (4.13 and 5.91 in.) (refer to the details in Table 5.2). The amount of shear reinforcement ρ_w (refer to the definition in Table 5.1) varied between 0.93% and 1.08% (refer to the details in Table 5.1) and was selected to attain the maximum punching resistance due to crushing of concrete between the column edge and the first perimeter of shear reinforcement [13]. To fix the position of the vertical double-headed shear studs, 5×40 mm (0.19 \times 0.78 in.) thin steel plates were welded to the bottom head of the shear studs. Details on the number of radii, studs per radius, and yield strength can be found in Table 5.2 for each specimen. The nominal concrete cover of the studs $c_{nom} = 20$ mm (0.79 in.) was kept constant for all specimens.

5.2.2 Horizontal studs

In addition to the conventional vertical shear studs, seven slabs (named PP) were equipped with additional double-headed studs installed horizontally (refer to Figure 5.5a). The horizontal studs were aimed to act as shear dowels with the anchorage heads located outside of the punching failure region [7]. The choice of horizontal studs allows for relatively short bar dimensions so as to allow preassembling the horizontal and vertical studs and ease placement during construction. The properties, head dimensions, and mechanical performance of this additional longitudinal reinforcement were the same as that of vertical shear studs (steel class B500B according to EN 10080 [14]) and can be consulted in Table 5.2. These bars had a total length of 1200 mm (3.94 ft) and were arranged with a constant spacing ranging between 80 and 100 mm (3.15 and 3.94 in.). The length of the horizontal studs was selected to locate the heads of the bars outside of the punching region. Details on the layout of these bars can be found in Figure 5.5c and Table 5.3, together with the location of the center of gravity of these horizontal studs represented by parameter c_d (defined in Figure 5.5b), which represents the distance of the interface between the two layers of horizontal studs with respect to the compression side.

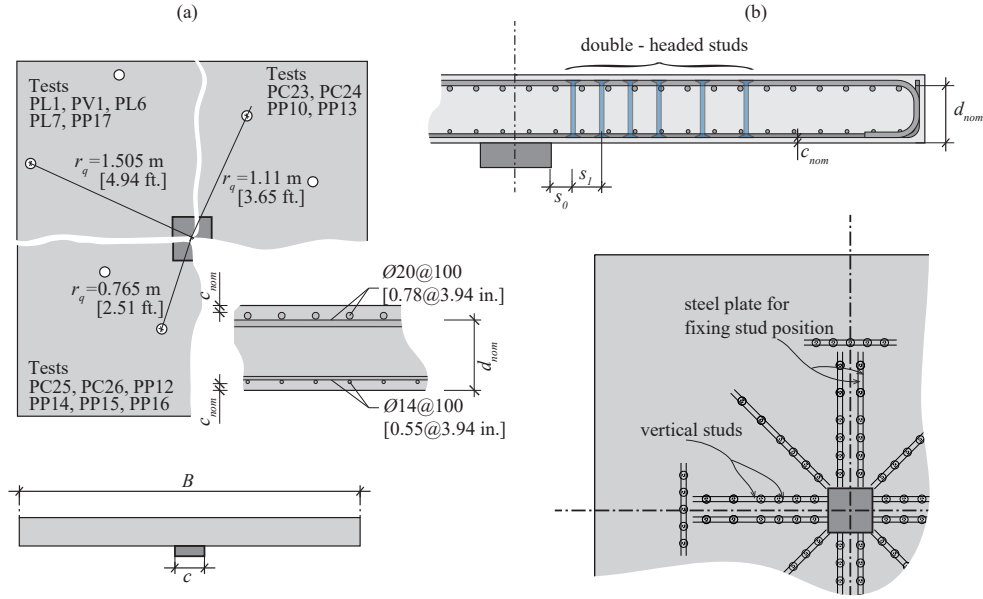


Figure 5.4: Test specimens: (a) geometric parameters and (b) arrangement of double-headed studs.

Table 5.1: Main parameters of test series

Slab	B m (ft)	c mm (in.)	r_q m (ft)	d mm (in.)	f_y MPa (ksi)	f_c MPa (ksi)	ρ %	ρ_w^* %
PL1	3.0 (9.84)	130 (5.12)	1.505 (4.94)	193 (7.60)	583 (84.6)	36.2 (5250)	1.63	–
PV1	3.0 (9.84)	260 (10.2)	1.505 (4.94)	210 (8.27)	709 (102)	34.0 (4900)	1.50	–
PL6	3.0 (9.84)	130 (5.12)	1.505 (4.94)	198 (7.79)	583 (84.6)	36.6 (5300)	1.59	1.01
PL7	3.0 (9.84)	260 (10.2)	1.505 (4.94)	197 (7.76)	519 (75.3)	35.9 (5200)	1.59	0.93
PC23	3.0 (9.84)	260 (10.2)	1.11 (3.65)	212 (8.34)	570 (82.7)	34.6 (5020)	1.48	–
PC24	3.0 (9.84)	260 (10.2)	1.11 (3.65)	209 (8.22)	570 (82.7)	37.0 (5370)	1.50	1.07
PC25	3.0 (9.84)	260 (10.2)	0.765 (2.51)	203 (7.99)	586 (85.0)	34.8 (5050)	1.55	–
PC26	3.0 (9.84)	260 (10.2)	0.765 (2.51)	204 (8.03)	586 (85.0)	31.9 (4630)	1.54	1.08
PP10	3.0 (9.84)	260 (10.2)	1.11 (3.65)	207 (8.15)	570 (82.7)	24.9 (3610)	1.52	0.92
PP12	3.0 (9.84)	260 (10.2)	0.765 (2.51)	212 (8.35)	569 (82.5)	29.7 (4300)	1.48	1.07
PP13	3.0 (9.84)	260 (10.2)	1.11 (3.65)	208 (8.19)	569 (82.5)	27.8 (4030)	1.51	1.07
PP14	3.0 (9.84)	260 (10.2)	0.765 (2.51)	214 (8.43)	557 (80.8)	34.9 (5060)	1.47	1.06
PP15	3.0 (9.84)	260 (10.2)	0.765 (2.51)	206 (8.11)	570 (82.7)	28.1 (4080)	1.53	1.08
PP16	3.0 (9.84)	260 (10.2)	0.765 (2.51)	213 (8.39)	557 (80.8)	35.0 (5080)	1.47	1.06
PP17	3.0 (9.84)	130 (5.12)	1.505 (4.94)	206 (8.11)	570 (82.7)	29.4 (4260)	1.52	1.56

* ρ_w is defined by considering the reference perimeter at $0.5d_{nom}$ from the edge of the column according to the following equation: $\rho_w = \frac{A_{sw,i} n_r}{u \cdot s}$, where u is the length of the perimeter at a distance $0.5d_{nom}$ from the edge of the column.

$A_{sw,i}$ is the cross-sectional area of a double-headed stud and $s = s_0 + s_1/2$

Table 5.2: Main parameters of shear studs

Slab	d_b	n_r	n_s	s_0	s_1	f_y
	m (in.)					
PL6	14 (0.55)	12	6	80 (3.15)	160 (6.30)	519 (75.3)
PL7	14 (0.55)	16	7	80 (3.15)	160 (6.30)	536 (77.7)
PC24	16 (0.63)	12	6	80 (3.15)	105 (4.13)	523 (75.9)
PC26	16 (0.63)	12	5	80 (3.15)	105 (4.13)	–
PP10	16 (0.63)	12	6	80 (3.15)	150 (5.91)	–
PP12	16 (0.63)	12	6	80 (3.15)	105 (4.13)	559 (81.1)
PP13	16 (0.63)	12	6	80 (3.15)	105 (4.13)	559 (81.1)
PP14	16 (0.63)	12	5	80 (3.15)	105 (4.13)	557 (80.8)
PP15	16 (0.63)	12	5	80 (3.15)	105 (4.13)	555 (80.5)
PP16	16 (0.63)	12	5	80 (3.15)	105 (4.13)	557 (80.8)
PP17	16 (0.63)	12	6	80 (3.15)	105 (4.13)	555 (80.5)

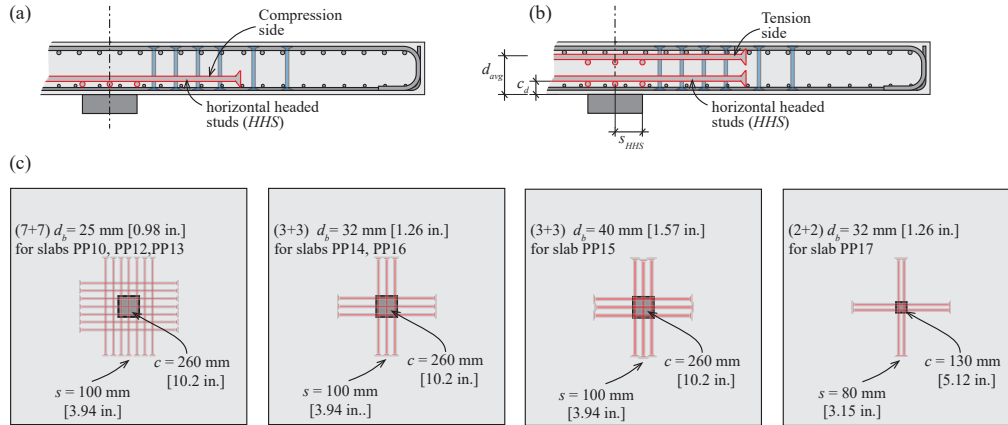


Figure 5.5: Shear dowels: (a) shear reinforcing system arrangement in bottom (compression) side; (b) shear reinforcing system arrangement in bottom (compression) and top (tension) side; and (c) amount of reinforcing bars, spacing, and reinforcing bar diameter for each specimen.

Table 5.3: Layout of shear reinforcing system

Slab	Description	s_1	s_{HHS}	c_d
		mm (in.)	mm (in.)	mm (in.)
PL6	Vertical shear studs (<i>VSS</i>)	160 (6.30)	–	–
PL7	<i>VSS</i>	160 (6.30)	–	–
PC24	<i>VSS</i>	105 (4.13)	–	–
PC26	<i>VSS</i>	105 (4.13)	–	–
PP10	<i>VSS</i> and <i>HHS</i> bars (top and bottom side)	150 (5.91)	100 (3.94)	73.0 (2.87)
PP12	<i>VSS</i> and <i>HHS</i> bars (top and bottom side)	105 (4.13)	100 (3.94)	59.0 (2.32)
PP13	<i>VSS</i> and <i>HHS</i> bars (bottom side)	105 (4.13)	100 (3.94)	59.0 (2.32)
PP14	<i>VSS</i> and <i>HH</i> bars (bottom side)	105 (4.13)	100 (3.94)	66.0 (2.60)
PP15	<i>VSS</i> and <i>HHS</i> bars (bottom side)	105 (4.13)	100 (3.94)	74.0 (2.91)
PP16	<i>VSS</i> and <i>HHS</i> bars (bottom side)	105 (4.13)	100 (3.94)	66.0 (2.60)
PP17	<i>VSS</i> and <i>HHS</i> bars (bottom side)	105 (4.13)	100 (3.94)	66.0 (2.60)

Three of these slabs (PP10, PP12, and PP14) were also reinforced with additional horizontal double-headed studs on the tension side; refer to Figure 5.5b and Table 5.4. This additional reinforcement was arranged to investigate their effect on the load-carrying capacity (studs acting predominantly as dowel and/or flexural reinforcement). In Table 5.4, when these bars are arranged, the flexural reinforcement amount is increased accordingly.

5.2.3 Test results

The measured load-rotation curves (the self-weight of the specimens is included in the resultant shear force) are presented in Figure 5.6 (both for the 11 specimens tested in this program and for the four additional reference specimens tested on other series but with the same geometric,

Table 5.4: Main parameters of shear reinforcing system

Slab	d_b	f_y	f_t	<i>HHS</i>	<i>HHS</i>	d_{avg}
	mm (in.)	MPa (ksi)	MPa (ksi)	bottom side	top side	mm (in.)
PP10	25 (0.98)	578 (83.8)	680 (98.6)	7+7 bars	7+7 bars	195 (7.7)
PP12	25 (0.98)	529 (76.7)	609 (88.3)	7+7 bars	7+7 bars	200 (7.9)
PP13	25 (0.98)	529 (76.7)	607 (88.0)	7+7 bars	–	–
PP14	32 (1.26)	534 (77.5)	629 (92.7)	3+3 bars	3+3 bars	203 (8.0)
PP15	40 (1.57)	576 (83.5)	690 (100)	3+3 bars	–	–
PP16	32 (1.26)	534 (77.5)	629 (92.7)	3+3 bars	–	–
PP17	32 (1.26)	504 (73.1)	623 (90.4)	2+2 bars	–	–

loading, and mechanical properties [13]). The rotation ψ , refer to Figure 5.6a, was measured by means of four inclinometers arranged along the two symmetry axes of the slab and approximately at the point of moment contraflexure (according to a linear-elastic calculation). The average of the four measured rotations was finally represented for the evaluation of the overall flexural behaviour (Figure 5.6). The saw-cuts of the specimens after testing are also presented in Figure 5.7. Failures for most tests occurred by punching at the slab-column connection prior to reaching the full development of a flexural mechanism. For one specimen (PP13), failure was controlled by bending, as delamination of the concrete cover in the compression face occurred, thus reducing the effective depth of the section. A similar failure mode controlled by delamination was also observed for specimen PP10, although a conical punching surface eventually developed (as can be seen in the saw-cut of Figure 5.7).

All reference slabs without shear reinforcement (PL1, PV1, PC23, and PC25) failed in a brittle manner by development of a localized shear crack. Reference slabs provided with vertical shear studs only (PL6, PL7, PC24, and PC26) failed in a more ductile manner developing a smeared cracking region between the column edge and the first perimeter of shear studs due to crushing of the concrete strut.

For the test specimens reinforced with a combination of vertical shear studs and longitudinal headed bars (tests PP10 and PP12 to PP17), a clear failure of the concrete strut between the column edge and the first perimeter of shear reinforcement was not observed, but rather a distributed inclined cracking within the region where horizontal headed bars were provided. This cracking was associated for most of the cases to large column penetrations and to the development of delamination cracks in the compression zone, exhibiting large deformation capacities prior to failure. The results are compared in Figure 5.8 with respect to the slenderness and reinforcement details of the specimens where the normalized strengths and the deformation capacities at maximum load are shown (to account for the differences on the concrete strength and effective depth of the members). The deformation capacity is presented in terms of the parameter ψ_R , which represents the average of the measured rotations (by means of four inclinometers) at maximum load. The influence of the slenderness on the response and strength of specimens without transverse reinforcement is shown in Figure 5.6a. It can be noted that reducing the mechanical slenderness (r_q/d) increases the flexural stiffness of the specimen and is associated with lower deformation capacities and higher punching shear strengths. This behaviour is in agreement with other experimental observations [15]. This response is also observed to be valid (even in a clearer manner) for the shear-reinforced specimens with headed studs as shown in Figure 5.6b.

With respect to the performance of the system, Figure 5.6c through Figure 5.6f and Figure 5.8 compare the response of the connection with respect to specimens without shear reinforcement or reinforced with conventional vertical studs only. In Figure 5.6c through Figure 5.6e, the results for the specimens with lower mechanical slenderness ($r_q/d=3.6$) are presented. A significant increase for the specimens with horizontal dowel studs is observed in terms of failure load (up to 250 to 270% of the failure load observed in the members without shear reinforcement) and of the deformation capacity (up to 700% of the value of specimens without shear reinforcement).

For the specimens with the highest mechanical slenderness and lowest column dimension ($r_q/d=7.2$; refer to Figure 5.6d and Figure 5.8), the system showed a similar behaviour with an enhanced performance both in terms of resistance and deformation capacity. For the tests with intermediate slenderness ($r_q/d = 5.3$; refer to Figure 5.6f), the resistance of the connection was increased when the influence of the compressive strength of concrete is accounted for (Figure 5.8). The deformation capacity was in any case notably increased.

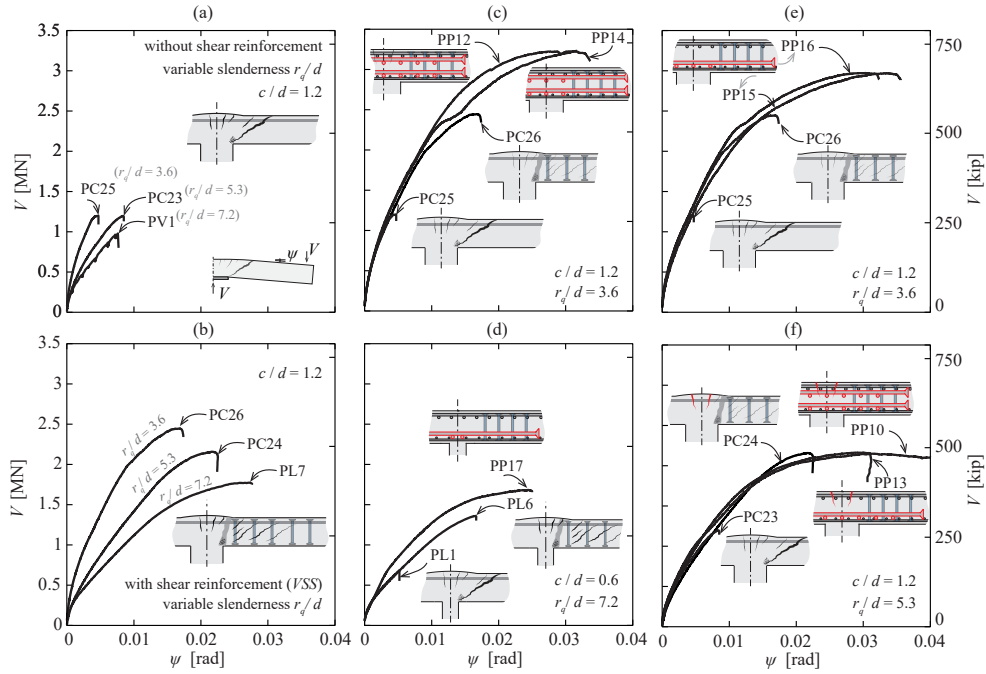


Figure 5.6: Load-rotation curves of specimens: (a) without shear reinforcement and variable slenderness; (b) with shear reinforcement and variable slenderness; (c) column size-slab depth ratio $c/d = 1.2$ and slab slenderness $r_q/d=3.6$; (d) column size-slab depth ratio $c/d=0.6$ and slab slenderness $r_q/d=7.2$; (e) column size-slab depth ratio $c/d=1.2$ and slab slenderness $r_q/d=3.6$; and (f) column size-slab depth ratio $c/d=1.2$ and slab slenderness $r_q/d=5.3$.

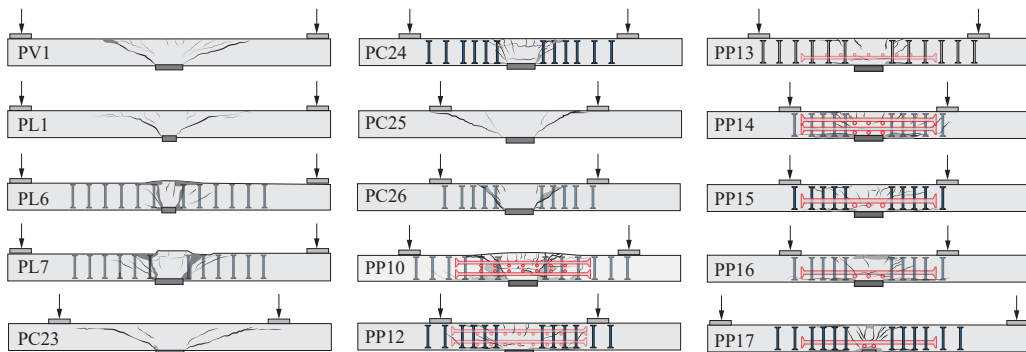


Figure 5.7: Saw-cuts of slabs along weak axis.

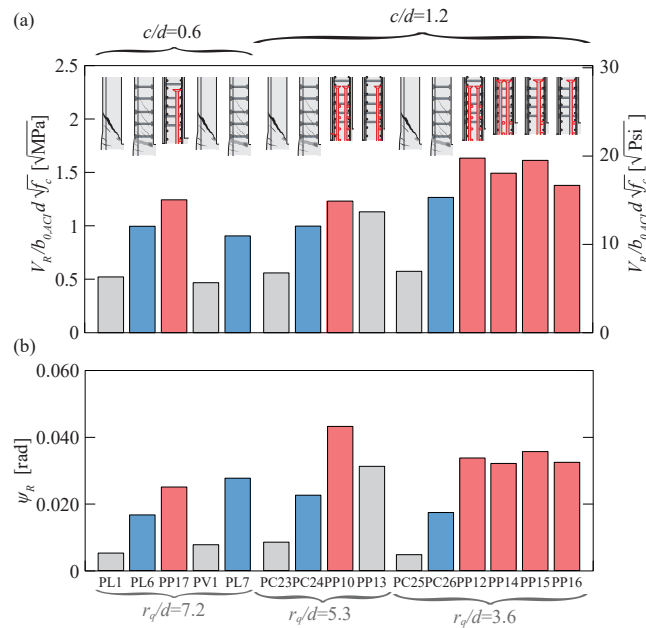


Figure 5.8: Comparison of test results: (a) punching strength; and (b) deformation capacity ψ_R at maximum load.

5.2.4 Activation of horizontal dowels

The enhanced performance of the specimens reinforced with the horizontal headed bars is justified by their activation as shear dowels, allowing to transfer a fraction of the total shear force. To investigate this phenomenon in detail, specific measurements were performed on these bars by means of strain gauges. Figures 5.9a–b show the location of these gauges glued on the top and bottom surface of the bars.

The experimental results for Specimen PP12 are shown in Figure 5.9c through Figure 5.9e. It can be noted that the gauges on the bottom side near the column were in compression while the gauges on the top side were in tension. Close to failure, significant plastic deformations were recorded in the bar near the column region as observed from the profiles of curvatures measured in Figure 5.9c. The opposite occurred for the gauges glued at a certain distance of the column, with tension on the bottom side and compression on the top side (the recorded strains being yet lower). These measurements clearly correspond to the expected profile for a dowelled bar with a point of contraflexure (refer to Figure 5.9c). It can be noted that the activation of the dowelling action was observed even for low levels of load, approximately 20% of the failure load, which corresponds to approximately 80% of the failure of the reference specimen without transverse reinforcement. This indicates that the dowelling action is already activated by the development of the inclined critical shear crack and increases during the test.

The activation of the dowelling action of the bars seems, however, to lead to an enhanced potential delamination of the concrete cover (refer to Figure 5.10). During the tests, such delamination cracks were observed in Specimens PP10 and PP13 at approximately 70% of the failure load. In general, specimens that for a given level of shear force are subjected to larger bending moments were more prone to develop such delamination failures. This was the case of Specimens PP10 and PP13, where the column size was large and the mechanical slenderness was relatively high ($r_q/d=5.3$) and thus large bending moments developed. For the most slender slabs ($r_q/d=7.2$), the column was relatively small and the bending moments were thus moderate for the same level of shear force (and delamination was not governing). For the most squat members ($r_q/d=3.6$), the bending moments were relatively low, thus minimizing such risk. With respect to the horizontal

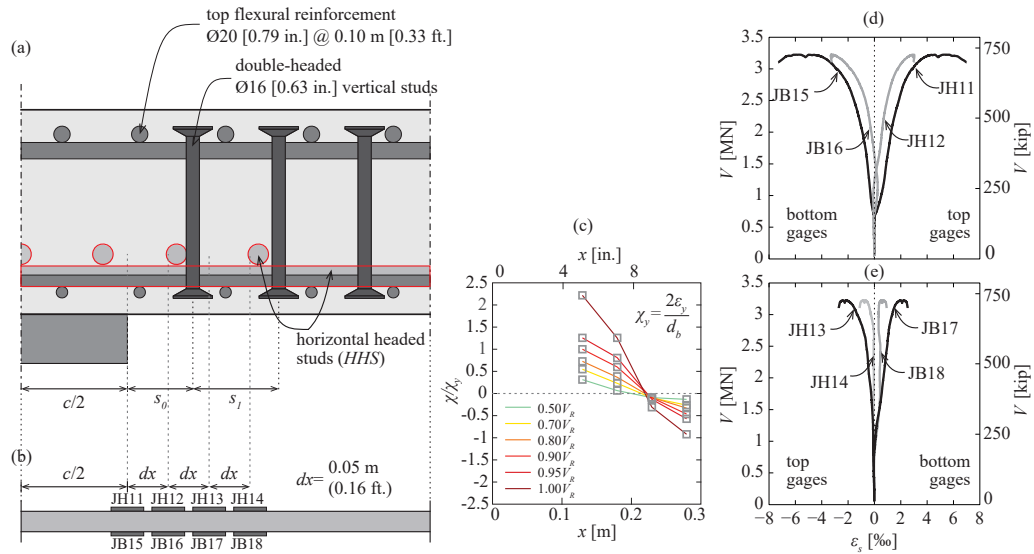


Figure 5.9: Activation of dowel reinforcement for test PP12: (a) location of *HHS* bar where strain measurements were performed (in red); (b) location of strain measurements; (c) curvature profiles along shear dowel; (d)-(e) load-steel strains curves of gauges shown in Figure (b).

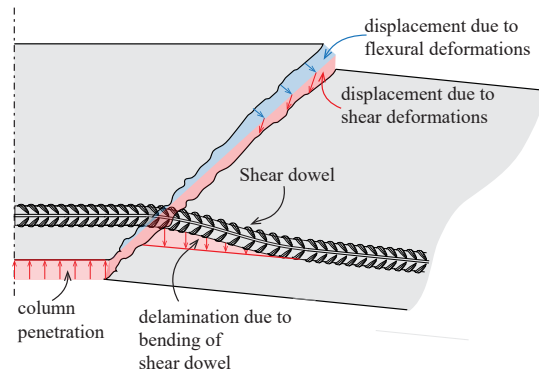


Figure 5.10: Dowelling of horizontal shear studs and delamination of concrete cover and assumed kinematics according to Simões et al. [16].

studs at the (top) tension side of the slab, they contribute as flexural reinforcement, enhancing the flexural stiffness of the slab, and also contribute carrying shear due to dowelling action. The former effect (enhancement of flexural stiffness) is directly considered in the load-rotation curve of the specimen, while the latter (dowelling contribution) is implicitly considered in the failure criterion [16]. The pertinence of this consideration is confirmed by the analysis of the three tests conducted with additional horizontal studs in the tension side (presented in the next section).

5.3 Design for punching of slab–column connections accounting for dowelling action

According to the experimental results, the bottom horizontal shear studs were carrying a significant fraction of the shear force, enhancing both strength and deformation capacity of the connections. This contribution can be consistently considered in combination with the other potential shear-transfer actions of concrete [16] and of the transverse steel [12]. To that aim, the theoretical

framework of the CSCT will be used in the following.

5.3.1 Basic assumptions of CSCT

A complete description of the mechanical model of the CSCT can be found elsewhere [11, 12, 16]. For members without transverse reinforcement (Figure 5.11a), the theory considers that failure is governed by the development of a critical shear crack whose kinematics are defined by two parameters [16]: the rotation of the slab ψ and the penetration of the failure surface δ . Because at failure both parameters are correlated [16, 17], the complete mechanical model can be eventually expressed in terms of the rotation of the slab [11]. The failure load can on this basis be calculated by intersecting the load-rotation response of the slab (defining the shear demand for a given level of deformation) with the failure criterion of concrete (defining the shear resistance for a given level of deformation); refer to Figure 5.11a. According to Muttoni [11], a suitable expression for the failure criterion can be adopted as follows (a detailed justification of this expression can be found elsewhere [16]):

$$V_c = 0.75 \frac{\sqrt{f_c} b_0 d}{1 + 15 \frac{\psi d}{d_g + d_{g0}}} \quad (5.1)$$

for SI units (m, MPa, and MN). For customary units (psi, in., and kip), parameter 0.75 has to be replaced by 9. The parameter b_0 refers to the length of a control perimeter located at $d/2$ from the edge of the column, d to the effective depth of the slab, d_g to the maximum aggregate size, and d_{g0} to a reference aggregate size of 16 mm (0.63 in.). When shear reinforcement is arranged [12], it is progressively activated by the deformation of the slab; refer to Figure 5.11b. As for the case of members without transverse reinforcement, the failure load can be calculated by intersection of the load-rotation response of the slab and the corresponding failure criterion. In this case, the failure criterion has to also account for the contribution of the transverse reinforcement [12] (refer to Figure 5.11b):

$$V_n = V_c + V_s \quad (5.2)$$

This reinforcement thus increases both the strength and deformation capacity of the slab–column connection (Figure 5.11b). Other than by intercepting the transverse reinforcement, failure can occur by punching outside the shear-reinforced area [12], Figure 5.11c, or by crushing of the first concrete strut [12, 13] (Figure 5.11d). For the former of the two, the failure criterion of concrete is considered along a suitable control perimeter located outside of the shear-reinforced area and accounting for a reduced effective depth (considering the location of the anchorage region of the transverse reinforcement). For the latter, the strength of the concrete is normally assessed by multiplying the failure criterion of concrete (Figure 5.11a) by a suitable factor, whose value depends on the anchorage properties of the shear reinforcement and on its detailing rules [5, 13, 18]:

$$V_{n,max} = \lambda V_c(\psi) \quad (5.3)$$

For the case of vertical shear studs, a typical value [19] of parameter λ is 3.0, while for stirrups, this value normally reduces to 2.6. It has to be noted that V_c depends on rotation ψ , which also increases in the case of shear-reinforced slabs. The maximum shear strength $V_{n,max}$ is thus smaller than λ times V_c of a slab without shear reinforcement.

5.3.2 Consideration of dowelling action on punching shear response

The model of the CSCT can be extended to shear-reinforced slabs by accounting for the contribution of the dowelled horizontal bars to carry shear forces. This contribution is originated by

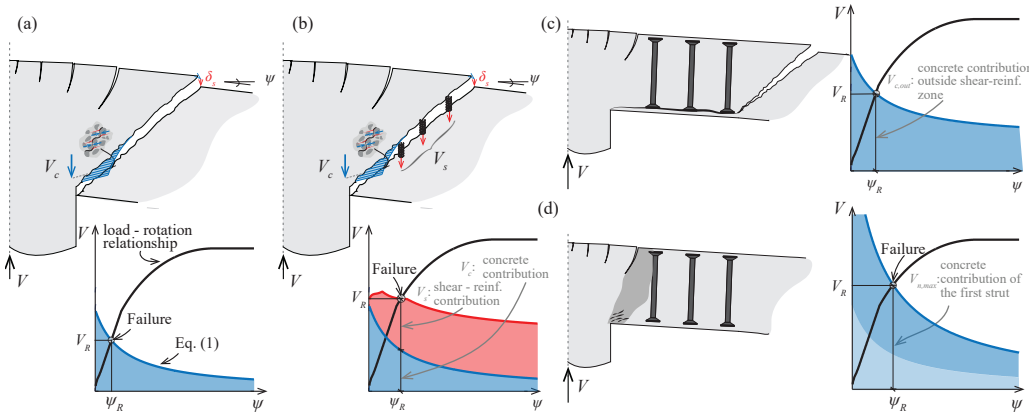


Figure 5.11: Shear-carrying actions in slab-column connections: (a) contribution of concrete; (b) contribution of shear reinforcement; (c) contribution of concrete for failures outside shear-reinforced zone; and (d) maximum punching capacity due to crushing of first strut.

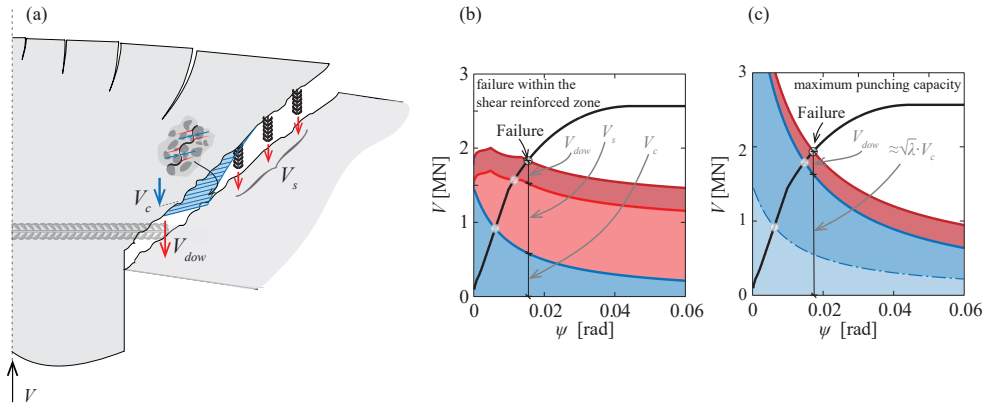


Figure 5.12: (a) kinematics of critical shear crack; contributions of shear-carrying mechanisms accounting for activation of shear dowels; (b) punching failure crossing shear-reinforced zone; and (c) maximum punching capacity due to crushing of first compression strut.

the penetration of the supported area (Figure 5.12a), which bends the horizontal bars over the column region (such penetration occurs even for low levels of rotation at failure [16]). Figure 5.13a presents the corresponding failure mechanism, which yields to the development of a delamination crack and also to the potential breakout of the concrete anchoring the dowel. On that basis, the failure criterion governed by the maximum punching capacity (governed by crushing of the concrete struts, Eq. 5.4) can be expressed as follows:

$$V_{n,max} = \lambda V_c + \sum V_{dow} \quad (5.4)$$

This equation reflects that a part of the shear force is not carried through the critical shear crack, but directly transferred by the dowelled bars (refer to 5.12a). The bars contributing to dowelling action are assumed to be only those located directly over the supported area, and the total shear force carried by them corresponds to the sum of all sections where the bar is suitably anchored (in the present case, two sections per bar; refer to Figure 5.13c). The calculation of the shear force carried by dowelling of these bars can be consistently performed accounting for equilibrium and kinematical conditions. This will be presented in the following.

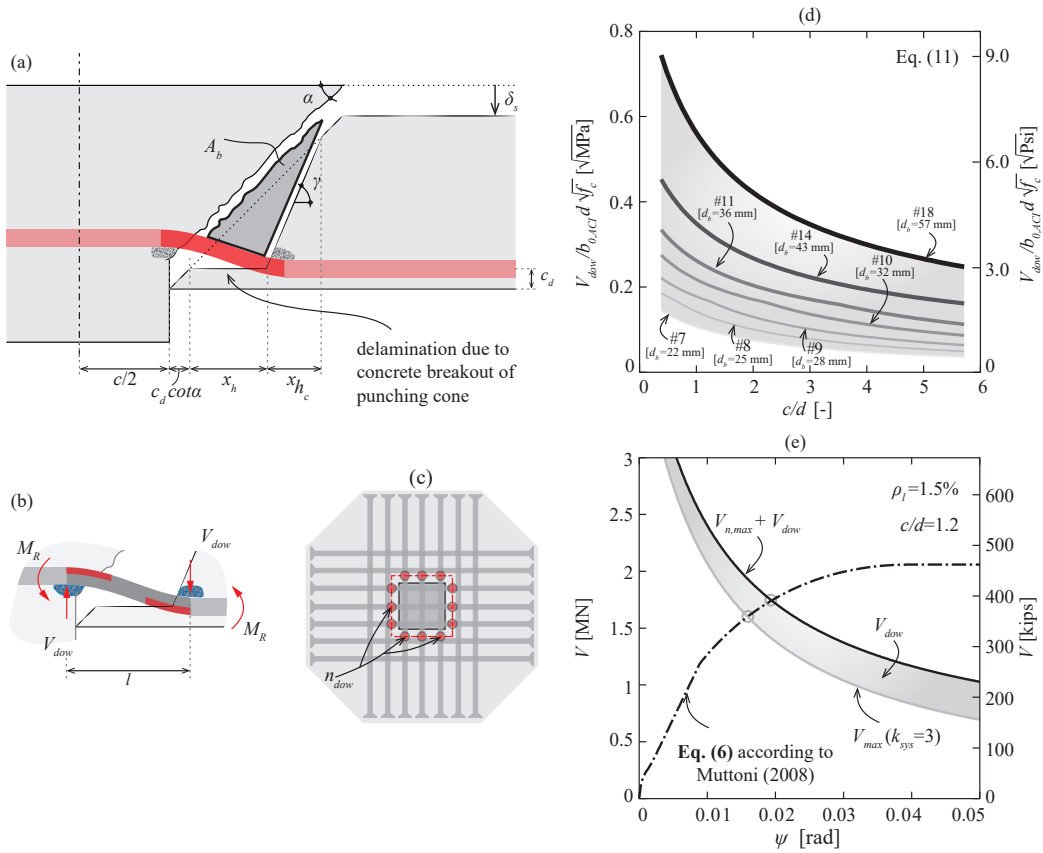


Figure 5.13: Assumed failure mechanism and kinematics: (a) parameters; (b) mechanical behaviour of dowel; (c) definition of number of intercepted sections n_{dow} ; (d) calculated dowel action contribution as function of column size–slab depth ratio; and (e) calculation of failure load by means of quadrilinear law and modified failure criterion.

Geometry and kinematics of horizontal shear dowel – The geometrical parameters defining the activation mechanism of the dowelled bars are presented in Figure 5.13a. The bar is dowelled between two hinges, assumed to reach their plastic condition. Such a plastic state was systematically confirmed by the measurements performed in the bars near the column region (as previously presented) and is assumed as a simplification for the outer hinge. Additionally, the assumed failure mechanism considers the potential presence of a delamination crack (observed in the tests as previously discussed) as well as the potential breakout of the concrete core of the slab. With respect to the breakout cracks, they were also clearly observed in the saw-cuts of the specimens; refer, for instance, to Specimens PP10, PP12, or PP16 in Figure 5.7.

Capacity of plastic hinges – The capacity of the horizontal bars to transfer shear forces and bending moments is limited by the yield condition of the bar. The interaction between bending moment and shear force is evaluated by considering an equivalent square section [20]. This equivalent section has a size b_e , whose value yields the same bending resistance as that of a circular section:

$$M_R = d_{b,HHS}^3 \frac{f_y}{6} = b_e^3 \frac{f_y}{4} \rightarrow b_e = d_{b,HHS} \sqrt[3]{2/3} \quad (5.5)$$

When the section is subjected to a shear force V_{dow} , the required height h_τ to carry the shear force can be calculated assuming a Von Mises yield criterion for steel [21]:

$$h_\tau = \frac{V_{dow}}{b_e f_y} \sqrt{3} \quad (5.6)$$

Neglecting the axial force, the height of the plastic parts carrying the bending moment is:

$$h_f = \frac{b_e - h_\tau}{2} \quad (5.7)$$

In light of this, the plastic strength of the hinges results:

$$M_R = b_e h_f f_y (b_e - h_f) = \frac{b_e^3}{4} f_y \left(1 - 3 \frac{V_{dow}^2}{b_e^4 f_y^2} \right) = \frac{d_{b,HHS}^3}{6} f_y \left(1 - 5.15 \frac{V_{dow}^2}{d_{b,HHS}^4 f_y^2} \right) \quad (5.8)$$

expressing the interaction of the shear and bending capacity for the simplified section of the bar at the yield condition.

Equilibrium conditions of dowelled bar – Based on the geometry of the dowelled bar (Figure 5.13b), the equilibrium equation between acting dowel force (V_{dow}) and the plastic bending moment (M_R) can be established:

$$M_R = V_{dow} \frac{l}{2} \quad (5.9)$$

where parameter l refers to the distance between plastic hinges (Figure 5.13b), whose value can be calculated geometrically as:

$$l = c_d \cot \alpha + x_h + \frac{V_{dow}}{\phi f_{cc}} \quad (5.10)$$

For the calculation of the length of the plastic hinge (latter term in Eq. 5.10), it is estimated, according to Rasmussen [22], by assuming a confined concrete strength $f_{cc}=5f_c$ and an effective width equal to the bar diameter. The angle α of the critical shear crack is assumed as 45 degrees according to the test observations on the saw-cuts (Figure 5.7). As a result, by combining Eq. 5.8 and Eq. 5.9, it results:

$$\frac{d_{b,HHS}^3}{6} f_y \left(1 - 5.15 \frac{V_{dow}^2}{d_{b,HHS}^4 f_y^2} \right) = V_{dow} \frac{l}{2} \quad (5.11)$$

This expression allows calculating the dowelling force that can be transferred by a bar for a given

length of the dowelled zone.

Concrete breakout conditions – To determine the length for the dowelled zone, it has to be considered the maximum capacity of the core to resist the dowelling force. This capacity of the concrete is limited by the breakout of the concrete above the outer plastic hinge (Figure 5.13a). When the capacity of the core is high, large shear forces can be carried and the delamination length is small. On the contrary, when this capacity is low, the delamination length increases and the dowel capacity is limited. A detailed review of the concrete breakout capacity for such situation can be consulted elsewhere [6, 8]. Most design approaches to this phenomenon propose to calculate this contribution by assuming an effective tensile strength developing at the region of concrete breakout surface. This area can be calculated by projecting the concrete breakout surface (assuming an axisymmetric shape). Using the sinus theorem, the distance x_{hc} is equal to:

$$x_{hc} = \min \left(x_h \frac{\sin \alpha \cos \gamma}{\sin(\gamma - \alpha)}; (d - c_d) \cot \gamma \right) \quad (5.12)$$

where γ refers to the angle of the concrete breakout surface. To respect the dilatancy of the friction angle of concrete ϕ and to have a vertical shift of the breakout wedge (Figure 5.13a), the angle γ results [23]:

$$\gamma = \frac{\pi}{2} - \varphi \quad (5.13)$$

The dowel force that can be anchored per bar results:

$$V_{dow} = f_{ct,eff} A_{b,dow} \quad (5.14)$$

where $A_{b,dow}$ refers to the effective concrete area opposing to the force of one dowel [6, 8] (Figure 5.13a). This area is calculated as the projection in the plane of the slab of the breakthrough surface A_b (assumed as the total available area activated under the projection of $x_h + x_{hc}$) (Figure 5.13a), divided upon the number of dowelled sections n_{dow} (Figure 5.13c):

$$A_{b,dow} = \pi \frac{(r_c + c_d \cot \alpha + x_h + x_{hc})^2 - (r_c + c_d \cot \alpha)^2}{n_{dow}} \quad (5.15)$$

Consistently with the work of Fernández Ruiz et al. [12], the following equation is adopted for the evaluation of the effective tensile strength:

$$f_{ct,eff} \approx 0.6 f_{ct} \quad (5.16)$$

For the evaluation of f_{ct} , the influence of the concrete strength, aggregate size, and size effect shall be considered. This is proposed to be performed in the following manner

$$f_{ct} \approx 0.5 \sqrt{f_c} k_d \quad (5.17)$$

Expression in SI units (in case of customary units [psi], 0.5 has to be replaced by 6). In this equation, the term k_d accounts for size effect and can be evaluated as:

$$k_d = \frac{2.5}{1 + \frac{1}{5} \frac{d}{d_g + d_{g0}}} \leq 1.2 \quad (5.18)$$

The values of d_g and d_{g0} refer to, respectively, the maximum and reference aggregate sizes consistently with those defined in Eq. 5.1. Thus, the shear force that can be transferred by dowelling

action results eventually:

$$V_{dow} = 0.3\sqrt{f_c}k_d\pi \frac{(r_c + c_d \cot \alpha + x_h + x_{hc})^2 - (r_c + c_d \cot \alpha)^2}{n_{dow}} \quad (5.19)$$

using SI units (in case of customary units [psi], 0.3 has to be replaced by 3.6). The calculation of the maximum force that can be activated for a dowel can be performed by solving the set of Eq.s 5.9 and 5.19. It can be noted that it is a set of nonlinear equations and requires to be solved by means of numerical means.

Load–rotation relationship

For the calculation of the failure load and of its associated deformation capacity, the failure criterion previously discussed has to be intercepted by the load–rotation relationship of the slab; refer to Figure 5.12. To that aim, various approaches are possible [11, 24–26] and the estimate of the failure load can be considered as more accurate when more refined estimates of the actual behaviour of the slab are considered. In the following, the load–rotation response of the slab will be calculated on the basis of the integration of a quadrilinear moment–curvature law (one of the most accurate approaches available), as proposed by Muttoni [11]. In addition, the resistance will also be calculated by using the simplified parabolic load–rotation response developed by Muttoni [11] for practical purposes (derived on the basis of the quadrilinear expression but adopting a parabolic law (3/2 exponent) as a function of the ratio V/V_{flex}). With respect to the flexural reinforcement amount, it is determined on the basis of the actual effective depth (Table 5.2) and considering, when applicable, the contribution of the top layers of double-headed studs (Specimens PP10, PP12, and PP14); refer to d_{avg} in Table 5.3.

Comparison to test results

By using the failure criterion, Eq. 5.4, and the load–rotation relationship, the failure loads can be calculated. This is presented for all specimens in Figure 5.14 for the refined model (Eq. (6) in Muttoni [11]) as well as for the simplified load–rotation curve (Eq. (8) in Muttoni [11]). The figure shows that both models finely reproduce the test results, with a consistent agreement in the failure load. The average of the measured–to–calculated punching strength results is, respectively, 1.04 and 1.08 with a coefficient of variation ranging between 4.2 and 5.3% (refer to Table 5.5). These values show sound agreement, with even lower scatter than for similar analyses on other punching reinforcing systems [12, 13]. The calculated delamination length (Table 5.6) resulting from the previous equations also shows reasonable values in fine agreement with the observed location in the saw-cuts (Figure 5.7).

Table 5.5: Comparison of experimental and calculated punching strengths

Slab	$V_{R,test}$	ψ	$V_{R,test}/V_{R,calc}$	$V_{R,test}/V_{R,calc}$
	MN (kip)	mRad	quadrilinear	parabolic
PL1	0.68 (153)	6.0	1.00	1.04
PV1	0.97 (219)	7.6	1.04	1.06
PL6	1.36 (306)	18.6	0.98	1.07
PL7	1.77 (399)	32.0	1.07	1.12
PC23	1.19 (268)	8.4	1.13	1.14
PC24	2.15 (483)	21.6	1.00	1.06
PC25	1.20 (270)	4.7	1.07	1.04
PC26	2.45 (551)	15.4	1.02	1.06
PP10	2.15 (483)	35.2	1.00	1.07
PP12	3.22 (724)	30.7	1.18	1.21
PP13	2.10 (472)	29.4	0.99	1.05
PP14	3.23 (726)	32.1	1.05	1.09
PP15	2.97 (668)	30.9	1.00	1.05
PP16	2.97 (668)	30.9	1.04	1.08
PP17	1.62 (364)	28.6	1.04	1.10
Mean			1.04	1.08
COV			5.3	4.3

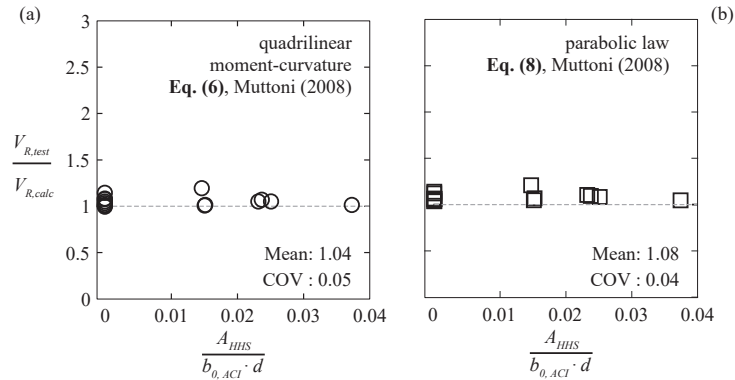


Figure 5.14: Comparison of measured and calculated responses: (a) quadrilinear moment-curvature law (Eq. (6) in Muttoni [11]); and (b) parabolic law (Eq. (8) in Muttoni [11]).

Table 5.6: Estimation of delamination length x_h according to proposed mechanical model

Slab	d_b	x_h^*
	mm (in.)	mm (in.)
PP10	25 (0.98)	27.1 (1.07)
PP12	25 (0.98)	24.0 (0.94)
PP13	25 (0.98)	27.4 (1.07)
PP14	32 (1.26)	55.5 (2.19)
PP15	40 (1.57)	104.8 (4.13)
PP16	32 (1.26)	55.6 (2.19)
PP17	32 (1.26)	60.7 (2.39)

* typos corrected from online version

5.4 Conclusions

In this paper, a punching shear reinforcing system comprising the use of large-diameter horizontal double-headed studs (studs arranged parallel to the plane of the slab in the compression zone) as shear dowels is presented. The performance of the system is verified by means of a specific testing program and compared to that of geometrically equivalent slabs without shear reinforcement or with conventional shear reinforcement (shear reinforcement arranged perpendicular to the plane of the slab). Design for the system is eventually investigated on the basis of the Critical Shear Crack Theory (CSCT). The main conclusions of this investigation are:

1. The system exhibits a significantly enhanced performance in terms of the punching strength and deformation capacity (rotation at maximum load) when compared to slabs without shear reinforcement or with conventional shear reinforcement. For the tests presented in this paper, the failure load increases up to 250 to 270% of the strength corresponding to members without shear reinforcement. The deformation capacity increases also to more than 700% of the corresponding value for specimens without shear reinforcement. Such enhancement is higher than for members with conventional shear reinforcement composed only of vertical studs, particularly with respect to the deformation capacity (which can be doubled when horizontal studs are arranged in addition to vertical studs).
2. Horizontal double-headed studs are shown to be an efficient solution as shear dowels. They allow transferring shear forces, which reduce the amount of shear that has to be transferred by the critical shear crack, thus enhancing the strength of the specimen.
3. The activation of the horizontal shear dowels is related to a penetration of the column in the slab. This yields to a failure mode with an enhanced deformation capacity when compared to slabs without shear reinforcement or with conventional shear reinforcement.
4. A mechanical model based on the theoretical framework of the CSCT is presented. The model consistently accounts for the contribution of the shear dowels in the punching failure criterion.
5. The model based on the CSCT is shown to provide sound and accurate predictions when compared to test results on specimens reinforced with this system. It further allows investigating on the actual contribution of this reinforcement to the total strength and to calculate some mechanical parameters as the extent of the potential delamination due to bending of the shear dowel.

Notation

A_b	breakthrough surface
$A_{b,dow}$	effective concrete area opposing to force of one dowel
A_{HHS}	gross area of horizontal headed bars (<i>HHS</i>)
B	side length of slab
$b_{0,ACI}$	perimeter of critical section according to ACI 318-14
b_e	width of equivalent section
c	side length of supporting area
c_d	distance between slab soffit and center of mass of HHS bars in bottom side
c_{nom}	nominal concrete cover
d	distance from extreme compression fiber to centroid of longitudinal tensile reinforcement
d_{avg}	nominal distance from extreme compression fiber to centroid of longitudinal tensile reinforcement in case of horizontal headed studs positioned in tensile zone
d_b	diameter of flexural reinforcement
$d_{b,HHS}$	diameter of <i>HHS</i> bars
d_g	aggregate size
d_{g0}	reference aggregate size
d_{nom}	nominal distance from extreme compression fiber to centroid of longitudinal tensile reinforcement
dx	spacing between gauges glued in <i>HHS</i> bars
f_c	average compressive strength of concrete (cylinder)
f_{cc}	compressive strength of confined concrete
f_{ct}	concrete tensile strength
$f_{ct,eff}$	effective concrete tensile strength
f_y	yield strength of flexural reinforcement
h_f	height of bar carrying bending moment
h_τ	height of bar carrying shear force
l	distance between plastic hinges
M_R	bending resistance of hinges
n_{dow}	number of dowelled sections
n_r	number of radii of shear reinforcement
n_s	number of shear reinforcements per radius
r_q	distance between load introduction point and axis of supported area
s_0	nominal distance with respect to slab plane between edge of support region and first shear stud
s_1	nominal distance with respect to slab plane between two adjacent studs of same radius
s_{HHS}	nominal distance between horizontal headed studs (<i>HHS</i>)
V	resultant shear force applied on supporting area
V_c	contribution of concrete
V_{dow}	contribution of dowelling action calculated with limit analysis
V_n	punching capacity

$V_{n,max}$	maximum punching capacity
V_R	punching shear strength
$V_{R,C SCT}$	design punching capacity according to CSCT accounting for dowelling action according to simplified parabolic law or quadrilinear moment-curvature relationship
$V_{R,calc}$	calculated/design punching capacity
$V_{R,test}$	experimental punching capacity
V_s	contribution of steel reinforcement
x_h	estimation of delamination length
α	angle of critical shear crack
χ	measured curvature of shear dowel
χ_y	yielding curvature of shear dowel
ϵ_s	steel strain
ϵ_y	steel strain at yielding
γ	angle of concrete breakout surface
λ	crushing strength parameter
ρ_l	flexural reinforcement ratio
ρ_w	shear reinforcement ratio
ψ	average of rotations at point of moment contraflexure
ψ_R	measured rotation at failure

Bibliography

- [1] S. Kinnunen and H. Nylander. Punching of Concrete Slabs Without Shear Reinforcement. Technical report, Transactions of the Royal Institute of Technology, Stockholm, Sweden, 1960.
- [2] FIB Bulletin 81. *Punching Shear of Structural Concrete Slabs: Honoring Neil M. Hawkins*. 2017.
- [3] Jürgen Einpaul, Miguel Fernández Ruiz, and Aurelio Muttoni. Influence of moment redistribution and compressive membrane action on punching strength of flat slabs. *Engineering Structures*, 86:43–57, 2015.
- [4] Jürgen Einpaul, C E Ospina, Miguel Fernández Ruiz, and Aurelio Muttoni. Punching Shear Capacity of Continuous Slabs. *ACI Structural Journal*, 113(4):861–872, 2016.
- [5] Jürgen Einpaul, Fabio Brantschen, Miguel Fernández Ruiz, and Aurelio Muttoni. Performance of Punching Shear Reinforcement under Gravity Loading : Influence of Type and Detailing. *ACI Structural Journal*, 113(4):827–838, 2016.
- [6] Yaser Mirzaei. *Post-punching behavior of reinforced concrete slabs*. PhD thesis, École polytechnique fédérale de Lausanne, 2010.
- [7] Miguel Fernández Ruiz, Yaser Mirzaei, and Aurelio Muttoni. Post-Punching Behavior of Flat Slabs. *ACI Structural Journal*, 110(5):801–812, 2013.
- [8] Farshad Habibi, William D. Cook, and Denis Mitchell. Predicting post-punching shear response of slab-column connections. *ACI Structural Journal*, 111(1):123–134, 2014.
- [9] Francesco Cavagnis, Miguel Fernández Ruiz, and Aurelio Muttoni. An analysis of the shear-transfer actions in reinforced concrete members without transverse reinforcement based on refined experimental measurements. *Structural Concrete*, 19(1):49–64, 2017.
- [10] Francesco Cavagnis, Miguel Fernández Ruiz, and Aurelio Muttoni. A mechanical model for failures in shear of members without transverse reinforcement based on development of a critical shear crack. *Engineering Structures*, 157:300–315, 2018.
- [11] Aurelio Muttoni. Punching shear strength of reinforced concrete slabs without transverse reinforcement. *ACI Structural Journal*, 105(4):440–450, 2008.
- [12] Miguel Fernández Ruiz and Aurelio Muttoni. Applications of critical shear crack theory to punching of reinforced concrete slabs with transverse reinforcement. *ACI Structural Journal*, 106(4):485–494, 2009.
- [13] Stefan Lips, Miguel Fernández Ruiz, and Aurelio Muttoni. Experimental Investigation on Punching Strength and Deformation Capacity of Shear-Reinforced Slabs. *ACI Structural Journal*, 109(6):889–900, 2013.
- [14] CEN10080:2005. *Steel for the reinforcement of concrete - Weldable reinforcing steel - General*. European Committee for Standardization, Brussels, Belgium, 2005.
- [15] Jürgen Einpaul, Jan Bujnak, Miguel Fernández Ruiz, and Aurelio Muttoni. Study on Influence of Column Size and Slab Slenderness on Punching Strength. *ACI Structural Journal*, 11:135–145, 2016.
- [16] João T. Simões, Miguel Fernández Ruiz, and Aurelio Muttoni. Validation of the Critical Shear Crack Theory for punching of slabs without transverse reinforcement by means of a refined mechanical model. *Structural Concrete*, 19(1):191–216, 2018.

-
- [17] Aurelio Muttoni, Miguel Fernández Ruiz, and João T. Simões. The theoretical principles of the critical shear crack theory for punching shear failures and derivation of consistent closed-form design expressions. *Structural Concrete*, 19(1):174–190, 2017.
- [18] Miguel Fernández Ruiz, Aurelio Muttoni, and Jakob Kunz. Strengthening of flat slabs against punching shear using post-installed shear reinforcement. *ACI Structural Journal*, 107(4):434–442, 2010.
- [19] Miguel Fernández Ruiz and Aurelio Muttoni. Performance and design of punching shear reinforcing systems. In *3rd International fib congress*, page 15, Washington, USA, 2010.
- [20] Jesper Harrild Sørensen, Morten Andersen Herfelt, Linh Cao Hoang, and Aurelio Muttoni. Test and lower bound modeling of keyed shear connections in RC shear walls. *Engineering Structures*, 155:115–126, 2018.
- [21] R V Mises. Mechanics of plastic deformation in crystals. *Math Mech*, 8:161–185, 1928.
- [22] B. H. Rasmussen. Strength of Transversely Loaded Bolts and Dowels Cast in Concrete. *Bygningstatiske Meddelelser*, 34(2):39–55, 1963.
- [23] M P Nielsen and Linh Cao Hoang. *Limit Analysis and Concrete Plasticity*. 2016.
- [24] Aurelio Muttoni, Miguel Fernández Ruiz, Evan C. Bentz, Stephen J Foster, and V. Sigrist. Background to the Model Code 2010 Shear Provisions - Part II Punching Shear. *Structural Concrete*, 14(3):204–214, 2013.
- [25] Beatrice Belletti, Matteo Scolari, Aurelio Muttoni, and Raffaele Cantone. Shear strength evaluation of RC bridge deck slabs according to CSCT with multi – layered shell elements and PARC_CL Crack Model. In *IABSE Conference Geneva 2015*, pages 1158–1165, Geneva, Switzerland, 2015.
- [26] Raffaele Cantone, Beatrice Belletti, Aurelio Muttoni, and Miguel Fernández Ruiz. Approaches for suitable modelling and strength prediction of reinforced concrete slabs. In *fib Symposium*, pages 21–23, Cape Town, South-Africa Year, 2016.

Chapter 6

Conclusions and Outlook

6.1 Introduction

The present thesis deals with the mechanics of shear failures in reinforced concrete slabs without shear reinforcement. The analysis of the structural response of these members can be cumbersome due to the presence of inclined cracking and the localization of strains within a critical shear crack leading to failure. With this respect, it becomes of great importance a suitable evaluation of the shear deformations, which govern in conjunction with the flexural behaviour, the load-carrying capacity of the member. In addition to Chapters 1 and 6, this thesis is thus a compilation of four scientific journal articles addressing different phenomena related to the behaviour of reinforced concrete slabs failing in shear. Most research on this topic was typically focused on the strength of the member neglecting, in most cases, the propagation of the failure surface, the influence of shear deformations and the redistribution of internal forces. This fact was mainly due to the lack of refined experimental observations on the concrete surface and on the interactions engaged between the reinforcing bars and the surrounding concrete.

Chapter 2 presents novel experimental data obtained with refined measurements of the concrete and rebar surfaces as an attempt to provide a promising methodology for a detailed investigation of concrete members tested in laboratory. In particular, an experimental programme on classical tests including two bond tests, eight tensile tests and three beam tests was carried out using Digital Image Correlation and Fibre Optic strain sensors with the aim to provide detailed findings on the evolution of bond stresses after cracking, on stress concentrations at cracks (and the associated residual stresses when subjected to cycles of loading/unloading). An analysis of the response of the reinforcement is performed, particularly regarding the development of bending/shear cracks associated to local kinking of the bar and dowel action. Moreover, this chapter presents an interpretation of the observed results which are compared to available theoretical approaches showing the complexity of the actual interactions as well as a number of implications for practical design.

Chapter 3 presents the analysis of detailed experimental observations of the concrete surface [1, 2] performed on cantilever beams without shear reinforcement (members governed by shear failures). In particular, the aim of this study was the investigation of the strain field of a concrete member due to the presence of inclined shear cracking as well as the characterization of the through-thickness distribution of the shear deformation with the level of load. The evaluation of the shear deformations can be instrumental for the correct estimate of the response of reinforced concrete members failing in shear. It is observed that the profile of shear strains is correlated to the prop-

agation of the shear crack giving rise to a rather significant contribution of the shear deformation when the sub-horizontal branch in the upper part of the shear critical crack develops. On this basis, a mechanical model is proposed for the characterization of the average response of the cross section as well as the associated through-thickness distribution of the shear deformation based on the theoretical principles of the Critical Shear Crack Theory [3, 4]. This comprehensive approach allows to determine the strain field of the cross section as a function of the acting moment and shear force showing its accuracy in the evaluation of the load-carrying capacity of selected test data on slabs failing in shear.

Chapter 4 introduces a review of tests results (collected from the literature) performed on wide reinforced concrete members subjected to strip and concentrated loads. Then, the results of a testing programme on three cantilever slabs subjected to different loading and geometrical conditions are presented. In order to better understand the redistribution of internal forces in reinforced concrete slabs and wide beams, refined measurements were performed on the concrete surface and on the reinforcement bars showing the significance of the propagation of the failure surface (and the associated redistributions when some regions are in softening while others have still not reached their local shear resistance). For wide members failing under predominant one-way action, experimental evidences show the influence of the width of the member on the development of the failure surface which presents an uneven shape over the width and local deviations. A detailed interpretation of these observations is thus provided within the framework of the Critical Shear Crack Theory [3, 4] giving new insights on the potential favourable effect of the shape of the crack on the load-carrying capacity for members with intermediate width-to-effective depth ratios.

For linearly supported slabs subjected to concentrated loads, it is observed that the shear resistance is affected by the clear shear span and by the width of the member. An interpretation of these observations are provided using the comprehensive approach presented in Chapter 3 for the characterization of the shear deformation of a cross section. Other than giving sound estimations of the failure loads (by comparison with different testing programmes [5–7]), such approach shows to provide a rational description of the response of reinforced concrete slabs with respect to the clear shear span, the width of the member and the boundary conditions. On this basis, practical recommendations for the design and assessment of reinforced concrete slabs based on level-of-approximations are finally proposed in order to account in a sound manner for the potential shear redistributions as well as for the influence of geometrical and mechanical parameters.

Chapter 5 presents the results of an extensive experimental programme on eleven axisymmetric punching tests on interior slab-column connections. Based on the principle of the dowel action of the compression reinforcement, this work introduces an innovative shear-reinforcing system to efficiently enhance the punching strength of slabs by using large diameter double-headed studs acting as shear dowels. The experimental evidences prove that the placement of horizontal double-headed studs in the compression zone can provide not only an increase of the punching strength but also of the deformation capacity of the member. Beyond the experimental results, this work presents the derivation of a design approach in accordance with the main principles of the Critical Shear Crack Theory [8, 9] accounting for the engagement of the horizontal studs as shear dowels. This design approach shows the contribution of such reinforcing system to enhance the performance of reinforced concrete slabs failing in punching showing good agreement with the test results.

6.2 Conclusions

Chapters 2–5 comprise a series of scientific publications [10–13] dealing with different aspects of the mechanics of shear failures in reinforced concrete slabs without shear reinforcement.

Chapter 2 presents a detailed view on the rebar–to–concrete interaction based on refined measurement techniques. The main conclusion of this chapter are listed below:

1. Local strain measurements at the ribs of the bars have pointed out large strain gradients originated by the mechanical engagement between the reinforcement and the surrounding concrete. These observations confirm that, when the strength is governed by the stress variation, the characterization of the material strength on bare rebars can be unsuitable to describe the response of embedded reinforcement.
2. Regarding the tests on reinforced concrete ties, the Fibre-Optic strain measurements allow to determine the negative tension-stiffening effects during the unloading process as well as the bond degradation with the number of cycles, providing results in accordance with the reductions proposed in the literature (both for the peak bond stress at maximum load and for the negative values of the bond stress at minimum load).
3. The analysis of the stress variations during unloading in reinforced concrete ties suggests that the values calculated on bare bars can differ significantly from the stress variations experienced by the embedded reinforcement due to a large extent by the imperfect closure of cracks.
4. In the case of beams subjected to concentrated loads, vertical cracks originated by bending forces give rise to the local kinking of the reinforcement (due to compatibility of deformations) and to the onset of transverse tensile stresses in the concrete which can trigger the potential development of delamination cracks and cover spalling.
5. When inclined cracking is present, the vertical component of the crack opening is associated to the development of delamination cracks and dowelling forces in the flexural reinforcement (which can be derived on the basis of the recorded strains and the calculated bending moments of the bar). In addition, delamination cracks give rise to a loss of the bond strength and to an increase of the opening of the critical shear crack.

Starting from the results obtained on beams without shear reinforcement in Chapter 2, the development of shear cracking was further investigated in Chapter 3 with respect to the characterization of the shear deformation of concrete members consistently with the shape and kinematics of a critical shear crack. The main findings of this work are the following:

1. When the distribution of shear forces is not uniform (such as for slabs subjected to concentrated loads), the role of the shear deformation becomes significant for the evaluation of the load-carrying capacity. In particular, the concentrations of shear forces give rise to local shear failures and the potential to redistribute shear forces, allowing to further increase the load-carrying capacity.
2. By means of refined measurements of the concrete surface of beams without shear reinforcement, it is recognized that the through-thickness distribution of shear strains depends upon the shape and kinematics of the critical shear crack. Before the development of the sub-horizontal branch of the shear crack, the profile of the shear deformation can be assumed to be linearly distributed over the cracked portion of the member, turning into bilinear-shaped at a level of load corresponding to the failure of the concrete tooth.
3. Based on the shape and kinematics of the critical shear crack, the flexibility matrix describing the average flexural and shear deformations of the member can be established showing how the shear deformation is significantly related to the acting bending moment at the tip of the crack.

Such contribution provided by the flexural deformations becomes particularly relevant after the formation of the sub–horizontal crack.

4. The comprehensive approach accounting for the development of shear deformations can be efficiently used in a condensed manner to characterize the response of reinforced concrete slabs by means of finite element models. This allows to model out-of-plane shear failures with structural shell elements taking into account the degradation of the shear stiffness due to the presence of inclined cracking. The application of this approach provides results in sound agreement with tests on slabs collected from the literature showing the significance of shear redistributions on the load–carrying capacity of members with different boundary conditions.

The phenomenon of shear redistributions in reinforced concrete slabs was further studied in Chapter 4 with an experimental programme on three cantilever slabs subjected to strip loads and concentrated loads with detailed observations of the kinematics of the concrete surface and of the strains in the flexural reinforcement. The main conclusions of this work are listed below:

1. The shear capacity of members subjected to predominant one–way action can be affected by the width of the member. In particular, in the case of wide beams subjected to strip loads with width-to-effective depth ratios (b/d) less than 5, a slight enhancement of the shear capacity was observed. This fact can be related to the variability of the failure surface (shape of the critical shear cracks) over the width of the member leading to potential redistributions of the internal forces.
2. For members subjected to strip loads with ratios $b/d > 5$, the increase of the shear capacity is less pronounced due to the potential concentrations of shear forces at the edges, to the difficulty to apply uniform load and support conditions over the width of the member and to the Poisson's effect of the compression zone.
3. In reinforced concrete slabs subjected to concentrated loads near linear supports, the role of the width of the member is more relevant than the one observed in wide beams. This is related to the fact that wider members have more potential to redistribute the internal forces while developing the complete failure surface allowing to enhance their load–carrying capacity. Thus, for these members it becomes important the consideration of shear redistributions for a realistic estimate of the failure load.
4. A Levels-of-approximation approach seems a suitable strategy for the design and assessment of reinforced concrete slabs subjected to concentrated loads. For design purposes, redistributions can be taken into account by averaging the shear forces over prescribed widths providing reasonable and safe predictions of the load–carrying capacity. A nonlinear analysis considering the development of the shear deformation is thus recommended for a more precise estimation of the strength and deformation capacity of the member.

Already mentioned in Chapters 2–4 with respect to the response of beams and slabs without shear reinforcement, the phenomenon of dowel action is investigated in Chapter 5 with respect to punching failures of interior slab–column connections, leading to the following conclusions:

1. The punching strength and the deformation capacity of interior slab–column connections can be efficiently enhanced when horizontal double–headed studs are placed in the shear critical region. This enhanced performance is related to the efficiency of the horizontal studs acting as shear dowels, which reduce the amount of shear to be transferred by the critical shear crack.
2. The activation of the dowelling forces is accompanied by a penetration of the column in the slab and by a significant increase of its deformation capacity (which can be doubled when horizontal studs are placed in addition to vertical studs).

3. On the basis of the main principles of the Critical Shear Crack Theory, a design approach accounting for the contribution of dowel action of compression reinforcement is introduced in the failure criterion for punching failures.
4. The model provides sound and accurate predictions of the load-carrying capacity. In addition, this approach allows gathering valuable insights on the amount of shear forces carried by dowel action and on the development of the delamination crack due to the dowelling of the reinforcement.

6.3 Outlook and future works

This work provided new findings for a better understanding of the mechanics of shear failures in reinforced concrete members but some questions remain open. In the following, some ideas for future research are given with respect to the different phenomena investigated in this thesis.

Phenomena related to rebar-to-concrete interaction

Systematic experimental programmes with detailed measurements are needed to establish a refined relationship between the bond stress and the crack opening. In particular, the residual stresses at cracks due to cycles of loading/unloading and the influence of negative tension-stiffening effects should be further investigated providing a rational model for the estimation of the stress variations of embedded reinforcement. A sound evaluation of such stress variations is instrumental for the verification of structural elements governed by fatigue of reinforcement or by the level of crack opening at serviceability limit states.

With respect to dowel action, Fibre Optic Measurements have shown to provide reasonable estimates of the bending and shear forces of the reinforcement. Similarly to the experimental works presented in [14], targeted experimental programmes with detailed measurements could be performed to analyse the contribution of dowel action as a function of the imposed crack kinematics under monotonic and cyclic loading (potentially, with different strain rates). These experimental data could play a significant role in the understanding of the contribution of dowel action in shear failures of reinforced concrete members as well as on the influence of the stress concentrations due to kinking of the reinforcement (see Chapter 2) when the concrete member is subjected to cyclic or fatigue loading [15]. The development of a comprehensive approach is thus needed to determine the internal forces of the reinforcement as a function of the geometrical and kinematical boundary conditions. This rational model should account for the shape and kinematics of the crack but also for the relationship between the bond stress and the crack opening.

Development of shear deformations and redistribution of internal forces

In chapter 3, an in-depth investigation of the development of the shear deformations was presented in the framework of beams and slabs without shear reinforcement failing in shear. These detailed findings allowed to establish a comprehensive approach for the description of the shear deformation of a concrete member as a function of the level of load, in agreement with the main principles of the Critical Shear Crack Theory [3, 4]. Nevertheless, scanty experimental data were available for the characterization of the shear deformation after attaining the maximum load. With this respect, systematic experimental programmes are needed to investigate the post-peak response of a concrete member as well as the contribution of the dowel action, which can be identified as the main shear-carrying action governing the post-peak resistance. On this basis, a mechanical model for the characterization of the post-peak response should be developed allowing to evaluate in a consistent manner the level of deformation of the cross-section in the post-peak stage. This aspect is instrumental for the response of redundant systems where local shear failures may occur giving

rise to the potential redistributions of internal forces and a further increase of the load-carrying capacity.

The response of wide beams and slabs

As presented in Chapter 4, there is still no general consensus in the scientific community about the response of wide beams and slabs. Novel experimental data and a detailed interpretation of the test results have shown that the width of the member can play an important role on the response of redundant members subjected to strip or concentrated loads. In particular, the propagation of the failure surface and the development of shear strains were identified as key aspects for a sound evaluation of the load-carrying capacity. With this respect, systematic experimental programmes with refined measurements are still needed to increase the knowledge on the behaviour of reinforced concrete wide members subjected to strip loads and concentrated loads.

Concerning members subjected to strip loads, care should be devoted to the application of the external load in order to provide a uniform distribution over the width of the member and to avoid stress concentrations at the edges. The influence of the width of the member on the load-carrying capacity should be investigated particularly for wide members with intermediated width-to-depth ratios (b/d) where the influence of the shape of the critical shear crack could provide a favourable effect on the resistance of the member.

Regarding reinforced concrete slabs subjected to concentrated loads, refined experimental data of the strain field are also required for the analysis of members subjected to two or four concentrated loads (as recommended by code provisions) and with dimensions similar to actual design conditions (particularly, concerning the width of the member). This may allow for a detailed interpretation of the propagation of the failure surface and to better understand the response of shear-critical regions in actual design conditions.

Modelling of reinforced concrete slabs

On the basis of the comprehensive approach presented in Chapter 3, a condensed response of the cross section shear force-shear strain relationship was used by means of a lumped approach accounting for the development of shear strains. Even though such technique proved to provide a coherent interpretation of the mechanics of reinforced concrete slabs, it represented a practical but simplified solution to describe their response. With this respect, in addition to the condensed response in which shear deformations were localized in selected control sections, Chapter 3 presented also an approach to describe the through-thickness distribution of the shear deformation. This technique could be particularly suitable for a potential implementation in finite element layered-shell models avoiding the assumption of a prescribed control section and evaluating the shear deformation as a function of the local acting bending moment and shear force. This should allow to describe the behaviour of members with curved-shaped failure surfaces (in which the failure mode is intermediate between shear and punching), providing instrumental findings on the response of these members and on the governing shear-critical perimeters.

Other than the validation with specimens tested in laboratory, the suitability of this approach requires a comparison with actual situations (with actual load combinations from code provisions) in order to establish a general frame for the design of actual reinforced concrete slabs, accounting for the mechanical and geometrical boundary conditions as well as for the influence of shear redistributions on the load-carrying capacity. In addition, practical rules for the verification of slabs are needed, particularly with respect to the position of the loads and the governing control perimeters (consistent with punching and shear verifications).

Bibliography

- [1] Francesco Cavagnis, Miguel Fernández Ruiz, and Aurelio Muttoni. Shear failures in reinforced concrete members without transverse reinforcement: An analysis of the critical shear crack development on the basis of test results. *Engineering Structures*, 103:157–173, 2015.
- [2] Francesco Cavagnis, Miguel Fernández Ruiz, and Aurelio Muttoni. An analysis of the shear-transfer actions in reinforced concrete members without transverse reinforcement based on refined experimental measurements. *Structural Concrete*, 19(1):49–64, 2017.
- [3] Aurelio Muttoni and Miguel Fernández Ruiz. Shear Strength of Members without Transverse Reinforcement as Function of Critical Shear Crack Width. *ACI Structural Journal*, 105(2): 163–172, 2008.
- [4] Francesco Cavagnis, Miguel Fernández Ruiz, and Aurelio Muttoni. A mechanical model for failures in shear of members without transverse reinforcement based on development of a critical shear crack. *Engineering Structures*, 157:300–315, 2018.
- [5] Karin Reissen and Josef Hegger. Experimentelle Untersuchungen zur mitwirkenden Breite für Querkraft von einfeldrigen Fahrbahnplatten. *Beton- und Stahlbetonbau*, 108(2):96–103, 2013.
- [6] G A Rombach and S Latte. Shear resistance of bridge decks without shear reinforcement. In *Tailor Made Concrete Structures – Walraven & Stoelhorst (eds)*, pages 519–526, 2008.
- [7] Eva Olívia Lantsoght, Cor Van Der Veen, Ane De Boer, and Joost C. Walraven. One-way slabs subjected to combination of loads failing in shear. *ACI Structural Journal*, 112(4):417–426, 2015.
- [8] Aurelio Muttoni. Punching shear strength of reinforced concrete slabs without transverse reinforcement. *ACI Structural Journal*, 105(4):440–450, 2008.
- [9] João T. Simões, Miguel Fernández Ruiz, and Aurelio Muttoni. Validation of the Critical Shear Crack Theory for punching of slabs without transverse reinforcement by means of a refined mechanical model. *Structural Concrete*, 19(1):191–216, 2018.
- [10] Raffaele Cantone, Miguel Fernández Ruiz, Jan Bujnak, and Aurelio Muttoni. Enhancing Punching Strength and Deformation Capacity of Flat Slabs. *ACI Structural Journal*, 116(5): 261 – 274, 2019.
- [11] Raffaele Cantone, Miguel Fernández Ruiz, and Aurelio Muttoni. A detailed view on the rebar–to–concrete interaction based on refined measurement techniques. *Engineering Structures*, 226, 2021.
- [12] Raffaele Cantone, Andri Setiawan, Miguel Fernández Ruiz, and Aurelio Muttoni. Characterization of shear deformations in reinforced concrete members without shear reinforcement. *Engineering Structures*, *Submitted for review*, 2021.
- [13] Raffaele Cantone, Miguel Fernández Ruiz, and Aurelio Muttoni. Shear force redistributions and resistance of slabs and wide beams. *Structural Concrete*, *Submitted for review*, 2021.
- [14] Mohit Pundir, Max Tirassa, Miguel Fernández Ruiz, Aurelio Muttoni, and Guillaume Anciaux. Review of fundamental assumptions of the Two-Phase Model for aggregate interlocking in cracked concrete using numerical methods and experimental evidence. *Cement and Concrete Research*, 125(105855):1–17, 2019.
- [15] Francisco Natário, Miguel Fernández Ruiz, and Aurelio Muttoni. Experimental investigation on fatigue of concrete cantilever bridge deck slabs subjected to concentrated loads. *Engineering Structures*, 89:191–203, 2015.

CURRICULUM VITAE - RAFFAELE CANTONE

Raffaele Cantone

21/09/1990

Caserta, Italy

Rue du Maupas 10, CH-1004 Lausanne

+41 76 268 6287

ing.rcantone@gmail.com



EDUCATION

2015-2021 PhD Candidate

Structural Concrete Laboratory (IBETON), *Swiss Federal Institute of Technology* (EPFL), Lausanne (CH)

2012-2015 Master in Civil Engineering

University of Parma, Italy

2009-2012 Bachelor in Civil Engineering

University of Parma, Italy

PERSONAL EXPERIENCE

2015-2021 PhD Assistant

Structural Concrete Laboratory (IBETON), *Swiss Federal Institute of Technology* (EPFL)

Experimental and theoretical work focusing on the mechanics of shear failures in reinforced concrete slabs based on refined measurements

LANGUAGES

native Italian

fluent English | French

SCIENTIFIC PUBLICATIONS

Cantone, R.; Belletti, B., Manelli L., M.; Muttoni, A. (2016). *Compressive membrane action effects on punching strength of flat RC slabs*. Key Engineering Materials. V. 711. pp. 698-705. Trans Tech Publications.

Cantone, R., Belletti, B., Muttoni, A., Fernández Ruiz, M. (2016). *Approaches for suitable modelling and strength prediction of reinforced concrete slabs*. fib Symposium. Cape Town. South Africa.

Cantone, R., Fernández Ruiz, M., Muttoni, A., Belletti, B. (2018). *Combining finite element analyses and mechanical models for the assessment of reinforced concrete slabs*. 12th International fib PhD Symposium. Prague. Czech-Republic.

Cantone, R., Fernández Ruiz, M., Bujnak, J., Muttoni, A. (2019). *Enhancing Punching Strength and Deformation Capacity of Flat Slabs*. ACI Structural Journal. V. 116(5). pp. 261-274.

Cantone, R., Fernández Ruiz, M., Muttoni, A. (2020). *A new view in the understanding of the mechanical response of structural concrete by means of refined measurements*. fib Symposium, Shanghai. China.

Cantone, R., Fernández Ruiz, M., Muttoni, A. (2021) *A detailed view on the rebar-to-concrete interaction by means of refined measurement techniques*. Engineering Structures. V. 226. 111332.

Cantone, R., Setiawan A., Fernández Ruiz, M., Muttoni, A. (2021). *Characterization of shear deformations in reinforced concrete members without shear reinforcement*. Submitted for Engineering Structures.

Cantone, R., Fernández Ruiz, M., Muttoni, A. (2021). *Shear force redistributions and resistance of slabs and wide beams*. Accepted for publication in Structural Concrete.

